UNIVERSITÀ DEGLI STUDI DI FIRENZE

Dottorato in Fisica, XII° ciclo

Measurement of direct CP violation with the NA48 experiment at CERN

Tesi di Dottorato di Ricerca in Fisica di
Giacomo Graziani

Firenze, 30 Dicembre 1999

Candidato: Dott. Giacomo Graziani

Relatore: Prof. Enrico Iacopini

Coordinatrice: Prof. Annamaria Cartacci

Contents

Introduction

Fundamental symmetries are often part of the axiomatic basis of theories in all fields of physics, being the mathematical foundation of the conservation principles observed in nature. The invariance of laws of physics with respect to the parity reflection (P) and to the charge conjugation (C) is well established for what concerns the interactions responsible for the formation of ordinary matter, namely the electromagnetic and nuclear strong interactions. Therefore, particle physicist were particularly surprised and intrigued after the discovery, dated 1957, that P and C symmetries are maximally violated in weak interaction phenomena.

A small violation of the combination of the two symmetries (CP) was unexpectedly discovered in 1964 and undoubtedly observed so far only in the mixing of K^0 and $\bar{K}^0$ mesons. Nowadays, the underlying mechanism of this violation is not yet clear and its deep understanding could have a great impact not only in particle physics, but also in cosmology, being CP violation required to justify the matter/antimatter asymmetry observed in the Universe. It is indeed the subject of many research efforts from both the theoretical and experimental sides.

The high–precision experiments in the field of kaon physics, together with the newcoming experiments to study the $B^0 - \bar{B}^0$ meson, constitute the frontier in the experimental search for CP violation. One of the major challenge of the two last decades consists in establishing if the violation does occur or not directly in the K meson decay.

This thesis is devoted to the first results of NA48, the CERN experiment conceived to investigate direct CP violation in kaon decays with unprecedented accuracy.

After an overview on CP violation in the first two chapters, the detector and the experimental technique are described in chapter 3. The method used is the measurement of the double ratio R of K_S and K_L to $\pi^+\pi^-$ and $\pi^0\pi^0$ decays, by collecting simultaneously the four decay modes from two collinear K_S and K_L beams. The deviation from 1 of the double ratio is a clear sign of direct CP violation, leading to a non zero value of the parameter $Re(\epsilon'/\epsilon) \simeq (1 - R)/6$.

The general strategy of the data analysis, that has been carried out through a large team effort inside the NA48 collaboration, is outlined in chapter 4. The next two chapters are devoted to our original contribution to the analysis. The problem of understanding the different acceptance for K_S and K_L is discussed in detail in chapter 5. The effect in the analysis of the residual K_S and K_S /K_L interference in the "K_L " beam line is the subject of chapter 6. Finally, in chapter 7 the final result for $Re(\epsilon'/\epsilon)$ is given. The result is based on the data collected during 1997, corresponding to about 10 % of the statistics the experiment aims to accumulate. Nevertheless, this early result by itself confirms the occurrence of direct CP violation in kaon decays.

Chapter 1

CP symmetry and its violation

The definition of left and right, as well as of positive and negative charge, is usually considered, even by common sense, as an arbitrary convention. In the language of physics, this is due to the fact that the fundamental interactions responsible for the nuclear, atomic and molecular bonds in ordinary matter, namely the electromagnetic and nuclear strong forces, are invariant with respect to the inversion of the three directions of space (P), and the exchange of all particles with the corresponding anti–particles (C).

Nevertheless, experiments in the field of nuclear and high–energy physics have shown that these invariances do not hold anymore for the nuclear weak interactions. The violation of the combined symmetry (CP) is even more surprising, since it allows for an absolute simultaneous definition of what is left and what is positive charge, and allows to break down the matter/antimatter symmetry of the Universe.

In this chapter we briefly summarize the phenomenology of CP violation and we give the status of the experimental search for the direct violation in the decay of neutral K mesons.

1.1 Fundamental discrete symmetries

A physical system exhibits a symmetry when every real physical state transforms under the symmetry operation into another real state, having the same energy. This implies that the equations governing the evolution of the system are invariant under such symmetry transformations. In quantum mechanics the invariance is expressed by the commutativity of the hamiltonian operator H and the operator S associated to the symmetry operation:

$$[H, S] = 0 \tag{1.1}$$

The eigenstates of S, that are physical states with a definite property under the symmetry transformation, conserve in time their eigenvalues. For example, if we assume the isotropy of three–dimensional space the laws of physics must be invariant with respect to rotations (in other words, the orientation of the reference frame used to describe the system can be chosen arbitrarily). Since the rotation operator is a function of the angular momentum operators, the symmetry causes the angular momentum of an isolated system to be conserved in time.

The existence of a conservation principle associated to a symmetry is demonstrated in general for all continuous symmetries (Noether's theorem). The most relevant fundamental examples other than the space isotropy, are the homogeneity of time, leading to the conservation of energy, and the homogeneity of space, leading to the conservation of three-momentum.

Up to 1957, three discrete symmetries were commonly assumed by physicists to be of general validity as the ones mentioned above:

Parity (P): it consists in inverting the direction of the three axes of the spatial reference frame. This operation transforms, for example, a right hand in a left one, a chiral L–type molecule into its R–type counterpart, and makes the clocks go counter–clockwise. The arbitrariness in the definition of left and right reflects the existence of this symmetry in our every–day life. To realize it, let's suppose to have a phone call with an extra–terrestrial friend living in a far galaxy, and to try to agree with him about what is left. Of course we could not use mere conventional facts as the sense of rotation of clocks, that would probably be opposite if an australian guy had fixed it. But we could not cite even more "natural" phenomena, as the fact that most of people are right–handed (actually, we are not even sure that our friend has two hands ...), or that natural amino–acids rotate plane polarized light to the left[1], since these are likely to be accidental facts in the evolution of our particular world.

This invariance is very practical in particle physics, since all particles have a definite parity, i.e. they are eigenstates of the parity operator, and the conservation of their eigenvalues ($\pm$ 1) puts strong constraints on the possible decay modes.

Charge Conjugation (C): this is the inversion of a particle with its anti–particle, and vice versa. Though our world is completely made of matter, for every known particle, a corresponding anti–particle has been found, having opposite charge and the same mass and life–time.

Time Inversion (T): it consists in inverting the direction of time. It is well known that the constant increase of entropy of an isolated system breaks this symmetry, but this law, having a statistical nature, applies only to macroscopic systems, while the microscopic reversibility of fundamental interactions is usually assumed.

The combination (in any order) of these symmetries (CPT) is proven to be true, assuming Lorentz invariance and the very first principles of any conceivable quantum theory, after a famous theorem by Schwinger and Lüders, then generalized by Pauli (CPT theorem [49, 28]). A major consequence of the theorem is the equality of mass and lifetime of particles and corresponding anti–particles, even if C symmetry is broken. When it was formulated, the CPT theorem sounded to many physicists as an academic exercise, since each of the three symmetries was believed to hold by itself, as it was proven with high level of accuracy for all phenomena governed by the electromagnetic and nuclear strong interactions.

[1]The fact that "right handed" amino–acids can be synthesized as well as the left handed ones seems to exclude an asymmetry of fundamental forces responsible for molecular bonds. Actually, some speculative models have been proposed to explain the chiral asymmetry of the organic molecules in terms of the parity violation of weak interactions, but without giving any strong proof.

1.2 Parity violation

The first doubts about the fact that parity is always conserved were raised by the so–called $\tau - \theta$ *puzzle*, from the name of the two weak–decaying particles that, having the same mass, lifetime, charge, spin and production cross section, were distinguished only by the parity of their decay products[2]. The possibility that the parity symmetry could be violated by weak interactions was first proposed by Lee and Yang [38] in 1957 and experimentally demonstrated during the same year by the famous experiment of madame Wu and others [59]. The experiment observed that the angular distribution of β decay electrons emitted from a polarized nucleus depends on the scalar product between the particle momentum and the nuclear polarization vector. Since this product changes sign after parity reflection, the dependence is an evidence of parity violation.

It was immediately clear that the violation was maximal, in the sense that only the left–handed components[3] of the particle wave functions (and right–handed for the anti–particles) take part in the weak interaction hamiltonian. The helicity of the neutrino, that interacts only through weak interactions, was indeed found to be always -1 in an experiment carried out during the same year by Goldhaber and others [32].

This discovery broke down an ancient prejudice, for which the physics community felt the parity violation as astonishing as thinking that "God was left–handed", to use Wolfgang Pauli's words. However, a way to recover a good symmetry also for weak interactions was identified, even before the result of madame Wu, by Landau [37] in the invariance under CP. In fact, all the experimental results were compatible with a theory in which the role of left–handed particles and right–handed anti–particles is exactly symmetric, as was the $V - A$ theory of weak interactions.

Coming back to our extra–terrestrial friend, we could now think to call him and to use the neutrino helicity as an absolute way to decide a common definition of left and right. Nevertheless, to agree about what is a neutrino and what is an anti–neutrino, we should share a common definition of positive charge. Since our friend

[2] This particle is now called charged kaon.

[3] For left–handed components, we mean the projections into the states of negative chirality, that, in the limit of mass much smaller than energy, coincide with the states of negative helicity $h = \vec{p} \cdot \vec{s} / |\vec{p} \cdot \vec{s}|$.

lives in a very far galaxy, we cannot be sure that his world is made of matter[4], so that, if CP symmetry holds, we are in troubles again.

1.3 CP violation in kaon decays

The decay of neutral kaons is the first, and so far the only one, phenomenon in which CP conservation has been found to be violated. The discovery, this time without any previous hint, was done in 1964 by the celebrated experiment of Christenson, Cronin, Fitch, and Turlay [18].

Before describing the experiment, let's introduce the formalism used to describe the neutral kaon system. Its peculiarity relies in the fact that the K^0 and its anti–particle, the $\bar{K^0}$, are distinguished by the strong interaction through the strangeness quantum number S, not conserved by the weak interaction, that is responsible for their decays. Thus, a K neutral meson is produced by the strong interaction in a state of definite strangeness (K^0 or $\bar{K^0}$), but the weak hamiltonian makes the system evolve into a strangeness–mixed state.

We describe the general neutral kaon state in a two–dimensional Hilbert space having the K^0 and $\bar{K^0}$ states as a basis. The CP operator connects the two basis states:

$$\begin{cases} CP|K^0\rangle = e^{i\phi_{CP}}|\bar{K^0}\rangle \\ CP|\bar{K^0}\rangle = e^{-i\phi_{CP}}|K^0\rangle \end{cases} \tag{1.2}$$

where ϕ_{CP} is an arbitrary[5] phase, that we choose to be zero.

To account for decays (without including all the possible decay final states in the Hilbert space) the time evolution is described by a non hermitian effective Hamiltonian of the form[6] [5]

$$\hat{H} \;=\; \hat{M} - i\frac{\hat{\Gamma}}{2} \;=\; \begin{pmatrix} M_{11} - i\frac{\Gamma_{11}}{2} & M_{12} - i\frac{\Gamma_{12}}{2} \\ M_{12}^{*} - i\frac{\Gamma_{12}^{*}}{2} & M_{22} - i\frac{\Gamma_{22}}{2} \end{pmatrix} \tag{1.3}$$

[4]The possible existence of galaxies made of antimatter is currently disfavored by cosmologists [21], but it has not yet been completely ruled out.

[5]The arbitrariness of the phase derives from the fact that the two states are not connected by the strong interaction that produces them.

[6]Throughout all the theoretical discussion on CP violation we will use the system of natural units ($\hbar = c = 1$).

where $\hat{M}$ and $\hat{\Gamma}$ are two hermitian matrices. Assuming CPT to be true, we get

$$\begin{aligned} \langle K^0|\hat{H}|K^0\rangle &= \langle K^0|CPT\ \hat{H}\ CPT|K^0\rangle = \langle \bar{K^0}|\hat{H}|\bar{K^0}\rangle \\ &\Longrightarrow \quad M_{11} = M_{22} = M, \qquad \Gamma_{11} = \Gamma_{22} = \Gamma \end{aligned} \tag{1.4}$$

Let's now assume that also CP symmetry holds. We get

$$\begin{aligned} \langle K^0|\hat{H}|\bar{K^0}\rangle &= \langle K^0|CP\ \hat{H}\ CP|\bar{K^0}\rangle = \langle \bar{K^0}|\hat{H}|K^0\rangle \\ &\Longrightarrow \quad M_{21}^* = M_{12}, \qquad \Gamma_{21}^* = \Gamma_{12} \end{aligned} \tag{1.5}$$

and $\hat{H}$ becomes a symmetric matrix. Therefore, the states with definite mass and lifetime, i.e. the eigenstates of the Hamiltonian, are equal mixtures of K^0 and $\bar{K^0}$:

$$|K_1\rangle = \frac{1}{\sqrt{2}}(|K^0\rangle + |\bar{K^0}\rangle) \tag{1.6}$$

$$|K_2\rangle = \frac{1}{\sqrt{2}}(|K^0\rangle - |\bar{K^0}\rangle) \tag{1.7}$$

The $|K_1\rangle$ and $|K_2\rangle$ states are clearly eigenstates of CP with eigenvalues, respectively, $+1$ and -1. Thus, CP conservation would put strong constraints on their decay modes: $|K_1\rangle$ would mainly decay into a two–pion state ($\pi^+\pi^-$ or $\pi^0\pi^0$) that is always a CP=1 eigenstate[7]. On the contrary, $|K_2\rangle$ would decay mainly into three pions ($\pi^+\pi^-\pi^0$ or $3\pi^0$) and *never* into 2 pions. Because of kinematical reasons, we expect $|K_1\rangle$ to have a much shorter lifetime than $|K_2\rangle$.

In fact, the neutral K mesons are found to decay with two components having very different lifetime: the K–short (K_S), with lifetime $\tau_S = .9\ 10^{-10}$ s, and the K–long (K_L), $\tau_L = 5\ 10^{-8}$ s.

Assuming CP conservation, K_S and K_L must coincide with K_1 and K_2, and a particle created in a pure K^0 state at time zero evolves as

$$\begin{aligned} |\psi(t)\rangle &= \frac{1}{\sqrt{2}}\left(e^{-i\left(M_S-\frac{i}{2\tau_S}\right)t}|K_S\rangle + e^{-i\left(M_L-\frac{i}{2\tau_L}\right)t}|K_L\rangle\right) = \\ &= \frac{1}{2}\left[\left(e^{-i\left(M_S-\frac{i}{2\tau_S}\right)t} + e^{-i\left(M_L-\frac{i}{2\tau_L}\right)t}\right)|K^0\rangle + \left(e^{-i\left(M_S-\frac{i}{2\tau_S}\right)t} - e^{-i\left(M_L-\frac{i}{2\tau_L}\right)t}\right)|\bar{K^0}\rangle\right] \end{aligned} \tag{1.8}$$

[7] Since the pions are spinless, the CP operation coincides with the interchange of the two particles. Because of Bose statistics, the two pions must be in a symmetric state, so that they must be CP eigenstates with eigenvalue $+1$.
For the $\pi^+\pi^-\pi^0$ and $3\pi^0$ states, we may think to add a π^0 to the CP=1 couple, and the CP eigenvalue will be

$$(CP)_{3\pi} = (CP)_{\pi^0}(-1)^{\ell} = (-1)^{\ell+1}$$

where ℓ is the relative orbital momentum of the π^0 with respect to the couple, and we have used the π^0 quantum numbers $C_{\pi^0} = 1$, $P_{\pi^0} = -1$. The small Q–value of the $K^0 \to 3\pi$ decay (<100 MeV) strongly favors the $\ell = 0$, thus CP=-1, state.

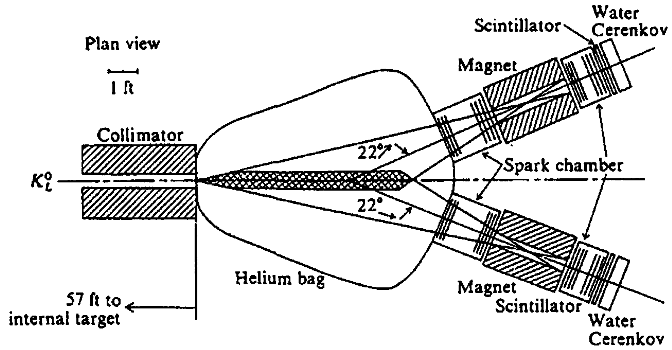

Figure 1.1: Scheme of the experimental arrangement used for the first detection of the CP violating $K_L \to \pi^+\pi^-$ decay [18].

where M_S and M_L are the mass eigenvalues of the two states. Therefore, the probability to detect a $\bar{K^0}$ after a time t is

$$|\langle \bar{K^0}|\psi(t)\rangle|^2 = \frac{1}{4}\left[e^{-\frac{t}{\tau_S}} + e^{-\frac{t}{\tau_L}} - 2e^{-\frac{t}{2}\left(\frac{1}{\tau_S}-\frac{1}{\tau_L}\right)}\cos(\Delta M t)\right] \tag{1.9}$$

This spectacular phenomenon of quantum interference is known as *strangeness oscillations*. The frequency of the oscillating term, coming from the interference of the K_S and K_L components, allows to measure with impressive level of accuracy the mass difference $\Delta M = M_L - M_S$. The present world average is [14]

$$\Delta M = M_L - M_S = 3.489 \pm 0.009 \ \mu eV/c^2 \tag{1.10}$$

meaning that the weak interaction splits by one part per 10^{14} the mass levels defined by the strong interaction, being the kaon mass about half GeV.

Up to 1964 all experiments on kaon physics were consistent with the identification of the mass and CP eigenstates. The CP–conserving scenario resulted to be only an approximate description of the real situation, after the discovery that the K_L mesons decay with a small ($2\ 10^{-3}$) branching ratio to $\pi^+\pi^-$.

The apparatus used by Cronin and his collaborators is sketched in fig. 1.1. A collimated neutral beam of about 1 GeV energy was entering a "cheap vacuum" plastic bag filled with helium at atmospheric pressure, placed 17.4 m away from the target in order to have a pure K_L beam. Two spectrometers consisting of bending magnets and spark chambers, triggered by the coincidence of water Čerenkov and scintillator counters, were detecting charged particles emitted from decays occurring inside the bag. The $\pi^+\pi^-$ events were identified by requiring the invariant mass of the two charged tracks to be compatible with the K^0 mass, and their total momentum to be aligned with the beam. The apparatus was tuned by placing a tungsten regenerator on the beam line, at different positions inside the bag, and by looking at the 2–pion decays of the regenerated K_S [8]. They recorded 45 ± 9 $\pi^+\pi^-$ events among an estimated sample of 22700 K_L decays, leading to a branching ratio of $(2.0 \pm 0.4) \cdot 10^{-3}$.

Another experimental evidence for CP violation in the neutral kaon system was soon detected [24] in the charge asymmetry of the semileptonic decays $K_L \to \ell^\pm \pi^\mp \overset{(-)}{\nu_\ell}$ (where ℓ is μ or e). It was found that the branching ratio for the decay with the positive lepton is higher by about 0.6 % than its CP–conjugate decay with the negative lepton.

"The charge of the lepton preferably emitted in the decays of long–lived neutral kaons" is a non–arbitrary definition of positive charge provided by CP violation, allowing us to finally define a common convention for left and right with all extraterrestrial particle physicists. We only need to be sure that the time in their reference frame flows in the same direction than in our.

The discovery that CP violation occurs in nature is also an important fact for Cosmology, since CP violation, together with the departure from thermal equilibrium during the Universe expansion and the non–conservation of baryon number, is one of the ingredients needed to explain within the Big Bang model the observed excess of matter over anti–matter in the Universe in terms of dynamics, without resorting to a whimsical initial condition [48].

---

[8]The relative K^0 and $\bar{K^0}$ amplitudes of a pure K_L state are changed by the interaction with matter, since K^0 and $\bar{K^0}$ have different interaction probability, so that the state becomes the superposition of a K_L and a "regenerated" K_S component.

1.4 Indirect CP violation

We now develop the formalism for the $K^0 - \bar{K^0}$ system without the CP conservation constrain. The diagonalization of the matrix in (1.3) leads to the eigenvalues

$$M_{L,S} = M \pm Re(Q) \tag{1.11}$$

$$\Gamma_{L,S} = \Gamma \mp 2Im(Q) \tag{1.12}$$

where

$$Q = \sqrt{\left(M_{12} - i\frac{\Gamma_{12}}{2}\right)\left(M_{12}^* - i\frac{\Gamma_{12}^*}{2}\right)} \tag{1.13}$$

The corresponding eigenstates are

$$|K_S\rangle = \frac{|K_1\rangle + \bar{\epsilon}|K_2\rangle}{\sqrt{1+|\bar{\epsilon}|^2}} \tag{1.14}$$

$$|K_L\rangle = \frac{|K_2\rangle + \bar{\epsilon}|K_1\rangle}{\sqrt{1+|\bar{\epsilon}|^2}} \tag{1.15}$$

where

$$\frac{1-\bar{\epsilon}}{1+\bar{\epsilon}} = \sqrt{\frac{M_{12}^* - i\frac{\Gamma_{12}^*}{2}}{M_{12} - i\frac{\Gamma_{12}}{2}}} = \frac{\Delta M - i\frac{i\Delta\Gamma}{2}}{2M_{12} - i\Gamma_{12}} \equiv r\ e^{i\kappa} \tag{1.16}$$

The $\bar{\epsilon}$ parameter expresses the CP–violating deviation of the mass eigenstates from the CP eigenstates, usually referred as **indirect CP violation**. It should be stressed that $\bar{\epsilon}$ depends on the phase convention for K^0 and $\bar{K^0}$ of equation (1.2), so that it may not be considered as a physical measure of CP violation. However, it can be shown that the physically meaningful parameters, independent from the phase convention, are $Re(\bar{\epsilon})$ and r .

We also notice that, unlike K_1 and K_2, the eigenstates K_S and K_L are not orthogonal[9]. This formally expresses the fact that they can decay to identical final states.

Indirect CP violation can be measured from the charge asymmetry of the semileptonic decays. In fact, in virtue of the empirical so–called $\Delta S = \Delta Q$ rule, the charge of the lepton in the final state selects the strangeness of the decayed kaon:

$$K^0 \rightarrow \ell^+\pi^-\nu_\ell \qquad \bar{K^0} \rightarrow \ell^-\pi^+\bar{\nu}_\ell$$

[9]We remind that, since the decay hamiltonian is not hermitian, the eigenstates corresponding to different eigenvalues do not need to be orthogonal.

so that, if we explicit the K^0 and $\bar{K^0}$ components of the K_S and K_L states as

$$|K_S\rangle = \frac{1}{\sqrt{2(1+|\bar{\epsilon}|^2)}}\left[(1+\bar{\epsilon})|K_0\rangle + (1-\bar{\epsilon})|\bar{K_0}\rangle\right] \tag{1.17}$$

$$|K_L\rangle = \frac{1}{\sqrt{2(1+|\bar{\epsilon}|^2)}}\left[(1+\bar{\epsilon})|K_0\rangle - (1-\bar{\epsilon})|\bar{K_0}\rangle\right] \tag{1.18}$$

the charge asymmetry of the K_L semileptonic decays will be

$$\begin{aligned}\delta_\ell &= \frac{\Gamma(K_L \to \ell^+\pi^-\nu_\ell) - \Gamma(K_L \to \ell^-\pi^+\bar{\nu}_\ell)}{\Gamma(K_L \to \ell^+\pi^-\nu_\ell) + \Gamma(K_L \to \ell^-\pi^+\bar{\nu}_\ell)} = \\ &= \frac{|\langle\ell^+\pi^-\nu_\ell|\hat{T}|K_L\rangle|^2 - |\langle\ell^-\pi^+\bar{\nu}_\ell|\hat{T}|K_L\rangle|^2}{|\langle\ell^+\pi^-\nu_\ell|\hat{T}|K_L\rangle|^2 + |\langle\ell^-\pi^+\bar{\nu}_\ell|\hat{T}|K_L\rangle|^2} = \\ &\simeq \frac{|1+\bar{\epsilon}|^2 - |1-\bar{\epsilon}|^2}{|1+\bar{\epsilon}|^2 + |1-\bar{\epsilon}|^2} \simeq 2Re(\bar{\epsilon})\end{aligned} \tag{1.19}$$

where $\hat{T}$ is the transition matrix and we have used the fact that CPT implies, for any final state f

$$\langle f|T|K^0\rangle = \langle\bar{K^0}|T|\bar{f}\rangle = \langle\bar{f}|T|\bar{K^0}\rangle^* \tag{1.20}$$

$$(|\bar{f}\rangle = CP|f\rangle)$$

so that

$$|\langle\ell^+\pi^-\nu_\ell|\hat{T}|K^0\rangle| = |\langle\ell^-\pi^+\bar{\nu}_\ell|\hat{T}|\bar{K^0}\rangle| \tag{1.21}$$

The relative effect on the asymmetry δ_ℓ from the possible violation of the $\Delta S = \Delta Q$ rule is known from the present experimental limits to be less than 10^{-4}.

The experimental value for $Re(\bar{\epsilon})$ from the δ_ℓ measurement is [14]

$$Re(\bar{\epsilon}) = (1.63 \pm 0.06) \cdot 10^{-3} \tag{1.22}$$

1.5 Direct CP violation

Coming back to the $K_L \to \pi\pi$ decay, the amount of CP violation is usually expressed by the parameters

$$\frac{\langle\pi^+\pi^-|\hat{T}|K_L\rangle}{\langle\pi^+\pi^-|\hat{T}|K_S\rangle} \equiv \eta_{+-} \equiv |\eta_{+-}|e^{i\phi_{+-}} \tag{1.23}$$

$$\frac{\langle\pi^0\pi^0|\hat{T}|K_L\rangle}{\langle\pi^0\pi^0|\hat{T}|K_S\rangle} \equiv \eta_{00} \equiv |\eta_{00}|e^{i\phi_{00}} \tag{1.24}$$

The indirect CP violation contributes to this process through the K_1 component of the K_L state, but we could also have an effect of **direct CP violation** in the decay $K_2 \to \pi\pi$, if the CP–conjugated decay amplitudes $\langle\pi\pi|\hat{T}|K^0\rangle$ and $\langle\pi\pi|\hat{T}|\bar{K^0}\rangle$ are not the same.

Assuming CPT, the decay amplitudes of two CP–conjugated processes must obey to equation (1.20). Therefore, they can differ only by the sign of their phase (often called *weak phase*). Equation (1.20) can be generalized to include the strong phase shift δ due to the final state interactions of the two pions, that is not CP–violating and appears with the same sign in both amplitudes (Watson's theorem [55]):

$$e^{-i\delta}\langle f|T|K^0\rangle \;=\; (e^{-i\delta}\langle\bar{f}|T|\bar{K^0}\rangle)^* \tag{1.25}$$

Of course, the phase of a single amplitude has not physical meaning by itself, so that direct CP violation can be detectable only if we are measuring final states where more than one amplitude enter the game. It is the case for the two pion final states that are the combination of two isospin states $|I, I_3 = 0\rangle$, with I =0 or 2 ($I = 1$ is forbidden by Bose statistics):

$$|\pi^+\pi^-\rangle = \sqrt{\frac{2}{3}}|0,0\rangle + \sqrt{\frac{1}{3}}|2,0\rangle \tag{1.26}$$

$$|\pi^0\pi^0\rangle = -\sqrt{\frac{1}{3}}|0,0\rangle + \sqrt{\frac{2}{3}}|2,0\rangle \tag{1.27}$$

The amplitudes for the different isospin states are defined as

$$\langle I,0|T|K^0\rangle \;=\; A_I e^{i\delta_I} \tag{1.28}$$

$$\langle I,0|T|\bar{K^0}\rangle \;=\; A_I^* e^{i\delta_I} \qquad (I = 0,2) \tag{1.29}$$

Since the kaons have isospin $I = 1/2$, the empirical $\Delta I = 1/2$ rule strongly favors the transitions to the $I = 0$ final state with respect to the $I = 2$ one. In fact, the ratio of the K_S branching ratios

$$\frac{BR(K_S \to \pi^+\pi^-)}{BR(K_S \to \pi^0\pi^0)} = \frac{|\langle\pi^+\pi^-|T|K_S\rangle|^2}{|\langle\pi^0\pi^0|T|K_S\rangle|^2} \approx 2\frac{|1 + \frac{1}{\sqrt{2}}\frac{Re(A_2)}{Re(A_0)}e^{i(\delta_2-\delta_0)}|^2}{|1 - \sqrt{2}\frac{Re(A_2)}{Re(A_0)}e^{i(\delta_2-\delta_0)}|^2} \tag{1.30}$$

has the experimental value 0.686/0.313=2.18, leading to ($\delta_2 - \delta_0 \simeq -\pi/4$)

$$\frac{Re(A_2)}{Re(A_0)} \approx 0.03 \tag{1.31}$$

Therefore, we introduce the variables

$$\xi_I \equiv \frac{Im(A_I)}{Re(A_I)} \tag{1.32}$$

$$\omega \equiv \frac{Re(A_2)}{Re(A_0)} e^{i(\delta_2-\delta_0)} \tag{1.33}$$

that will be developed to the first order. After some algebra, we obtain

$$\eta_{+-} = \frac{\bar{\epsilon} + i\xi_0 + (\bar{\epsilon}\omega + i\xi_2\omega)/\sqrt{2}}{1 + i\bar{\epsilon}\xi_0 + (\omega + i\xi_2\bar{\epsilon}\omega)/\sqrt{2}} \tag{1.34}$$

$$\eta_{00} = \frac{\bar{\epsilon} + i\xi_0 - (\bar{\epsilon}\omega + i\xi_2\omega)\sqrt{2}}{1 + i\bar{\epsilon}\xi_0 - (\omega + i\xi_2\bar{\epsilon}\omega)\sqrt{2}} \tag{1.35}$$

and, neglecting terms of $o(\bar{\epsilon}^2, \omega^2, \bar{\epsilon}\omega)$ and in any phase convention where $|\bar{\epsilon}\xi_0| << 1$, we finally get

$$\eta_{+-} \simeq \epsilon + \frac{\epsilon'}{1 + \omega/\sqrt{2}} \sim \epsilon + \epsilon' \tag{1.36}$$

$$\eta_{00} \simeq \epsilon - \frac{2\epsilon'}{1 - \sqrt{2}\omega} \sim \epsilon - 2\epsilon' \tag{1.37}$$

where

$$\epsilon \equiv \bar{\epsilon} + i\xi_0 = \bar{\epsilon} + i\frac{Im(A_0)}{Re(A_0)} \tag{1.38}$$

$$\epsilon' \equiv \frac{i\omega(\xi_2 - \xi_0)}{\sqrt{2}} = \frac{i}{\sqrt{2}}\frac{Re(A_2)}{Re(A_0)}\left[\frac{Im(A_2)}{Re(A_2)} - \frac{Im(A_0)}{Re(A_0)}\right] e^{i(\delta_2-\delta_0)} \tag{1.39}$$

ϵ is a physical parameter that quantifies the indirect violation (one can check that ϵ is independent from the phase convention). In a (often used) phase convention where A_0 is real, it coincides with $\bar{\epsilon}$, and in any case $Re(\epsilon) = Re(\bar{\epsilon})$.

Using the experimental result[10] $2\Delta M \simeq -\Delta\Gamma$ and the smallness of the CP violating effects, it can be shown [5] that an approximate formula for ϵ is

$$\epsilon \simeq e^{i\,\mathrm{arctg}\left(-\frac{2\Delta M}{\Delta\Gamma}\right)} \frac{Im(M_{12}) - iIm(\Gamma_{12})/2}{\sqrt{(\Delta M)^2 + (\Delta\Gamma)^2/4}} + i\frac{Im(A_0)}{Re(A_0)} \simeq e^{i\frac{\pi}{4}}\left(\frac{Im(M_{12})}{\sqrt{2}\Delta M}\right) \tag{1.40}$$

As a matter of fact, the phase of ϵ is found to be very close to $45°$.

The parameter ϵ' quantifies the direct CP violation. As we could expect, it depends from the difference of the weak phases of the amplitudes in different isospin channels.

[10] This result could be expected from the Heisenberg uncertainty relation $\Delta E \cdot \Delta T \gtrsim 1/2$, if we think that the K_L and K_S states, whose mass differ by ΔM, are decoupled, thus distinguishable, after a time of the order $1/\Gamma_S \simeq -1/\Delta\Gamma$.

The current experimental values [14]

$$|\eta_{+-}| = (2.285 \pm 0.019) \cdot 10^{-3} \qquad |\eta_{00}| = (2.275 \pm 0.019) \cdot 10^{-3} \tag{1.41}$$

are both compatible with $|\epsilon|$, showing that the K_L in two pion decay is dominated by the contribution of indirect violation.

From equation (1.39) we see that the phase of ϵ' is $\pi/2 + \delta_2 - \delta_0$ and, since $\delta_2 - \delta_0 \sim -\pi/4$, we get that the phases of ϵ and ϵ' are very close:

$$\frac{\epsilon'}{\epsilon} \approx Re\left(\frac{\epsilon'}{\epsilon}\right) \tag{1.42}$$

This is likely to happen accidentally, since there is no conceivable connection between the strong phases and the phase of ϵ.

1.6 Measurements of direct CP violation

As it will be discussed in the next chapter, the empirical results about CP violation can be accommodated within the Standard Model, but as of today there is no mechanism that explains naturally where CP violation comes from and why it seems to be so elusive. The determination of other CP violating parameters than the few that were measured so far could give an insight, since the Standard Model puts strong constraints about them.

The fact that CP seems to be a quasi–exact symmetry and that direct CP violation could be vanishing, triggered many ideas about new models where CP violation is attributed to a new kind of interaction. The most famous one is the *super–weak model* by Wolfenstein [57], where the $\Delta S = 2$ transitions between K^0 and $\bar{K}^0$ are attributed to a CP–violating effective four–fermion interaction, having a coupling constant of the order G_F^2 (where G_F is the Fermi constant). The model is consistent with the fact that the interaction is detectable only in the neutral kaon system, and predicts all the CP violating effects to be included in the mixing, namely $\epsilon' = 0$.

In order to check this prediction against the Standard Model where a non zero value of ϵ' is possible, the measurement of the amount of direct CP violation has been (and is being) the most afforded and challenging task of experimental kaon physics in the last two decades. The difficulty of such measurement mainly comes from the need to detect with high statistics and purity the decays of K_L into $\pi^0\pi^0$, that occur with $9 \cdot 10^{-4}$ branching ratio. The two pions immediately[11] decay into 2 gammas, and very precise calorimetry is needed to identify the events with kinematical criteria, in order to discriminate them from background, starting from the detection of the four gamma showers. The background is mainly due to $3\pi^0$ events, that have a 226 times larger branching ratio than $2\pi^0$, with two undetected photons. As a matter of fact, all the pioneering experiment of kaon physics were based on the detection of decays into two or three charged pions or to semileptonic modes, usually by mean of magnetic spectrometers.

The most convenient way to determine the ϵ' parameter from the experimental point of view is to measure the double ratio of $K \to \pi\pi$ decay intensities

$$R \;=\; \frac{\Gamma(K_L^0 \to \pi^0\pi^0)}{\Gamma(K_L^0 \to \pi^+\pi^-)}\frac{\Gamma(K_S^0 \to \pi^+\pi^-)}{\Gamma(K_S^0 \to \pi^0\pi^0)} = \frac{|\eta_{00}|^2}{|\eta_{+-}|^2} \;\simeq\; 1 - 6\ Re\left(\frac{\epsilon'}{\epsilon}\right) \tag{1.43}$$

where we have used equations (1.36) and (1.37). In fact, if the same apparatus is used to detect the four decay modes from the same beams, the intensity normalization factors and many experimental effects as efficiencies and acceptances cancel in the ratio.

Two experiments measured the double ratio with accuracy $6 \cdot 10^{-4}$ during the eighty:

NA31: this experiment was installed at the CERN Super–Proton–Synchrotron (SPS). The $\pi^+\pi^-$ and $\pi^0\pi^0$ events were detected concurrently from high–energy ($\sim$ 100 GeV) kaon beams. Two beams, of primary intensity 10^{11} and 10^7 protons per pulse, respectively, were alternately produced at two different targets located at a distance from the detector such to obtain pure beams of K_L and K_S particles (the layout is sketched in fig. 1.2). In order to obtain the same decay distribution, thus the same acceptance, despite the different lifetimes, the K_S target was displaced during the run in steps of 1.2 m throughout the 50 m fiducial volume.

Charged pions were identified using two wire chambers (there was no magnetic spectrometer), while a liquid argon–lead calorimeter was used to measure photons from $\pi^0\pi^0$ events. The calorimetric measurement of the pion energy was obtained using also an hadron calorimeter, followed by muon veto counters to

[11]The π_0 lifetime is $(8.4 \pm 0.6)10^{-17}$ s [14].

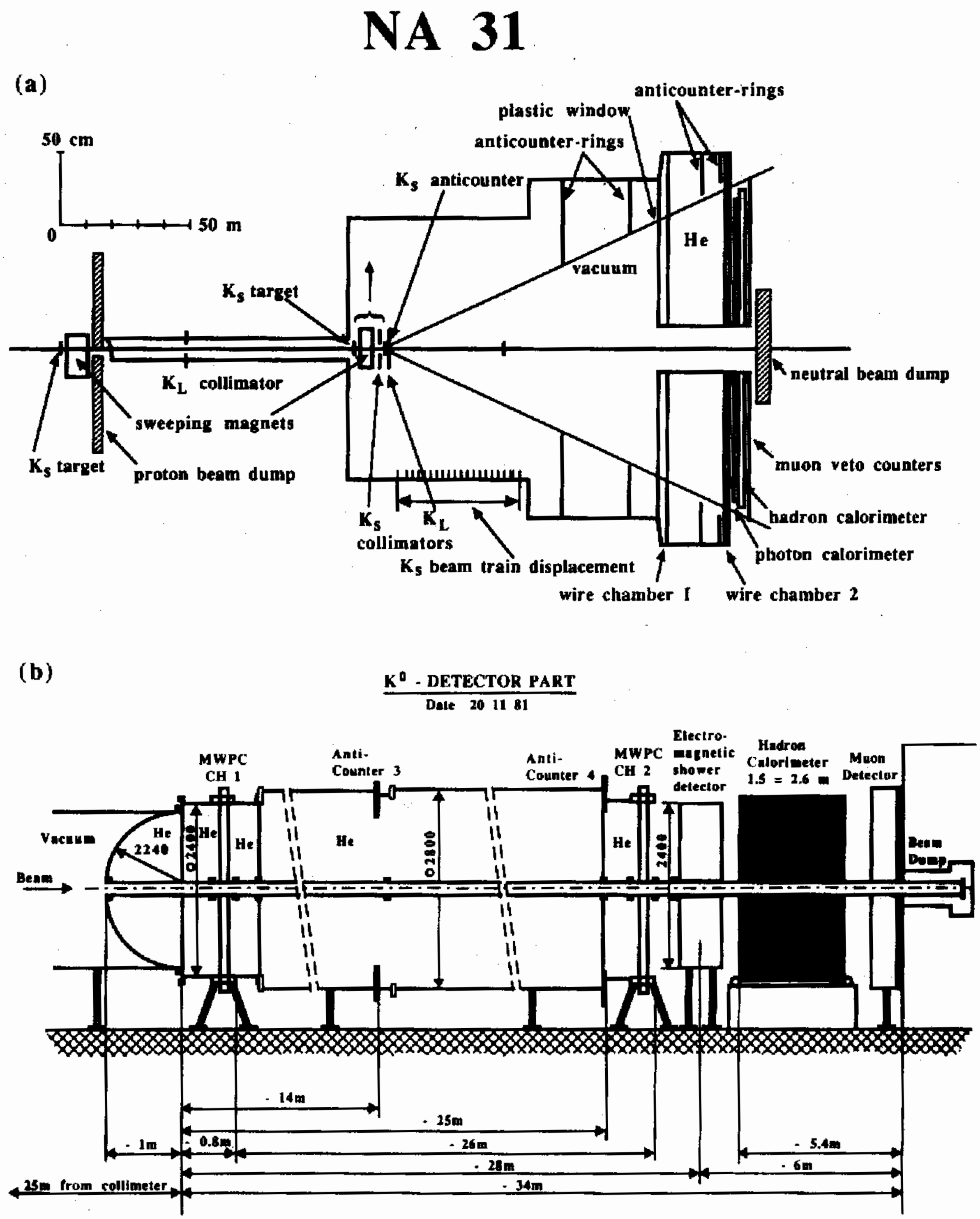

Figure 1.2: Layout of the NA31 experiment at CERN

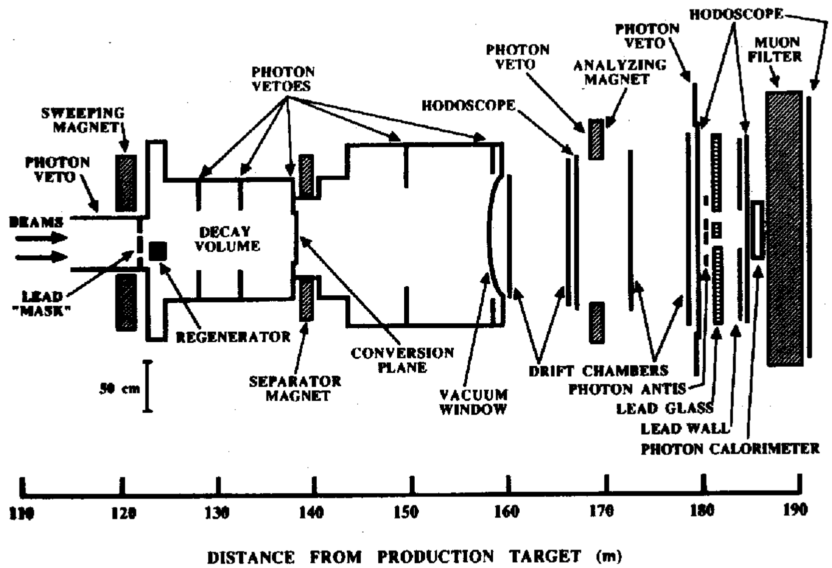

Figure 1.3: Layout of the E731 experiment at Fermilab

suppress the $K_{\mu 3}$ background. Anti–counter rings around the detector fiducial region were useful in rejecting the background from three pion events.

The final result based on three years of data–taking (1986, 1988 and 1989) was [4]

$$Re\left(\frac{\epsilon'}{\epsilon}\right) = (23.0 \pm 6.5)\ 10^{-4} \tag{1.44}$$

The main sources of error were, in order of importance:

- the statistics of $K_L \to \pi^0\pi^0$;
- the accidental activity in the detector, that was not the same for K_L and K_S due to the different intensities;
- the background to neutral events from $K_L \to 3\pi^0$ (amounting to 2.7 %);
- the uncertainty on the relative energy scale for neutral and charged events;
- the background to charged events, mainly from K_{e3} decays of K_L (amounting to 0.7 %);
- the uncertainty on the residual acceptance difference between K_L and K_S;

- the inefficiency of wire chambers.

E731: Another experiment based on high–energy kaon beams, but using a different technique, was performed at Fermilab. All the four decay modes were acquired concurrently from two parallel identical K_L beams, one of which was hitting on a regenerator to obtain the K_S events, as sketched in fig. 1.3. The regenerator was alternated once every minute between the two beams, in order to cancel the residual differences in intensity and acceptance. Charged events were detected by mean of a drift chamber spectrometer, while a lead glass calorimeter was used for the neutral events. A muon veto detector and anticounter rings were used to reject background.

The data analysis strongly relied on Montecarlo simulation, tuned using $K_{\ell 3}$ and $3\pi^0$ decays, to correct for the acceptance difference due to the different longitudinal distributions of the decays from the two beams, and to evaluate backgrounds. The ratio of the events from the two beams was fitted, simultaneously for the two decay modes, with ϵ' and the regeneration amplitude as free parameters. The result was [29]

$$Re\left(\frac{\epsilon'}{\epsilon}\right) = (7.4 \pm 5.9)\ 10^{-4} \tag{1.45}$$

The error was dominated by the statistics of the $K_L \to \pi^0\pi^0$ sample. The major sources of systematic error were the uncertainties on the acceptance correction, the calibration of the lead–glass calorimeter, the accidental activity and the backgrounds (amounting to 2.53 % and 2.26 % for the regenerator and vacuum beams, respectively).

While the NA31 result can be taken as a first evidence for the occurrence of direct CP violation in kaon decays, the E731 result was compatible with $\epsilon' = 0$, and the agreement between the two measurements is marginal. Therefore, despite the large experimental efforts in the two laboratories, no clean answer about a non zero value of ϵ' was obtained.

Both CERN and Fermilab groups used the earned experience to project upgraded experiments, aiming to reach an accuracy on $Re(\epsilon'/\epsilon)$ of $2 \cdot 10^{-4}$. The two new experiments are presently running and completing their data–taking. The measurement of $Re(\epsilon'/\epsilon)$ with the CERN experiment NA48 is the subject of this thesis. The new Fermilab experiment KTEV retains all the basic features of its predecessor. The main improvements are the capability to stand much higher rates and the better resolution of the electromagnetic calorimeter, made of 3100 CsI crystals.

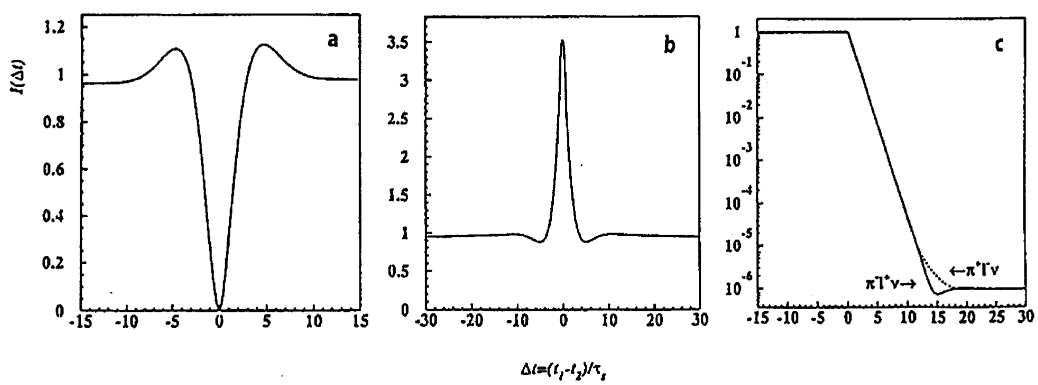

Figure 1.4: Calculated interference patterns for the following $\phi \to K\bar{K} \to f_1 f_2$ decays: a) $f_1 = \pi^+\pi^-, f_2 = \pi^0\pi^0$; b) $f_1 = \ell^+\pi^-\nu, f_2 = \ell^-\pi^+\bar{\nu}$; and c) $f_1 = 2\pi, f_2 = \ell\pi\nu$.

Finally, another experiment is going to measure direct CP violation in kaon decays with hopefully the same level of accuracy then NA48 and KTEV, but with a completely different technique. The KLOE detector is installed at the DAΦNE ϕ factory of the LNF laboratory in Frascati. It will study the ϕ decay at rest

$$\phi \to K\bar{K} \to f_1 f_2$$

where $K\bar{K}$ is an antisymmetric state of two neutral kaons

$$\frac{1}{\sqrt{2}}(|K^0(z)\bar{K}^0(-z)\rangle - |\bar{K}^0(z)K^0(-z)\rangle) = \frac{1}{\sqrt{2}}(|K_L(z)K_S(-z)\rangle - |K_S(z)K_L(-z)\rangle) \tag{1.46}$$

allowing to tag $K^0, \bar{K}^0, K_L$ and K_S events and to measure the interference pattern for a number of f_1, f_2 final states. Some examples of such patterns are shown in fig. 1.4. For the cases $f_1 = f_2 = \pi^+\pi^-$ and $f_1 = f_2 = \pi^0\pi^0$, the amplitude for time difference $\Delta t \equiv (t(f_1) - t(f_2))/\tau_S = 0$ must be null, since Bose statistics forbids the simultaneous existence of the two couples, that would behave as two bosons in a antisymmetric state. This is also the case of $f_1 = \pi^+\pi^-, f_2 = \pi^0\pi^0$ in the absence of direct CP violation. Thus, the simultaneous detection of two distinct CP eigenstates is a clear signature of direct CP violation. From the interference pattern both $Re(\epsilon'/\epsilon)$ and $Im(\epsilon'/\epsilon)$ can be inferred.

Chapter 2

CP violation in the Standard Model

The existence of three quark generations allows CP violation to be accommodated within the Standard Model of electroweak and strong interactions. The amount of violation depends on free parameters that are unknown a priori and there is no mechanism explaining naturally the smallness of the CP violation effects in kaon decays. The particular constraints imposed to all CP violating decays make precision measurements of such processes extremely appealing, since CP violation could be the first probe to evidence physics beyond the Standard Model.

2.1 The CKM matrix and the unitarity triangle

In the Standard Model (SM) of electroweak interactions the quark eigenstates for the strong and electromagnetic interaction (i.e. the mass eigenstates) and for the weak interaction do not coincide, as first realized by Cabibbo [12], who introduced its famous angle to describe the mixing of the d and s quarks. After the charm quark was introduced, the mixing was represented by a 2x2 matrix $\hat{V}$, whose unitarity assures the absence of flavor changing neutral current transitions (this property is known as GIM mechanism [31]).

The charged current quark interactions are described by the Lagrangian term

$$\mathcal{L}_W = -\sum_i \frac{g}{2\sqrt{2}} \bar{\mathrm{u}}_i \gamma^\mu (1-\gamma_5)(\hat{V}_{\mathrm{ud}})_{ij} \mathrm{d}_j \, W^\dagger_\mu \; + \; h.c. \tag{2.1}$$

where u_i and d_i are the fields for the quark mass eigenstates with $+2/3$ and $-1/3$ charge, respectively, and the index i spans on the quark families. It can be shown [44] that the Lagrangian is not CP invariant only if the $\hat{V}$ matrix is not real[1]. A complex mixing matrix could be generated by complex couplings for the Yukawa interactions between quarks and the Higg's sector, that are responsible, after spontaneous symmetry breaking, for the generation of quark masses.

With two quark families, the unitary mixing matrix must be real and does not allow for CP violation, so that mechanisms going beyond the SM, as the super–weak hypothesis, were formulated to account for it.

In 1973, before the discovery of the b and t quarks, Kobayashi and Maskawa [36] were the first to realize that in the presence of a third quark generation, CP violation was indeed possible within the SM framework. In fact the 3x3 mixing matrix

$$\hat{V}_{CKM} = \begin{pmatrix} V_{ud} & V_{us} & V_{ub} \\ V_{cd} & V_{cs} & V_{cb} \\ V_{td} & V_{ts} & V_{tb} \end{pmatrix} \tag{2.2}$$

known as Cabibbo–Kobayashi–Maskawa (CKM) matrix, can be parameterized in

[1]Actually, non–perturbative corrections to the SM tree level lagrangian from strong interactions could be a second (and flavor–diagonal) source of CP violation, that is parameterized through the angle θ_{QCD}. The experimental limits on the electric dipole moment of the neutron imply $\theta_{QCD} < 10^{-9}$. The minimal form of the SM model offers no natural explanation of the smallness of θ_{QCD}, though models involving a new global $U(1)$ simmetry (that would lead to the existence of a new neutral pseudoscalar boson, the ***axion***) have been proposed to solve this so–called "strong CP problem" [47, 56].

general by three angles and a single complex phase. The latter accounts for the imaginary part of the matrix, allowing for CP violation.

Among the 9 possible parameterizations, a standard one has been recommended by the Particle Data Group [14], in terms of the three angles θ_{ij} and the phase δ:

$$\hat{V}_{CKM} = \begin{pmatrix} c_{12}c_{13} & s_{12}c_{13} & s_{13}e^{-i\delta} \\ -s_{12}c_{23} - c_{12}s_{23}s_{13}e^{i\delta} & c_{12}c_{23} - s_{12}s_{23}s_{13}e^{i\delta} & s_{23}c_{13} \\ s_{12}s_{23} - c_{12}c_{23}s_{13}e^{i\delta} & -c_{12}s_{23} - s_{12}c_{23}s_{13}e^{i\delta} & c_{23}c_{13} \end{pmatrix} \tag{2.3}$$

where $c_{ij} = \cos(\theta_{ij})$ and $s_{ij} = \sin(\theta_{ij})$ $(i, j = 1, 2, 3)$ can be chosen to be positive and δ may vary in the range $0 \leq \delta \leq 2\pi$, but it is forced to be $< \pi$ to account for CP violation in K decays.

From phenomenology we know that s_{13} and s_{23} are of the order 10^{-3} and 10^{-2} respectively, so that, with very good approximation, we have

$$s_{12} = |V_{us}|, \qquad s_{13} = |V_{ub}|, \qquad s_{23} = |V_{cb}| \tag{2.4}$$

In order to make the contents of the matrix more transparent, using the hierarchy of the mixing angles, an approximate parameterization has been introduced by Wolfenstein [58], where each element is expanded as a power series in the parameter $\lambda = |V_{us}| = 0.22$:

$$\hat{V}_{CKM} = \begin{pmatrix} 1 - \frac{1}{2}\lambda^2 - \frac{1}{8}\lambda^4 & \lambda & A\lambda^3(\rho - i\eta) \\ -\lambda + \frac{1}{2}A^2\lambda^5\left[1 - 2(\rho + i\eta)\right] & 1 - \frac{1}{2}\lambda^2 - \frac{1}{8}\lambda^4(1 + 4A^2) & A\lambda^2 \\ A\lambda^3\left[1 - (\rho + i\eta)(1 - \frac{1}{2}\lambda^2)\right] & -A\lambda^2 + A\left[\frac{1}{2}(1 - 2\rho) - i\eta\right]\lambda^4 & 1 - \frac{1}{2}A^2\lambda^4 \end{pmatrix} + \mathcal{O}(\lambda^6) \tag{2.5}$$

The free parameters are now λ, A, ρ, η, connected with the previous ones by the following relations:

$$\begin{cases} \lambda = s_{12} \\ A = \frac{s_{23}}{s_{12}^2} \\ \rho = \frac{s_{13}}{s_{12}s_{23}} \cos\delta \\ \eta = \frac{s_{13}}{s_{12}s_{23}} \sin\delta \end{cases} \tag{2.6}$$

The order λ^5 in the expansion is needed to have the proper accuracy for the analysis of K decays.

The unitarity of the CKM matrix implies various relations among its elements, in particular

$$V_{ud}V_{ub}^* + V_{cd}V_{cb}^* + V_{td}V_{tb}^* = 0 \tag{2.7}$$

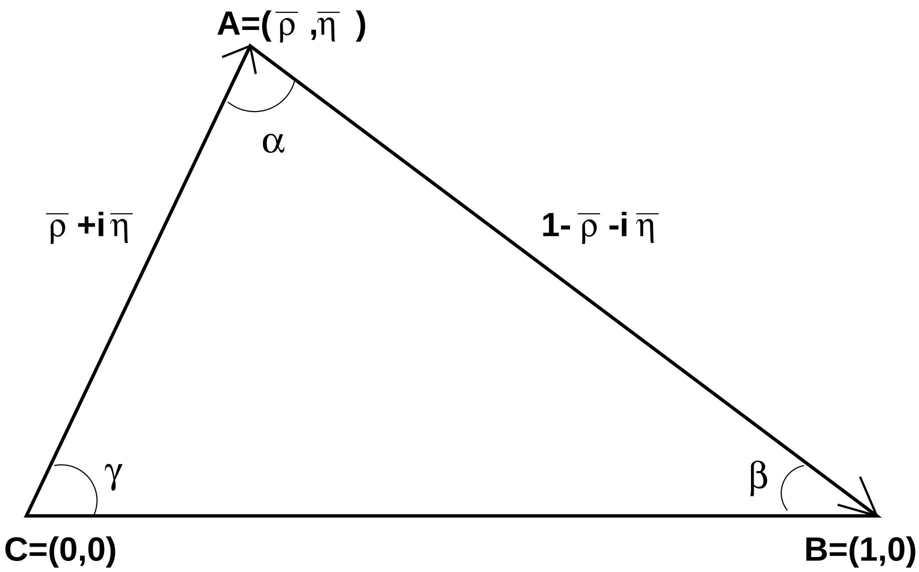

Figure 2.1: The unitarity triangle.

From (2.5) we see that

$$V_{cd}V_{cb}^* = -A\lambda^3 + \mathcal{O}(\lambda^7) \tag{2.8}$$

$$V_{ud}V_{ub}^* = A\lambda^3(\bar\rho + i\bar\eta) + \mathcal{O}(\lambda^7) \tag{2.9}$$

$$V_{td}V_{tb}^* = A\lambda^3(1-\bar\rho - i\bar\eta) + \mathcal{O}(\lambda^7) \tag{2.10}$$

where

$$\bar\rho = \rho\left(1-\frac{1}{2}\lambda^2\right) \qquad \bar\eta = \eta\left(1-\frac{1}{2}\lambda^2\right) \tag{2.11}$$

Therefore, the unitarity relation (2.7) can be graphically represented in the $(\bar\rho, \bar\eta)$ plane as a triangle having a unity length side, and the other sides of length

$$R_b = \frac{|V_{ud}V_{ub}^*|}{|V_{cd}V_{cb}^*|} = \sqrt{\bar\rho^2+\bar\eta^2} = \left(1-\frac{\lambda^2}{2}\right)\frac{1}{\lambda}\left|\frac{V_{ub}}{V_{cb}}\right| \tag{2.12}$$

$$R_t = \frac{|V_{td}V_{tb}^*|}{|V_{cd}V_{cb}^*|} = \sqrt{(1-\bar\rho)^2+\bar\eta^2} = \frac{1}{\lambda}\left|\frac{V_{td}}{V_{cb}}\right| \tag{2.13}$$

This *unitarity triangle* is depicted in fig. 2.1. Its sides and angles are physical observables, since any phase transformation simply rotates the triangle in the plane. Its area is a measurement of the amount of CP violation and can be obtained, at least in principle, by measuring $|V_{us}|, |V_{ub}|, |V_{cb}|$ and $|V_{td}|$ through CP conserving decays.

Assuming the SM provides a complete description of all the measurements, the unitarity triangle can be obtained using the following informations:

- the scale of the triangle is given by $|V_{cb}|$ that can be measured with good accuracy from exclusive and inclusive B meson decays. The semileptonic modes $B \to D\ell^+\nu_\ell$ are the most useful, since a nearly model–independent treatment of such processes is provided by the heavy quark effective theory (HQET). The present value is [14]

$$|V_{cb}| = 0.0395 \pm 0.0017 \tag{2.14}$$

- The ratio $|V_{ub}|/|V_{cb}|$ is obtained from inclusive semileptonic decays of B mesons, by measuring the lepton energy spectrum above the endpoint for $b \to c\ell^-\bar{\nu}_\ell$. The interpretation of the result is limited by the theoretical uncertainties on the shape of the generated lepton energy spectrum, resulting in a 25 % relative error. The precision can be improved by using also the measurement of $|V_{ub}|$, performed at LEP from the inclusive charmless semileptonic branching fraction of beauty hadrons. The combined result is [43]:

$$|V_{ub}|/|V_{cb}| = 0.093 \pm 0.016 \tag{2.15}$$

- The $\Delta S = 2$ transitions between K^0 and $\bar{K^0}$ are induced, at the first order, by the box diagrams shown in figure 2.2 and are dominated by the diagrams containing quarks c and t. The parameter ϵ of indirect CP violation can be computed in terms of the CKM matrix elements, defining an allowed region

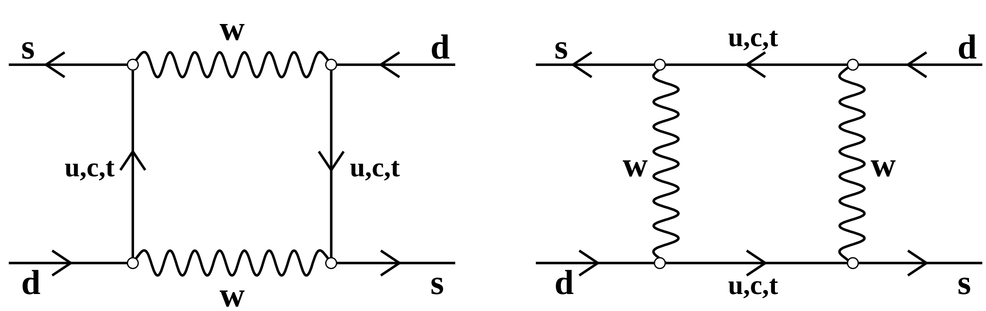

Figure 2.2: Feynman box diagrams contributing to the first order to indirect CP violation in the $K^0 - \bar{K}^0$ system.

around an hyperbola in the $(\bar{\rho}, \bar{\eta})$ plane. The relative accuracy of this computation is about 20 %, dominated by the uncertainties on non–perturbative QCD contributions.

- The $B_d^0 - \bar{B}_d{}^0$ mixing provides informations on the side of length R_t, through $|V_{td}|$, that can be obtained using the measured mass difference ΔM_d and the mass of top quark (the box diagrams with the top quark are the main sources of mixing). Again, uncertainties from the hadronic long–distance contributions are the main source of error, leading to a 20% relative error.

- Another limit on R_t is obtained from the B_s^0 mesons that are believed to undergo a mixing analogous to the B_d^0 one, but with a larger mass difference that induces faster oscillations, undetected so far.

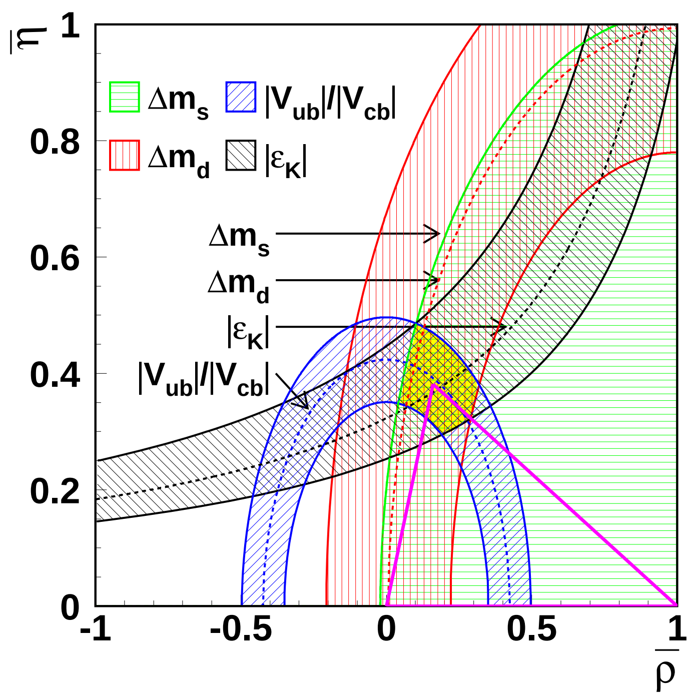

Figure 2.3: Allowed region in the plane $(\bar{\rho}, \bar{\eta})$ from different measurements and the favoured unitarity triangle. The constraint coming from B_s^0 oscillations is a limit at 95 % confidence level, while the others represent a $\pm 1\sigma$ error band (from [43]).

All measurements performed so far are consistent with the SM picture (see fig. 2.3) and lead to the following estimates for the unitarity triangle parameters [19, 43, 46]:

$$\bar{\rho} = 0.17 \pm 0.09 \tag{2.16}$$

$$\bar{\eta} = 0.36 \pm 0.06 \tag{2.17}$$

$$\sin(2\alpha) = 0 \pm 0.4 \tag{2.18}$$

$$\sin(2\beta) = 0.74 \pm 0.09 \tag{2.19}$$

$$\gamma = 65^\circ \pm 15^\circ \tag{2.20}$$

2.2 The prediction for ϵ' and the penguin diagrams

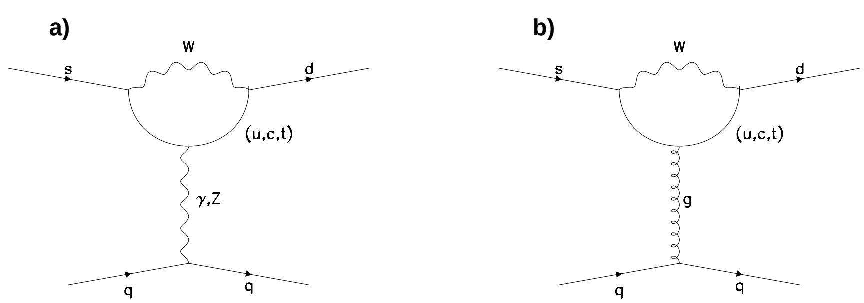

Figure 2.4: Electroweak (a) and strong (b) penguin diagrams, responsible for direct CP violation in kaon decays.

The direct CP violation parameter ϵ', defined in (1.39), can be predicted by evaluating the amplitudes for the $\Delta S = 1$ transitions.

The diagrams that are responsible for a different weak phase of the amplitudes for the two isospin channels A_0 and A_2 are called *penguin diagrams*[2] (see fig. 2.4). The $s \to d$ transition proceed through a one–loop flavor changing neutral current, with the exchange of a virtual gluon (*strong penguin*) or a photon or Z^0 (*electroweak penguin*). The strong penguin only contributes to A_0, since the isospin can change

[2]The name comes after a paper [25] where John Ellis was forced to include the word "penguin" because of a lost bet. He noticed the striking resemblance of the diagram with a penguin after having "smoked some illegal substance" [52].

only by $1/2$, while the electroweak penguin generates also a phase in A_2, since the electromagnetic current is a mixture of $\Delta I = 0$ and $\Delta I = 1$ transitions, so that the total isospin variation can be $3/2$. Of course, the electroweak diagram is suppressed by a factor $\alpha/\alpha_S \sim 10^{-2}$ with respect to its strong counterpart, but on the other hand the contribution of A_2 to ϵ' is enhanced by a factor $Re(A_0)/Re(A_2) \simeq 22$, so that the two contributions are of the same order, but have opposite sign. The accidental cancellation of the two contributions is indeed responsible for the smallness of ϵ'.

Actually, the calculations are very complex and suffer from large hadronic uncertainties. The result is also critically dependent from the value of the top quark mass.

Most of the computations [20, 19, 11] quote a value between 0 and $10 \cdot 10^{-4}$, even if a wider range of 0 to $20 \cdot 10^{-4}$ is obtained by pushing simultaneously all the relevant parameters to the extreme values of their predicted range.

2.3 Possible scenarios

The Standard Model provides a description of CP violation with some unique features:

- there is a single source of CP violation, namely the phase of the CKM matrix, so that CP–violating observables in all conceivable processes must be strongly correlated;

- CP violation is limited to the flavor changing quark interactions;

- CP is not an approximate symmetry, since $\bar{\eta}/\bar{\rho} = \mathcal{O}(1)$. The smallness of effects for processes mainly involving the first two quark generations, as it is the case for $K \to \pi\pi$, is explained by the small values of the mixing angles and not by the CP–violating phase of the CKM matrix. As a matter of fact, CP violating asymmetries of order 1 are predicted for some processes, all of them having unfortunately a small branching ratio. The main examples are $B \to \psi K_S$, that is going to be experimentally investigated at B factories, and $K_L(K^+) \to \pi^0(\pi^+)\nu\bar{\nu}$, for which the SM predicts a branching ratio of the order 10^{-11}, well below the present experimental sensitivity.

Most of the predictions of the SM scenario still have to be tested, due to the experimental difficulties. Different scenarios, as the supersymmetric ones, predict very different features for CP violation, that is thus a powerful probe for new physics. Therefore, it is important to collect all accessible informations by studying a number of possible processes. In the near future our knowledge of CP violation will probably substantially improve, since several experiments are on their way to produce new results. High–precision experiments on kaon physics will study direct CP violation and kaon rare decays, and dedicated experiments at B factories (as Babar at SLAC) will measure CP violation in the $B^0 - \bar{B}^0$ system.

Chapter 3

The NA48 experiment

NA48 is an experiment, installed at the CERN SPS accelerator, that aims at a substantial improvement in the accuracy of the ϵ'/ϵ measurement through the double ratio method. The simultaneity of data taking for the four $K \to \pi\pi$ decay modes, the quasi–collinearity of beam lines and the tagging method are the main ingredients of its innovative technique, that, together with the capability to stand very high rates and the impressive performances of its electromagnetic calorimeter, should allow to reach an overall accuracy of $2 \cdot 10^{-4}$ on $Re(\epsilon'/\epsilon)$.

The experiment started its data–taking with the full detector installed in the summer of 1997 and it is currently completing its program.

3.1 First principles

The NA48 experiment aims to measure ϵ'/ϵ with $2\cdot10^{-4}$ accuracy through the double ratio

$$R \;=\; \frac{\Gamma(K_L^0 \to \pi^0\pi^0)}{\Gamma(K_L^0 \to \pi^+\pi^-)}\frac{\Gamma(K_S^0 \to \pi^+\pi^-)}{\Gamma(K_S^0 \to \pi^0\pi^0)} \;=\; 1 - 6\ Re\left(\frac{\epsilon'}{\epsilon}\right) \tag{3.1}$$

by collecting the four decay modes simultaneously with the same apparatus. The advantage of this method consists in the fact that many experimental effects cancel in the ratio, being common to K_S and K_L or to charged and neutral events. The event reconstruction is based on a high–resolution electromagnetic calorimeter for the neutral ($2\pi^0$) events and on a magnetic spectrometer for the charged ($\pi^+\pi^-$) events.

The guidelines of the experimental project[3], based on the previous experience of NA31, are the following:

Statistics: The most limiting decay mode is $K_L^0 \to \pi^0\pi^0$, that is CP–violating and has lower branching ratio [1] and acceptance than $K_L^0 \to \pi^+\pi^-$. The statistical error is thus

$$\Delta\left(\frac{\epsilon'}{\epsilon}\right) \;\approx\; \frac{1}{6\sqrt{N_L^{00}}} \tag{3.2}$$

so that about 3 10^6 $K_L^0 \to \pi^0\pi^0$ decays are needed to reach a statistical accuracy of $1\cdot10^{-4}$. The experiment has been built to stand very high rates (1 MHz of instantaneous particle flux) in order to accumulate statistics of this order within 3 years of data–taking. This requires the implementation of very fast and sophisticated read–out and trigger systems.

Acceptance: the illumination of the detectors from K_S and K_L events is made as equal as possible by using nearly collinear beams, converging at the detector position. The longitudinal decay distributions, that are naturally very different, can be made equal by weighting offline the K_L events according to their reconstructed proper time. In this way the acceptances cancel (at least to a first approximation) in the double ratio and the result does not critically depend on the accuracy of Montecarlo simulations.

[1] BR $(K_L^0 \to \pi^+\pi^-) = (2.067 \pm .035)\ 10^{-3}$ BR$(K_L^0 \to \pi^0\pi^0) = (0.936 \pm .020)\ 10^{-3}$ [14]

K_S /K_L identification: the novel method used to distinguish K_S and K_L events consists in tagging in time each proton of the K_S beam line (the less intense one) with a detector that must be capable to stand rates of order 10 MHz. K_S events are identified through the time coincidence between the proton time and the event time in the detector. Therefore, both times must be measured with a resolution $<$ 500 ps.

Background: $K_L^0 \rightarrow 3\pi^0$ decays for the neutral mode and K_{e3} , $K_{\mu 3}$ and $\pi^+\pi^-\pi^0$ K_L decays for the charged mode are expected to be the main sources of background. A much better background rejection than the one obtained in NA31 is achieved by improving the performances of the electromagnetic calorimeter and by using a high–resolution magnetic spectrometer. 3π events having one pion outside the detector acceptance can be also vetoed by a set of anticounters placed around the fiducial volume of the detector.

Energy scale: The uncertainty on the difference of energy scale between the charged and neutral mode was one of the largest systematic error in the NA31 experiment[4]. In fact, since for neutral events the decay longitudinal position is obtained from the energy measurement, the accuracy in the size of the fiducial decay region, which is critical for this kind of measurement, translates in the accuracy of the energy and transverse scales of the calorimetric measurement. Excellent performances are required to the NA48 calorimeter also to considerably reduce this error.

Efficiency and accidental activity: both of these effects are canceled, at least to the first order, by the simultaneity of data taking. However, to avoid second–order biases, the trigger systems have been designed to have very low inefficiency, while high segmentation and excellent time resolutions are required to the main detectors in order to discriminate accidental activity.

3.2 The Beam

The beam lines for the NA48 experiment have been designed to fulfill the following requests:

- the two beam must illuminate the detector in the same way;

- the kaon beam energy must be high enough ($\sim$ 100 GeV) to have a good detector acceptance though covering small solid angles and to allow, in virtue of the relativistic lifetime dilation, the proper collimation of K_S beam without losing the short–lived component. High energies are also required to obtain the required beam rate and resolution of the calorimetric measurement. The spectra of the two beams should be as similar as possible in a wide energy range;

- the observed decay region must be close to the K_S target in order to have a practically pure beam of K_S particles; on the other hand the K_L target must be far enough to let the K_S component decay away;

- the K_S to K_L beam intensity ratio should be of the order $|\eta|^2 \sim .5 \cdot 10^{-5}$ in order to have comparable number of events in the detector from the two beams;

The beams are produced starting from the 450 GeV protons accelerated by the CERN Super–Proton–Synchrotron (SPS), according to the scheme sketched in figure 3.1. The primary beam, having a nominal flux of $1.5 \cdot 10^{12}$ protons per SPS pulse (2.5 s spill every 14.4 s cycle), is focused onto the K_L target, a 2 mm diameter, 400 mm long rod of beryllium, followed by a copper collimator of 15 mm aperture and a sweeping magnet to deflect charged particles away from the beam line.

The K_L beam is produced with an angle of 2.4 mrad, in order to increase the ratio of K^0 particle with respect to neutrons and photons. It is collimated in three stages: a first collimator defining the beam divergence ($\pm$ 0.15 mrad), a "cleaning" collimator to stop particles generated or scattered in the defining collimator's lips, and a final collimator located 2 meters upstream the beginning of the decay region.

The non–interacting protons ($\sim$ 50 %) cross a **bent crystal**, illustrated in figure 3.2, that, through the phenomenon of *channeling*[2] takes care of splitting off a small ($\sim 5 \cdot 10^{-5}$) fraction of proton beam. The method used has the advantage to deflect the protons with a well defined angle, resulting in a beam with small emittance. A mono–crystal of silicon having dimensions of $60 \times 18 \times 1.5$ mm^3 is used to obtain

[2]A charged particle can be channeled by the collective Coulomb field inside a crystal, if it enters with a small angle with respect to its planes. The crystal can be mechanically bent with an angle chosen according to the beam energy, such that the particles will follow the planes and a beam deflection is obtained.

Figure 3.1: Layout of the $K_S + K_L$ beam (from [8])

a deflection of 9.6 mrad, which can be fine–tuned by rotating the crystal through a motorized goniometer [23]. The resulting secondary beam, made of $\sim 3 \cdot 10^7$ protons per pulse, is then deflected by a set of magnets and transported parallelly to the K_L beam onto the K_S target, which is located 120 m downstream the K_L one. Along the transport line, the secondary beam protons cross the tagging station, which is described later on.

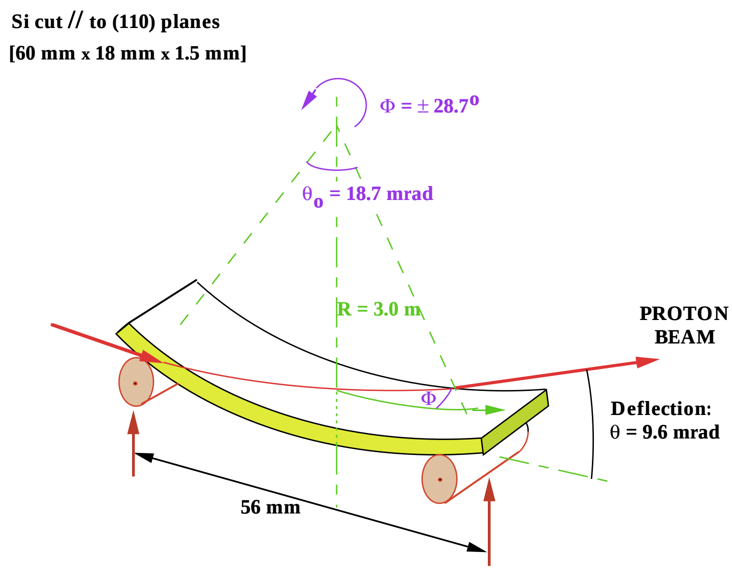

Figure 3.2: sketch of the bent crystal arrangement

The K_S beam is obtained from a target analogous to the K_L one, followed by a sweeping magnet and a collimator. The latter defines a production angle of 4.2 mrad that has been chosen in order to make the ratio of K_S and K_L decay spectra approximately equal, in a fiducial region chosen with length proportional to the energy–dependent K_S lifetime, and in a energy range of 70 to 170 GeV (see fig. 3.3). The beam divergence is $\pm$ 0.375 mrad.

The decay region begins right after the K_S collimator, 6 meters downstream the K_S target. Since the two kaon beams are vertically separated by 6.8 cm at this point, the angle between the two beam axes is chosen to be 0.6 mrad, so that the beams converge in the region of the central detector, about 120 m downstream the K_S target.

The decay volume is enclosed in a 89 m long evacuated cylindrical tank, having inner diameter of 1.92 m at the beginning, increasing up to 2.4 m to follow the

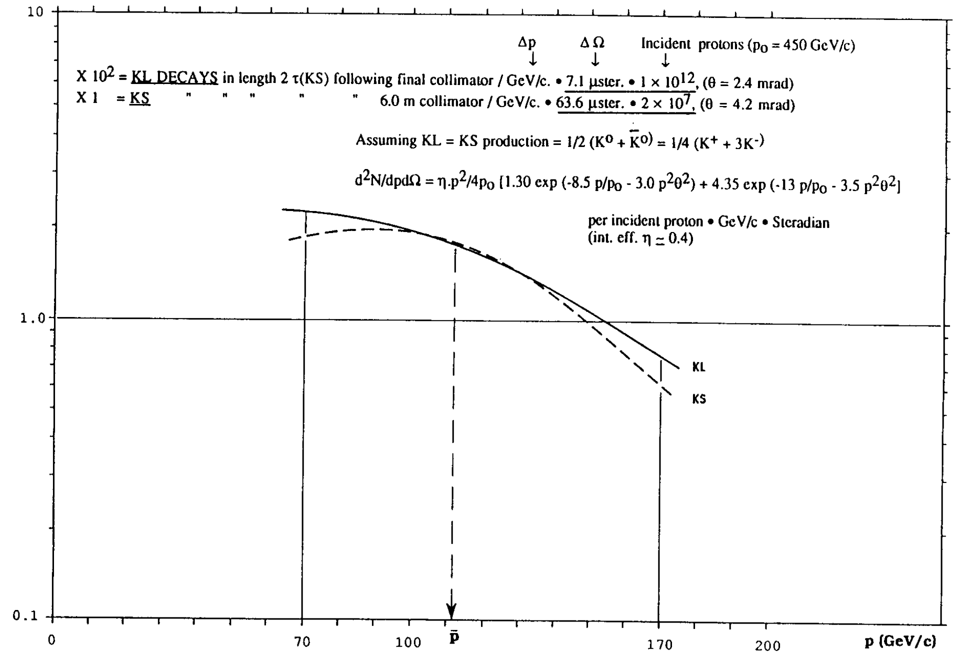

Figure 3.3: K_S and K_L decay spectra in a region within 2 K_S lifetimes from the final collimator (from the NA48 proposal [3]). The plotted region, where the difference of spectra is $\pm 10\%$, defines the nominal energy range of the experiment

beam divergence. The size is chosen in order to allow the useful decay products to propagate in vacuum. The tank is closed by a Kevlar window that separates it from the spectrometer volume, which is filled with helium gas at 1 atm pressure. The window's average thickness is 0.9 mm, corresponding to $\sim 3 \cdot 10^{-3}$ radiation lengths. The vacuum region continues inside a 152 mm diameter beam pipe that crosses all the succeeding detectors to avoid interactions in the detector volume of the undecayed particles (including gammas and neutrons). The pipe is connected to the tank through an aluminum ring glued at the center of the Kevlar window.

3.2.1 The Tagger

The tagging station is required to measure the time of each proton of the K_S beam line with minimal inefficiency and deadtime, and with a time resolution < 500 ps. It has to stand rates of order 10 MHz and a radiation exposure of 1 Gy per burst. The detector material must be light in order to preserve the beam quality. This

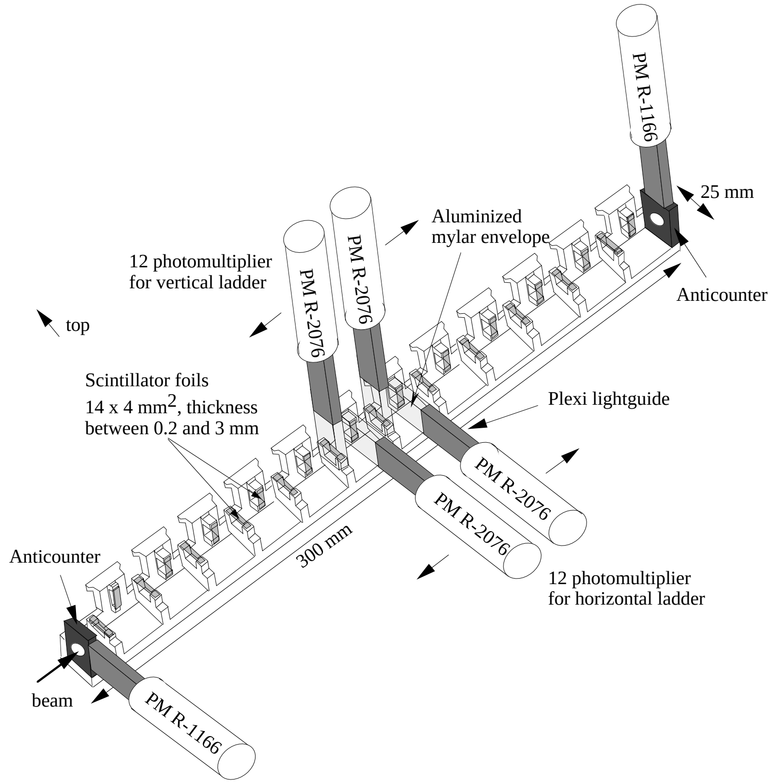

Figure 3.4: Artist's view of the NA48 tagging station (from [6]).

requirement, together with the radiation–hardness one, excludes the use of silicon or crystal counters.

The chosen setup consists in two arrays, one for each view, of 12 very thin plastic scintillators (NE102A) placed one after the other to share the beam flux. Their thickness varies from the 200 μm of the most inner one to the 2500 μm of the most outer one, according to the beam profile (see fig. 3.5), in order to equalize the rate of each counter to about 1 MHz. There is an overlap of 50 μm between each couple of adjacent counters to avoid acceptance losses. Along the beam direction, the counters are 4 mm long and 15 mm laterally wide to reach the supporting mechanical structure, that can be remotely moved with high precision.

The counters are readout by photomultipliers, placed in front of the 4×15 mm^2 surface. The light from the counters is collected onto the photocatode by lucite light guides through a 8 mm air gap, in order to avoid the effect of beam halo[3]. The

[3]some background due to Cerenkov light emitted by halo particle in the light guides was actually seen, but it is easily discrimated because of the very different timing shape of the readout signals

readout electronics samples the PM pulses using 8 bit, 960 MHz FADC[4] chips, that, with respect to conventional TDCs[5], are virtually deadtime–free. The amplitude and arrival time of the pulses with respect to the clock are obtained by fitting their shape.

The shortness of the photon optical path to the photocatode (1–2 cm) allows for an excellent light yield (about 400 photoelectrons per pulse), resulting in a time resolution of 100 ps.

Landau tails in the pulseheight distribution were considerably suppressed due to the scattering of δ rays out of the thin scintillator foils, allowing to reduce the dinamic range of electronics and, together with the very high readout frequency, to obtain a two pulse separation of 8 ns.

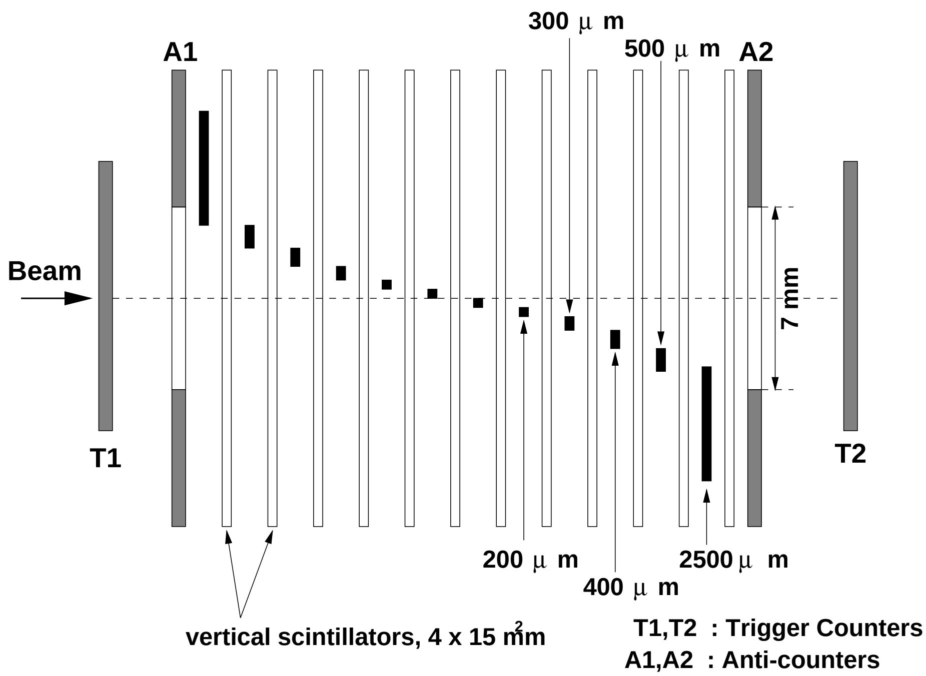

Figure 3.5: Schematic view of the tagger profile (from [33])

3.2.2 Beam Monitors

Informations about the overall beam intensity (essentially given by the K_L beam) are recorded by a beam counter (BCTR) located in the monitor station at the very end of the neutral beam line, where a mylar window closes off the beam pipe. It

[4]Flash Analog–to–Digital Converter
[5]Time–to–Digital Converter

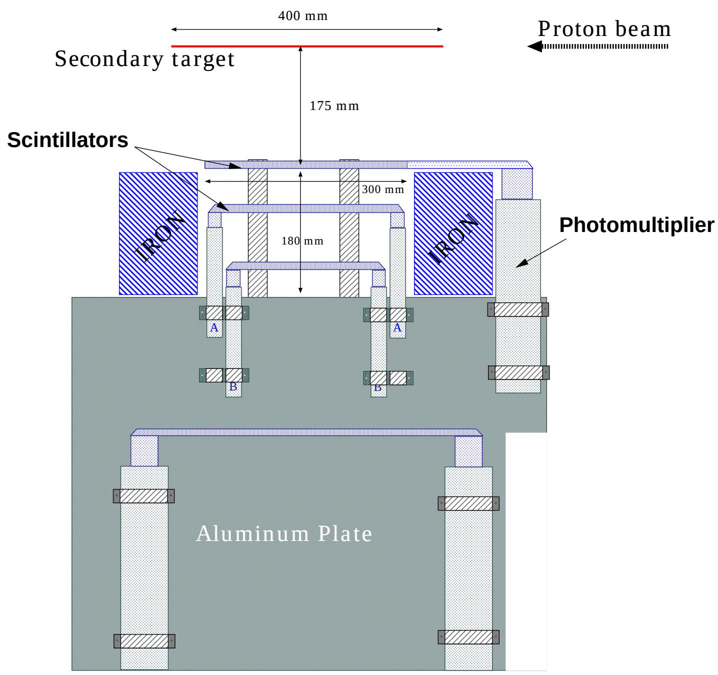

Figure 3.6: Schematic layout of the KSM detector (from [9])

consists in scintillating fibre bundles, of 18 fibres each, sampling the horizontal and vertical projections of the neutral beam flux and spaced 7.8 mm apart. Each group of 3 bundles is read out by a single photomultiplier.

A counter telescope (KSM), located in the vicinity of the K_S target, is used to monitor the K_S beam intensity by counting the particles emitted from the target perpendicularly to the beam direction. It consists in four plastic scintillators, surrounded by larger veto counters (see fig. 3.6). Three scintillators are read out by photomultipliers at both ends, the fourth at one side only because of space limitations.

These two monitors are helpful in tuning the beams. It is particularly important to render the intensity ratio stable along the spill time, to avoid effects related to differences in the instantaneous rates of the two beams. Time–variations of the intensity ratio are primarily caused by the sensitivity of the K_S beam intensity to the angle of the proton beam to the bent crystal, which can drift during the spill if the trimming magnets of the proton extraction from the SPS are not properly tuned.

The monitors are also used to trigger the acquisition of "random" events, useful to study the accidental activity in the detector (see section 4.9), and for offline studies of effects related to beam intensity.

3.2.3 AKS counter

The beginning of the fiducial region for the K_S beam line is defined by a detector that vetoes all the decays occurring upstream it. As discussed in the next chapter, this is useful to avoid the effect of different vertex position resolution for K_S charged and neutral events, and to adjust the reconstructed distance scales.

The detector is placed a few cm after the K_S collimator end. It consist in an photon converter followed by three 5 mm thick scintillators of 8×4.5 mm transverse size. A fourth scintillator with a central hole acts as a veto for the halo particles. The converter is made of a 3 mm thick iridium mono-crystal that, if its planes are aligned with the beam direction, provides 1.79 radiation lengths. With respect to amorphous iridium, it improves by a factor 2 the ratio of radiation length to scattering length.

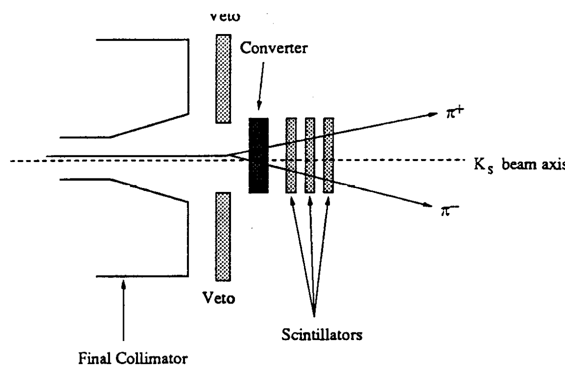

Figure 3.7: Schematic view of the AKS detector

3.3 The detector

The layout of the central detector is shown in figure 3.8. It consists of a magnetic spectrometer for the reconstruction of charged pion tracks, a Liquid Kripton electromagnetic calorimeter (LKr) for the photon reconstruction, a charged and a neutral hodoscope system (CHOD, NHOD) for the precise measurement of event time, an hadron calorimeter (HAC) that complements the calorimetric measurement for pions, a set of muon counters (MUV) to veto $K_{\mu 3}$ decays and a set of anticounters

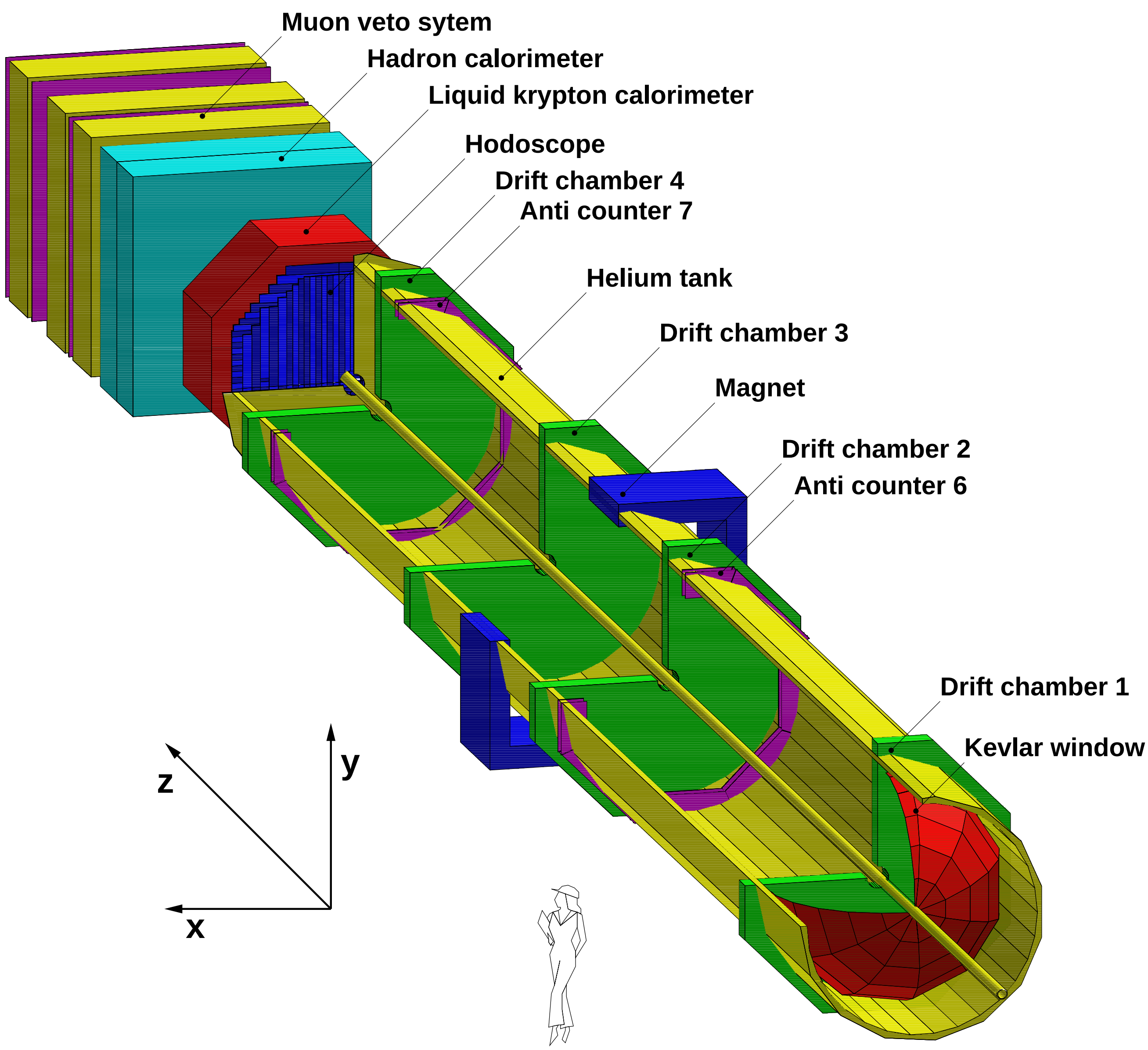

Figure 3.8: Layout of the NA48 central detector.

(AKL) to veto 3π decays.

The x, y, z directions of the reference frame used throughout this thesis are defined in figure 3.8.

3.3.1 Magnetic Spectrometer

The momentum of charged particles is measured by a spectrometer, consisting in a dipole magnet and two couples of drift chambers (DCH) that track the particles before and after they are bended by the field of the magnet. Since the chamber walls cannot stand a large pressure gradient, the detector volume is at atmospheric pressure, filled with helium in order to reduce the multiple Coulomb scattering.

The magnet aperture measures 2.45 x 2.20 m^2. It provides an integrated field of about 1 Tm, corresponding to a momentum kick of 250 MeV/c [34].

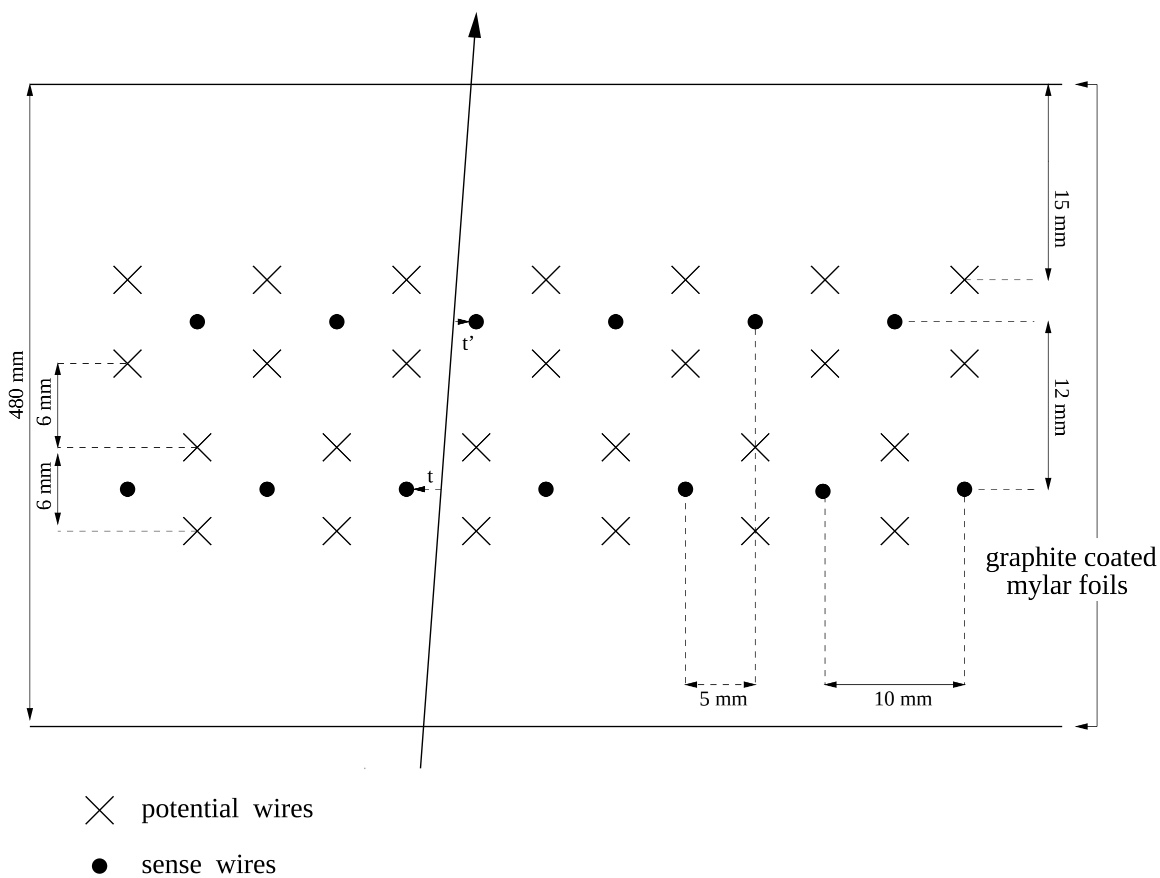

Figure 3.9: Schematic arrangement of the drift chamber wires used for one view.

The chambers are operated with a mixture of Argon and Ethane + 1% of H_2O and have a gain of about $6 \cdot 10^4$. In order to stand high accidental rates, the

maximum drift distance is limited to 5 mm (100 ns). Each chamber performs a redundant measurement of the position of passing particles, which are detected in Y, X, U, V views (with angles $0°, 90°$ and $\pm 45°$ with respect to the vertical direction), except for chamber 3 that has only X and Y views. There are two scattered planes for each view, in order to resolve the ambiguity between the two possible positions compatible with the measurement of a single wire (see fig. 3.9)
The 7680 channels are read by 40 MHz TDC with 25/16 ns fine time.
The resulting space–point resolution is 90 μm both in x and y.
The momentum resolution is measured to be

$$\frac{\sigma(P)}{P} = 0.48\% \oplus 0.009 \; P(GeV/c)\% \tag{3.3}$$

where the first term is due to Coulomb scattering and the second one to space resolution. The two terms have about the same importance for the average momentum of the observed pion ($\sim$ 50 GeV/c).

3.3.2 Charged Hodoscope

The event time of the $\pi^+\pi^-$ events is measured by the charged hodoscope, consisting of two planes of plastic scintillators, separated by 50 cm. Each plane is formed by 64 counters, divided in 4 quadrants and readout at their outer edge (fig. 3.10).

The fast signals are used for the first level of charged trigger. To this extent, the geometrical division in quadrants is useful to select $\pi^+\pi^-$ events that, due to the transverse momentum balance, hit typically opposite quadrants.

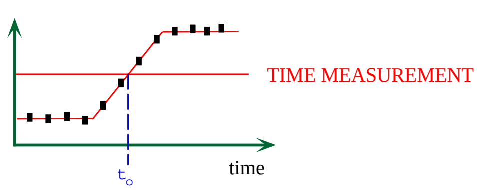

Figure 3.12: Time measurement from ramp fitting

The readout electronics is hosted in some VME modules called PMB (Pipeline Memory Board), whose conceptual design is illustrated in fig. 3.11. The analog signal is first discriminated and sent to a 10 bit 40 MHz FADC/FTDC card together with the discriminator output. While the analog signal is shaped and digitized to get the signal pulseheight, the digital input signal triggers a TDC ramp counting between two fixed levels, that is also sampled. By fitting the ramp (fig. 3.12) it is possible to reconstruct the time with better accuracy than from the sampled pulse shape. The PMB modules have been specifically

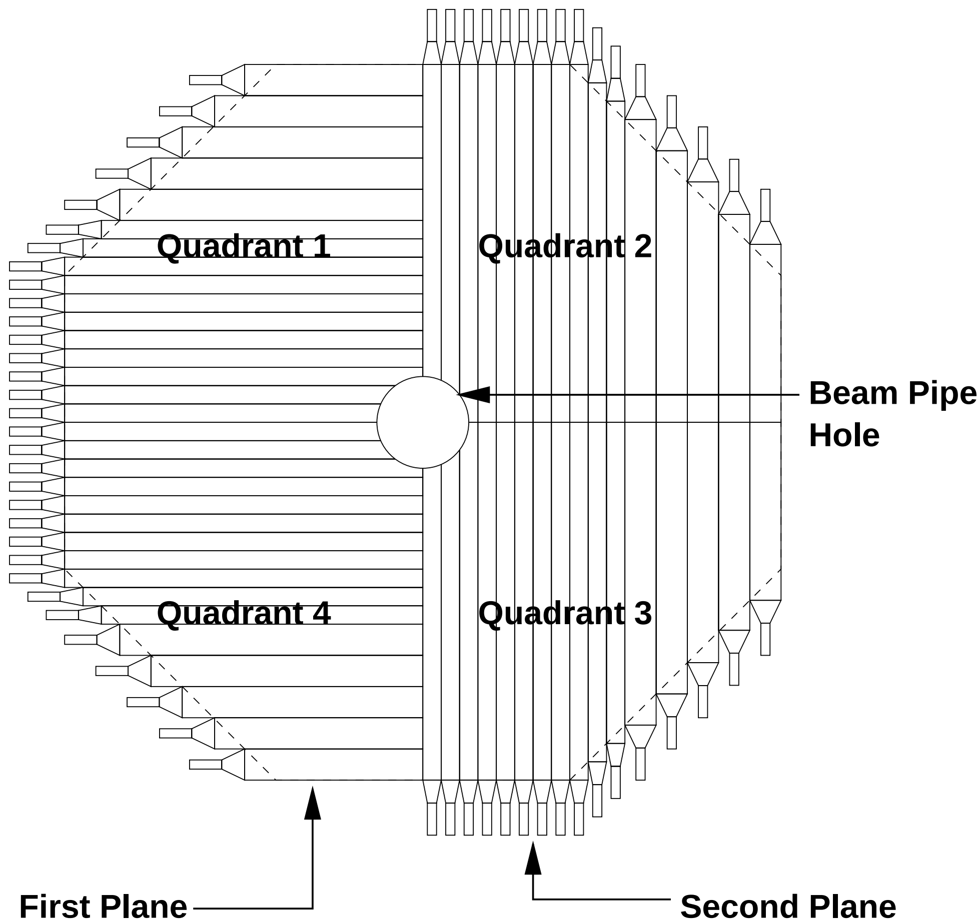

Figure 3.10: Layout of the charged hodoscope.

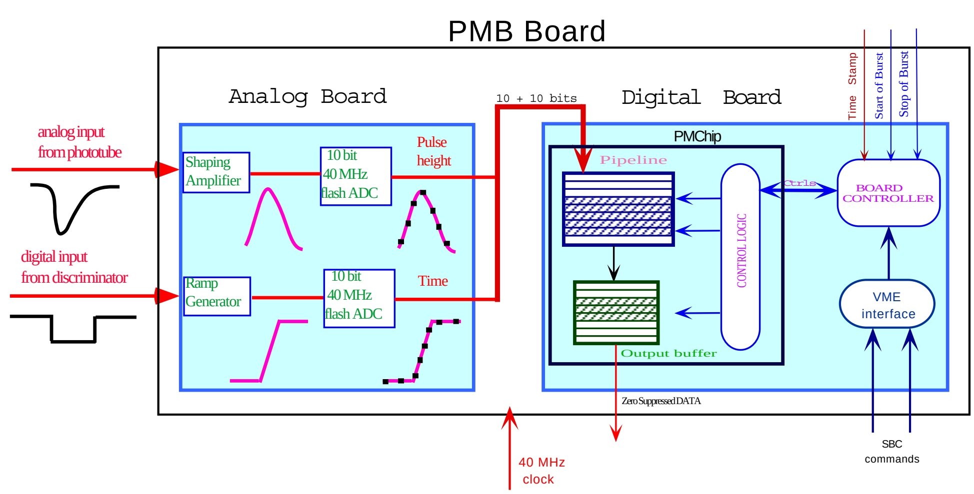

Figure 3.11: Conceptual scheme of PMB boards.

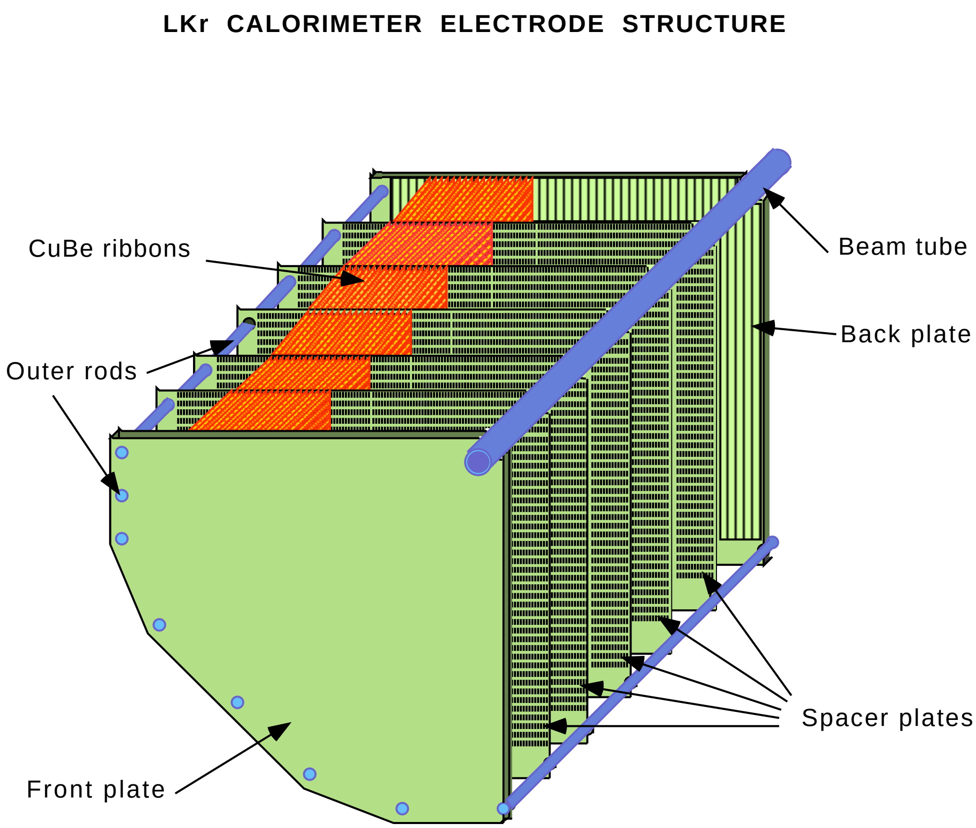

Figure 3.13: Section of a LKr calorimeter quadrant

designed for the charged hodoscope system, but are also used for the readout of the AKS, AKL, NHOD, KSM detectors and of the Neutral Trigger (NUT) system.

The typical time resolution for a single counter, after offline correction, is 220 ps. The inefficiency of each counter is tipically 1–2 per mill.

3.3.3 Liquid Krypton Calorimeter

This cold homogeneous calorimeter is undoubtedly the masterpiece of the experiment. In order to efficiently reject $3\pi^0$ background and to control the absolute energy scale at the level of a few 10^{-4}, the calorimeter is requested to fulfill the following requirements in the useful energy range (3–100 GeV):

- excellent energy resolution (better than 1 % above 20 GeV);
- excellent position resolution (about 1 mm);
- the geometrical scale must be known at the level of 0.2 mm over the distance of 1 m;

- response non–uniformity and non–linearity should not exceed 0.5 %.

A high segmentation is required also to reduce the effect of accidental activity. An excellent time resolution ($< 500\ ps$) is needed for event tagging and to have further rejection of background and accidentals.

Density		2.41 g/cm^3
Radiation length		4.7 cm
Molière radius		4.7 cm
Boiling point at 1 bar		119.8 K
Radioactivity		500 Bq/cm^3
Electron drift velocity at	1.5 kV/cm	0.27 cm/μs
	5 kV/cm	0.36 cm/μs
Dielectric constant		$\sim$ 1.7

Table 3.1: Properties of liquid Krypton (from [45]).

To meet all these requirements an homogeneous ionization detector based on liquid Krypton with tower readout was chosen. The physical properties of liquid Krypton are listed in table 3.1. The detection technique offers high resolution and stability. The large signal to noise ratio allows short shaping time.

The design of the readout cells is shown in figure 3.14. Each cell has a transverse size of 2×2 cm^2, defined by 40 μm thick ribbon electrodes made of Cu–Be. The ribbons are stretched between the front and back plates, and guided in **accordion geometry** by 5 spacer–plates, longitudinally spaced by 21 cm (fig. 3.13). The accordion angle (± 48 mrad) is introduced in order to reduce the non uniformity caused by the response dependence from the position of the shower with respect to the electrodes. The total length of the active volume is 127 cm, corresponding to 27 radiation lengths.

The detector surface has octagonal shape with 128 cm apothem. The total number of cells is 13248. Their transverse size increases linearly along the longitudinal direction, with a total variation of 1.1 %, in order to achieve a **projective geometry**, i.e. the photons originated in the observed decay region, 110 ± 6 m upstream, develop their showers parallelly to the electrodes independently from their impact positions. This is essential to not introduce an uncertainty in the reconstructed position due to the fluctuation of the depth of the shower maximum.

The precision used to machine each individual ribbon and the spacer plates guarantees the required level of uniformity and accuracy in the knowledge of the transverse scale.

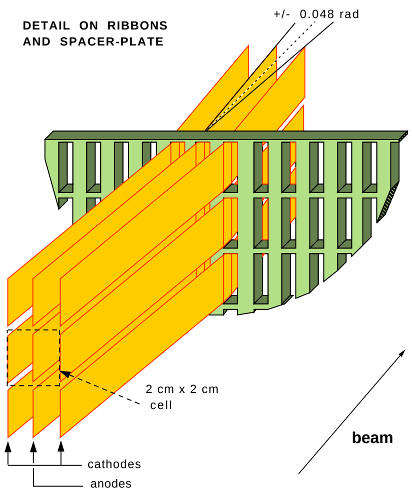

Figure 3.14: Sketch of the readout cells with ribbon electrodes and spacer plate.

The detector is contained in a cryostat, formed by an outer aluminum vessel and an inner steel vessel, which maintains about 9 m^3 of liquid Krypton at a temperature of 121 K. Front windows are 4 mm (Al) and 2.9 mm (steel) thick and, together with the 53 mm thick front plate, made of fiber–glass reinforced epoxy, constitute 0.58 radiation length of material upstream the active volume.

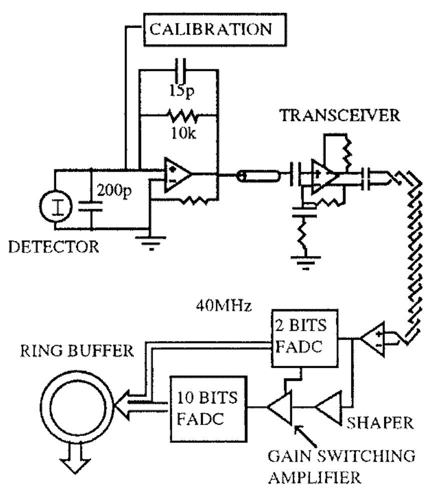

Figure 3.15: Scheme of the LKr readout electronics.

The front–end "cold" electronics is directly mounted on the detector back–plate in order to minimize noise and timing of signal extraction. It includes a preamplification stage and a calibration system (see fig. 3.15). Just outside the detector, a transceiver drives the output signals to custom readout modules, called CPD (Calorimeter Pipeline Digitizer), where they are shaped and sampled by a 10 bit 40 MHz FADC. Since the required range (3.5 MeV to 50 GeV) corresponds to 14 bits, the gain of the amplifier is switched among four possible values, depending on the signal amplitude. The selected gain is recorded through 2 additional bits. The CPDs also provides the input signals for the neutral trigger.

During 1997 data–taking, some problems with the electrode decoupling capacitors were experienced and the detector had to be operated at half of the nominal

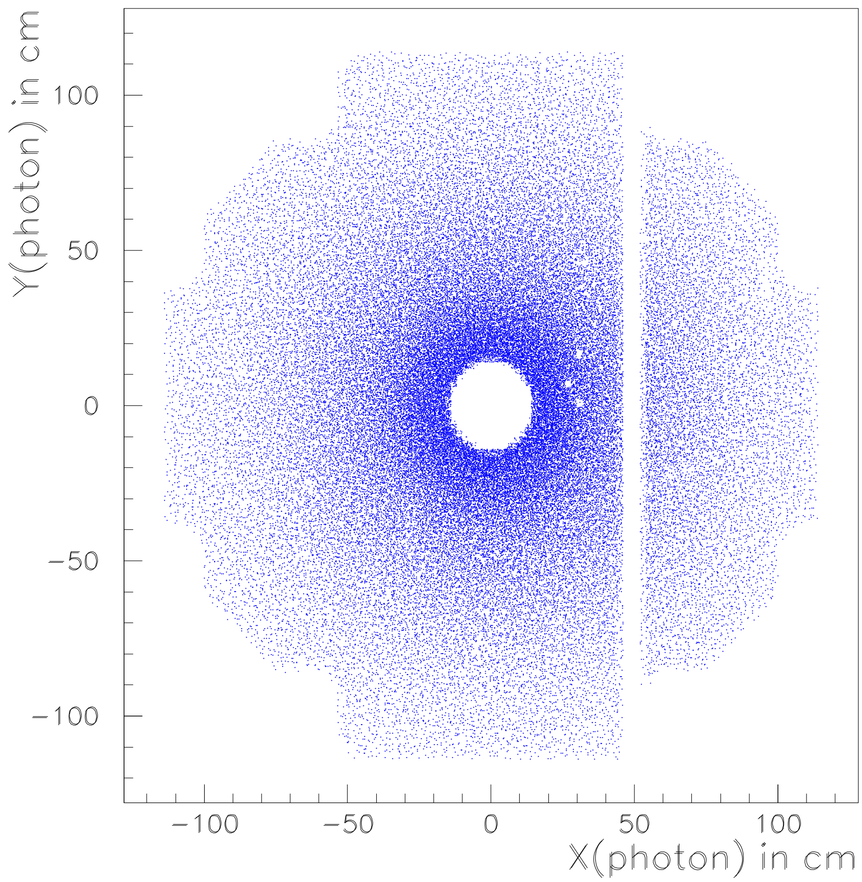

Figure 3.16: Reconstructed positions of clusters in the LKr during 1997 data–taking. The dead column at $x = 50$ cm is clearly visible.

3 kV High Voltage. A 4 cm wide column (called *dead column* in the following) was not connected to HV because of a broken capacitor. Other 40 channels were not working (*dead cells* in the following). The reduced HV caused a ~ 20 % increase in the electronic noise and a small ($\lesssim .5\%$) space charge effect, that has been corrected offline.

The electronic intercalibration of cells was regularly done along the data–taking, and stability in time was at the 0.1 % level. A correction factor was computed for each cell using electrons from K_{e3} decays (the measured energy of electrons can be compared with the momentum measured by the spectrometer).

The measured performances achieved during the 1997 run are the following:

Energy resolution

$$\frac{\sigma(E)}{E} = \left(\frac{3.5}{\sqrt{E(GeV)}} \oplus \frac{0.04}{E(GeV)} \oplus 0.42\right) \%$$

Position resolution

$$\sigma_x = \left(\frac{4.1}{\sqrt{E(GeV)}} \oplus 0.5\right) \text{mm}$$

$$\sigma_y = \left(\frac{4.4}{\sqrt{E(GeV)}} \oplus 0.5\right) \text{mm}$$

Time resolution

$$\sigma_t = 263 \text{ ps}$$

Linearity

maximum non linearity is 0.3 % over the range 3 to 100 GeV

3.3.4 Neutral Hodoscope

Though the LKr calorimeter is able to reconstruct the time of neutral events with excellent resolution, another detector was foreseen to do another time measurement, completely independent from the energy measurement. It consists of 256 bundles of scintillating fibers, each one contained in a epoxy-fiberglass tube having 7 mm diameter and 2 m length, immersed in the LKr volume. The tubes are fixed to the second spacer–plate, at a depth of 9.5 radiation lengths, and extend horizontally from the center to the outer edge where the signals are readout by 32 PMs.
The time resolution on the event time is < 300 ps for energy > 15 GeV.

The NHOD signals are also used to form a minimum–biased trigger that allows to measure the neutral trigger efficiency.

3.3.5 Hadronic Calorimeter

A conventional iron–scintillator sandwich calorimeter, 6.7 interaction lengths thick, follows the LKr detector, to contain the hadronic showers leaking out from the electromagnetic calorimeter. It is formed by two modules (*front* and *back*), each made of 24 scintillator planes, arranged alternatively along the x or y direction. Signals from groups of planes are readout by 176 channels.

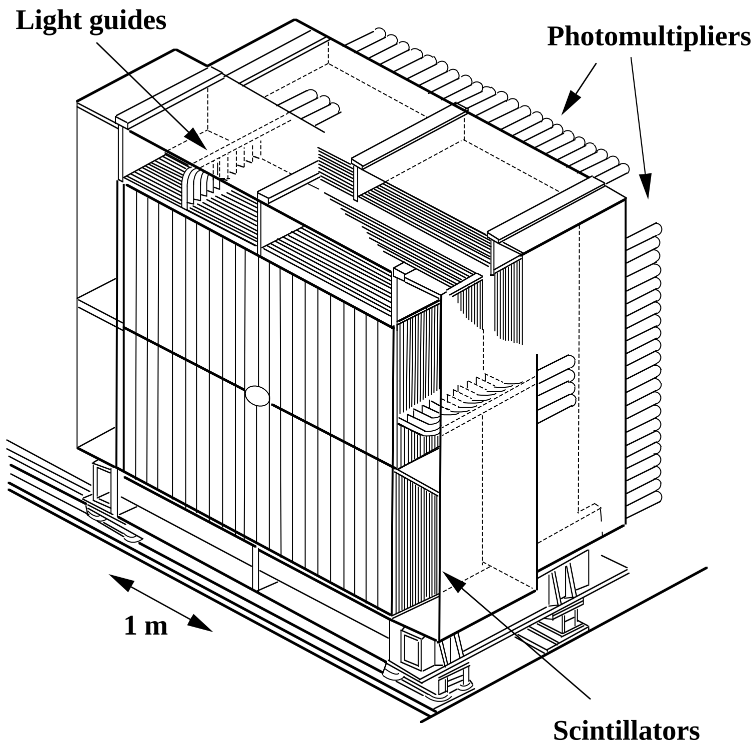

Figure 3.17: Schematic layout of the hadronic calorimeter.

The energy resolution is $65\%/\sqrt{E(GeV)}$.

Its main use is to provide, together with the LKr, the total energy of the event ($ETOT$), that is used by the first level charged trigger.

3.3.6 Muon Veto Counters

Three planes of scintillators, each one preceded by an 80 cm thick iron layer, are located at the end of the NA48 detector to detect, thus identifying, the muons. The first two planes, each measuring the position in one view, are segmented in 11 counters, 25 cm wide. The third plane consist of 6 horizontal counters. All counters are readout at both sides to keep the $K_{\mu3}$ veto inefficiency at per mill level. The readout TDCs provide a time reconstruction with resolution below 1 ns.

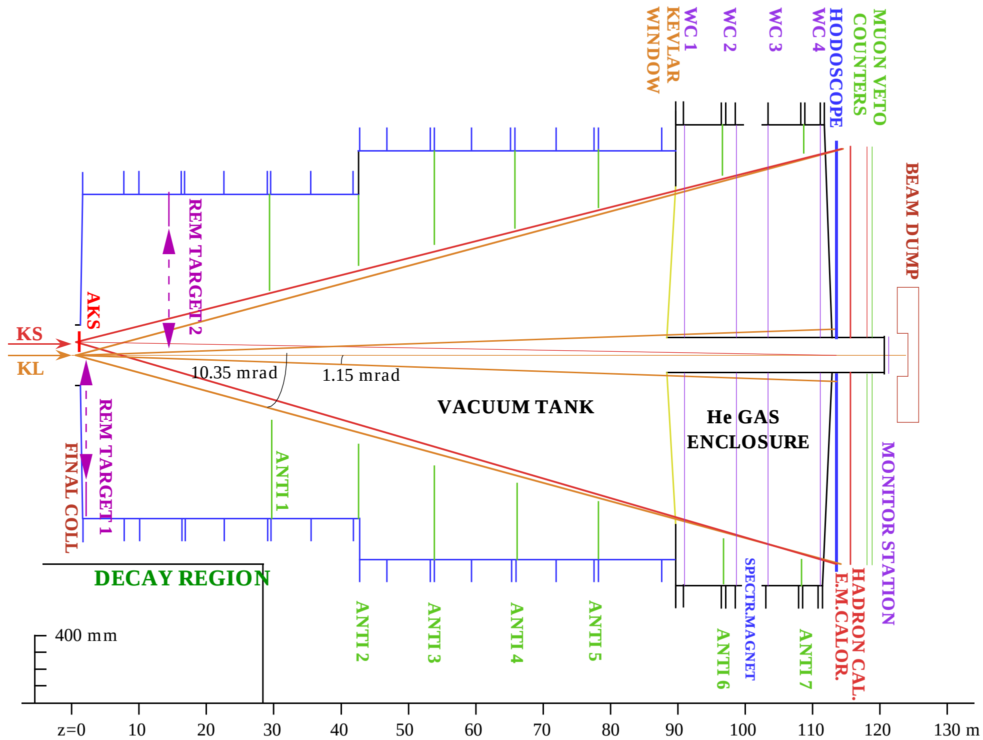

Figure 3.18: Position of the AKL rings around the decay region.

3.3.7 Anticounters

A system of anticounters surrounding the decay region was foreseen to fight the background from $K_L \to 3\pi$ and particularly the $3\pi^0$ that was expected to be the most dangerous background source. Seven rings of scintillators were instrumented, covering an acceptance region which is complementary to the central detector one, as shown in figure 3.18 (where the AKL rings are marked as Anti 1–7). Each ring consists in two planes of counters, each of which is preceded by a 3.5 cm thick iron layer, acting as photon converter with $\sim$ 95 % efficiency. A total of 144 counters are present, all readout on both sides.

An important use of the AKL regards the study of accidental activity.

3.4 Dataflow

The counting rates of the various detectors are of the order of 1 MHz. The trigger and data acquisition (DAQ) systems are required to cope with this amount of data with high efficiency and minimum deadtime. To this extent, the online selection performed by the trigger should reduce the rate to about 5 kHz and the DAQ was designed to stand peak rates of 10 kHz.

The data volume is about 10 kbytes per event (10 bytes $\times \sim 10^4$ channels, reduced on average by a factor 10 after zero suppression), so that a bandwidth of 100 Mbytes/s is requested to the DAQ.

One of the key–feature of the acquisition system is the **pipeline** architecture, that allows to virtually suppress the deadtime. The signals from all detectors are digitized, tipically with 10 bits, using a unique 40 MHz clock signal, that is broadcasted to all readout systems. The sampled signals are stored in a pipeline (i.e. a circular buffer), whose deepness of 200 μs determines the maximum data latency time. In the meantime, the various trigger sources provide their informations, that are processed and correlated by a digital pipelined system called Trigger Supervisor (TS), that is in charge to decide if the event has to be accepted. In the positive case, the TS broadcasts to all the detector readout systems a request containing the trigger code, the event number and a timestamp, that is the event time measured in units of clock pulses from the beginning of the burst. The readout systems asynchronously extract the event information around the requested timestamp and send them through an optical link to another pipelined system, the Data Merger (DM), that is in charge to synchronize the data coming from different subdetectors and to format and compress them. The complete event is then sent to the Front End Work Station (FEWS) that, after checking the integrity of data, sends it to the CERN central computing facility through a Gigabit link, without significant local data storage.

Starting from 1998, the DM and FEWS systems have been replaced by a more powerful Linux PC farm, allowing to increase the DAQ bandwith from 70 to 150 Mbytes/s.

In the computing center, the data are processed online on a powerful cluster of unix workstations (called cs2), gradually replaced since 1998 by a Linux pc farm,

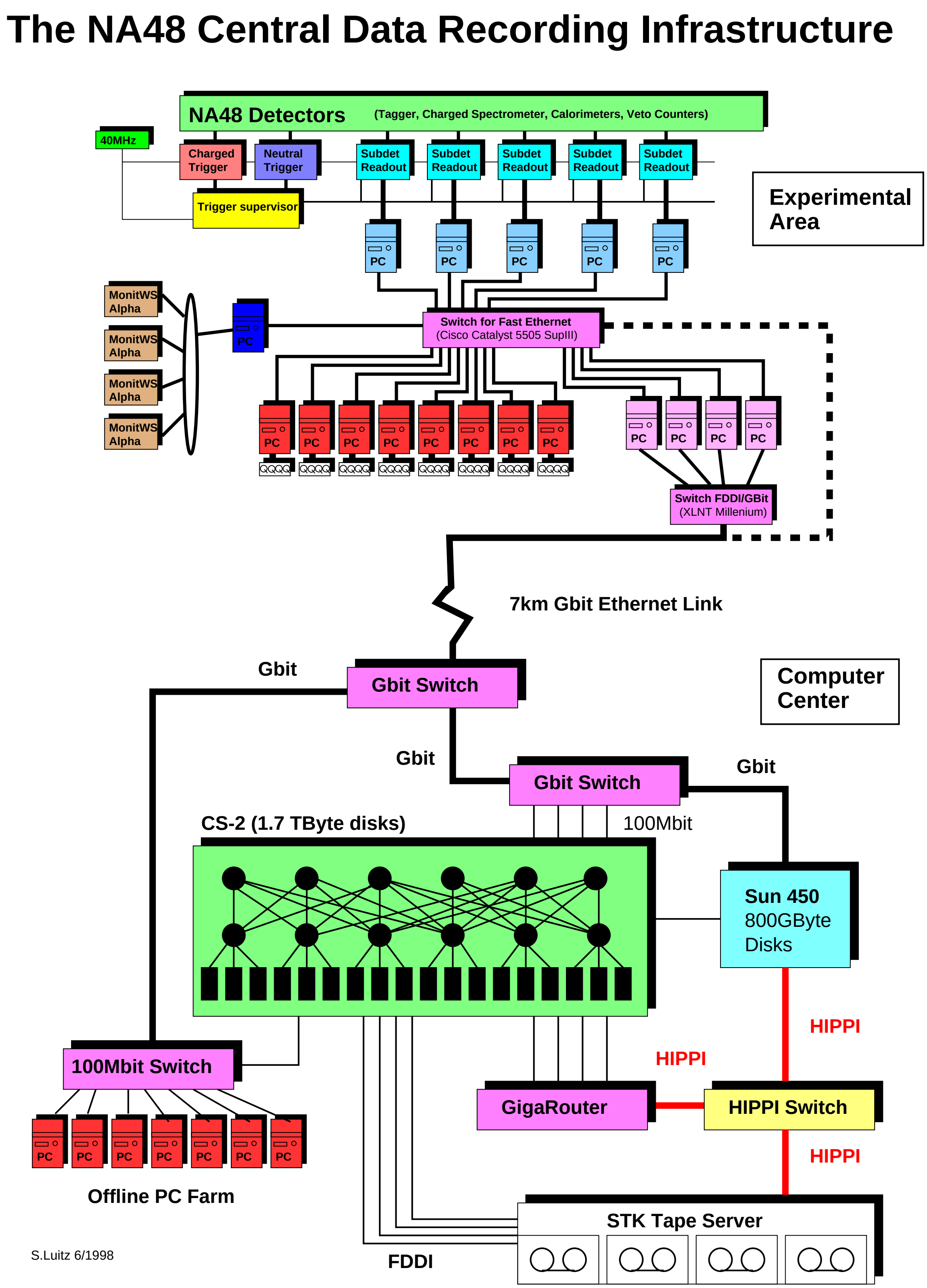

Figure 3.19: Logical scheme of dataflow from detectors to tape servers as for the 1998 data–taking

through a software third level trigger (L3). The L3 divides the events in various streams according to their characteristics and performs a first processing resulting in a reduced output, but no further selection is done to avoid unrecoverable biases due to software bugs. The data are finally sent to tape servers for tape storage. The whole sample of data taken in one year is reprocessed one or more times after the end of the run, as soon as the reconstruction program and the calibrations are optimized.
The scheme of data recording as for the 1998 run is showed in figure 3.19.

During the 42 days of 1997 run 25 Tbytes of data were written on tapes, and about other 170 Tbytes were acquired during the longer 1998 and 1999 runs. To cope with these huge amount of data, massive distributed computing resources have been allocated both at CERN and in the outer laboratories.

3.5 The Trigger

The main components of the multilevel trigger system of the experiment, illustrated in fig. 3.20, are a charged branch, a neutral branch, and the already cited Trigger Supervisor.

3.5.1 Charged Trigger

The charged chain of the NA48 trigger has been designed to efficiently select the $K^0 \rightarrow \pi^+\pi^-$ events out from a 10^4 times larger background of events having charged tracks. To this extent, it is mandatory to reconstruct online the decay vertex and the two pion invariant mass.

This operation, that requires to process a large amount of informations from the drift chambers through complex algorithms, is performed by the so–called Mass Box (MBX), a mixed hardware and software real–time processing system based on a farm of programmable processors. Since this system cannot stand the 300 kHz rate seen by the drift chambers, a first fast selection is needed and the MBX is indeed used as a second level charged trigger (L2C).

The first level charged trigger (L1C) aligns in time some signals coming from the hodoscopes, the hadronic calorimeter, the muon veto and the AKL, and produces 16 logical combinations, useful for various trigger conditions. The signal for the $\pi^+\pi^-$

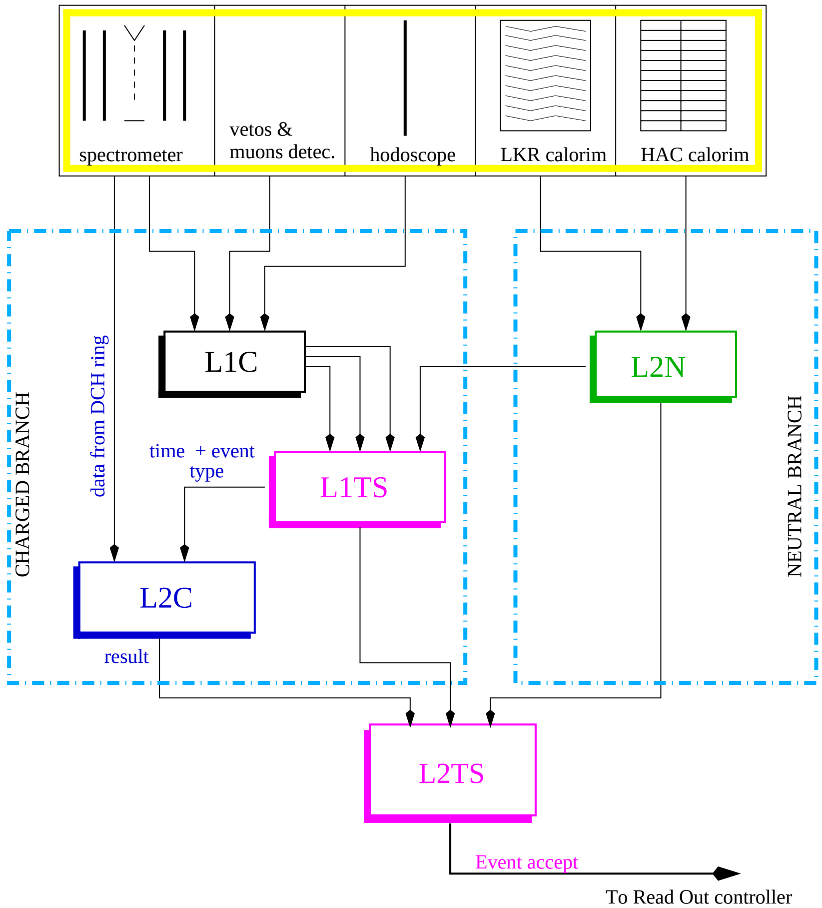

Figure 3.20: Logical scheme of the NA48 trigger system.

trigger is the so–called **QX**, that is the time coincidence of signals from opposite quadrants of the charged hodoscope. To form this signal, the quadrants of each plane are extended to include the closest counter of the adjacent quadrant, in order not to lose events having tracks passing close to the quadrant boundaries. The OR of two planes is then used to suppress inefficiencies.

The timeslice (25 ns) of the QX signal gives the trigger time, but, since the Mass Box needs a more precise time information, a further division of the timeslice in steps of 6.25 ns is provided, through two additional bits, by a *Fine Time* (FT) module, which uses a 160 MHz clock synchronized with the 40 MHz main one.

The level 1 Trigger Supervisor (L1TS) is a digital, fully pipelined system that is in charge to send the requests to the L2C trigger. It receives every 25 ns the output of L1C as well as a track multiplicity trigger signal formed from the DCH, and a total energy signal (**ETOT**) formed by the neutral trigger from the informations of both calorimeters. The $ETOT$ signal is found on when the total energy is above about 30 GeV.

For the $\pi^+\pi^-$ trigger, a narrow coincidence between the $ETOT$ and QX signals is required.

During the 1997 run, the QX was downscaled by a factor of 2 in order to reduce the input rate to the L2C to about 70 kHz. This does not affect very much the statistical error of the double ratio measurement,that is limited by the K_L neutral mode.

If the trigger condition is satisfied, the L1TS sends a request to the DCH readout and to the L2C with a fixed delay of 4 μs with respect to the event time.

The L2C trigger system (Mass Box), provides the online reconstruction of $\pi^+\pi^-$ invariant mass, using the data from the drift chambers 1,2 and 4. It consists of four subsystems [53]:

the Coordinate Builder (CB) that receives the hit times from the drift chambers and computes the coordinates, relying on the event time provided by the L1TS as the timestamp and the fine time bits;

the Event Builder and Dispatcher (EBD), consisting of a programmable switch with 16 channels that builds the event by putting together the 12 coordinate packets (4 planes x 3 chambers) that are serialized and sent to the processing stage;

the Event Worker Farm that computes the space–points, tracks and magnetic deflections and checks if they are compatible with the kaon invariant mass, assuming a $\pi^+\pi^-$ decay. It consists of eight parallel event workers (EW), each of which was based initially on a cluster of 4 DSP processors, then upgraded (since 1998 run) to a 200 MHz PowerPC;

the Event Worker Farm Manager that receives the EWs output, communicates to the EBD the list of free EWs and interfaces the system with the level 2 Trigger Supervisor.

The L2C response must arrive within 100 μs from the event time. The maximum rate it can stand was above 100 kHz before the upgrade, about 200 kHz afterward. The online resolution on the kaon mass is 5 MeV/c^2, allowing for an output rate

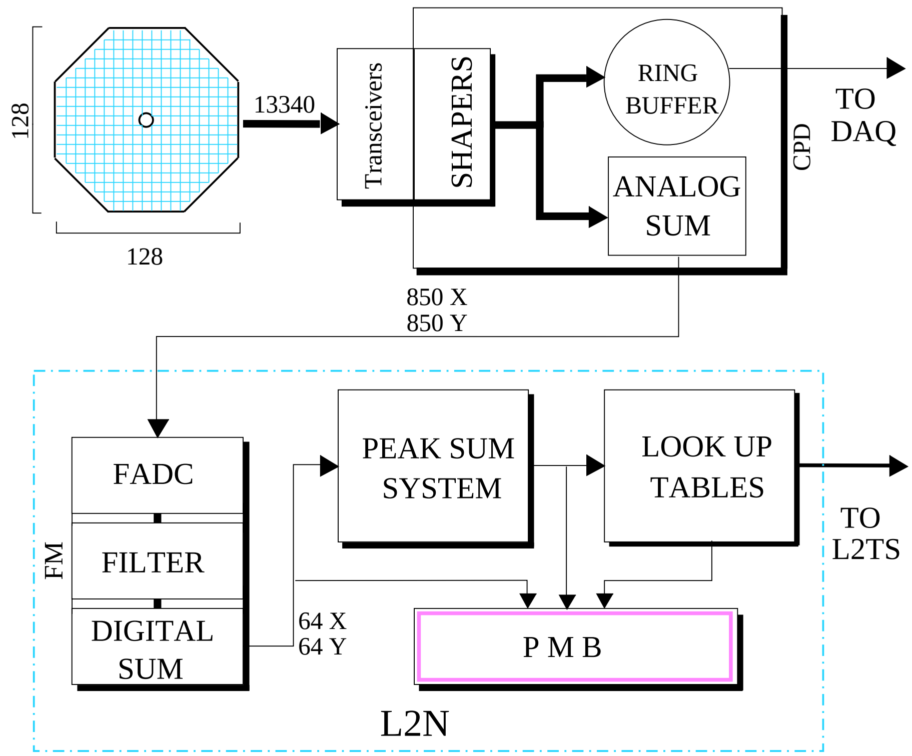

Figure 3.21: Logical scheme of the neutral trigger chain.

of about 2 kHz with conservative cuts on the invariant mass and the decay vertex longitudinal position.

3.5.2 Neutral Trigger

The neutral trigger system (NUT or L2N) is in charge to identify $\pi^0\pi^0$ events with minimal inefficiency and deadtime, by processing the information from the 13248 cells of LKr. It is required to have an output rate < 3 kHz, starting from the 110 kHz rate of the events releasing at least 30 GeV in the LKr.

To this extent, the system is implemented as a deadtime–free 40 MHz pipeline, that, every clock pulse, computes the total energy, the center of gravity (cog), the vertex position and the number of peaks, starting from the two orthogonal projection of the energy releases in the calorimeter.

Its input signals are formed in the CPD boards, that provides the analog sum of 16 (8x2) cells to form super-cells. The pulse of each cell is used twice to get both the x and y orientations.

The trigger chain is formed by three electronic subsystems [27] (as sketched in fig. 3.21):

the Filter Module (FM) digitizes the analog input signals using a 10 bit FADCs and applies a zero suppression. The filtered super cells are then added to form 64 projections for each view;

the Peak Sum System (PSS) looks for maxima in time for each projection. By interpolating the rising edge of the pulse, a 3 bit fine time information is obtained for the peak reference time, so that the number of peaks is counted in bins of 3.125 ns in order to better resolve accidentals. The system also computes the total energy m_0 and the first and second moments of position m_1 and m_2 for both projections

$$m_{nx} = \sum_i x_i^n \, E_i \qquad m_{ny} = \sum_i y_i^n \, E_i \qquad ; \quad n = 1, 2$$

the Look–Up Table (LUT) computes the relevant physical quantities allowing to take the final trigger decision: the total energy E_{LKR} obtained from three timeslices around the maximum using a parabolic fit, the center of gravity of the energy deposits

$$cog = \frac{\sqrt{m_{1x}^2 + m_{1y}^2}}{E_{LKR}}$$

and the decay vertex (obtained imposing the K^0 mass to the invariant mass of the photon clusters, see discussion in section 4.2)

$$z_V = z_{LKR} + \frac{\sqrt{E_{LKR}(m_{2x} + m_{2y}) - (m_{1x}^2 + m_{1y}^2)}}{m_K}$$

The LUT defines the $\pi^0\pi^0$ by conservatively cutting on these quantities and on the number of peaks. Other trigger configurations are defined as well, for different decay modes such as Dalitz and $\mu\mu\gamma$.

The total latency time is below 100 μs. The obtained online resolution for the kaon energy is 2.7 % over the full energy range. Conservative cuts on number of peaks, energy, *cog* and kaon decay proper time allow to get an output rate of about 2 kHz.

The NUT also computes in similar way the total energy of the hadron calorimeter, that is summed to E_{LKR} to form the $ETOT$ signal. All the measured variables are recorded using some dedicated PMB boards.

The output of the L1TS, L2C and L2N systems is sent to the last trigger stage, the **level 2 Trigger Supervisor** (L2TS), that correlates all the informations to build the final trigger word. The main trigger conditions for the ϵ'/ϵ analysis are:

- the $\pi^+\pi^-$ MBX trigger;
- the control trigger for the Mass Box, defined as

  $$QX/2 \times ETOT + QX/D$$

  where the time coincidence is looser than the one formed by L1TS and the downscaling factor D was 32 in the first part of the run and 128 afterwards;
- the $\pi^0\pi^0$ NUT trigger;
- the control trigger for the NUT, defined as (the overline stands for anti–coincidence)

  $$NHOD \times \overline{1\mu} \times \overline{AKL}$$

  for the first part of the run, and only by $NHOD$ for the second part.

Chapter 4

Measuring ϵ'/ϵ : the strategy

The data analysis for the ϵ'/ϵ measurement must be very accurate to exploit all the experiment capabilities and take into account all effects perturbing the measured double ratio at $> 10^{-4}$ level. This chapter is devoted to outline and justify the analysis procedure adopted in NA48. All the systematic corrections and uncertainties that have been obtained through detailed studies by experts, and must be considered in the final analysis of 1997 data sample, are also given.

4.1 Charged reconstruction

The two charged tracks of the $K^0 \rightarrow \pi^+\pi^-$ decays are reconstructed using the magnetic spectrometer, by building, from the drift chamber hits and drift times, the track segments before (DCH 1 and 2) and after (DCH 3 and 4) the magnet. The track momenta are obtained using a detailed map of the magnet field. A vertex is defined at the longitudinal position where the tracks are closest. A small correction was needed to take into account the presence of a magnetic field in the vacuum tube before the spectrometer[1].

Being the chamber space–point resolution $\sim$ 90 μm and the distance between the first two chambers $\sim$ 9 m, we get a resolution of the track angle of $\sim 10^{-5}$ rad, resulting in a vertex position resolution of $\sim$ 50 cm in the longitudinal direction and $\sim$ 2 mm in the transverse direction (see fig. 4.1). This allows to identify with negligible error the K_S and K_L events, since the two beams are vertically separated by at least 6 cm in the fiducial decay region (fig. 4.2).

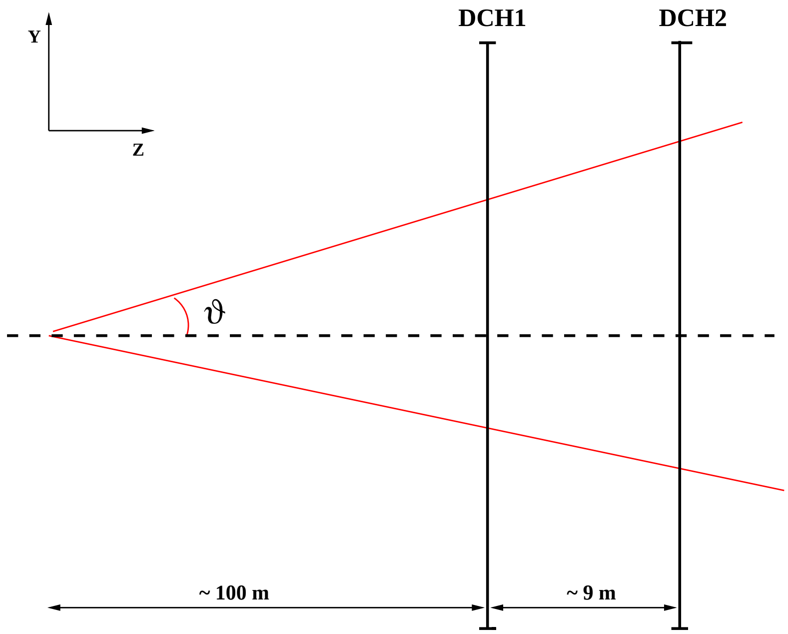

Figure 4.1: Vertex reconstruction using the first 2 chambers. Being $\Delta\theta \sim 10^{-5}$, $\theta \sim 10^{-3} \div 10^{-2}$, we have $\Delta Y \sim \Delta\theta \cdot 100$ m $\sim$ 1 mm, $\Delta Z \sim \frac{\Delta\theta\ Z}{\theta} \sim 10 \div 100$ cm

[1]After observing a dependence of the measured $\pi\pi$ invariant mass from the azimuthal angle of the decay plane, the field was accurately measured before the 1998 data–taking and its map included in the reconstruction program. The integral $\int |\vec{B} \times \vec{dl}|$ of this spurious field amounts to $\simeq 2\ 10^{-3}$ Tm.

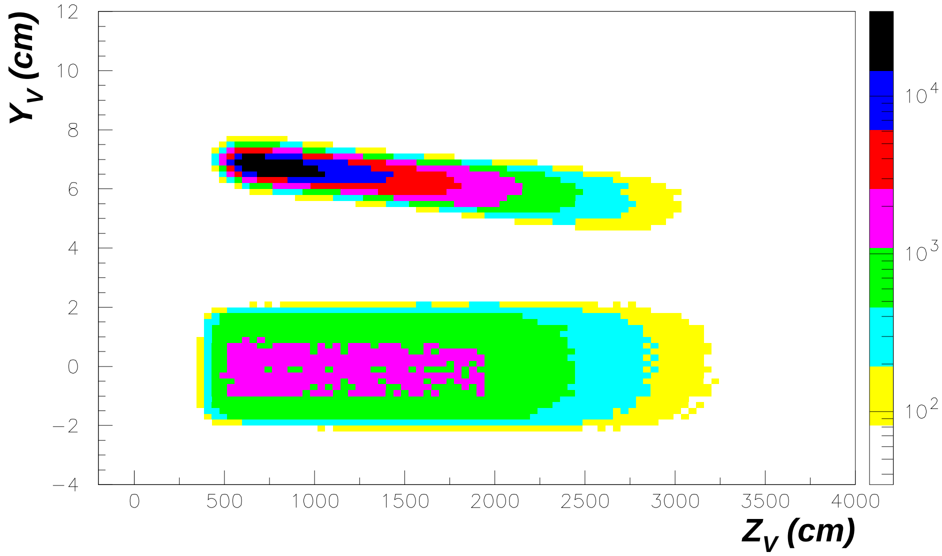

Figure 4.2: Reconstructed vertex position in the vertical plane for $K^0 \to \pi^+\pi^-$ events.

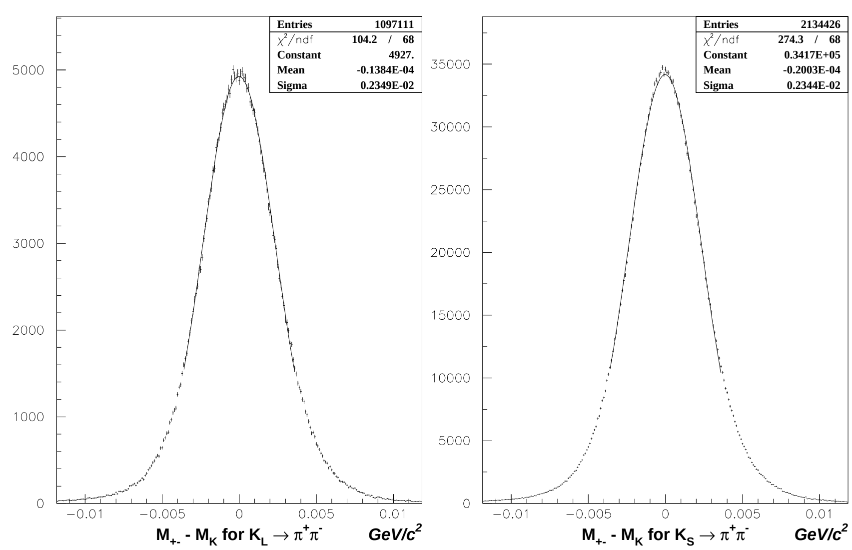

Figure 4.3: $\pi^+\pi^-$ invariant mass for K_L and K_S events.

The resolution in invariant mass is 2.4 MeV/c^2 (see fig. 4.3).

4.2 Neutral reconstruction

The $K^0 \to \pi^0\pi^0 \to 4\gamma$ decays are reconstructed starting from the detected showers in the liquid Krypton calorimeter. The energy of each shower is measured using the cells within a radius of 11 cm around the maximum energy cell. A set of small corrections is applied to account for:

- the energy lost outside the cluster boundary;
- the energy lost in the *dead* (not working) cells;
- the energy sharing with the other showers of the event;
- the small residual dependence from the impact point within the cell;
- the small space charge effect from accumulation of positive ions, due to the low drift voltage used during the 1997 run (1.5 kV instead of the nominal 3 kV).

The average energy resolution obtained for the kaon energy as the sum of the 4 cluster energies E_i is 0.6 %. Using the positions x_i and y_i of each cluster, it is possible to reconstruct the longitudinal vertex position Z_v, by requiring the 4γ invariant mass to be equal to the kaon mass M_K:

$$M_K^2 c^4 \; = \; \sum_i \sum_{j>i} 2 E_i E_j \left(1 - \cos\theta_{ij}\right) \; \simeq \; \sum_i \sum_{j>i} E_i E_j \theta_{ij}^2 \tag{4.1}$$

being θ_{ij} the angle between 2 photons, usually $\lesssim$ 10 mrad. If δ is the angle between the beam axis and the direction of the π^0 decaying in the two photons detected in the LKr calorimeter, we have (see fig. 4.4)

$$\theta_{ij} \simeq \frac{d_{ij}\cos\delta}{\Delta Z/\cos\delta} \simeq \frac{d_{ij}}{\Delta Z}(1-\delta^2) \tag{4.2}$$

$$\left(d_{ij} = \sqrt{(x_i - x_j)^2 + (y_i - y_j)^2} \qquad\qquad \Delta Z = Z_{LKR} - Z_v \right)$$

and, since $\delta \lesssim$ 10 mrad, we can write with approximation better than 10^{-4}

$$\theta_{ij} \simeq \frac{d_{ij}}{\Delta Z} \tag{4.3}$$

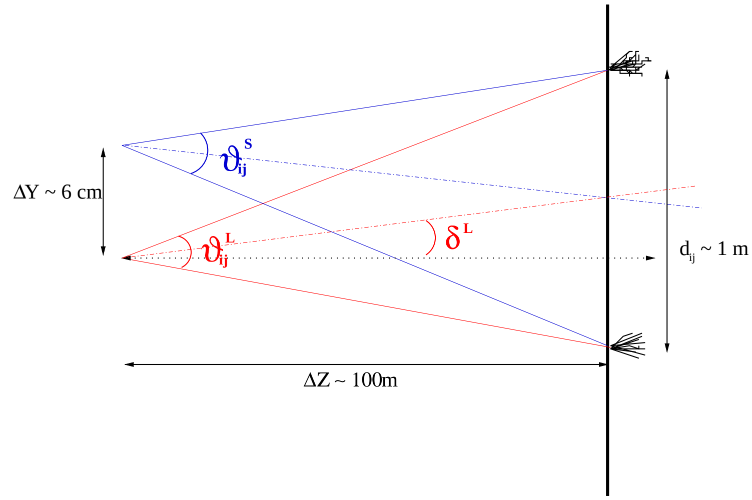

Figure 4.4: Comparison of neutral reconstruction in the hypothesis of K_S or K_L event.

$$\Longrightarrow \boxed{Z_v = Z_{LKR} - \frac{1}{M_K c^2}\sqrt{\sum_i \sum_{j>i} E_i E_j d_{ij}^2}} \tag{4.4}$$

We can also notice from figure 4.4 that, in order to discriminate between K_S and K_L events, we should be sensitive to

$$\theta_{ij}^L - \theta_{ij}^S \simeq \frac{d_{ij}}{\Delta Z} 2\delta(\delta^S - \delta^L) \lesssim 10^{-7}\text{rad} \tag{4.5}$$

Thus, even with the very good performances of the NA48 calorimeter, it is clearly impossible to distinguish K_S and K_L as for the charged events, and the use of the tagging method is mandatory.

A small correction to Z is applied to account for the photon impact angle on the calorimeter surface, i.e. the deviations from projective geometry due the extension of the observed decay region.

The resolution of Z_v can be naively inferred from equation 4.4 as

$$\sigma^2(Z_v) = \sum_i \left[\left(\frac{\partial Z_v}{\partial E_i}\sigma(E_i)\right)^2 + \left(\frac{\partial Z_v}{\partial x_i}\sigma(x_i)\right)^2 + \left(\frac{\partial Z_v}{\partial y_i}\sigma(y_i)\right)^2 \right] \tag{4.6}$$

$$\frac{\partial Z_v}{\partial E_i} = -\frac{\sum_{j\neq i} E_j d_{ij}^2}{2M_K^2 c^4 \Delta Z} \approx -\frac{\Delta Z}{4 < E >} \tag{4.7}$$

$$\left|\frac{\partial Z_v}{\partial x_i}\right| = \left|-\frac{\sum_{j\neq i} E_i E_j (x_i - x_j)}{M_K^2 c^2 \Delta Z}\right| \approx \frac{\Delta Z}{2 < d >} \tag{4.8}$$

Using typical values $\Delta Z \sim 100$ m, $\sigma(E)/E \sim 1$ %, $\sigma(\Delta x)/\Delta x = \sigma(\Delta y)/\Delta y \sim 0.5$ %, we get $\sigma(Z_v) \sim 70$ cm, with a similar contribution from energy and position resolutions. The longitudinal vertex position can thus be measured with about the same accuracy than for charged events.

Since the neutral reconstruction is not sensitive to the transverse decay position, we assume all decay to occur along the K_L beam axis, so that the kinematics is fully described by Z_v and the four photon quadrimomenta. This corresponds to 17 real variables, that are reduced to 10 by the mass constraints (the kaon, the 2 π_0 and the 4 γ). Since we measure 12 real quantities (4 energies and 8 positions), we still have a redundancy of 2 variables. In fact, we have not used the π^0 mass constraints yet, so that to check against background that the event is a well reconstructed $K^0 \to \pi^0\pi^0$ decay, we can verify that, for one of the three possible 2–gamma pairings, the $\gamma\gamma$ invariant masses

$$m_{12} = \sqrt{E_1 E_2}\frac{d_{12}}{\Delta Z c^2} = \frac{\sqrt{E_1 E_2} M_K d_{12}}{\sqrt{\sum_i \sum_{j>i} E_i E_j d_{ij}^2}} \tag{4.9}$$

$$m_{34} = \sqrt{E_3 E_4}\frac{d_{34}}{\Delta Z c^2} = \frac{\sqrt{E_3 E_4} M_K d_{34}}{\sqrt{\sum_i \sum_{j>i} E_i E_j d_{ij}^2}} \tag{4.10}$$

coincide with the π^0 mass.

However, because of the kaon mass constraint, m_{12} and m_{34} are anticorrelated. For example, for the dependence on energy:

$$\frac{\partial m_{12}}{\partial E_1} \sim \frac{M_{\pi^0}}{2E_1}\left(1 - \frac{\mu_1^2}{M_K^2}\right) \tag{4.11}$$

$$\frac{\partial m_{34}}{\partial E_1} \sim -\frac{M_{\pi^0}}{2E_1}\frac{\mu_1^2}{M_K^2} \tag{4.12}$$

$$\left(\mu_1^2 = \frac{E_1 \sum_{j\neq 1} E_j d_{1j}^2}{\left(\Delta Z c^2\right)^2} = M_K^2 \; \frac{E_1 \sum_{j\neq 1} E_j d_{1j}^2}{\sum_i \sum_{j>i} E_i E_j d_{ij}^2}\right)$$

The quantity μ_1^2/M_K^2 varies by construction between 0 and 1 and is expected to fluctuate symmetrically around the value 0.5; therefore, the two derivatives always have opposite sign. If we now consider

$$m_+ = \frac{m_{12} + m_{34}}{2} \qquad m_- = \frac{m_{12} - m_{34}}{2}$$

we get

$$\frac{\partial m_+}{\partial E_1} \sim \frac{M_{\pi^0}}{4E_1}\left(1 - \frac{2\mu_1^2}{M_K^2}\right) \tag{4.13}$$

$$\frac{\partial m_-}{\partial E_1} \sim -\frac{M_{\pi^0}}{4E_1} \tag{4.14}$$

so that we expect the sum and the difference of m_{12} and m_{34} to be essentially uncorrelated and to have a different resolution (lower for the sum). Similar conclusions can be drawn for the dependence from x_i and y_i.
Eventually, we introduce a χ^2 variable to test the $2\pi^0$ hypothesis:

$$\chi^2_{2\pi^0} = \left(\frac{m_+ - M_{\pi^0}}{\sigma(m_+)}\right)^2 + \left(\frac{m_-}{\sigma(m_-)}\right)^2 \tag{4.15}$$

where for the resolutions $\sigma(m_+)$ and $\sigma(m_-)$ we use values parametrized as a function of the lowest photon energy. Typical values are $\sigma(m_+) \simeq 0.45$ MeV$/c^2$, $\sigma(m_-) \simeq 1.1$ MeV$/c^2$. The 2γ paring is chosen according to the best χ^2 value, that will be used to reject background. The ellipses drawn in figure 4.6 define events with a given best $\chi^2_{2\pi^0}$ value.

4.3 Quality cuts and background rejection

4.3.1 Charged events

Good $K \rightarrow \pi^+\pi^-$ candidates are first selected through a set of quality cuts:

- closest distance of approach (CDA) of the two tracks < 3 cm. This cut is effective against bad track association and events with pion decay;
- the reconstructed charge of the two tracks must have opposite sign and tracks must be fitted with good χ^2;
- pion momentum > 10 GeV/c;
- the *center of gravity (cog)* of the event, built from the momentum–weighted track positions at LKr surface X_i, Y_i, extrapolated from DCH 1 and 2, as

$$cog = \frac{\sqrt{\left(\sum_{i=1,2} X_i|P_i|\right)^2 + \left(\sum_{i=1,2} Y_i|P_i|\right)^2}}{\sum_{i=1,2}|P_i|} \tag{4.16}$$

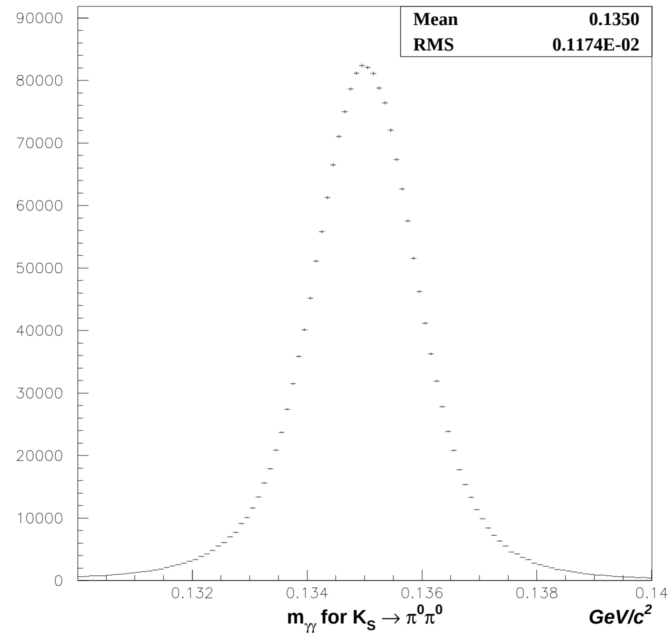

Figure 4.5: Reconstructed π^0 mass for $K_S \to \pi^0\pi^0$ events.

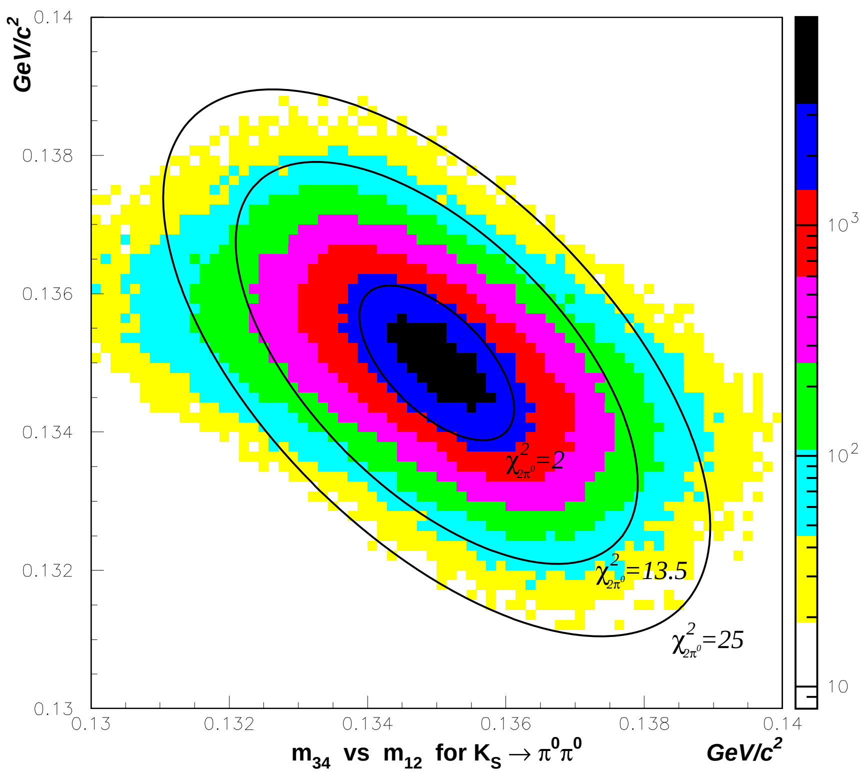

Figure 4.6: Correlation between the invariant masses of the two $\gamma\gamma$ couples for $K_S \to \pi^0\pi^0$ events.

must be < 10 cm. This cut cleans the sample from kaons scattered in the K_S collimator and in the AKS, and also improves background rejection;

- time difference between the tracks < 6 ns to avoid accidental tracks;

- vertex time within $\pm$ 20 ns from the center of the trigger timeslice. This avoids events triggered by QX afterpulses (affecting 14 % of charged events [22]) and not triggered by the main pulse because of the downscaling factor of 2 that was applied to QX.

To reject the large amount of 2–tracks background events (mainly from $K_{\mu 3}$, K_{e3} and $\pi^+\pi^-\pi^0$ decay of K_L , having branching ratios up to 200 times larger that $\pi^+\pi^-$), the following cuts are applied:

- the $\pi^+\pi^-$ invariant mass M_{+-} is required to be equal to the kaon mass within 3 times the resolution, that has been parametrized as a function of the energy;

- the reconstructed kaon transverse momentum is required to be null within errors. Due to the fact that the distance between the target and the spectrometer differs by a factor 2 between K_S and K_L , some care is needed to choose the most appropriate kinematical variable in order to have a symmetric cut for K_S and K_L . For a good event, a transverse momentum can be generated because of an error $\Delta\theta$ ($\lesssim 10^{-5}$ rad) in the kaon direction, as reconstructed by the spectrometer, and an error ΔX ($\lesssim 100$ μm) in the kaon position at the chamber (i.e. the center of gravity at DCH1). Thus, the kaon transverse momentum p_T with respect to the direction given by the target and the reconstructed vertex position will be (see fig. 4.7a):

$$p_T \;=\; P_K \sin\alpha \simeq P_K \frac{\Delta X + \Delta\theta(Z_{DCH1} - Z_V)}{Z_V - Z_T} \;\simeq\; P_K \frac{\Delta\theta(Z_{DCH1} - Z_V)}{Z_V - Z_T} \tag{4.17}$$

which is strongly dependent from the target position Z_T, chosen according to the vertex identification of the event. Since the error on the reconstructed vertex position comes from $\Delta\theta$ more than from ΔX, we see that a better and, what is more important, K_S /K_L symmetric reconstruction of transverse momentum can be obtained by using for the kaon direction the line connecting the target and the kaon reconstructed position at DCH1 (fig. 4.7b):

$$p'_T \;=\; P_K \sin\beta \simeq P_K \left(\Delta\theta + \frac{\Delta X}{Z_{DCH1} - Z_T}\right) \;\simeq\; P_K \Delta\theta \tag{4.18}$$

We see that p'_T is to a good approximation independent from the target position, so that we can apply a cut $(p'_T)^2 \;<\; 0.0002$ GeV^2/c^2, that produces a symmetric loss of good events $< 0.1\%$, mainly due to misreconstruction tails;

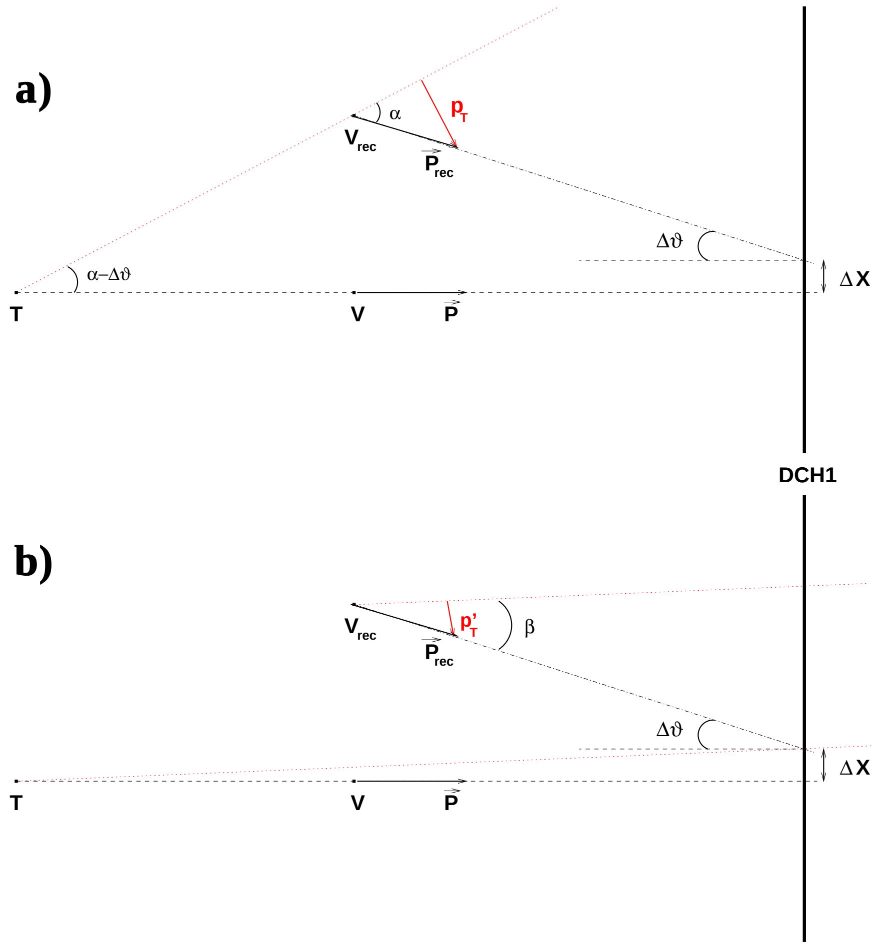

Figure 4.7: Definitions of the p_T and p'_T variables, describing the reconstructed kaon transverse momentum. V and P are the true kaon vertex and momentum, V_{rec} and P_{rec} the reconstructed ones. The misreconstruction effects are clearly exaggerated in this sketch.

- the electrons from K_{e3} are rejected by comparing the track momentum P (expressed in GeV/c) measured by the spectrometer with the track energy E (expressed in GeV) measured by the LKr calorimeter, that, contrary to the case of pions, contains all the energy of electrons. A cut $E/P < 0.8$, having an efficiency of 95 % on good events and a rejection factor 500 on K_{e3} , has been chosen. In order to make this cut effective, track extrapolations to the LKr surface are required to be within the detector acceptance and to be at least 2 cm far from the dead column and the other dead cells;

- events having tracks that match both in space (with a momentum–dependent cut to account for multiple scattering) and time (with a cut at ± 4 ns) a hit in the muon veto detector are rejected. Track extrapolations are required to be inside the acceptance of the muon counters. The rejection factor of $K_{\mu 3}$ events is about 500, while a few per cent of good events are lost, mainly because of pion decay;

- to reject $\Lambda^0 \to p\pi^-$ decays from the K_S beam, we apply a cut on the momentum asymmetry $|P_{\pi^+} - P_{\pi^-}|/|P_{\pi^+} + P_{\pi^-}|$, which is typically larger than 0.5 for such events. An energy dependent asymmetry cut, that is also useful to minimize the $K_S - K_L$ acceptance difference, will be discussed in section 5.3;

After these cuts, Montecarlo simulations show that the residual background is at the level of a few per mill and is dominated by K_{e3} and $K_{\mu 3}$ events. As will be shown in section 7.3, it is possible to directly measure the background contamination in the final K_L charged sample, by selecting high–statistics samples of K_{e3} and $K_{\mu 3}$ events and using the different shape of the 2–dimensional $(M_{+-}, {p'_T}^2)$ distribution for $K_{\mu 3}$, K_{e3} and signal events. The resulting error on the double ratio is limited to a few 10^{-4}.

4.3.2 Neutral events

The quality cuts applied to the reconstructed neutral events are the following:

- photon energy 3 GeV $<$ E_γ $<$ 100 GeV;

- distance between the two closest clusters $>$ 10 cm;

- clusters must be within the fiducial volume of the calorimeter and be at least 2 cm far from the dead column and the others dead cells;

- the difference between any cluster time and the average time of the four clusters must be < 5 ns;
- the *center of gravity (cog)* of the event

$$cog = \frac{\sqrt{\left(\sum_{i=1,4} x_i|E_i|\right)^2 + \left(\sum_{i=1,4} y_i|E_i|\right)^2}}{\sum_{i=1,4}|E_i|} \qquad (4.19)$$

  must be < 10 cm. The cut must be the same than for charged event. A possible bias from different resolution is expected to be negligible, and will anyway be included in the acceptance correction.

The main source of background for the neutral case comes from the 3 π^0 decays of K_L . Two cuts are applied in order to minimize it:

- events with an extra–cluster of sensible energy (> 1.5 GeV) which is in time ($\pm$ 3 ns) with the time average of the four photon candidates are rejected;
- 2γ invariant masses must agree with π^0 masses: best $\chi^2_{2\pi^0} < 13.5$

Since the surviving $3\pi^0$ events have 2 clusters undetected in the calorimeter, their energy is underestimated and consequently their reconstructed vertex is shifted toward the calorimeter. Therefore, we expect to obtain a better rejection of this background also by tightening the cut on the maximum allowed Z_v, that will be discussed in the next sections.

Anyway, the residual background is of order 0.1% and can be directly measured from data. In fact, Montecarlo simulations show that the $\chi^2_{2\pi^0}$ distribution for background events is approximatively flat, so that the background contamination in the signal region can be obtained by extrapolating the number of events in the tails outside the signal region, after subtracting the true signal contribution obtained from K_S events. As will be shown in section 7.4, the error introduced in the double ratio is $2 \cdot 10^{-4}$.

4.4 Energy binning and K_L weighting

After having shown how it is possible to reconstruct and purify from background the $K \to \pi\pi$ events, we now come to discuss how to minimize the two main differences between the samples of K_S and K_L decays:

Energy spectrum: in order to avoid the effect of different spectrum distributions without relying on their *a priori* knowledge, it is sufficient to perform the analysis in **energy bins**, provided we limit ourselves to the energy range for which the beam lines have been designed, namely 70 to 170 GeV, where the spectrum difference is contained within $\pm$ 10%. To avoid any residual effect, a number of bins larger than 10 is sufficient, as can be checked through Montecarlo simulations or, more directly, by plotting the result as a function of the number of bins used. The double ratio in each bin must be estimated from the four event counts using an unbiased estimator of $\ln R$.

Lifetime: the distributions of longitudinal vertex position z are clearly very different for K_S and K_L events because of the lifetime ratio $\tau_L/\tau_S = 579.6$. To avoid the resulting large acceptance difference, the two distributions are equalized by **weighting** the K_L events as a function of the reconstructed decay proper time

$$t \ = \ \frac{Z \ M_K}{P_K} \tag{4.20}$$

with the function

$$w(t) \ = \ \mathcal{N} \ e^{-t\left(\frac{1}{\tau_S}-\frac{1}{\tau_L}\right)} \tag{4.21}$$

where $\mathcal{N}$ is an arbitrary normalization constant. In chapter 6 we will show how this weighting function has to be modified in order to take into account the residual pure K_S and K_S $/K_L$ interference in the K_L beam.

The weighting procedure avoids to rely on the accuracy of the Montecarlo simulation of the experiment. In fact, as discussed in detail in chapter 5, the residual acceptance difference after weighting is of the order of per mill, thus it can be computed with a large relative error. Furthermore, the weighting minimizes all the effects related to geometry, as the detector efficiencies, and considerably suppresses the neutral background, because of the shift on the Z decay position for the $3\pi^0$ events. The price to pay is the loss ($\sim$ 40%) in statistical power of the K_L samples.

At this point a question could be arisen: why not to perform the analysis in bins of Z as we do for the kaon energy? The problem has to do with the definition of decay fiducial region, that, in the case of the analysis in bins of Z, should be done through the reconstructed Z position in the same way for K_S and K_L . In this case, the effect of different resolution in Z for charged and neutral events could become dangerous for K_S events due to the steepness of the Z distribution[2]. This is one of the main motivations[3] to put an anticounter, the **AKS**, on the K_S beam line in order to veto all the decays occurring upstream, thus defining the beginning of fiducial region without any bias from reconstruction. For the K_L beam the anticounter method cannot be applied because of the much higher beam intensity, and it is mandatory to use $Z > z_{AKS}$. However, since the vertex distribution is approximatively flat, we expect the event gains and losses due to resolution effects to be equal.

The length of the fiducial decay region is chosen as a number n_τ of K_S lifetimes. For $n_\tau > 2$ the statistics of good events after weighting is not critically dependent from the chosen cut.

The fiducial regions defined via AKS for the two decay modes are actually shifted by 21.0±0.5 mm, namely the width of the AKS scintillators. In fact, the AKS won't detect neutral decays occurring inside the scintillators, being negligible the photon conversion probability inside it, while it will detect charged decays. This causes a distortion of the ratio of charged to neutral K_S, that is compensated by weighting, provided that the same fiducial region is chosen for K_L and K_S , and that the weighting is a function of the absolute z position (i.e. the normalization constant $\mathcal{N}$ in eq. (4.21) is the same for charged and neutrals):

[2]The distribution of K_S reconstructed vertex $g(z)$ is given, for an energy bin, by the convolution of the true exponential distribution $f(z) = \frac{1}{\lambda}e^{-\frac{z}{\lambda}}$ with a gaussian function:

$$g(z) = \int \frac{1}{\sigma\sqrt{2\pi}} e^{-\frac{(z-z')^2}{2\sigma^2}} \frac{1}{\lambda} e^{-\frac{z'}{\lambda}} dz'$$

we can neglect the distortion due to the resolution (i.e. we have $g(z) = f(z)$) only in the limit $\sigma \ll \lambda$. In our case $\sigma \sim 10 \div 100$ cm while $\lambda \sim 350 \div 900$ cm and the distortion is not negligible

[3]The other main reason is that the AKS is essential to fix the neutral energy scale and to reduce its impact on the double ratio, as discussed in next section.

$$R = \frac{\int_{Z_N}^{Z_N+n_\tau c\tau_S} n_L^{00}(Z)\, w(Z)\, dZ}{\int_{Z_C}^{Z_C+n_\tau c\tau_S} n_L^{+-}(Z)\, w(Z)\, dZ} \cdot \frac{\int_{Z_C}^{Z_C+n_\tau c\tau_S} n_S^{+-}(Z)\, dZ}{\int_{Z_N}^{Z_N+n_\tau c\tau_S} n_S^{00}(Z)\, dZ} = \frac{n_L^{00}(0)}{n_L^{+-}(0)} \frac{n_S^{00}(0)}{n_S^{+-}(0)} \tag{4.22}$$

being $w(Z) \propto n_S(Z)/n_L(Z)$. The effect on the double ratio from the uncertainty on the two positions Z_C and Z_N can be neglected, as well as the effect of AKS converter inefficiency (0.4%) and AKS counter inefficiency (0.36 ± 0.03 % for $\pi^0\pi^0$, 0.77 ± 0.10 % for $\pi^+\pi^-$), being the fraction of reconstructed decays occurring upstream the AKS ~ 5 % [7].

4.5 Energy and geometrical scales

Since two different detectors are used to measure the kaon energy and vertex position for charged and neutral decays, a difference in the absolute energy and geometrical scales can produce a distortion of the measured double ratio. The error on the neutral energy scale was in fact one of the main sources of systematic error in the NA31 experiment.

4.5.1 Neutral energy scale

To evaluate this effect, let's define the true decay distributions for K_S and K_L neutral events as

$$\frac{dn_L}{dz} = \frac{1}{n_\tau \lambda_S} \qquad \frac{dn_S}{dz} = \frac{e^{-\frac{z}{\lambda_S}}}{(1 - e^{-n_\tau})\ \lambda_S} \tag{4.23}$$

where $\lambda_S = P_K \tau_S / M_K$, the AKS position is taken as origin of the z coordinate ($z_{AKS} = 0$) and we have neglected the slopes of the K_L distributions ($\lambda_L \gg \lambda_S$) Both distributions are normalized so that the total number of events between $z = 0$ and $z = n_\tau \lambda_S$ are $n_L = n_S = 1$. The number of K_L weighted events will be

$$n_{LW} = \int_0^{n_\tau \lambda_S} \frac{dn_L}{dz} e^{-\frac{z}{\lambda_S}} dz = \frac{(1 - e^{-n_\tau})}{n_\tau} \tag{4.24}$$

If we now suppose to have a relative error α, realistically $< 1\%$, on the neutral energy scale and we denote with a prime the measured quantities, we have,

$$P_K' = P_K(1+\alpha) \quad \Longrightarrow \quad \lambda_S' = \lambda_S(1+\alpha) \tag{4.25}$$

and, from equation (4.4),

$$(z_{LKR} - z') \; = \; (z_{LKR} - z)\,(1+\alpha) \tag{4.26}$$

expressing the fact that the longitudinal distance scale is also given by the energy scale. The measured number of events, neglecting the distortions due to acceptance, will be

$$\begin{aligned} n'_S \; &= \; \int_{z=0}^{z'=n_\tau \lambda'_S} \frac{dn_S}{dz} dz \; = \; = \; \int_0^{n_\tau \lambda_S + \alpha z_{LKR}/(1+\alpha)} \frac{e^{-\frac{z}{\lambda_S}}}{(1-e^{-n_\tau})\;\lambda_S} dz \\ &\simeq \; 1 + \frac{e^{-n_\tau}}{1-e^{-n_\tau}} \frac{\alpha}{1+\alpha} \frac{z_{LKR}}{\lambda_S} \end{aligned} \tag{4.27}$$

$$n'_{LW} \; = \; \int_0^{n_\tau \lambda'_S} \frac{dn_L}{dz'} e^{-\frac{z'}{\lambda'_S}} dz' \; = \; \frac{(1-e^{-n_\tau})}{n_\tau} \; = \; n_{LW} \tag{4.28}$$

$$\Longrightarrow \quad \frac{n'_{LW}}{n'_S} \; \simeq \; \frac{n_{LW}}{n_S} \left(1 - \frac{e^{-n_\tau}}{1-e^{-n_\tau}} \frac{z_{LKR}}{\lambda_S}\, \alpha \right) \tag{4.29}$$

Thus, the effect of an error α on the energy scale causes a distortion $(1+\Gamma\alpha)$ on the double ratio with

$$\Gamma \; \simeq \; -\frac{e^{-n_\tau}}{1-e^{-n_\tau}} \frac{z_{LKR}}{\lambda_S} \tag{4.30}$$

We see that the effect can be suppressed by enlarging the fiducial region, but this conflicts with the need to reject neutral background that populates regions with large Z. The chosen value $n_\tau = 3.5$ is a compromise between the two requests. For such value, Γ varies between -0.4 and -1 depending on the kaon energy. We conclude that

$$(\Delta R)_{energy\ scale \times (1+\alpha)} \;\sim\; -\alpha \tag{4.31}$$

It is important to stress that if we had not used the AKS to define the initial K_S decay region, the effect would have been much larger:

$$n''_S \; = \; \int_{\alpha z_{LKR}/(1+\alpha)}^{n_\tau \lambda_S + \alpha z_{LKR}/(1+\alpha)} \frac{e^{-\frac{z}{\lambda_S}}}{(1-e^{-n_\tau})\;\lambda_S} \; = \; e^{-\frac{\alpha z_{LKR}}{(1+\alpha)\lambda_S}} \; \simeq \; 1 - \alpha \frac{z_{LKR}}{\lambda_S} \tag{4.32}$$

We also notice that $n'_L = n_L$, so that the K_L events are not affected by the error on energy scale independently from the fact that the weighting is applied or not.

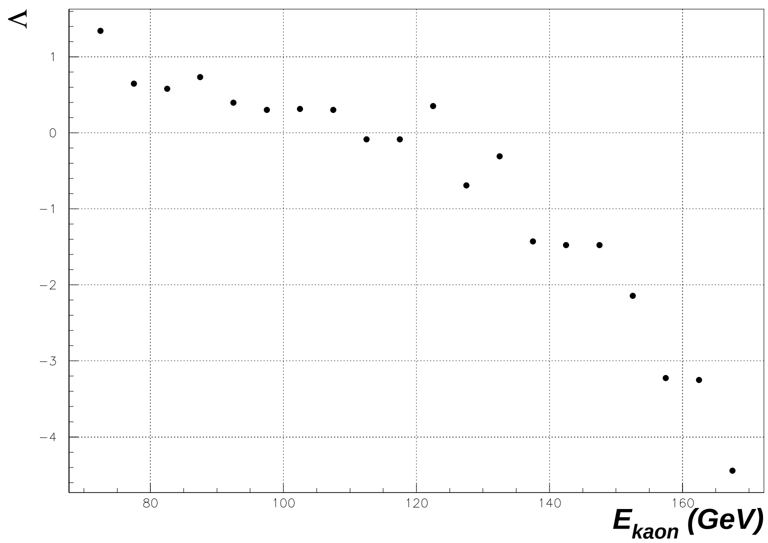

Figure 4.8: Effect of bin migration due to the error on the energy scale, expressed through the parameter Λ of equation (4.33)

We have not considered so far a second effect of energy scale, namely the migration of events from an energy bin to another one, that, due to the fact that the spectra of K_S and K_L are different, can introduce a distortion of the double ratio. Let's denote with $s_{L(S)} = dn_{L(S)}/dE$ the energy spectra and with $E_i, \bar{E}, E_f$ the minimum, mean and maximum energy of a given energy bin. The relative error α on the energy scale will cause the observed spectra for neutral events to shift by the quantity αE. Therefore, the effect on R can be estimated, neglecting acceptance variations inside an energy bin, as

$$\begin{aligned} \frac{R_{measured}}{R_{true}} &\simeq \frac{\left[\int_{E_i}^{E_f} s_L(E)dE + (s_L(E_i) - s_L(E_f))\alpha\bar{E}\right]}{\left[\int_{E_i}^{E_f} s_S(E)dE + (s_S(E_i) - s_S(E_f))\alpha\bar{E}\right]} \; \frac{\left[\int_{E_i}^{E_f} s_S(E)dE\right]}{\left[\int_{E_i}^{E_f} s_L(E)dE\right]} = \\ &= 1 + \Lambda\alpha \end{aligned} \tag{4.33}$$

where, if we approximate the spectrum in a given bin with a straight line,

$$\Lambda \simeq \left(\frac{1}{s_S(\bar{E})}\frac{ds_S}{dE}(\bar{E}) - \frac{1}{s_L(\bar{E})}\frac{ds_L}{dE}(\bar{E})\right) \bar{E} \tag{4.34}$$

We have extracted Λ from linear fits of the measured spectra in 5 GeV wide bins. The result is shown in figure 4.8. Since the $K_S - K_L$ difference of spectrum slopes, thus Λ, changes sign along the nominal energy range (see fig. 3.3), the migration manifests itself mainly by introducing an energy dependence of the measured R

value, while the variation of the average value is less important than the previous effect. In fact, the weighted average of Λ between 70 and 170 GeV is -0.3.

As already mentioned, the AKS can be used to define the energy scale with great accuracy. In fact, the longitudinal decay vertex distribution of the events passing the AKS veto should exhibit a sharp edge corresponding to the anticounter position. Thus, the energy scale correction factor $(1-\alpha)$, that must be applied to the reconstructed cluster energies, can be obtained by fitting the decay distribution, in energy bins, with the function

$$\phi(Z) \;=\; B + N\int_{-\infty}^{\infty} e^{-\frac{(Z-Z')^2}{2\sigma^2}}\psi(Z')dZ' \tag{4.35}$$

where

$$\psi(Z) \;=\; \begin{cases} 0 & \text{if } Z \;<\; -z_{LKR}\frac{\alpha}{(1-\alpha)} \\ e^{-\frac{M_K}{P_K\tau_S}\left(Z+Z_{LKR}\frac{\alpha}{1-\alpha}\right)} & \text{if } Z \;>=\; -z_{LKR}\frac{\alpha}{(1-\alpha)} \end{cases} \tag{4.36}$$

where the other fit parameters are [30]

- the normalization factor N;
- the baseline B that accounts for a possible error in subtracting the K_L events that have been mistagged as K_S and for the AKS inefficiency;
- the vertex resolution σ;
- the K_S lifetime $c\tau_S$ that is usually left free to account for shape distortion due to the acceptance and the spectrum shape inside the energy bin.

An example is showed in figure 4.9.

The result is stable with the kaon energy within $\pm 2 \cdot 10^{-4}$. Variations of α along the run were within $\pm 5 \cdot 10^{-4}$, reflecting the level of stability of calorimeter response.

The fit function described above doesn't take into account non–gaussian resolution tails, that were observed from the distribution of E/P for electrons and are presumably due to the effect of hadroproduction in the electromagnetic showers [15]. These tails were modeled in a simple Montecarlo simulation and α was corrected in order to match the average Z position in a region around the AKS obtained from the Montecarlo. The correction amount to $5 \cdot 10^{-4}$.

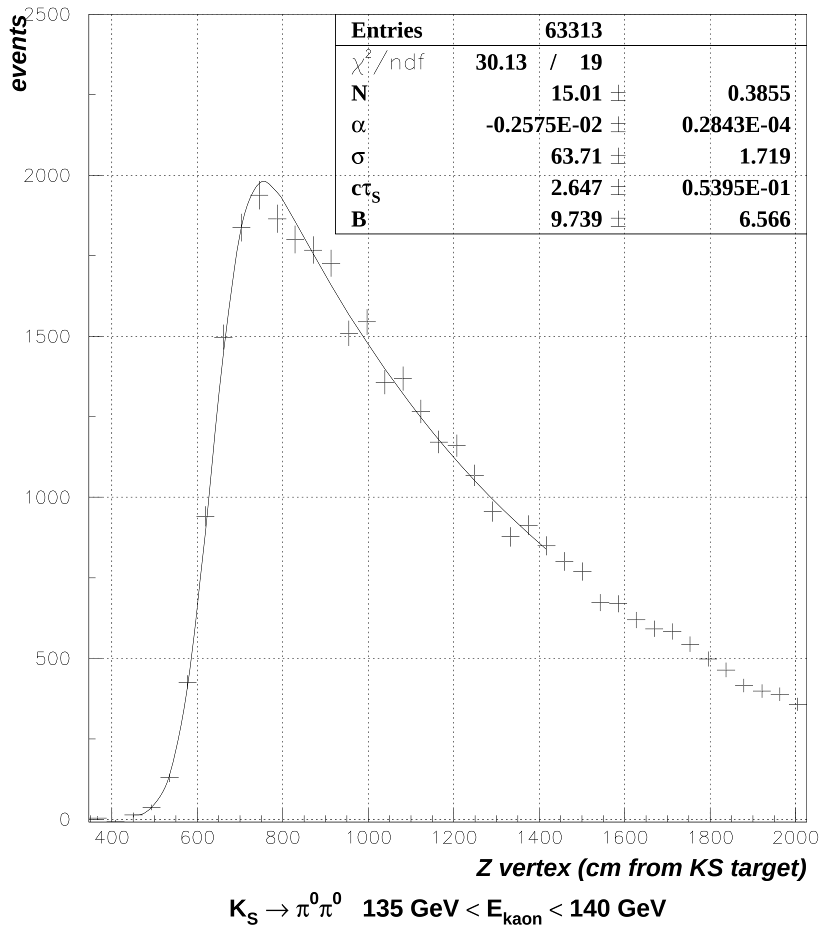

Figure 4.9: Example of AKS fit in an energy bin for neutral events. The fit parameters are described in the text.

Further studies have been done using data from some special runs where a π^- beam was sent on a thin target placed in a known position in the vicinity of the AKS. The decay distribution for the reconstructed $\pi^0 \to 2\gamma$,$\eta \to 2\gamma$ and $\eta \to 3\pi^0 \to 6\gamma$ decays is expected in this case to be a gaussian centered in the target position. Using these data, the energy scale has been studied for wider ranges of energy and inter–cluster distance (the latter is much larger on average for $\eta \to 2\gamma$ than $\pi^0 \to 2\gamma$), so that the effect on the scale of various reconstruction effects (as non–gaussian tails and residual effect of energy sharing and non–projectivity) could be investigated. The final uncertainty on the energy scale was estimated to be [50, 30]

$$\Delta\alpha \;=\; 5 \cdot 10^{-4}$$

4.5.2 Charged energy scale

The kaon energy for charged decays can be determined using only the knowledge of the chamber geometry. If we write the $\pi^+\pi^-$ invariant mass as

$$\begin{aligned} M_{+-}^2 c^4 &= 2M_\pi^2 c^4 + 2\left(E_{\pi^+}E_{\pi^-} - P_{\pi^+}P_{\pi^-}c^2\cos\theta\right) \\ &\simeq 2M_\pi^2 c^4 + 2P_{\pi^+}P_{\pi^-}c^2\left[\left(1+\frac{M_\pi^2 c^2}{2P_{\pi^+}^2}+\frac{M_\pi^2 c^2}{2P_{\pi^-}^2}\right)-\left(1-\frac{\theta^2}{2}\right)\right] \end{aligned} \tag{4.37}$$

and we define $\rho = P_{\pi^+}/P_{\pi^-}$, $P_K = P_{\pi^+} + P_{\pi^-}$, we get

$$cP_K = \frac{(1+\rho)}{\theta\sqrt{\rho}}\sqrt{(M_K c^2)^2 - (M_\pi c^2)^2\left(2+\rho+\frac{1}{\rho}\right)} \tag{4.38}$$

so that the kaon energy is obtained only in terms of the $\pi^+\pi^-$ opening angle θ and the momentum ratio ρ which is independent from the spectrometer magnetic field. In this way the accuracy of the geometry, which is known from precision measurements, fixes not only the transverse scale, but, similarly to the neutral case, the energy and longitudinal geometrical scale ($Z_{DCH} - Z_{Vertex} \propto \theta$) at the same time. The AKS fit can be used as a check, as well as the position of the reconstructed kaon mass (in this case the knowledge of magnetic field is also needed).

The uncertainty on the geometry, combined with the residual effect of the magnetic field in the decay region, produces a systematic error on the double ratio that has been estimated to be

$$(\Delta R)_{charged\ scale} = \pm 5 \cdot 10^{-4}$$

The accuracy in the knowledge of the **transverse geometrical scale** of the spectrometer can be also used to check the calorimeter transverse scale. From equation 4.4 we see that a distortion of the neutral transverse scale has the same effect that a distortion of the energy scale. Thus, to contain the effect on the double ratio to a few 10^{-4}, the scale of the distance among photon clusters must be known to an accuracy of a few hundred μm over 1 m. Though the detector has been machined with this level of accuracy, the geometry has been also checked at the level of 300 μm/m by comparing the extrapolated tracks and the calorimeter shower positions of electrons acquired during a special run without magnetic field in the spectrometer, with a resulting uncertainty on R

$$(\Delta R)_{transverse\ scale} = \pm 3 \cdot 10^{-4}$$

A cross–check of the neutral and charged longitudinal scales can be obtained from events with a π^0 Dalitz decay, where the vertex position is measured by both the charged and the neutral reconstruction. They are found to agree within the uncertainties quoted above.

4.6 Other systematic effects from neutral reconstruction

Calorimeter non–linearity: The linearity of the calorimeter has been extensively studied using E/P for electrons from K_{e3} decays, and also using $2\pi^0$ and η decays. In the useful range (3 to 100 GeV) the maximum non–linearity amounts to 0.3 %. The effect on the double ratio can be estimated by looking at the changes of R after applying a similar distortion to the measured energies and is found to be

$$(\Delta R)_{non-linearity} = \pm 9 \cdot 10^{-4}$$

Calorimeter non-uniformity: The uniformity of the calorimeter response is guaranteed at the level of per mill by the continuous electronic intercalibration of cell and by checking it with K_{e3} data. The resulting uncertainty on the double ratio is

$$(\Delta R)_{non-uniformity} = \pm 3 \cdot 10^{-4}$$

Corrections of neutral reconstruction: The uncertainties in the corrections applied to account for energy sharing between clusters, space charge effect and deviations from projectivity produce an effect on R estimated to be

$$(\Delta R)_{neutral\ corrections} = \pm 4 \cdot 10^{-4}$$

4.7 K_S tagging

The identification of K_S and K_L events through the tagging technique can fail for two reasons:

- the accidental coincidence between a proton in the tagger and a K_L event in the detector, causing a K_L event to be mistagged as K_S with a probability α_{LS};

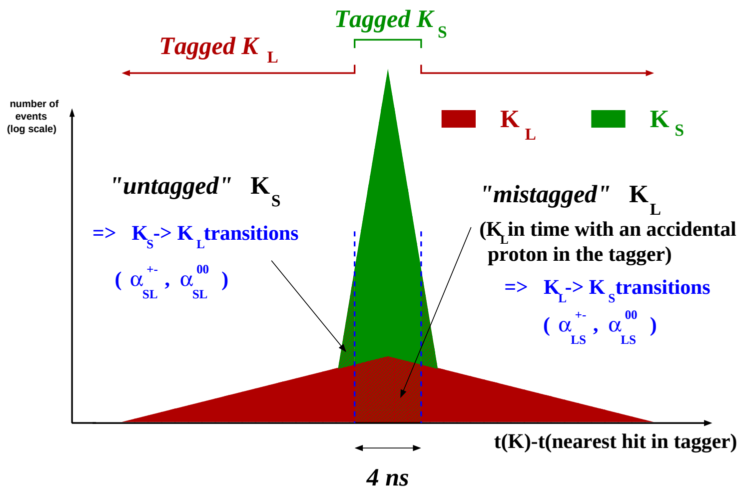

Figure 4.10: Definition of the α_{LS} and α_{SL} mistagging probabilities.

- the lost of time coincidence between a K_S event and its proton, causing a K_S event to be mistagged as K_L with a probability α_{SL}.

The meaning of the two parameters is illustrated in figure 4.10.

If we neglect all modulations of beam rates, we expect both effects to be equal for charged and neutral events. In fact, with a flat time distribution for the accidental protons, α_{LS} is independent from the event time resolution[4], that is different for charged and neutral events. By choosing a tagging window of 4 ns, α_{SL} is dominated by the tagger inefficiency[5], that is independent from the kaon decay mode.

Nevertheless, rate effects can produce some asymmetry: if the instantaneous rate seen by charged and neutral events is not the same because of trigger effects (for example, different dead times), the effective rates of accidental protons and the effective tagger inefficiencies can turn out to be different. Furthermore, modulation of accidental proton rate can introduce a dependence of α_{LS} from the event time resolution.

In order to have the best symmetry of effects, **the tagger will be used to identify both charged and neutral events**, and **all the cuts that can affect the rate** (as the overflow cut, see section 4.9) **are made symmetric**.

[4]In fact, the convolution of a flat and a gaussian distribution still results in a flat distribution with the same level.

[5]In fact, the resolution is <300 ps for both charged and neutral event time reconstruction, and the tails have been checked through detailed study to give a marginal contribution.

Both α_{LS} and α_{SL} can be measured with an error of order 10^{-4} for charged events, by comparing the tagging result with the vertex identification, which has negligible error. For a tagging window of 4 ns it turns out that $\alpha_{LS} \sim 10\%$ (meaning that the effective proton rate in the tagger is $\sim$ 25 MHz), while $\alpha_{LS} \sim 10^{-4}$.

Let's now give an *a priori* evaluation of the effect of mistagging on the double ratio. If we define

$N^{00(+-)}_{L(S)}$ as the measured event counts;

$n^{00(+-)}_{L(S)}$ as the true event counts, unweighted;

$n^{00(+-)}_{L(S)w}$ as the true event counts, weighted;

$n_{L(S)m}$ as the true "mistagged" counts, i.e. the K_L (K_S) events, treated as if they were K_S (K_L) for what concerns the weight and the definition of the decay region;

we get

$$R_{measured} = \frac{N^{00}_L}{N^{+-}_L}\frac{N^{+-}_S}{N^{00}_s} = \frac{n^{00}_{Lw}(1-\alpha^{00}_{LS}) + \alpha^{00}_{SL}n^{00}_{Sm}}{n^{+-}_{Lw}(1-\alpha^{+-}_{LS}) + \alpha^{+-}_{SL}n^{+-}_{Sm}} \cdot \frac{n^{+-}_S(1-\alpha^{+-}_{SL}) + \alpha^{+-}_{LS}n^{+-}_{Lm}}{n^{00}_S(1-\alpha^{00}_{SL}) + \alpha^{00}_{LS}n^{00}_{Lm}} =$$
$$= R_{true}\frac{1-\alpha^{00}_{LS} + \alpha^{00}_{SL}n^{00}_{Sm}/n^{00}_{Lw}}{1-\alpha^{+-}_{LS} + \alpha^{+-}_{SL}n^{+-}_{Sm}/n^{+-}_{Lw}} \cdot \frac{1-\alpha^{+-}_{SL} + \alpha^{+-}_{LS}n^{+-}_{Lm}/n^{+-}_{S}}{1-\alpha^{00}_{SL} + \alpha^{00}_{LS}n^{00}_{Lm}/n^{00}_{S}} \quad (4.39)$$

The effect of weighting, neglecting $1/\tau_L$ with respect to $1/\tau_S$ and acceptance effects, is

$$n_{Sw} \simeq n_s/2 \quad (4.40)$$
$$n_{Lw} \simeq n_L/n_\tau \quad (4.41)$$

where n_τ is the size of fiducial region in K_S lifetimes (3.5 in the present analysis). Therefore, we can write

$$\frac{n^{00}_{Lw}}{n^{00}_S} = R_I|\eta_{00}|^2 = I\left(1 - 4Re\left(\frac{\epsilon'}{\epsilon}\right)\right) \quad (4.42)$$
$$\frac{n^{+-}_{Lw}}{n^{+-}_S} = R_I|\eta_{+-}|^2 = I\left(1 + 2Re\left(\frac{\epsilon'}{\epsilon}\right)\right) \quad (4.43)$$

where R_I accounts for the K_L to K_S beam intensity ratio and $I = R_I|\epsilon|^2 \sim 0.12$

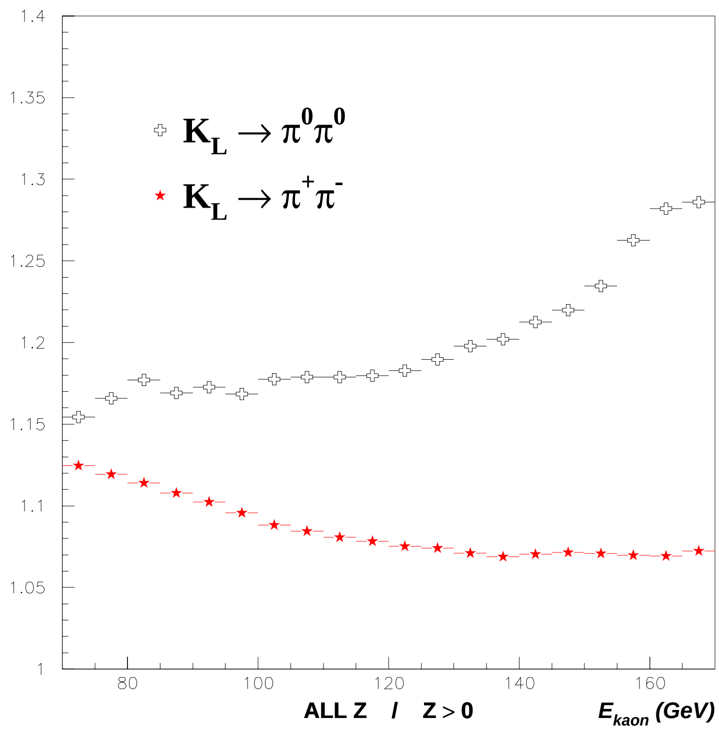

Figure 4.11: Ratio of K_L events before and after the $Z > z_{AKS}$. The average is 1.20 for the neutral case and 1.09 for the charged case. This is the main acceptance effect that contributes to the difference of ratio between the "mistagged" K_L and the K_S events, expressed in the text with the parameter Δu.

The "mistagged" K_L events n_{Lm}, compared to the unweighted events n_L, contain a relevant fraction of events with $Z_{vertex} < z_{AKS}$, because the beginning of fiducial region is erroneously defined using the AKS veto instead of the reconstructed Z_{vertex}. This fraction is different for the charged and neutral cases, due to the different acceptance (see fig. 4.11), that also affect the ratio of unweighted K_L to K_S . Thus, we write

$$\frac{n^{00}_{Lm}}{n^{00}_S} = u^{00}\ In_\tau \left(1 - 4Re\left(\frac{\epsilon'}{\epsilon}\right)\right) \tag{4.44}$$

$$\frac{n^{+-}_{Lm}}{n^{+-}_S} = u^{+-}\ In_\tau \left(1 + 2Re\left(\frac{\epsilon'}{\epsilon}\right)\right) \tag{4.45}$$

where the factor u takes into account the acceptance effects. The difference $u^{+-} - u^{00}$ can be of order 10^{-1}. The analogous effect for mistagged K_S events is smaller[6] and,

[6]in fact, using $Z_{vertex} > z_{AKS}$ instead of the AKS veto produces an event loss of only 1%. Furthermore, the ratio n_{Sw}/n_{Lw} is less distorted by acceptance effects than the ratio n_L/n_S.

being also $\alpha_{SL} << \alpha_{LS}$, will be neglected:

$$\frac{n^{00}_{Sm}}{n^{00}_{Lw}} \simeq \frac{W}{In_\tau \left(1 - 4Re\left(\frac{\epsilon'}{\epsilon}\right)\right)} \tag{4.46}$$

$$\frac{n^{+-}_{Sm}}{n^{+-}_{Lw}} \simeq \frac{W}{In_\tau \left(1 + 2Re\left(\frac{\epsilon'}{\epsilon}\right)\right)} \tag{4.47}$$

where the factor $W = n_\tau/2$ is due to the weighting.

Finally, we disentangle the common and the asymmetric part of the effects by writing

$$\alpha^{00}_{LS} = \frac{\alpha^{00}_{LS} + \alpha^{+-}_{LS}}{2} + \frac{\alpha^{00}_{LS} - \alpha^{+-}_{LS}}{2} = \overline{\alpha_{LS}} + \frac{\Delta\alpha_{LS}}{2} \tag{4.48}$$

$$\alpha^{+-}_{LS} = \frac{\alpha^{00}_{LS} + \alpha^{+-}_{LS}}{2} - \frac{\alpha^{00}_{LS} - \alpha^{+-}_{LS}}{2} = \overline{\alpha_{LS}} - \frac{\Delta\alpha_{LS}}{2} \tag{4.49}$$

and the same for α_{SL} and u, so that

$$\begin{aligned} R_{measured} =& R_{true} \cdot \frac{1 - \overline{\alpha_{LS}} - \frac{\Delta\alpha_{LS}}{2} + \frac{(\overline{\alpha_{SL}} + \Delta\alpha_{SL}/2)W}{In_\tau\left(1-4Re\left(\frac{\epsilon'}{\epsilon}\right)\right)}}{1 - \overline{\alpha_{LS}} + \frac{\Delta\alpha_{LS}}{2} + \frac{(\overline{\alpha_{SL}} - \Delta\alpha_{SL}/2)W}{In_\tau\left(1+2Re\left(\frac{\epsilon'}{\epsilon}\right)\right)}} \cdot \\ & \cdot \frac{1 - \overline{\alpha_{SL}} + \frac{\Delta\alpha_{SL}}{2} + (\overline{\alpha_{LS}} - \frac{\Delta\alpha_{LS}}{2})In_\tau(\overline{u} - \frac{\Delta u}{2})\left(1 + 2Re\left(\frac{\epsilon'}{\epsilon}\right)\right)}{1 - \overline{\alpha_{SL}} - \frac{\Delta\alpha_{SL}}{2} + (\overline{\alpha_{LS}} + \frac{\Delta\alpha_{LS}}{2})In_\tau(\overline{u} + \frac{\Delta u}{2})\left(1 - 4Re\left(\frac{\epsilon'}{\epsilon}\right)\right)} \end{aligned} \tag{4.50}$$

We develop now to first order all the terms $\lesssim 10^{-2}$, using

$$\alpha_{LS} \sim 10^{-1} \qquad \alpha_{SL} \sim 10^{-4} \qquad \Delta\alpha_{LS}, \Delta\alpha_{SL} \lesssim 10^{-3} \qquad \Delta u \lesssim 10^{-1}$$

$$\begin{aligned} R_{measured} = R_{true} \cdot \Bigg[1 + & \frac{\Delta\alpha_{LS} + \overline{\alpha_{SL}}\frac{W}{In_\tau}6Re\left(\frac{\epsilon'}{\epsilon}\right) + \Delta\alpha_{SL}\frac{W}{In_\tau}\left(1 + Re\left(\frac{\epsilon'}{\epsilon}\right)\right)}{1 - \overline{\alpha_{LS}}} + \\ & + \frac{\Delta\alpha_{SL} + In_\tau\left(-1 + Re\left(\frac{\epsilon'}{\epsilon}\right)\right)(\overline{\alpha_{SL}}\Delta u + \Delta\alpha_{LS}\overline{u}) + 6In_\tau\overline{\alpha_{LS}}\ \overline{u}Re\left(\frac{\epsilon'}{\epsilon}\right)}{1 + In_\tau\overline{\alpha_{LS}}\ \overline{u}} \Bigg] \end{aligned} \tag{4.51}$$

and we finally write the equation in the form

$$R_{measured} = A\left[1 - 6Re\left(\frac{\epsilon'}{\epsilon}\right)(1 - D)\right] \tag{4.52}$$

with

$$A \ \simeq \ 1 + \frac{In_\tau\Delta u\overline{\alpha_{LS}}(-1 + \overline{\alpha_{LS}}) - \Delta\alpha_{LS}(1 + In_\tau\overline{u}) + \Delta\alpha_{SL}\left(1 + \frac{W}{In_\tau} + \overline{\alpha_{LS}}\ (W\overline{u} - 1)\right)}{1 - \overline{\alpha_{LS}}\ (1 - In_\tau\overline{u})} \tag{4.53}$$

$$D \ \simeq \ \frac{\overline{\alpha_{LS}}\ In_\tau\ \overline{u}}{1 + \overline{\alpha_{LS}}\ In_\tau} \tag{4.54}$$

From these last equations we conclude that:

- the mistagging produces a dilution D of the measured value of ϵ'/ϵ , amounting to $\sim \alpha_{LS}/2 \sim 5\%$. This small effect, that can be corrected with negligible error, would be the only one if we had a perfect symmetry between charged and neutral events ($\Delta\alpha_{LS} = \Delta\alpha_{SL} = \Delta u = 0$);

- the large value of α_{LS} in conjunction with the charged/neutral asymmetry of acceptance produces a sizeable ($In_\tau\ \overline{\alpha_{LS}}\Delta u \sim 0.5\%$) systematic distortion to the double ratio. However, after subtracting the "mistagged" events from the measured event counts using the known value of α_{LS}[7], the effect is corrected with accuracy $0.5\% \cdot \sigma(\alpha_{LS})/\alpha_{LS}\ \sim\ 10^{-4}$;

- the most dangerous effect of mistagging comes from the charged/neutral difference of α_{LS} and α_{SL}, causing a systematic on the double ratio

$$\Delta R \sim -1.6\ \Delta\alpha_{LS} + 5\ \Delta\alpha_{SL} \tag{4.55}$$

  we notice that the weighting increases the sensitivity to $\Delta\alpha_{SL}$ (from 3 to 5), while n_τ has an opposite effect on $\Delta\alpha_{SL}$ and $\Delta\alpha_{LS}$.

Several detailed studies were done within the collaboration in order to accurately measure $\Delta\alpha_{LS}$ and $\Delta\alpha_{SL}$.

The difference of accidental proton rate between charged and neutral events is obtained by measuring the average number of offset coincidences between a tagged K_L event and a proton in 4 ns windows outside the tagging window, but still close to the event time (i.e. applying an offset to the event time in the range ± 40 ns), as shown in figures 4.12 and 4.13. To check that the measured difference in the offset windows reproduces the difference inside the tagging window, vertex–identified $K_L \to \pi^+\pi^-$ events and $K_L \to 3\pi^0$ [8], that can be selected from the sample acquired with the neutral trigger, are used. The result is [35, 39]

$$\Delta\alpha_{LS}\ =\ (10\ \pm\ 5)\cdot 10^{-4} \tag{4.56}$$

[7]It is worth stressing here that the accuracy of this correction depends essentially from the accuracy to which α_{LS} is known, since the "mistagged" events are measured with large statistics. No *a priori* knowledge of the Δu quantity is thus required.

[8]To this extent, the $K_S \to 3\pi^0$ branching ratio can be neglected, while the small fraction of K_L events from K_S target is accounted for.

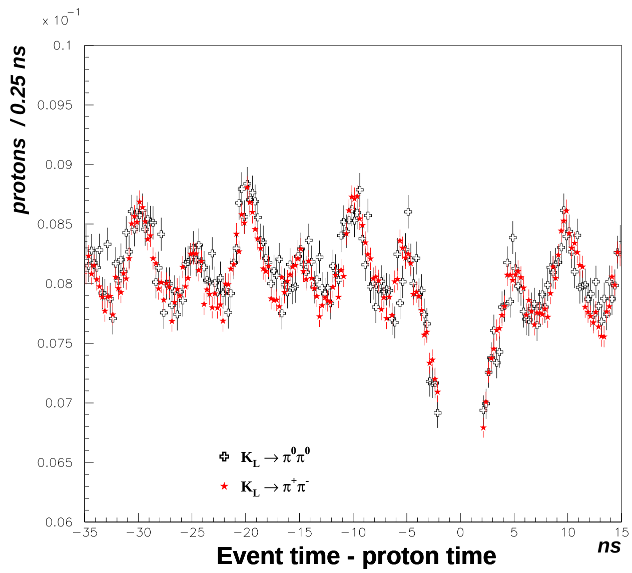

Figure 4.12: Accidental proton rates (per event) for tagger–identified K_L events. A modulation due to the 200 MHz SPS frequency is clearly visible.

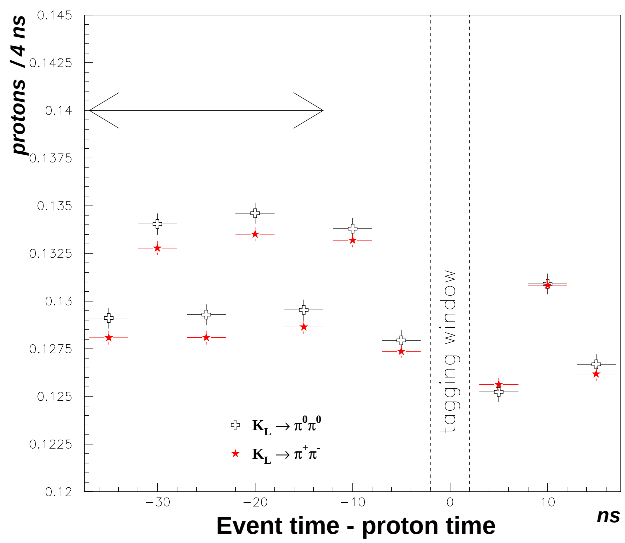

Figure 4.13: Average number of protons per event in 4 ns wide windows. In order to follow the SPS frequency the windows are centered on the maxima of the modulation. The arrow marks the region used to derive $\Delta\alpha_{LS}$, being exempt by biases from QX afterpulses and difference in the readout windows for charged and neutral events.

The α_{SL}^{00} parameter can be directly measured from the sample of $K \rightarrow \pi^0\pi^0 \rightarrow e^+e^-3\gamma$ Dalitz decays, that can be identified using the e^+e^- vertex. Unfortunately, the statistics of this sample is poor (the branching ratio for π^0 Dalitz decay being 1.2 %) and the error on α_{SL}^{00} is $3 \cdot 10^{-4}$ [54]. Nevertheless, the contribution to α_{SL} coming from the tagger inefficiency is found to be the same for charged and neutral events using data from K_S only runs, while the comparison of the reconstructed charged and neutral time, in $K_S + K_L$ run condition, is investigated using neutral events containing π^0 Dalitz decays or photon conversions. These studies lead to the result [40]

$$|\Delta\alpha_{SL}| \; < \; 10^{-4} \tag{4.57}$$

4.8 Trigger efficiencies

Due to the simultaneity of data–taking and the weighting procedure that equalizes the illumination of the various detectors by the two beams, the effect of efficiency for K_S and K_L events is expected to cancel in the double ratio. However, possible asymmetries may be caused by the difference of the instantaneous rate seen by the two classes of events. Thus, the inefficiencies of the charged and neutral triggers have been kept as low as possible and have been continuously monitored by acquiring a fraction of events using downscaled control triggers.

4.8.1 Charged Trigger efficiency

As explained in section 3.5.1, the charged trigger for the 1997 run was formed by the coincidence of the $Q_X/2$ and $ETOT$ signals (L1C) and by the MassBox (L2C). The main control trigger was $Q_X/2 \times ETOT$, but with a wider coincidence window to avoid any bias, and also events triggered by Q_X only were taken to check the $ETOT$ efficiency.

The measured inefficiency of the charged trigger was around 10 % for most of the run. Its main sources were [22]:

- the "pure" MBX inefficiency, coming (in about equal parts) from the drift chamber and the reconstruction algorithm inefficiencies and varying during the run from 5 % to the optimized level of 2 %.

- the unperfect alignment ("edge effect") of L1 signals, causing the MBX to be inefficient, since its reconstruction algorithm strongly relies on the information from the hodoscope *fine time* bits. This inefficiency was also varying during the run, depending on the alignment quality, around 1–2 %.

- the limited time budget allowed to the MBX to complete its reconstruction. This inefficiency changed from ~ 3 % to ~ 1 % during the run, according to the changes of time budget.

- the inefficiency of the $Q_X/2 \times ETOT$ time coincidence, that was rather tight in order to keep the L1 rate low. Usually around 1 %, this effect amounted to 7 % for part of the run, because of a bad alignment.

We should also mention that the MBX had a dead time of 1 % due to the limited rate ($\sim$ 100 kHz) it could stand. The signal sent in this case to disable L1 triggers is recorded, so that the dead time can be applied offline also to neutral events to avoid rate effects.

Inefficiencies of $ETOT$, QX (using the neutral control triggers) and the coincidence used in the control trigger (using a dedicated special run) were also measured to be at the per mill level, and their effect on the double ratio can be neglected.

Anyway, no statistically significant asymmetries between K_S and K_L events were found (see section 7.5).

4.8.2 Neutral Trigger efficiency

The neutral trigger (NUT) was checked using a completely independent trigger formed from the signals of the neutral hodoscope. The inefficiency is very small, around 0.2 % with negligible impact on the double ratio (see section 7.6).

4.9 Accidental activity

Accidental events that superimpose on the triggered events are essentially coming from the K_L target and their effect is expected to be made symmetrical for K_L and K_S by the simultaneity of data–taking.

The rate of accidental events can be directly measured by looking at the out–of–time activity in the detectors (as for the case of protons in the tagger), being the detector readout windows at least 250 ns wide (up to 1.2 μs in the case of DCH).

The largest effect on the detector response is the *overflow* condition in the drift chamber read–out, that affects about 20 % of charged events. This condition occurs when more than seven hits are recorded in a plane within 100 ns and is caused by electromagnetic showers produced upstream the spectrometer. The events with an overflow within $\pm$ 312.5 ns are rejected to avoid the bias from the loss of information. The overflow rate is found to be the same for K_S and K_L within the statistical error of 0.1 %. However, the cut is applied also to neutral events to obtain the best symmetry of rates seen by neutral and charged events.

A K_S / K_L asymmetry dur to accidentals can be generated if the ratio of the two beam intensities is not constant in time. In fact, if we denote with $dn_{L(S)}/dt$ the event rates and we assume that the probability to lose an event is proportional to the K_L beam intensity, the number of lost events $L_{L(S)}$ will be in the ratio

$$\frac{L_L}{L_S} = \frac{\int \frac{dn_L}{dt}(t)\frac{dn_L}{dt}(t)\ dt}{\int \frac{dn_S}{dt}(t)\frac{dn_L}{dt}(t)\ dt} \tag{4.58}$$

In principle, the simplest way to correct for this effect would be to weight the K_S events with the ratio of K_L to K_S beam intensities, but this requires a reliable way to measure the instantaneous intensities for each event on a 100 ns time scale. Unfortunately, this is not possible because of the limited counts of the available beam monitors.

Instead, event losses and gains are measured with the **overlay** method. It consists in simulating the effect of accidentals by artificially overlaying good events with events recorded using "randomly" triggered events. In order to realistically represent the accidental activity "seen" by the two beams, the "random" K_L and K_S triggers are actually generated by the intensity monitors (KL monitor, KSM). The trigger from the KL monitor signal is taken with a fixed delay of 69.3 μs, corresponding to the periodicity of the slow SPS proton extraction (three revolutions), in order to avoid correlations with events in the detector. This is not needed for the KSM signal, since it is sensitive only to the K_S beam halo, which is essentially uncorrelated with the activity in the detector. Random events are acquired without zero suppression, with a rate of about 10 per burst for each type.

About 20 % of the normal events are overlayed offline, at raw data level, with the random that is closest in time. The contribution of noise is subtracted from random events before the overlay. The resulting event is then processed like normal events. Since the statistics is limited, each random event is used several times.

Actually, the correlation of the two beam intensities is very high (the correlation factor is found to be 99 % [2]), so that no large K_S / K_L asymmetry of the effect is expected. Indeed, the time distributions inside the burst of K_S and K_L randoms is the same to a very good approximation, so that we can overlay also events of different type (K_S with random K_L , and vice versa), gaining a factor $\sqrt{2}$ on the statistical error of the computed effect.

As will be shown in section 7.7, the correction to the double ratio obtained in this way results compatible with zero.

The overlay method doesn't account for the possible "in–time" accidental activity, i.e. the accidentals coming from the same proton that produced the triggered event. This is a potentially dangerous effect, since it can realistically affect only K_S events. It has been investigated mainly by mean of the AKL counters, and results to be negligible.

Chapter 5

The acceptance correction and its systematic error

Due to the principles of the experiment (namely, the collinearity of beam lines and the weighting procedure), the correction to the double ratio induced by the different acceptance for K_L and K_S events is expected to be small and understandable by mean of a relatively simple Montecarlo simulation.

In this chapter we present our estimation of this correction and a study of its stability against "reasonable" changes of the simulation parameters and of the acceptance cuts.

5.1 Montecarlo generators

Two different Montecarlo programs where developed inside the collaboration:

- the NA48 SIMulation (NASIM) program, based on GEANT [16];
- the New Montecarlo Program (NMC) [51], written from scratch and intended to be faster and simpler than the GEANT program.

In order to avoid the time–consuming tracking of showers in the calorimeters, a set of showers for electrons and pions of various energy was generated once for all using NASIM. Both programs can access this collection of showers using a shower library.

The effects that are included in the simulation used for this analysis (thus, in the resulting *acceptance correction*) are the following ones:

- the geometry of the beam lines, including K_S halo from scattering in the collimator and in the AKS;
- the detector geometry;
- the secondary interactions upstream the LKr calorimeter (as multiple scattering, nuclear interactions, gamma conversions) and the pion decay;
- the reconstruction of charged tracks and LKr clusters.

while the following ones are **not** included:

- detector inefficiencies, that can be measured by mean of downscaled triggers;
- effect of accidentals, measurable using overlayed events;
- mistagging, intrinsically independent from decay topology;
- tails of E/P and of the event time reconstruction, that cannot be easily simulated. However, these effects are known to be smaller than 0.1 % and are in principle K_S / K_L symmetric;
- K_L scattering and regeneration in the collimators (see section 7.8).

5.2 Correlated Montecarlo

The Montecarlo data samples used for most of this analysis have been generated using version 28 of the NASIM generator, modified in order to produce correlated couples of K_S and K_L events. The variables which are common to the couple are:

- the true Kaon energy. This makes sense because the effect of the different energy spectra of the two beams is avoided by performing the analysis in energy bins;
- the true decay position along the beam direction z. This is also not the case in true life, but is justified by the weighting procedure that is applied on real data to equalize the reconstructed decay Z distributions. The events are simulated according to the K_S lifetime, starting from the AKS position (end of counters for charged and end of converter for neutrals), up to 5 $c\tau_S$;
- the $K \rightarrow \pi\pi$ and $\pi^0 \rightarrow \gamma\gamma$ decay kinematics in the K^0 rest frame;

To account for the differences of the beam lines, the transverse decay vertex position and the kaon direction are simulated independently, as well as the event propagation inside the detector.

The high degree of correlation obtained with this technique (i.e. the 2 events of a couple are usually both accepted or both rejected) has two obvious advantages with respect to uncorrelated Montecarlo :

- the reduction of statistical error on the K_S / K_L acceptance ratio;
- the possibility to disentangle more easily the sources of K_S / K_L asymmetry.

On the other side, some approximations not present in the uncorrelated MC are introduced:

- the residual difference of energy spectra after binning is neglected;
- the difference of the distributions of the true z vertex position at the beginning of the fiducial region (defined using the AKS veto for the K_S beam and the reconstructed vertex for the K_L) is not taken into account;

- the correction, that is applied to bins of reconstructed energy, must be computed in bins of true energy, neglecting the effect of energy smearing.

The effect of these approximations will be discussed in section 5.7.

Let's now define how the correction is computed in this framework. For each of the N event couples we define a variable $X_i^{S(L)}$ which is 1 if the event is accepted and 0 otherwise. This variable follows a binomial distribution with expectation value equal to the acceptance $A_{S(L)}$. Thus, we will use the following estimators for the acceptances and their covariance matrix:

$$a_{S(L)} = \frac{\sum_i X_i^{S(L)}}{N} \tag{5.1}$$

$$\sigma^2_{a_{S(L)}} = \frac{a_{S(L)}(1-a_{S(L)})}{N} \tag{5.2}$$

$$Cov(a_S, a_L) = \frac{\sum_i (X_i^S - a_S)(X_i^L - a_L)}{N^2} \tag{5.3}$$

The error on the acceptance ratio $r = A_L/A_S$ will be

$$\left(\frac{\sigma_r}{r}\right)^2 = \left(\frac{\sigma_{a_L}}{a_L}\right)^2 + \left(\frac{\sigma_{a_S}}{a_S}\right)^2 - 2\frac{Cov(a_S,a_L)}{a_S a_L} \tag{5.4}$$

and with the approximation $a = (a_S + a_L)/2 \simeq a_S \simeq a_L$

$$\sigma_r^2 = 2\frac{\sigma_a^2}{a^2}(1-\rho) \tag{5.5}$$

where $\rho = Cov(a_S, a_L)/(\sigma_{a_S}\sigma_{a_L})$ is the correlation factor.
Finally, the correction factor to be applied to the double ratio and its error will be estimated as [1]

$$\alpha^{MC} = \frac{a_S^{00}\, a_L^{+-}}{a_L^{00}\, a_S^{+-}} \tag{5.6}$$

$$\sigma^2_{\alpha^{MC}} = (\alpha^{MC})^2\left[\left(\frac{\sigma_{r^{+-}}}{r^{+-}}\right)^2 + \left(\frac{\sigma_{r^{00}}}{r^{00}}\right)^2\right] \simeq 2\left(\frac{\sigma_{a^{+-}}}{a^{+-}}\right)^2(1-\rho^{+-}) + 2\left(\frac{\sigma_{a^{00}}}{a^{00}}\right)^2(1-\rho^{00}) \tag{5.7}$$

Figure 5.1 shows the correlation factors measured on the produced data samples, which allow to obtain the same precision of an uncorrelated MC that uses a number of events larger by a factor 3–4.

[1] due to the high statistics of the Montecarlo sample, the bias of this simple estimator is found to be $< 1\cdot 10^{-4}$ for all bins.

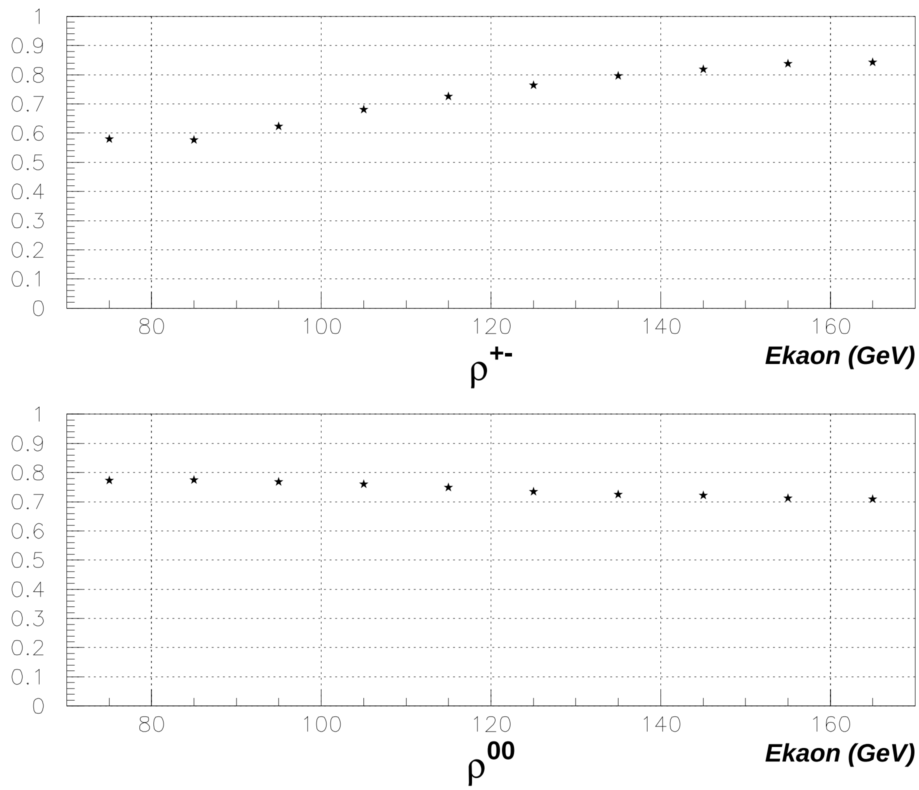

Figure 5.1: Correlation factor for the generated samples of $K^0 \to \pi^+\pi^-$ and $K^0 \to \pi^0\pi^0$ events as a function of energy.

Using the naive values $a^{+-} \simeq 0.4$ and $a^{00} \simeq 0.25$, one gets from the formula above $\sigma_{\alpha^{MC}} \simeq \sqrt{0.9/N^{+-} + 1.5/N^{00}}$.
The sample used in this analysis consists of $4 \cdot 10^6$ charged couples and $6.4 \cdot 10^6$ neutral ones (corresponding to about 2 GBytes of data), allowing to reach a precision of $7 \cdot 10^{-4}$ on the correction to the double ratio (to be compared with the statistical error of 1997 data, that is $28 \cdot 10^{-4}$).

The correction will be computed in 10 energy bins between 70 and 170 GeV. The final correction to the average double ratio R is obtained from the difference of the R values measured on real data with and without the acceptance correction applied to each bin.

5.3 Acceptance cuts

The Montecarlo events that are reconstructed (i.e. at least one reconstructed vertex with two tracks for charged events, at least four photon candidates for neutrals) are selected with the same cuts that are applied to the real data.

The geometrical acceptance of the NA48 detector is defined by the standard cuts listed below.

CHARGED EVENTS: tracks must fall in the acceptance of spectrometer, LKr calorimeter (to identify electrons from K_{e3}) and MUV counters (to identify muons from $K_{\mu 3}$)

- 12 cm $<$ radial track position at DCH 1,2,4 $<$ 150 cm;
- track extrapolation inside standard LKr fiducial volume, including inner radial cut at 15 cm;
- distance from closest LKr dead cell $>$ 2 cm. The list of dead cells (not including the dead column) changes along the sample's statistics following the actual situation of 97 run;
- dead column cut: remove events having track extrapolation at LKr with $|X - 50\text{cm}| < 4$ cm ;
- MUV fiducial volume: remove events having track extrapolation inside a square with side of 25 cm and outside a square with side of 260 cm.

NEUTRAL EVENTS: photons must fall well within LKr sensitive volume and be far enough to be resolved

- standard LKr fiducial volume, with inner radial cut at 15 cm;
- distance from closest LKr dead cell $>$ 2 cm;
- dead column cut: remove events having clusters with $|X - 50\text{cm}| < 4$ cm ;
- distance between 2 clusters $>$ 10 cm.

The largest acceptance difference between K_S and K_L is expected to come from the inner hole of drift chamber 1, where the two beams are still vertically separated by $\sim$ 1.4 cm. This asymmetry is evident by looking at the distributions of the momentum asymmetry variable

$$ASP = \frac{|P_{\pi^+}| - |P_{\pi^-}|}{|P_{\pi^+}| + |P_{\pi^-}|} \tag{5.8}$$

which is K_S / K_L symmetric by construction, being simply proportional to the cosine of the π^+ production angle in the K^0 rest frame [2]. The drift chamber hole produces an acceptance difference for events with large ASP, having a track close to the beam pipe (see fig. 5.2). Nevertheless, a cut against large ASP values is needed to reject $\Lambda^0 \to p\pi^-$ events in the K_S beam. Figure 5.3 shows how the energy–dependent ASP cut

$$ASP < MIN(0.62, 1.08 - .0052 * E_{kaon})$$

can be used to minimize the acceptance difference between K_S and K_L , by removing the events with tracks close to the central hole in a symmetric way. The same effect cannot be achieved using the radial position of tracks, which is not K_S / K_L symmetric, as shown in figure 5.4.

The other standard cuts of the ϵ'/ϵ analysis, mainly motivated by background rejection, which have been included in the acceptance correction, are the following ones:

CHARGED EVENTS:

- pion momentum $(P_\pi) > 10$ GeV/c ;

[2] In fact, if p is the modulus of the pion momentum and θ the π^+ production angle in the K^0 rest frame, in the lab frame we will have

$$|P_{\pi^+}| = \sqrt{\left(\gamma_K p\cos\theta + \beta_K\gamma_K\sqrt{p^2 + (cm_\pi)^2}\right)^2 + (p\sin\theta)^2} \simeq p\gamma_K\left(\sqrt{1 + (cm_\pi/p)^2} + \cos\theta\right)$$

$$|P_{\pi^-}| = \sqrt{\left(-\gamma_K p\cos\theta + \beta_K\gamma_K\sqrt{p^2 + (cm_\pi)^2}\right)^2 + (p\sin\theta)^2} \simeq p\gamma_K\left(\sqrt{1 + (cm_\pi/p)^2} - \cos\theta\right)$$

$$ASP \simeq \frac{\cos\theta}{\sqrt{1 + (cm_\pi/p)^2}} = \frac{\cos\theta}{\sqrt{m_K^2/(m_K^2 - 4m_\pi^2)}} = 0.83\cos\theta$$

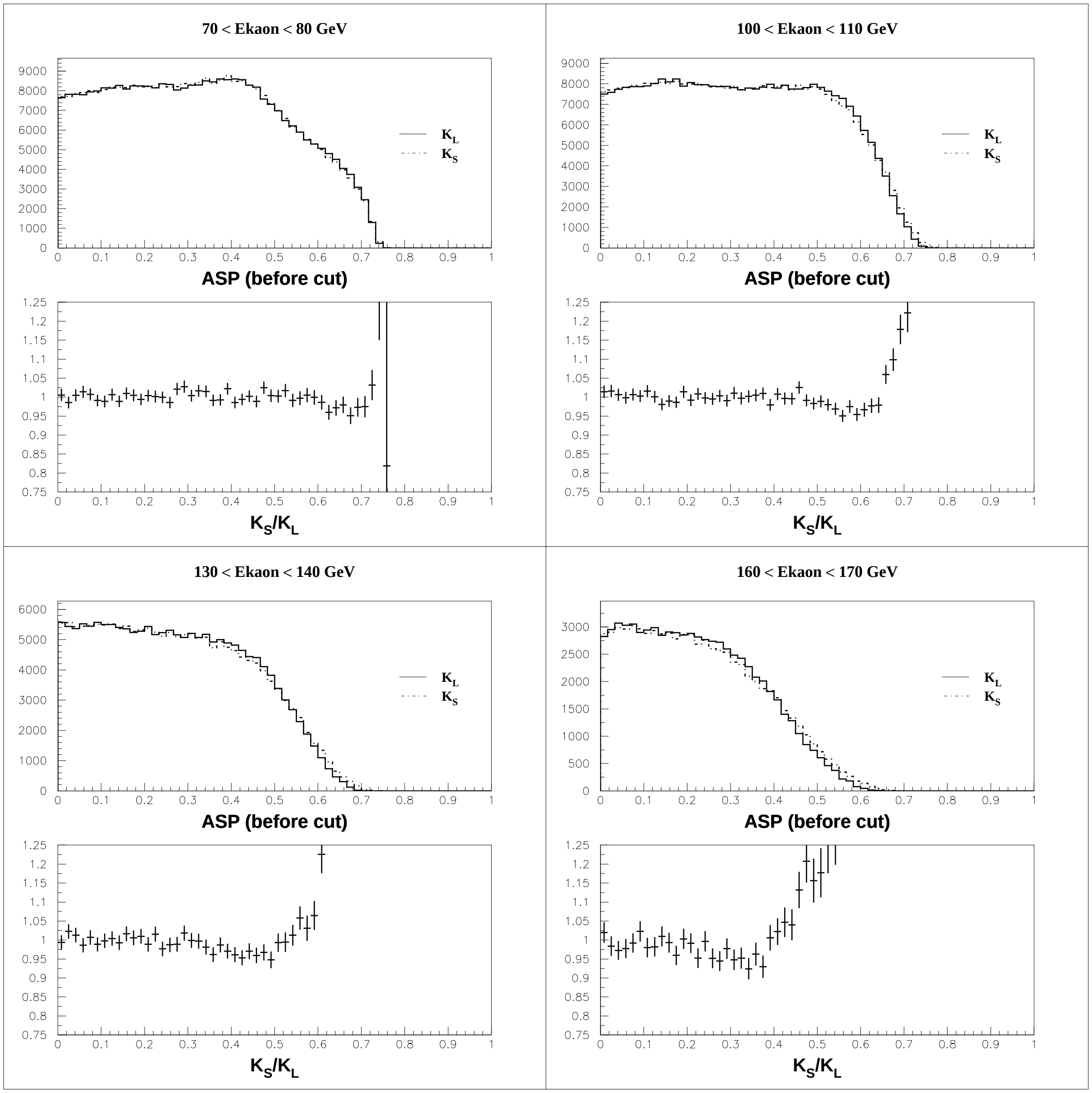

Figure 5.2: Comparison of ASP distributions for K_S and K_L in various energy bins.

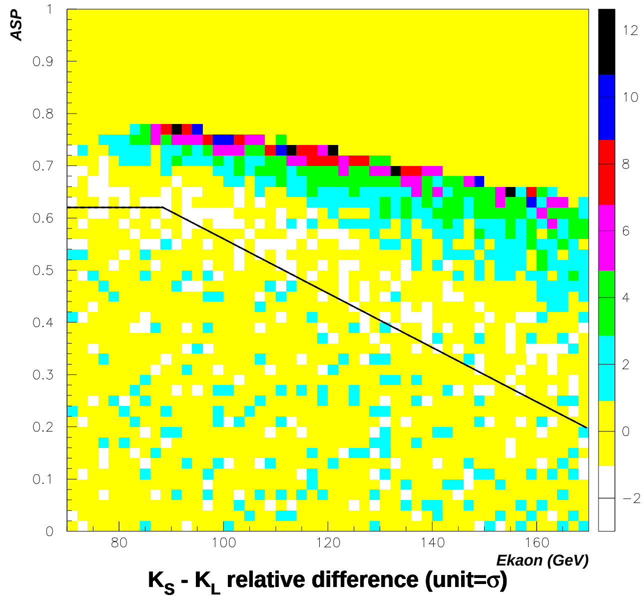

Figure 5.3: $K_S - K_L$ relative difference, expressed as a number of σ, as a function of kaon energy and ASP. The line drawn on the plot shows the applied ASP cut.

- *track fit quality* > 70 % ;
- closest distance of approach (CDA) of the tracks < 3 cm ;
- time difference of tracks < 6 ns ;
- center of gravity (*cog*) at LKr surface < 10 cm ;
- lifetime cut $c\tau < 3.5$ where $c\tau = Z/\beta\gamma c\tau_S$;
- rejection of events with tracks having a spatial match with MUV hits (the timing cut is not simulated), to take into account pion decay;
- $|M_{\pi^+\pi^-} - M_{K^0}|/c^2 < 3 * (1.755MeV + E_{kaon} * 0.007372)$ MeV ;
- $(p_T')^2 < 0.0002$ (GeV/c)^2 .

NEUTRAL EVENTS:

- $3 < E_\gamma < 100$ GeV ;
- *cog* at LKr surface < 10 cm ;

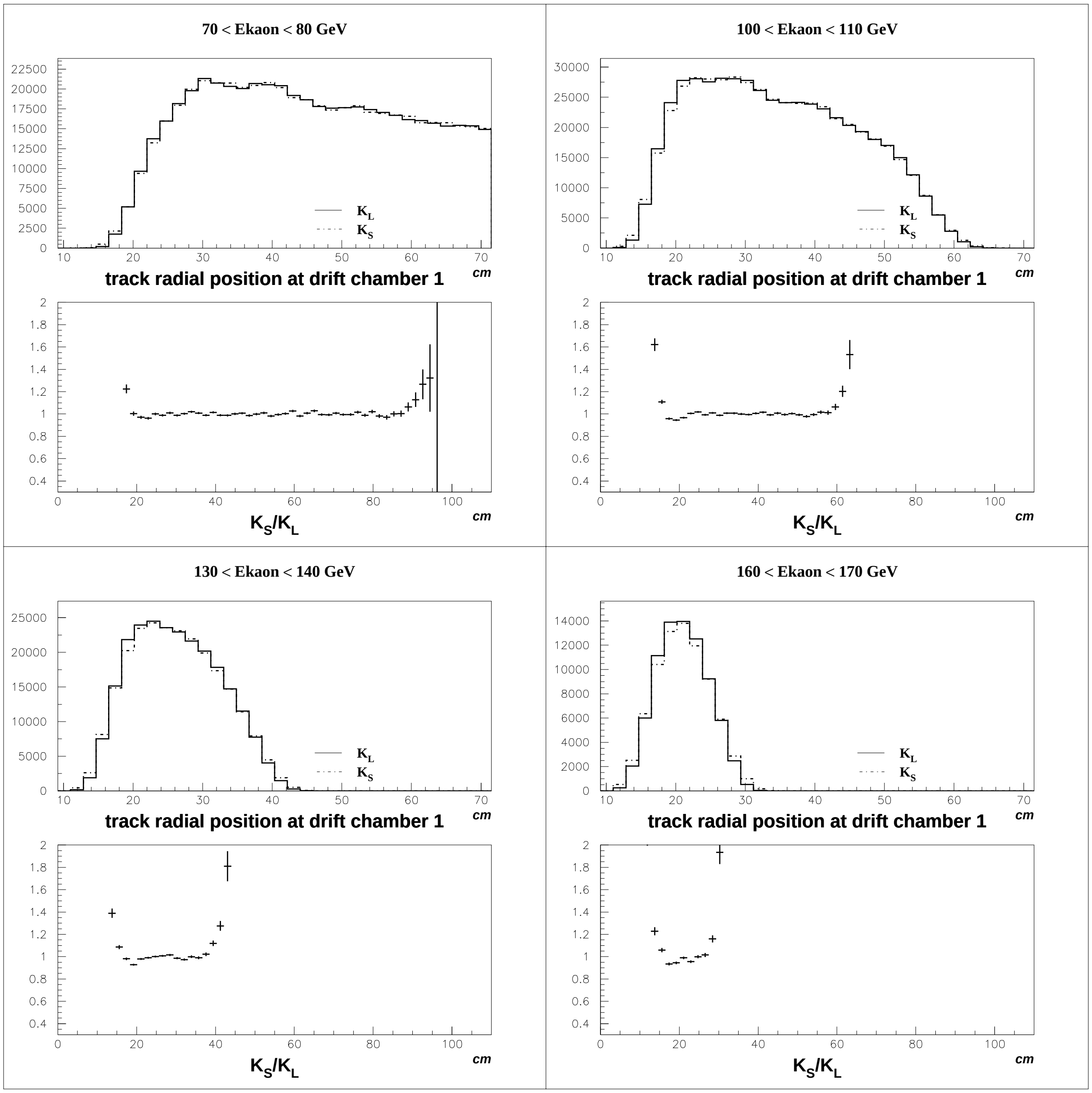

Figure 5.4: Comparison of radial distributions of tracks at drift chamber 1 in different energy bins.

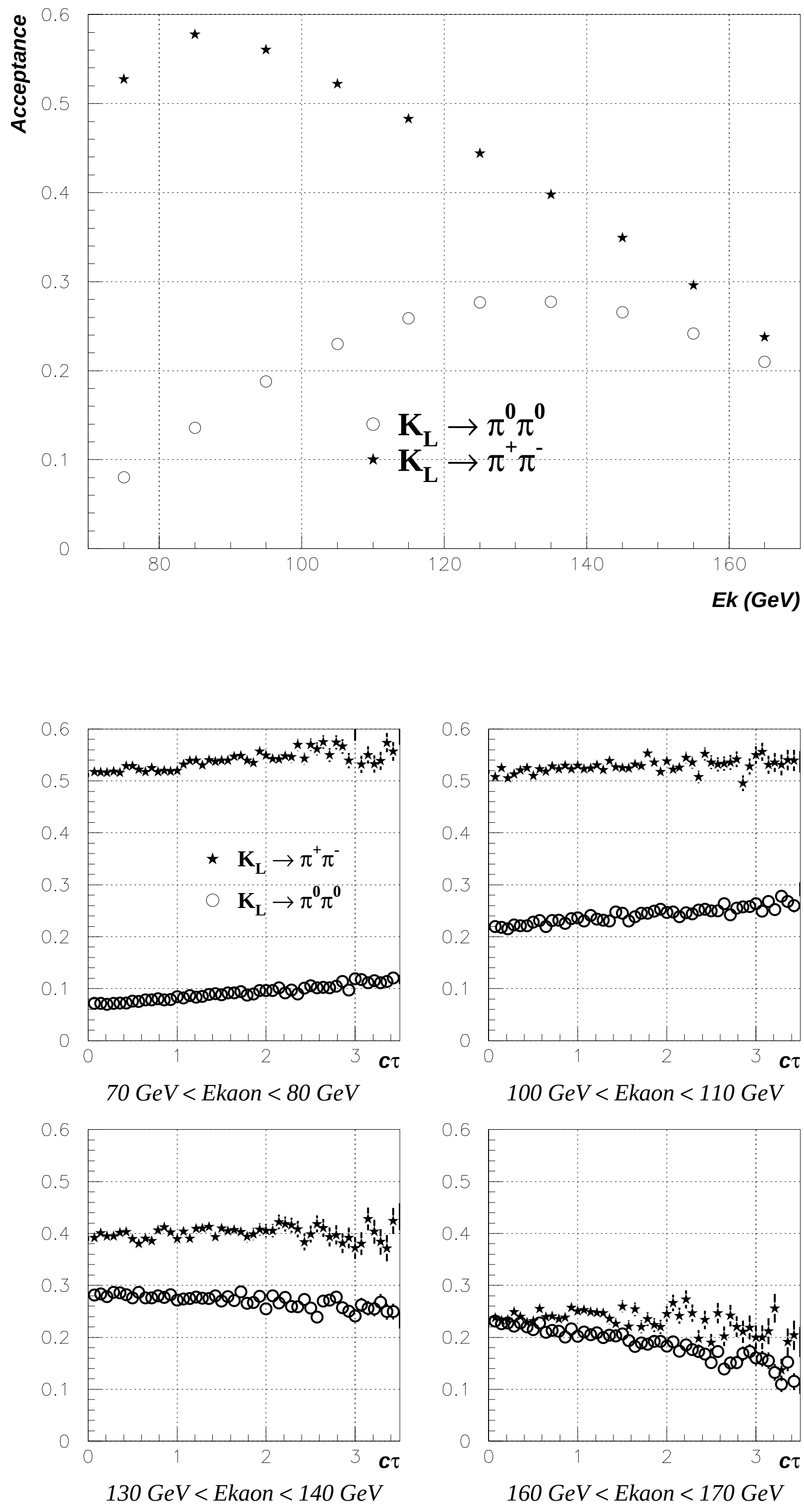

Figure 5.5: Acceptance for K_L events as a function of energy and $c\tau$ for various energy bins.

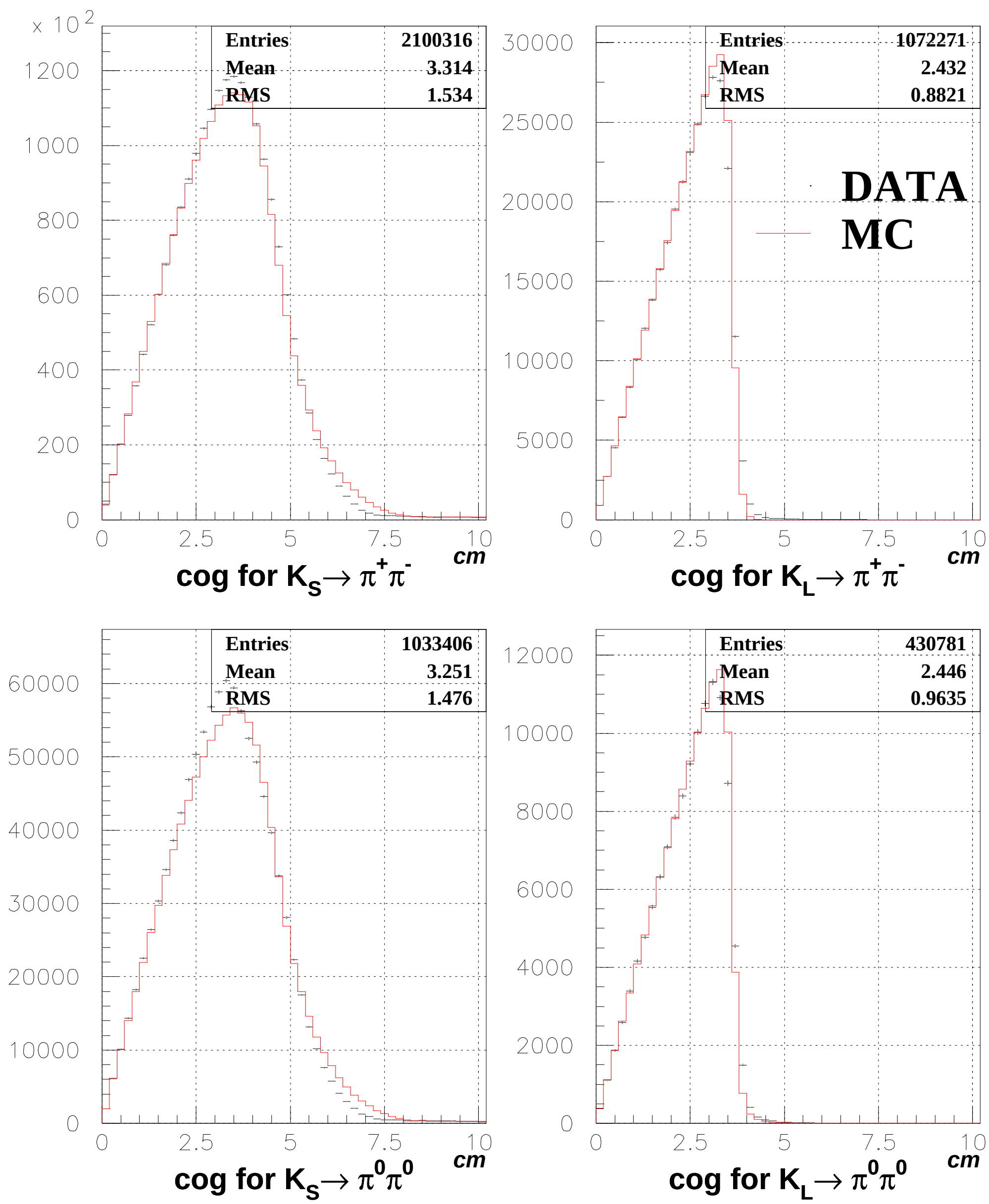

Figure 5.6: *cog* distributions for the four decay modes for both real data and MC events. We see that the profiles of the two beams are quite different, but the distributions for neutral and charged events are very similar so that the effect of the cut cancels in the double ratio.

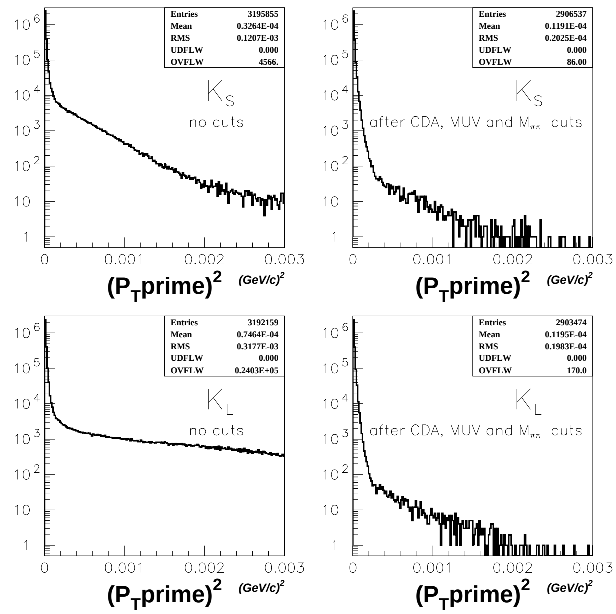

Figure 5.7: MC distributions of $(P_T')^2$ for K_S and K_L events before and after the rejection of $\pi \rightarrow \mu\nu_\mu$ decay

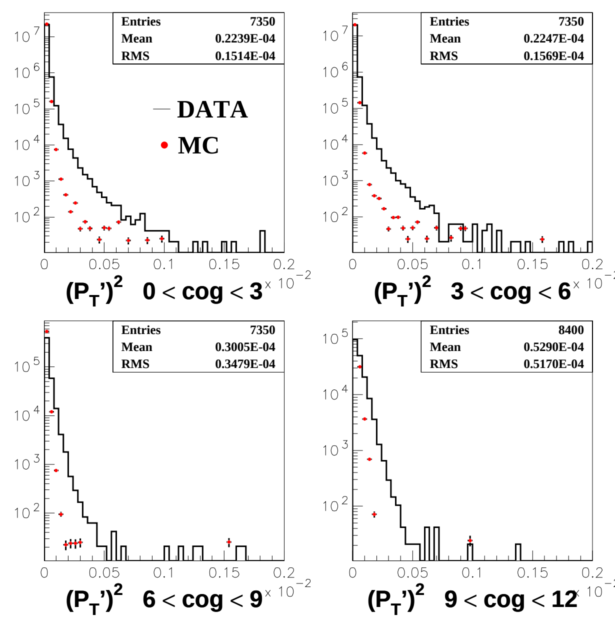

Figure 5.8: $(P_T')^2$ distributions (in GeV^2/c^2) for real K_S data, in different ranges of *cog*. The Montecarlo distributions are also shown (normalized to the real data for the first plot). Though the simulation of tails for $(P_T')^2 > 0.0002\ GeV^2/c^2$ is not accurate, one can see that, as expected from the Montecarlo, they are generated essentially by misreconstruction and not by the halo.

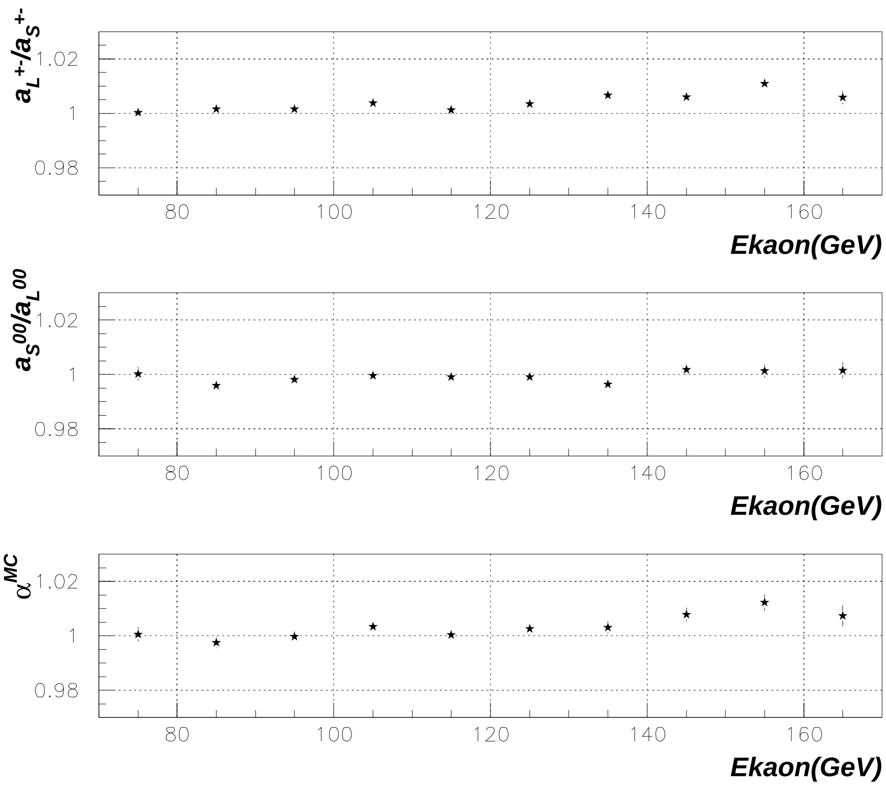

Figure 5.9: Acceptance correction from charged and neutral events separately, as a function of kaon energy. The *cog* cut is not applied in this plot.

- no extra clusters with energy > 1.5 GeV within $\pm$ 3 ns ;
- $c\tau < 3.5$;
- best $\chi^2_{2\pi^0} < 13.5$

The final acceptances as a function of energy and decay z position are plotted in figure 5.5.

Table 5.1 shows the K_S /K_L symmetry of each cut. The asymmetry introduced by the **cog** cut is due to the K_S beam halo and is expected to be compensated between charged and neutral events (see fig. 5.6). The $\boldsymbol{p'_T}$ variable has been defined in order to be symmetric for $\pi^+\pi^-$ events, but it introduces an asymmetry for events with pion decay. In fact, the expected symmetry is recovered when the cuts against pion decay (CDA, MUV, $M_{\pi^+\pi^-}$) are also applied (see also figure 5.7).

cut	$1 - A_{KS}$ (%)	$1 - A_{KL}$ (%)	ρ (%)	$1 - A_{KS}/A_{KL}$ (%)
CHARGED EVENTS				
reconstructed (>= 1 vertex)	18.703 $\pm$ 0.020	18.797 $\pm$ 0.020	63	-0.116 $\pm$ 0.021
$P_\pi > 10$ GeV/c, $track\ Q\ > 0.7$	1.086 $\pm$ 0.006	0.991 $\pm$ 0.006	30	0.096 $\pm$ 0.007
$CDA < 3$ cm	1.241 $\pm$ 0.007	1.231 $\pm$ 0.007	0	0.010 $\pm$ 0.009
$\Delta T_{track} < 6$ ns	0.034 $\pm$ 0.001	0.033 $\pm$ 0.001	0	0.001 $\pm$ 0.001
R_{DCH} cut	8.127 $\pm$ 0.015	8.146 $\pm$ 0.015	23	-0.021 $\pm$ 0.021
ASP cut	28.759 $\pm$ 0.025	28.650 $\pm$ 0.025	70	0.153 $\pm$ 0.027
cog cut	2.747 $\pm$ 0.009	1.215 $\pm$ 0.006	0	1.550 $\pm$ 0.011
LKr fiducial volume	9.453 $\pm$ 0.016	9.495 $\pm$ 0.016	40	-0.046 $\pm$ 0.020
LKr dead cells	2.168 $\pm$ 0.008	2.162 $\pm$ 0.008	19	0.006 $\pm$ 0.010
LKr dead column	6.374 $\pm$ 0.014	6.423 $\pm$ 0.014	60	-0.053 $\pm$ 0.013
$c\tau < 3.5$	0.955 $\pm$ 0.005	0.947 $\pm$ 0.005	54	0.008 $\pm$ 0.005
MUV fiducial volume	6.148 $\pm$ 0.013	5.933 $\pm$ 0.013	39	0.228 $\pm$ 0.016
MUV hit rejection	8.114 $\pm$ 0.015	8.110 $\pm$ 0.015	0	0.004 $\pm$ 0.023
$M_{\pi^+\pi^-}$ cut	6.593 $\pm$ 0.014	6.583 $\pm$ 0.014	0	0.010 $\pm$ 0.021
$(p'_T)^2 cut$	3.586 $\pm$ 0.010	5.903 $\pm$ 0.013	0	-2.462 $\pm$ 0.018
$(p'_T)^2$ + anti–π–decay cuts	9.023 $\pm$ 0.016	9.005 $\pm$ 0.016	0	0.020 $\pm$ 0.025
NEUTRAL EVENTS				
reconstructed (>= 4 clusters)	53.666 $\pm$ 0.020	53.642 $\pm$ 0.020	78	0.051 $\pm$ 0.029
$3 < E_\gamma < 100$GeV	9.580 $\pm$ 0.017	9.554 $\pm$ 0.017	58	0.028 $\pm$ 0.018
LKr fiducial volume	30.722 $\pm$ 0.027	30.738 $\pm$ 0.027	32	-0.022 $\pm$ 0.046
LKr dead cells	4.675 $\pm$ 0.012	4.658 $\pm$ 0.012	17	0.018 $\pm$ 0.017
LKr dead column	12.693 $\pm$ 0.020	12.801 $\pm$ 0.020	54	-0.123 $\pm$ 0.021
$\gamma\gamma$ distance > 10 cm	2.365 $\pm$ 0.009	2.346 $\pm$ 0.009	38	0.020 $\pm$ 0.010
cog cut	12.476 $\pm$ 0.020	11.060 $\pm$ 0.019	6	1.592 $\pm$ 0.029
no extra cluster	7.460 $\pm$ 0.016	7.463 $\pm$ 0.016	11	-0.004 $\pm$ 0.023
$c\tau < 3.5$	18.577 $\pm$ 0.023	18.553 $\pm$ 0.023	11	0.029 $\pm$ 0.038
$\chi^2_{2\pi^0} < 13.5$	34.088 $\pm$ 0.028	33.918 $\pm$ 0.028	15	0.257 $\pm$ 0.055

Table 5.1: Fraction of lost events from each cut (independently from the others), with respect to the number of reconstructed events. The fraction of reconstructed events with respect to the generated sample is given in the first row. The correlation factor and K_S / K_L symmetry are also shown.

Figure 5.8 shows that the tails in transverse momentum going over the p_T' cut are not essentially enhanced by the K_S halo (events with high *cog*) so that there is no evidence for interference between the *cog* and p_T' cuts. This means that a detailed simulation of the halo and of the tails in the spectrometer reconstruction are not essential for the acceptance correction. The systematic uncertainty in the correction coming from the halo simulation will be discussed in section 5.6.

The final acceptance correction as a function of kaon energy is plotted in fig. 5.9, without applying the *cog* cut in order to disentangle the charged and neutral contributions. One can see that the acceptance difference mainly comes from the charged events in the hardest part of the spectrum.

The values of the correction obtained in each bin after all cuts are showed in table 5.2.

Energy bin	α^{MC}
$70 \div 80$ GeV	1.0007 ± 0.0027
$80 \div 90$ GeV	0.9976 ± 0.0021
$90 \div 100$ GeV	0.9992 ± 0.0019
$100 \div 110$ GeV	1.0023 ± 0.0018
$110 \div 120$ GeV	0.9994 ± 0.0019
$120 \div 130$ GeV	1.0010 ± 0.0020
$130 \div 140$ GeV	1.0015 ± 0.0023
$140 \div 150$ GeV	1.0060 ± 0.0026
$150 \div 160$ GeV	1.0107 ± 0.0031
$160 \div 170$ GeV	1.0053 ± 0.0038
global	1.0015 ± 0.0007

Table 5.2: Acceptance correction in energy bins

5.4 Some data/MC comparison

In figures 5.10 to 5.14 the distributions of the most important variables (such as Rdch and ASP for charged tracks, X and Y LKr cluster position for neutral events) obtained with the Montecarlo simulation are compared to the distributions of real data, after normalizing to the same number of events for each bin.

Though the effect of inefficiencies is not taken into account in the simulation, the distributions for K_S ad K_L are well reproduced and, what is more important,

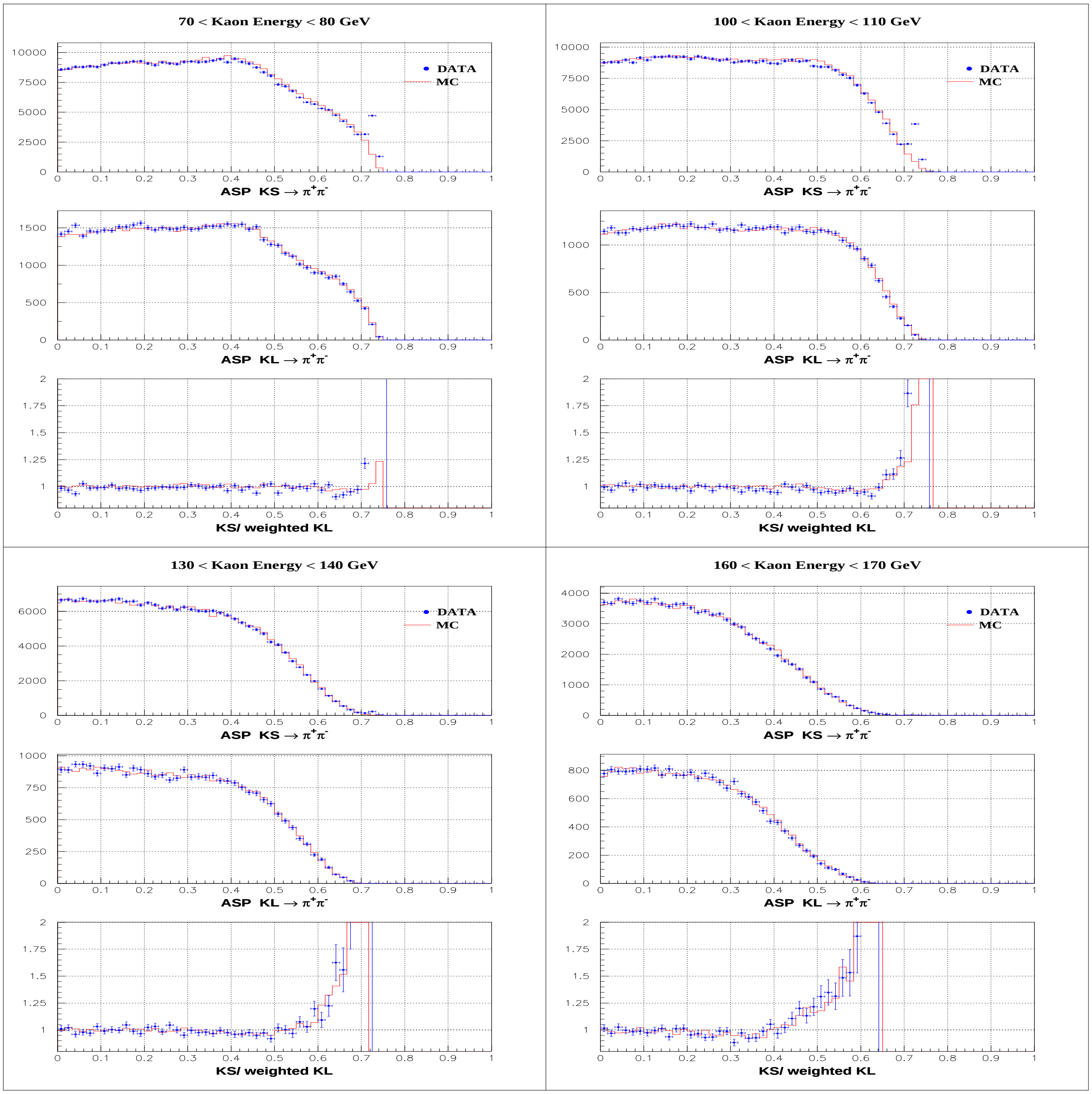

Figure 5.10: DATA/MC comparison of the ASP distributions before the ASP cut. The contribution of Λ, not present in the simulation, is evident in the real K_S sample.

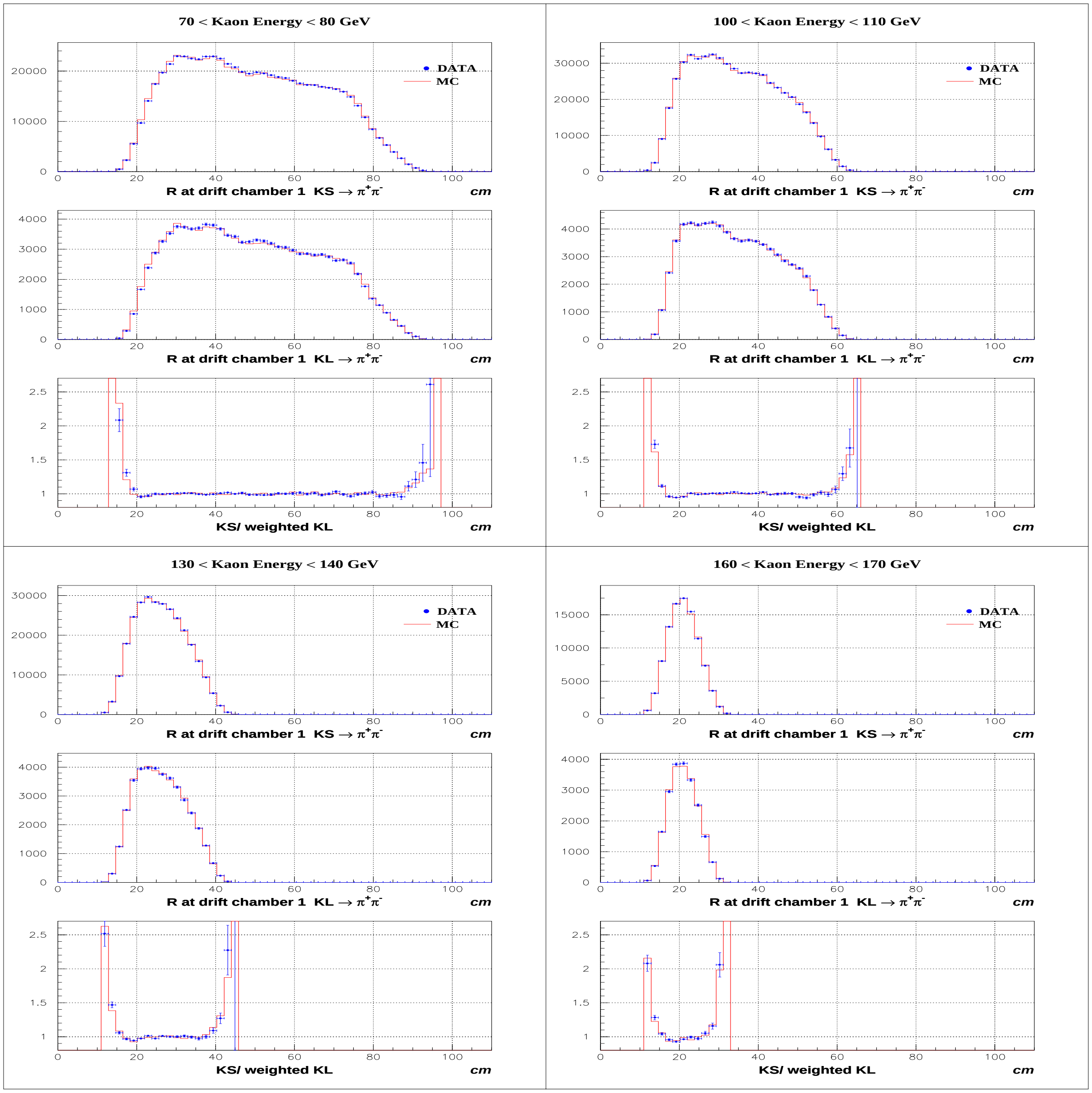

Figure 5.11: DATA/MC comparison of track radial position at drift chamber 1.

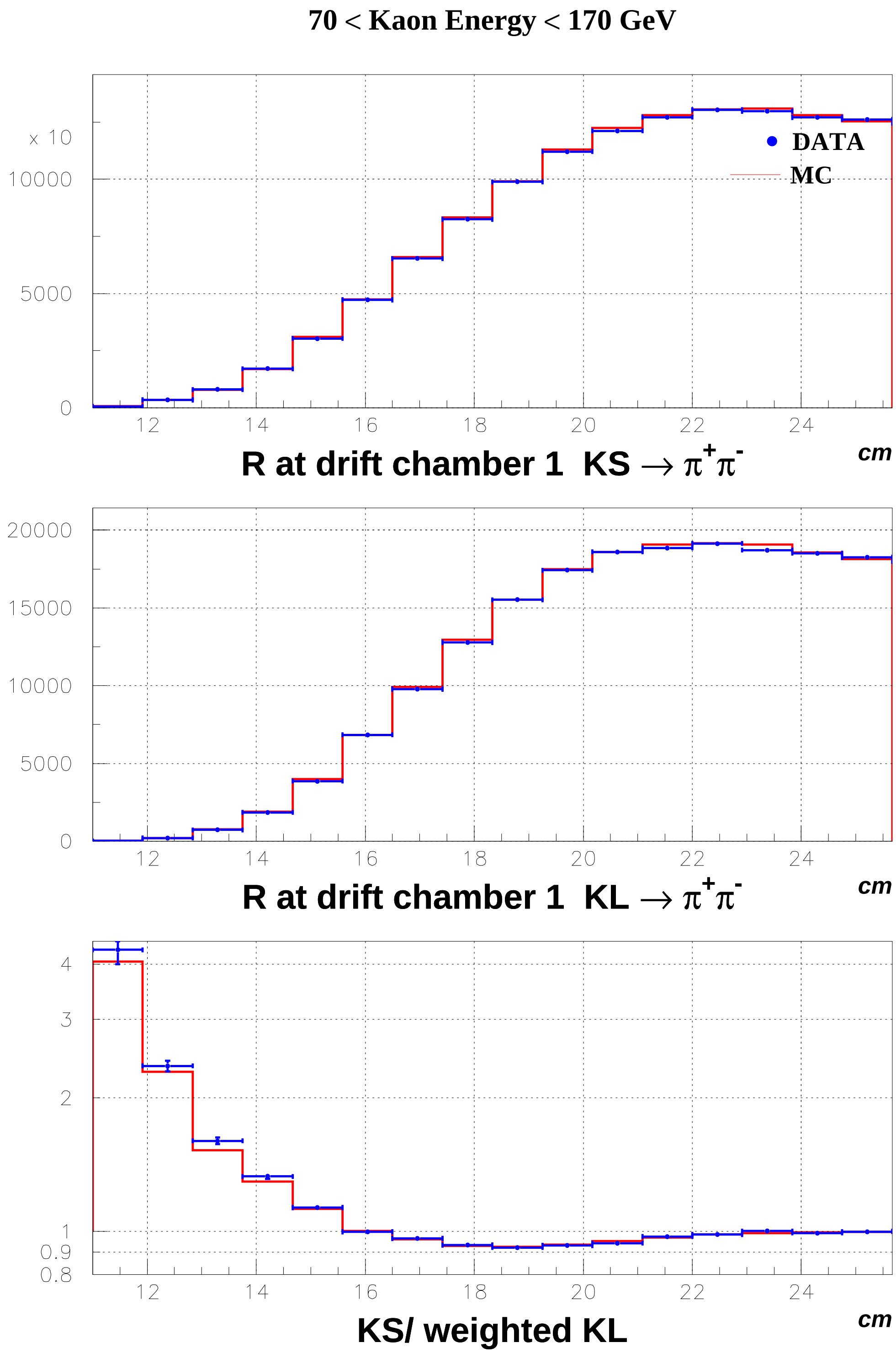

Figure 5.12: Detail of radial position distribution in the most inner region of drift chamber 1, where we find the largest acceptance asymmetry, that is well reproduced by the Montecarlo. The distributions contain all the energy bins, but a momentum–dependent weight has been applied to the MC events in order to match the energy spectra of real data.

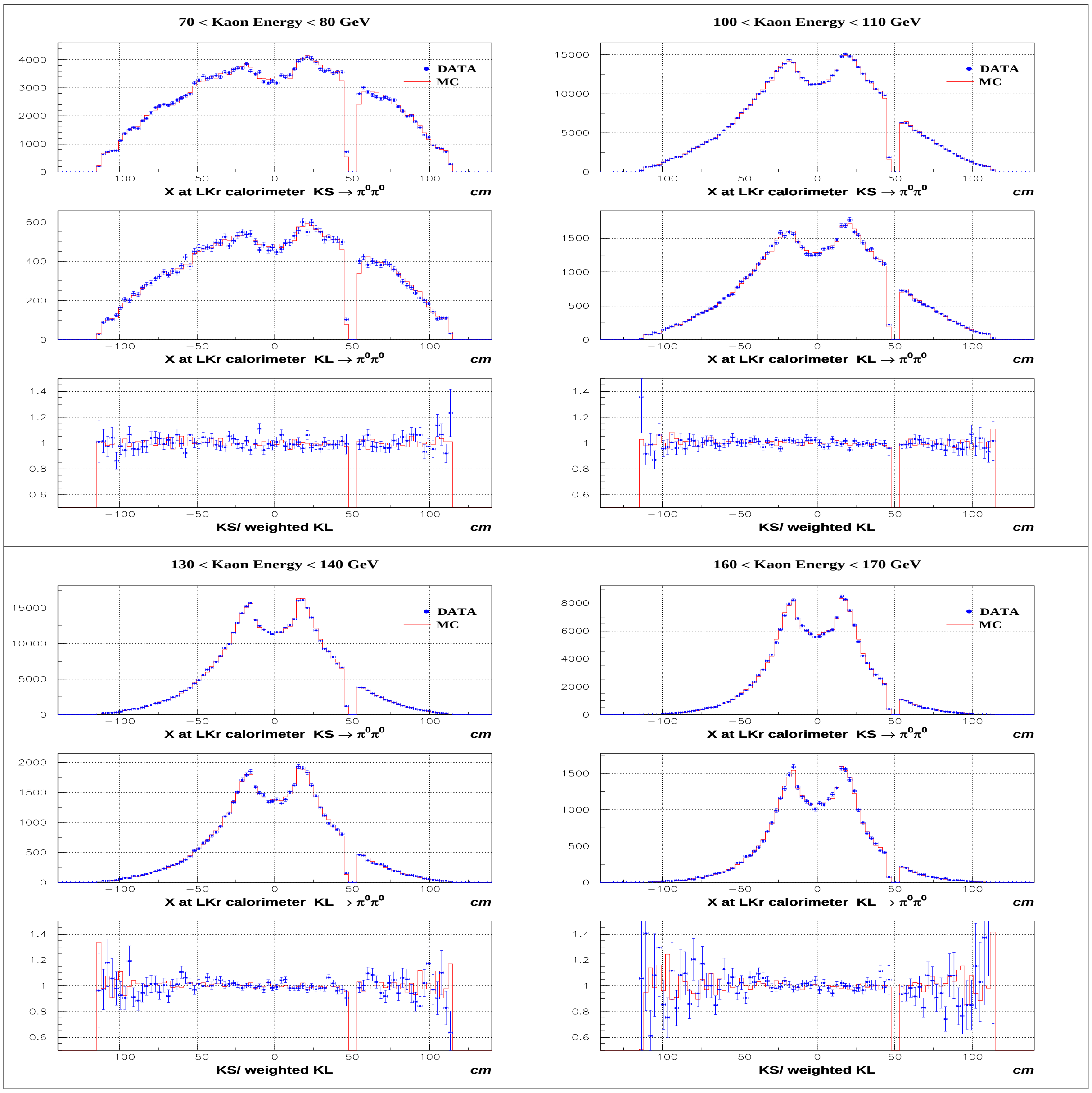

Figure 5.13: DATA/MC comparison of the X cluster position distributions for neutral events. The presence of the *dead* column is evident

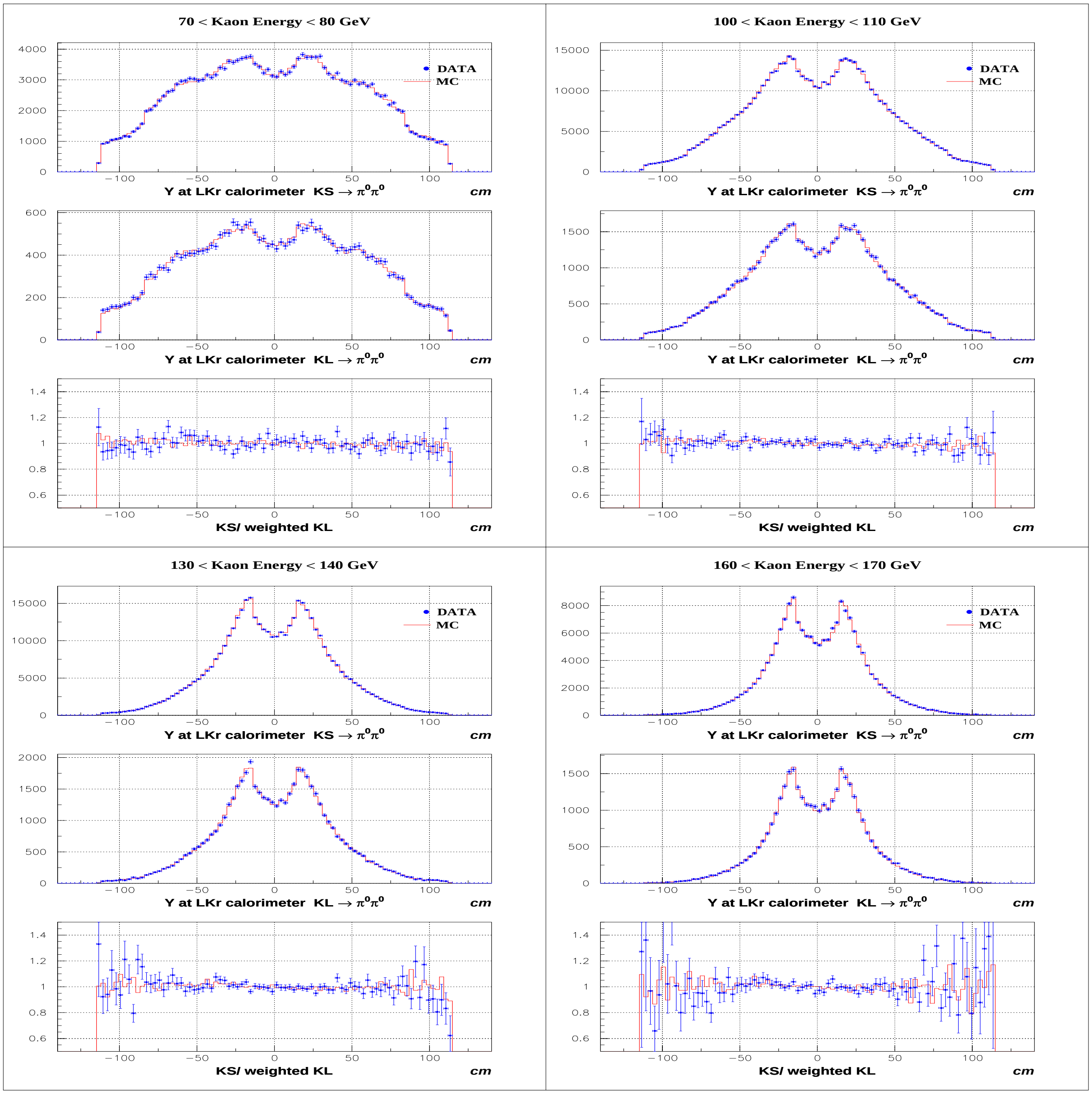

Figure 5.14: DATA/MC comparison of the Y cluster position distributions for neutral events.

a good agreement is found for the ratio of K_S to K_L, showing that the acceptance differences are well understood in the simulation. In all plots the real K_L events are weighted. For the real events, the effect of mistagging is subtracted from the neutral K_S events, while the charged events are identified by mean of the vertex.

5.5 Systematic error from beam geometry

The imperfection in the simulation of the beam line geometry can produce a systematic bias of the calculated acceptance correction. To give an estimate of such effect, the geometry of the two beams has been changed in the simulation until the agreement with the real data is lost, to see the corresponding changes of the acceptance correction.

We have tried to shift the beams along the x and y coordinates and we see that the simulation reproduces the vertex position distribution within $\pm$ 1 mm (see fig. 5.15).

To evaluate the effect of such small displacements we don't need different sets of Montecarlo data, because the events which are not reconstructed before the shift (due, for example, to a track missed in the beam pipe) are too far from the fiducial volume to be accepted after the shift. Thus, we apply the shift to the tracks and clusters of the same set of events before applying the acceptance cuts.

We also tried to change the shape of the vertex distributions by weighting [3] the Montecarlo events with the function

$$w(\xi) = 1 + A \cdot exp((\xi - \bar{\xi})^2/(2\sigma_\xi^2)) \tag{5.9}$$

(ξ = x or y generated vertex position for K_S or K_L)

[3] to conserve the correlation the same weight must be applied to both events of each couple, but, because of the uncorrelation of the transverse vertex position, the weight changes the effective position distribution for one beam only.
The equations 5.1–5.3 become

$$a_{S(L)} = \frac{\sum_i w_i X_i^{S(L)}}{\sum_i w_i} \qquad \sigma^2_{a_{S(L)}} = \frac{N\sum_i (w_i X_i^{S(L)})^2 - (\sum_i w_i X_i^{S(L)})^2}{N(\sum_i w_i)^2}$$

$$Cov(a_S, a_L) = \frac{N^2}{(\sum_i w_i)^2}\frac{\sigma_{(wX^S)(wX^L)}}{N} = \frac{\sum_i w_i^2 X_i^S X_i^L}{(\sum_i w_i)^2} - \frac{a_S a_L}{N}$$

so that the events in the peak have a weight $(1 + A)$ with respect to the events in the tails.

We see that a conservative range for A is $\pm$ 30 % (see fig. 5.16).

The variations of the correction with these changes in the simulation are shown in figure 5.17. The order of the effect is a few 10^{-4}, similar for K_S and K_L. We observe that the shift has a larger effect than the change of shape, and that the beam x position is the most critical variable. To understand why, the exercise has been repeated after releasing one by one the main acceptance cuts (see table 5.3). This shows that the sensitivity to the shift comes essentially from the presence of the dead column (see figure 5.18). In fact, in the absence of this sharp dishomogeneity of the calorimeter surface, all variations are within $\pm 1 \cdot 10^{-4}$.

	X shift		Y shift		X shape		Y shape	
	-1 mm	+1 mm	-1 mm	+1 mm	A=-0.3	A=+0.3	A=-0.3	A=+0.3
$\mathbf{K_S}$								
all cuts	-2.5	+2.0	-1.1	+1.1	+0.4	-0.3	+1.0	-0.7
all cuts but DCH accept.	-2.6	+2.1	-0.8	+1.0	+0.0	+0.0	+1.0	-0.6
all cuts but LKR accept.	-3.0	+2.3	-0.7	+0.5	-0.3	+0.2	+1.0	-0.7
all cuts but dead column	-0.8	+0.8	-1.1	+1.1	+0.2	-0.7	+1.0	-0.5
all cuts but dead cells	-1.3	+2.7	-0.9	+0.8	+1.0	-0.6	+1.1	-0.8
all cuts but MUV accept.	-2.5	+2.0	-1.1	+1.0	+0.2	-0.1	+0.9	-0.7
$\mathbf{K_L}$								
all cuts	-0.7	+2.7	-1.3	+0.4	+0.2	-0.1	-0.8	+0.8
all cuts but DCH accept.	-0.7	+2.7	-1.1	+0.3	+0.3	-0.2	-0.7	+0.7
all cuts but LKR accept.	-0.3	+2.0	-1.2	+0.5	+0.0	+0.1	-0.5	+0.4
all cuts but dead column	+0.1	-0.7	-1.1	+0.3	+0.2	-0.1	-0.8	+0.7
all cuts but dead cells	-0.7	+2.9	-0.8	+0.5	-0.3	+0.2	-0.7	+0.7
all cuts but MUV accept.	-0.6	+2.7	-1.3	+0.4	+0.0	+0.1	-0.8	+0.8

Table 5.3: Variations of the acceptance correction (units 10^{-4}) after changing the beam geometry, with different sets of cuts.

5.5.1 The effect of dead column

In the sample used so far, we have applied geometrical cuts against the dead calorimeter cells (including the dead column), but the missing cells were not simulated in the Montecarlo. Thus, the photon energy misreconstruction around the dead column is not taken into account and a possible underestimation of its effect could arise.

A second sample of neutral events was generated, including this time all the dead cells. With this new sample the correction becomes 1.0018 ± 0.0007, which

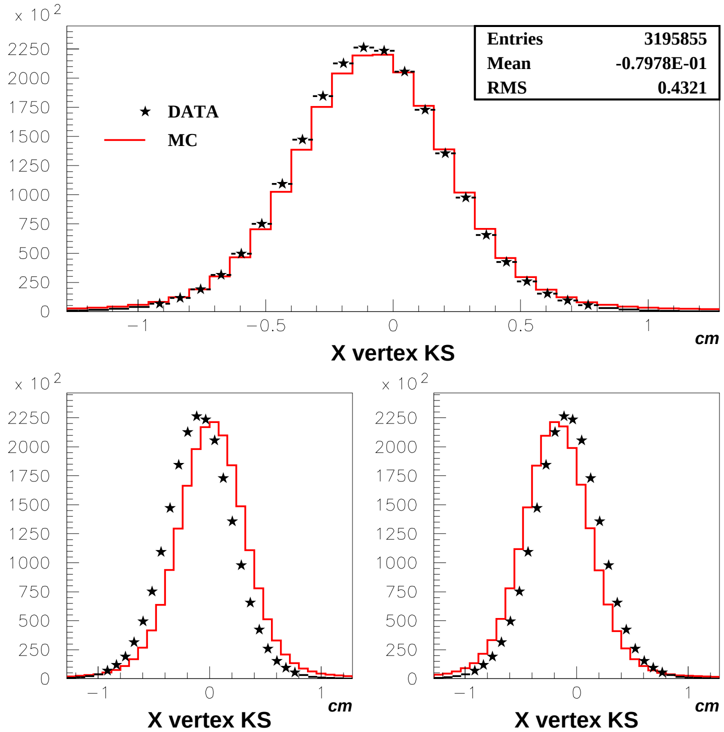

Figure 5.15: X vertex distribution for real and Montecarlo K_S events. In the bottom plots, the MC distributions have been shifted by $\pm$ 1 mm, producing a sizeable loss in agreement with real data.

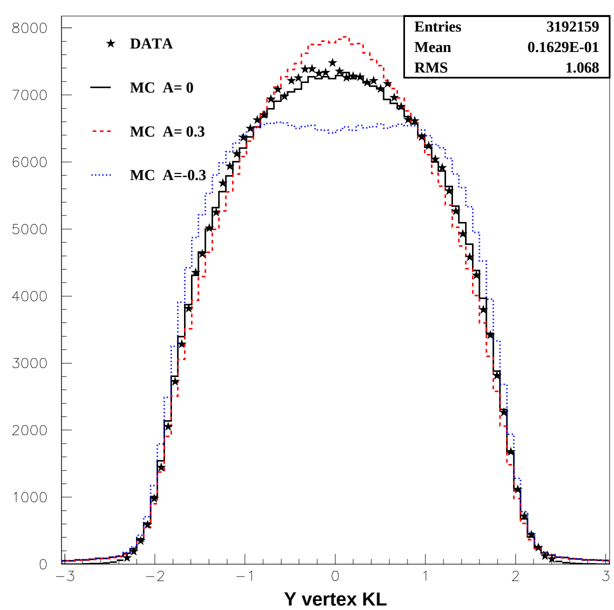

Figure 5.16: Y vertex distribution for real data and Montecarlo events with different weight parameter A.

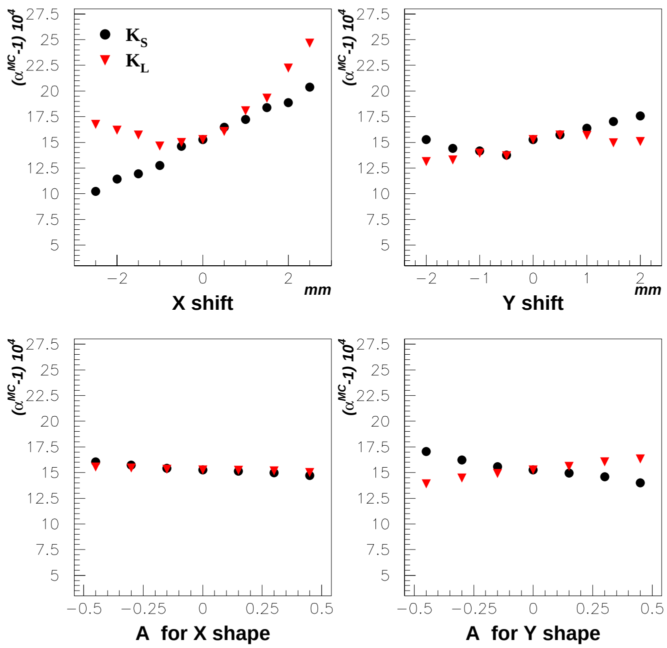

Figure 5.17: Effect on the acceptance correction of the changes in the simulated beam geometry.

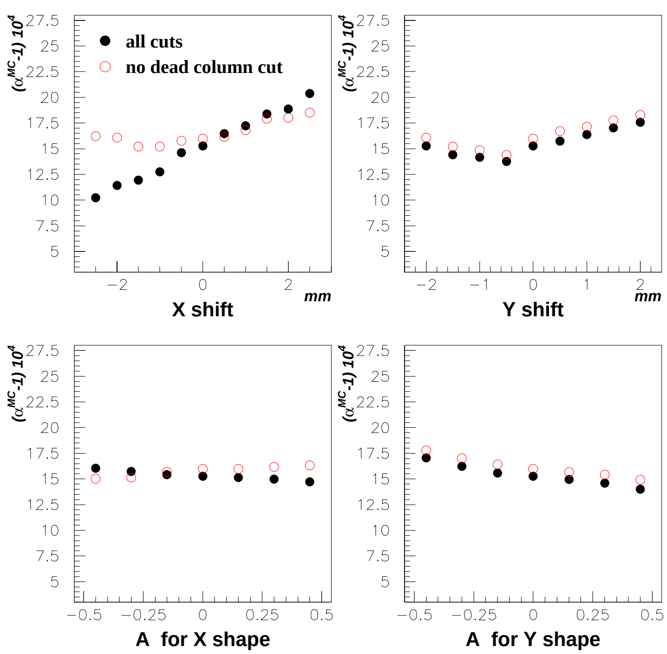

Figure 5.18: Sensitivity of the correction to the K_S beam geometry with and without the cut against dead column

is compatible, within statistical errors, with the previous value. Nevertheless, the sensitivity to the shift along x of the beams is much larger (fig. 5.19), but is over-estimated because the photons that are not properly reconstructed because of the dead column, but would have been after the shift, cannot be recovered. However, the result should be reasonable if the shift is small with respect to the cell size (2 cm).

To summarize, the estimation of the systematic from the beam geometry in connection with the presence of the dead column is too optimistic when using the first sample and too pessimistic using the second one. From the plot of fig. 5.19 we conclude that a conservative estimate of this effect is an uncertainty of $\pm 4 \cdot 10^{-4}$.

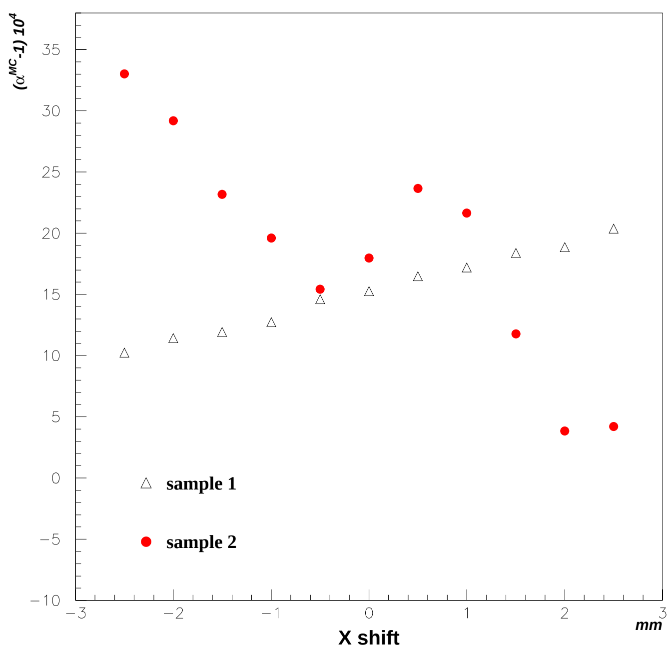

Figure 5.19: Sensitivity of the correction to the shift along x of K_S beam with the two sample of neutral events (sample 2 includes the simulation of dead cells).

5.6 Other possible sources of systematic error

5.6.1 K_S beam halo

In the previous section we have tried to change the shape of the beam core. We try now to estimate the effect of the uncertainty in the simulation of the K_S beam halo, which, as discussed in section 5.3, could generate some asymmetry in the p'_T distributions.

We consider as halo particles the K_S having $\theta_K > 0.6$ mrad, where

$$\theta_K = \sqrt{\left(\frac{P_x}{P_z} - (-0.1 \cdot 10^{-4})\right)^2 + \left(\frac{P_y}{P_z} - (-6.3 \cdot 10^{-4})\right)^2} \tag{5.10}$$

is the angle between the kaon direction and the nominal K_S beam axis.

From the data/MC comparison of the θ_K distributions (fig. 5.20) we see that the halo is reproduced within $\pm$ 50 %. Thus, we estimate the systematic error from the variation of the acceptance correction after applying a weight to the halo events in the simulation between 0.5 and 1.5. From the result shown in fig. 5.21 we conclude that the error is $\pm 2 \cdot 10^{-4}$.

5.6.2 Invariant mass cut

The cut on the $\pi^+\pi^-$ invariant mass around the K^0 mass for the charged events, has been included in the simulation, though the resolution of the spectrometer is not well reproduced in NASIM. Although no K_S $/K_L$ asymmetry is expected to be produced by this cut, we have checked for a possible effect by varying the mass window of the cut.

The result (fig. 5.22) shows that the effect should not exceed $\pm 1 \cdot 10^{-4}$.

5.7 Comparison with uncorrelated MC

The official Montecarlo sample of 1997 analysis consists of $50 \cdot 10^6$ events for each of the 4 decay modes (corresponding to 16 GBytes of data), generated using NMC without K_S $/K_L$ correlation.

These events can be analyzed in the very same way as real data and the resulting acceptance correction is the inverse of the double ratio obtained from the Montecarlo

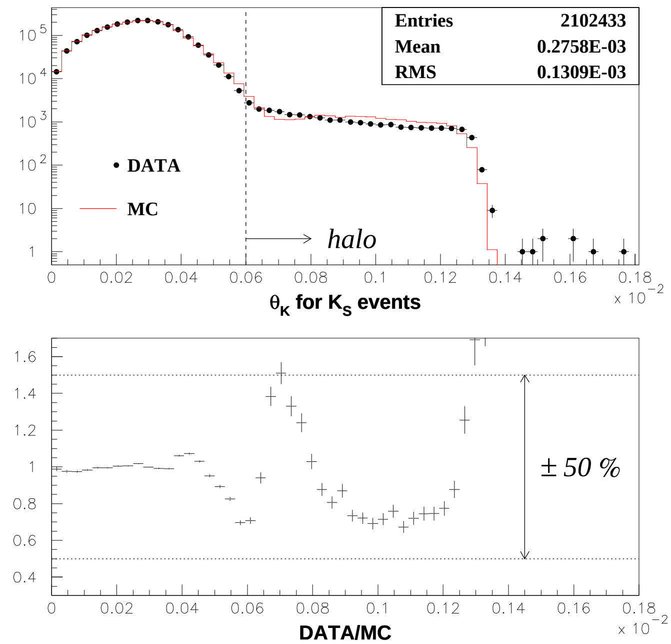

Figure 5.20: Comparison of the θ_K distributions for Montecarlo and real K_S events for events selected without the *cog* and p'_T events.

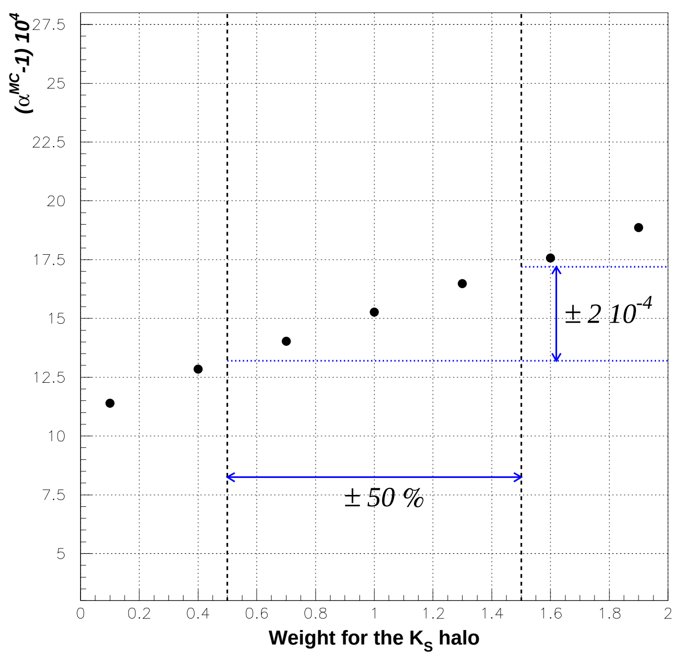

Figure 5.21: Behavior of the acceptance correction with the weight applied to the halo events (having $\theta_K > 0.6$ mrad).

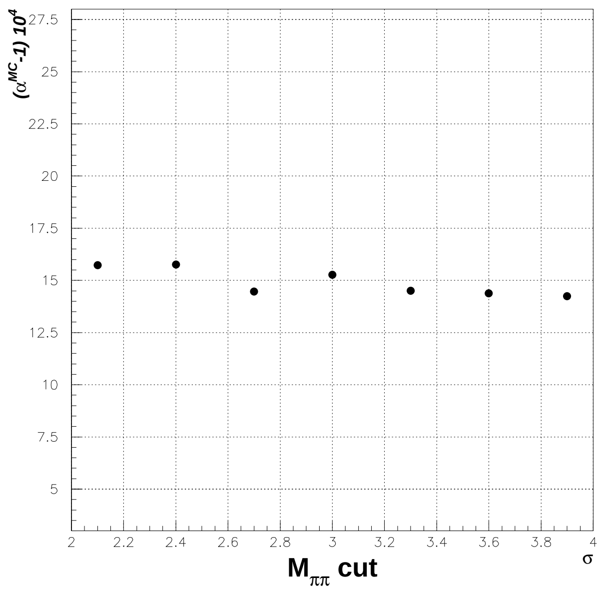

Figure 5.22: Behavior of the acceptance correction with the width of the mass window for $\pi^+\pi^-$ events, expressed in σ of spectrometer resolution.

events. We get

$$(\alpha^{MC})_{uncorr.} = 1.0028 \pm 0.0012 \tag{5.11}$$

that is compatible, within the statistical error, with the correction computed with correlated NASIM (1.0015 ± 0.0007). No disagreement is found between the two simulations also after plotting the correction as a function of energy (fig. 5.23).

As discussed in section 5.2, some approximations are introduced by the correlation method which are not present in the uncorrelated Montecarlo. To evaluate their effect, the uncorrelated events have been analyzed as the correlated ones, in order to introduce the same approximations: the correction has been computed in bins of true energy and the fiducial volume for K_L events has been defined using the generated z vertex position instead of the reconstructed one. We obtain that the global correction changes by $2.3 \cdot 10^{-4}$ (see also fig. 5.24), showing that the error introduced by the correlation technique can be neglected with respect to the total statistical and systematic error quoted so far.

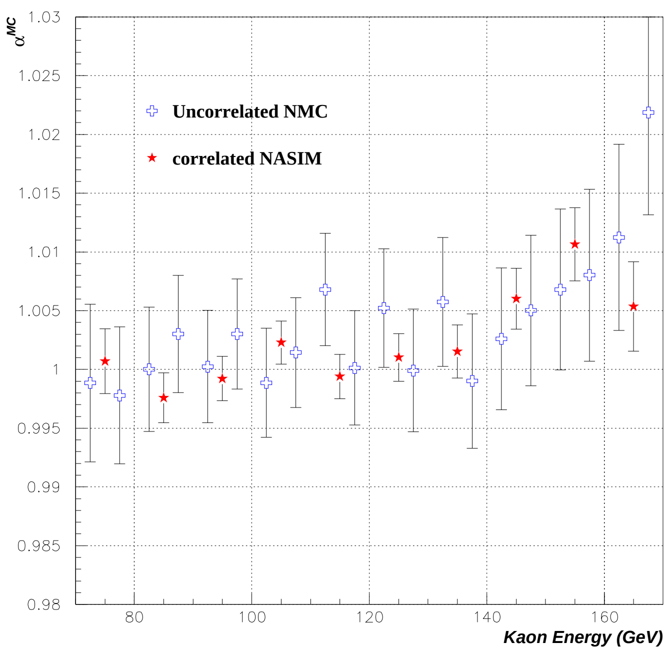

Figure 5.23: Comparison of the acceptance correction obtained with correlated NASIM and uncorrelated NMC

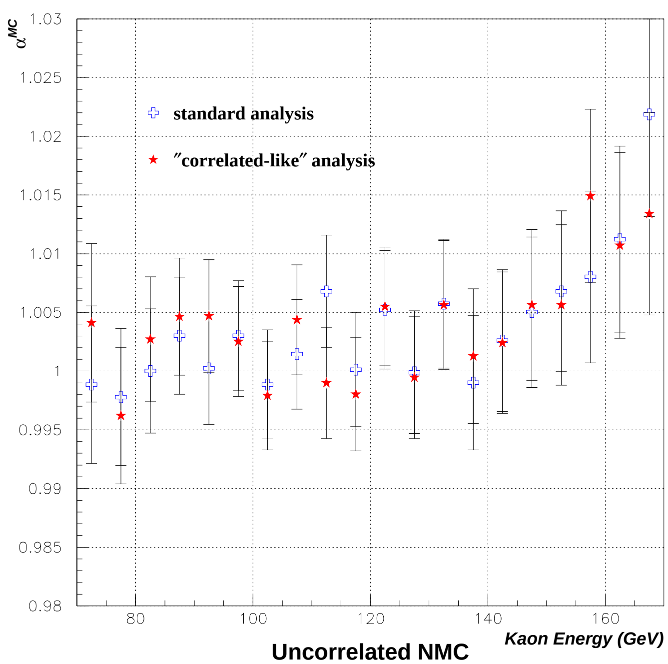

Figure 5.24: Comparison of the acceptance correction obtained from the uncorrelated NMC sample using two different analyses: the standard one (equivalent to the analysis on real data) and the correlated–like one, where the approximations described in section 5.2 are introduced.

5.8 Stability of the double ratio with the acceptance cuts

We perform now a check of the behavior of the acceptance correction by varying the main acceptance cuts in both real data and MC events and looking at the stability of the measured double ratio. We expect that the "raw" double ratio changes mainly because of the acceptance effects, though other systematic effects possibly depending on the geometry, as trigger inefficiencies or accidental activity, could arise.

In figures 5.25 and 5.26, the double ratio R, corrected only for mistagging and background, is plotted as a function of the radial cuts at drift chamber 1 and LKr calorimeter, before and after the acceptance correction.

By varying the DCH radial cut between 11 and 18.5 cm, we get a maximum variation of R of $74 \cdot 10^{-4}$ before the acceptance correction, that becomes $9 \cdot 10^{-4}$ after it is applied. For the LKr cut between 13 and 17.5 cm, we pass from $39 \cdot 10^{-4}$ to $15 \cdot 10^{-4}$.

From the difference ΔN of the statistics in each decay mode between the two extreme cases, we can naively estimate the expected statistical fluctuation of R as

$$\delta R = \sqrt{\frac{\Delta N_L^{00}}{(N_L^{00})^2} + \frac{\Delta N_S^{00}}{(N_S^{00})^2} + \frac{\Delta N_L^{+-}}{(N_L^{+-})^2} + \frac{\Delta N_S^{+-}}{(N_S^{+-})^2}} \tag{5.12}$$

In both cases we find $\delta R \sim 5 \cdot 10^{-4}$.

We conclude that no evidence for systematic effects larger than 10^{-3} (and not necessarily coming from the acceptance correction) is found.

5.9 Conclusions

The acceptance correction to the double ratio has been evaluated using a correlated sample of Montecarlo events.

The main contribution to the systematic error is found to come from the uncertainty in the simulation of beam geometry, estimated to be $\pm 4 \cdot 10^{-4}$.
This error is due essentially to the presence of the dead column, so that is expected to become $< 2 \cdot 10^{-4}$ for the analysis of 1998 data.

No other effect producing a systematic beyond $2 \cdot 10^{-4}$ has been found. By adding in quadrature the contributions of beam geometry and K_S halo, we quote a total

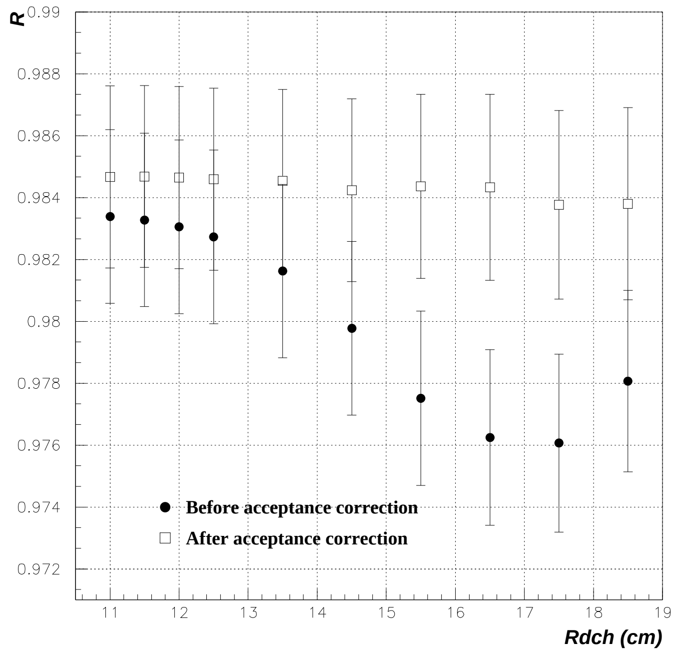

Figure 5.25: The double ratio R, measured on 97 data (corrected only for mistagging and backgrounds), as a function of the inner radial cut at the first drift chamber for charged events.

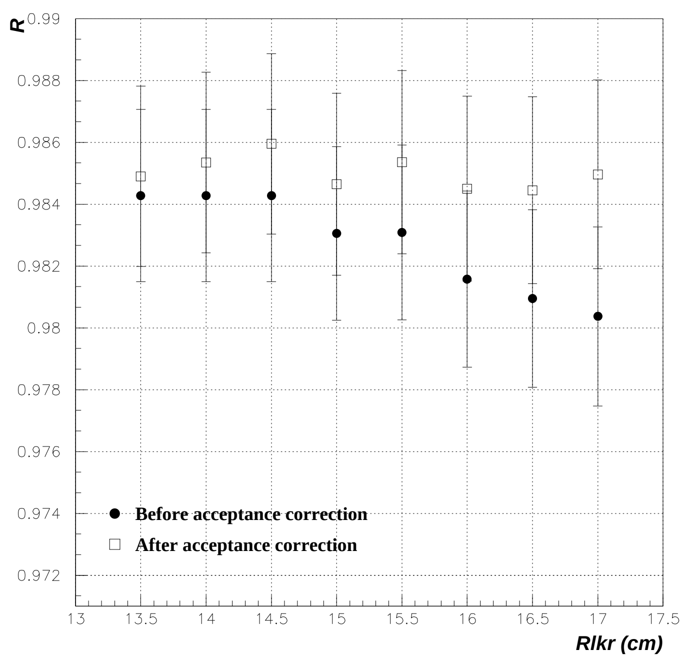

Figure 5.26: The same as previous plot varying the inner cut at LKr for both charged and neutral events.

systematic error of $\pm 5 \cdot 10^{-4}$.

The correction computed using the correlated Montecarlo sample is thus

$$(\alpha^{MC})_{corr.} = 1.0015 \pm 0.0007\ (stat.) \pm 0.0005\ (syst.) \tag{5.13}$$

Since we have verified that the correlated Montecarlo method does not introduce relevant biases, we quote the final acceptance correction as the weighted average of the correlated and uncorrelated samples:

$$\alpha^{MC} = 1.0018 \pm 0.0006\ (stat.) \pm 0.0005\ (syst.) \tag{5.14}$$

Chapter 6

K_S/K_L interference and pure K_S in the "K_L" beam

So far, we have silently assumed to deal with two pure beams of K_S and K_L particles. Actually, a relevant fraction of the $K^0 \to \pi\pi$ events from the highest energy part of the K_L beam is due to pure K_S and K_S/K_L interference. The size of the interference term depends from the production asymmetry parameter $D = (N_{K^0} - N_{\bar{K^0}})/(N_{K^0} + N_{\bar{K^0}})$, whose *a priori* knowledge is rather approximate ($\gtrsim 30$ %). In this chapter we present our analysis aimed to measure D directly from the 1997 data and to estimate the effect on the ϵ'/ϵ measurement of the interference and K_S terms (including the uncertainty on D).

6.1 Introduction

The time evolution of a particle state initially created as a K^0 ($\bar{K^0}$) is

$$|\psi(t)\rangle \;=\; \frac{N}{(1\pm\epsilon)}\left(e^{-i\frac{c^2 M_{KS} t}{\hbar}} e^{-\frac{t}{2\tau_S}}\;|K_S\rangle \;\pm\; e^{-i\frac{c^2 M_{KL} t}{\hbar}} e^{-\frac{t}{2\tau_L}}\;|K_S\rangle\right) \tag{6.1}$$

where t is the kaon proper time and N a normalization constant. The rate of $\pi\pi$ decays for a K^0 ($\bar{K^0}$) can thus be written as

$$\begin{aligned}\Gamma_{\pi\pi} \;&\propto |\langle\pi\pi|T|\psi(t)\rangle|^2 \;= \\ &= \frac{|N|^2}{|1\pm\epsilon|^2}\left\{\;e^{-\frac{t}{\tau_S}} + |\eta|^2 e^{-\frac{t}{\tau_L}} \pm 2|\eta| cos\left(\frac{c^2\Delta M t}{\hbar} - \phi\right) e^{-\frac{t}{2}\left(\frac{1}{\tau_S}+\frac{1}{\tau_L}\right)}\right\}\end{aligned} \tag{6.2}$$

where

$$\eta = \frac{\langle\pi\pi|T|K_L\rangle}{\langle\pi\pi|T|K_S\rangle} = |\eta|e^{i\phi} \qquad\qquad \Delta M = M_{KL} - M_{KS}$$

If we deal with a mixture of N_{K^0} K^0 and $N_{\bar{K^0}}$ $\bar{K^0}$, the number of decays in the laboratory frame with kaon momentum P_K at a distance Z from the production target, will be, neglecting terms of $o(|\epsilon|^2)$

$$\begin{aligned} r_{\pi\pi}(Z, P_K) \;\propto\; & e^{-\frac{ZM_K}{\tau_S P_K}} + |\eta|^2 e^{-\frac{ZM_K}{\tau_L P_K}} + \\ & 2\left(D(P_K) - 2Re(\epsilon)\right)|\eta| e^{-\frac{ZM_K}{2P_K}\left(\frac{1}{\tau_S}+\frac{1}{\tau_L}\right)} cos\left(\frac{c^2\Delta M}{\hbar}\frac{ZM_K}{P_K} - \phi\right)\end{aligned} \tag{6.3}$$

where

$$D(P_K) = \frac{N_{K^0} - N_{\bar{K^0}}}{N_{K^0} + N_{\bar{K^0}}} \tag{6.4}$$

In fig. 6.1 the relative contribution of not–pure–K_S in the K_S beam and not–pure–K_L in the K_L beam has been computed after integrating the different contributions between z_{AKS} and $z_{AKS} + 3.5\ c\tau_S$, assuming a constant value of 0.3 for $D(P_K)$ [1]. We get that the "impurity" of the K_S beam is at the level of a few 10^{-3}, while for the K_L beam it reaches 15 % in the highest energy part of the spectrum, so that it should be considered in the ϵ'/ϵ analysis, by including it in the K_L weighting

[1] the other constants used in equation (6.3) are (from PDG [14]):

$$M_K = 497.672\ \mathrm{MeV}/c^2 \qquad c\tau_S = 2.6762\ \mathrm{cm} \qquad c\tau_L = 1551\ \mathrm{cm}$$

$$c\Delta M/\hbar = .1769\ \mathrm{cm}^{-1} \qquad |\eta| = 2.28\cdot 10^{-3} \quad \phi = .76\ \mathrm{rad}$$

function:

$$w(Z) = \frac{r_{\pi\pi}(Z - Z_{KST})}{r_{\pi\pi}(Z_{AKS} - Z_{KST})} \cdot \frac{r_{\pi\pi}(Z_{AKS} - Z_{KLT})}{r_{\pi\pi}(Z - Z_{KLT})} \simeq e^{-\frac{(Z-Z_{AKS})M_K}{c\tau_S\ P_K}} \cdot \frac{r_{\pi\pi}(Z_{AKS} - Z_{KLT})}{r_{\pi\pi}(Z - Z_{KLT})} \tag{6.5}$$

where Z_{KST} and Z_{KLT} are the positions of the beam targets.

The largest uncertainty in estimating this contribution comes from the production asymmetry parameter D, whose value in the energy region relevant for NA48 can be inferred from NA31 measurements and theoretical models with $\gtrsim 30\%$ accuracy. From now on, we will neglect $2Re(\epsilon)$ with respect to D.

6.2 Measurement of the production asymmetry parameter D

We now try to extract D directly from the 1997 data sample, by comparing the Z vertex distributions of the events $N(Z)$ from the two beams, in energy bins. Being the acceptances the same to a first–order approximation, the ratio of K_S to K_L distributions can be fitted with the function

$$f(Z; \mathbf{A}, \mathbf{D}) = \mathbf{A}\frac{r_{\pi\pi}(Z - Z_{KST}, P_K; \mathbf{D})}{r_{\pi\pi}(Z - Z_{KLT}, P_K; \mathbf{D})} \propto \mathbf{A}\frac{exp\left(-\frac{(Z-Z_{KST})M_K}{c\tau_S P_K}\right)}{r_{\pi\pi}(Z - Z_{KLT}, P_K; \mathbf{D})} \tag{6.6}$$

having two free parameters D and A, the latter giving the intensity ratio of the two beams, that is momentum dependent.

The fit has been done in 10 energy bins between 70 and 170 GeV. The charged decays are identified by mean of the vertex, while for the neutral decays we have to correct for the mistagging, so that the quantities to be fitted with f are

$$R^{+-}(Z) = \frac{N_S^{+-}(Z)}{N_L^{+-}(Z)} \tag{6.7}$$

$$R^{00}(Z) = \frac{N_S^{00}(Z)}{N_L^{00}(Z)}(1 - \alpha_{LS}) - \alpha_{LS} \tag{6.8}$$

Due to the different way in which the beginning of the fiducial region is defined for the two beams, the two distributions have very different shape close to the AKS position. Thus, the fit must begin at a distance from the AKS d_{AKS} much larger

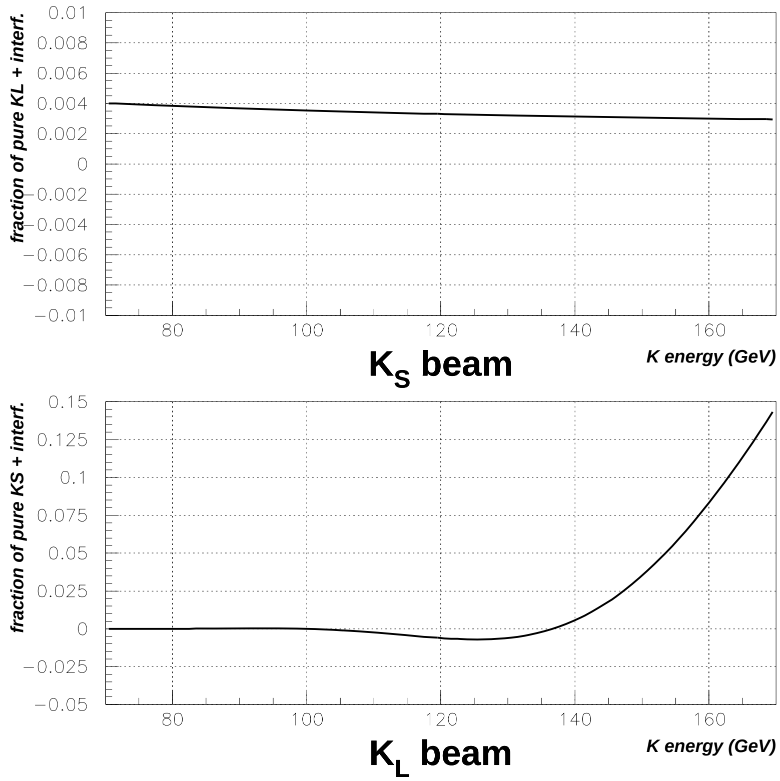

Figure 6.1: Fraction of "impure" 2 pion decays within 3.5 $c\tau$ from AKS. A constant value of 0.3 for D has been used in both cases. Note the different scale in ordinate.

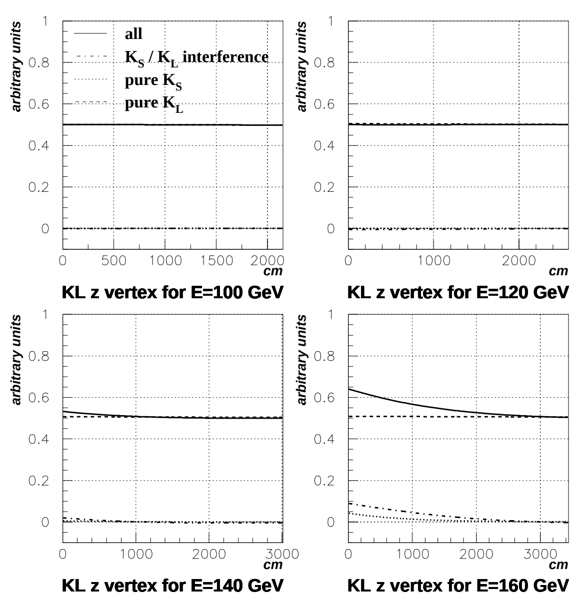

Figure 6.2: Contributions of pure K_S , pure K_L and interference to the K_L beam at different energies.

than the Z vertex position resolution. We choose $d_{AKS} > 3.5m$ for charged events and $d_{AKS} > 4.0m$ for neutral events, after having checked the stability of the result with this parameter (see figure 6.3).

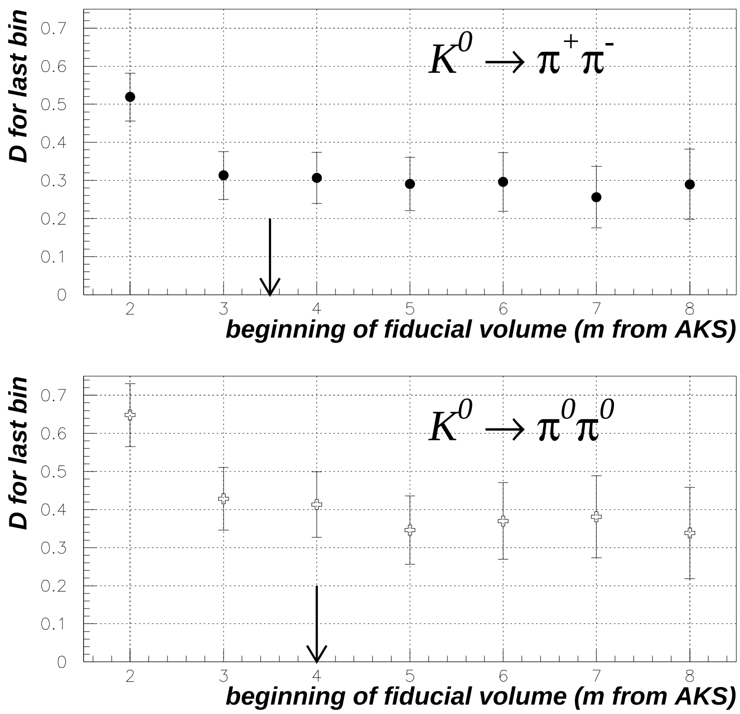

Figure 6.3: Behavior of the D values (obtained for the range $160 < E_K < 170$ GeV) varying the beginning of the fiducial region. The arrows mark the final choices.

To check for the possible effect of the acceptance difference, the acceptance ratio A_L/A_S as a function of P_K and z has been computed using the sample of correlated MC events used in the analysis of previous chapter, that gives a small statistical error with respect to the real data. We find that for charged events the acceptance ratio tends to increase with z, producing a possible underestimation of D. Thus, the measured ratio has been corrected for the acceptance ratio [2].

Figures 6.5 and 6.6 show the result of the fits for some energy bins. As we could expect from fig. 6.1, we obtain sensible values for D only for kaon energy > 130 GeV.

[2]To contain the statistical error, the acceptance ratio has been obtained in bins of 2 m. The correction applied to a given z value is obtained by linear interpolation of the closest 2 points.

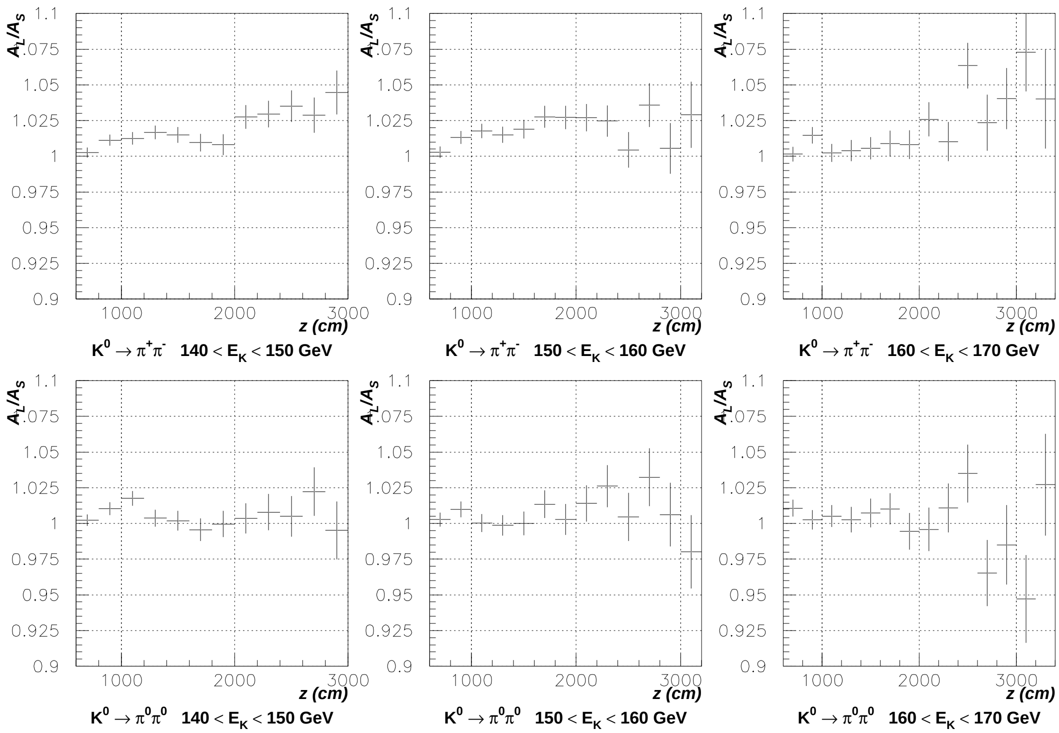

Figure 6.4: Ratio of K_L to K_S acceptance as a function of z for the highest energy bins.

To test the coherence of this procedure, the values of the normalization parameter $A(p)$ obtained independently using charged and neutral events, are compared in fig. 6.7 and they show to be compatible.

The effect of the acceptance correction is shown in fig. 6.8. As expected, we get a relevant effect only for charged events.

Finally, the results obtained from charged and neutral events are compared in fig. 6.9. From the weighted average of the two measurements we get the following results:

Kaon energy (GeV)	D
135	0.24 ± 0.16
145	0.29 ± 0.07
155	0.33 ± 0.05
165	0.34 ± 0.05

The systematic error can be conservatively estimated as the size of the acceptance

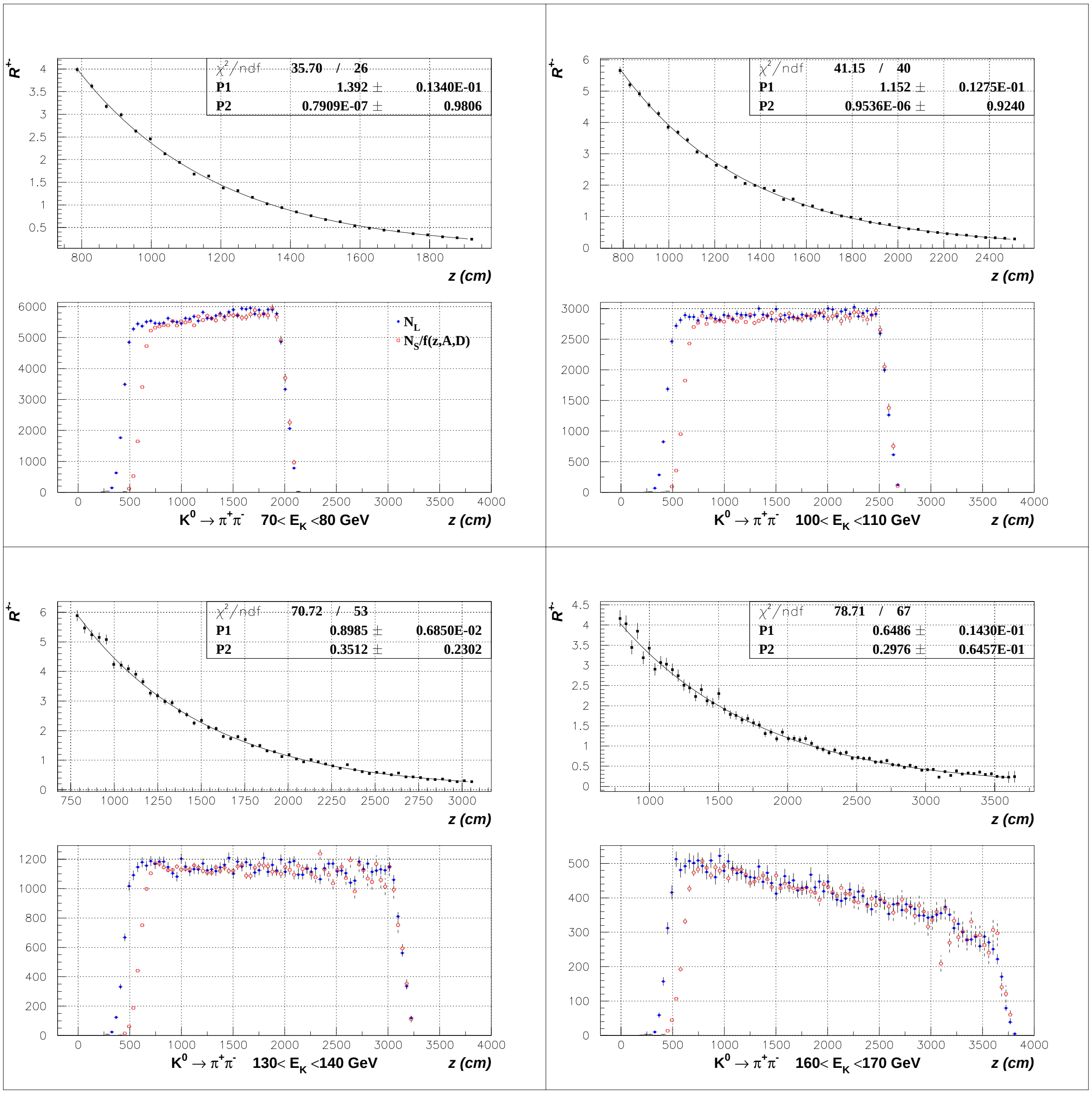

Figure 6.5: Results of the fit for charged events. For each energy bin, the vertex distributions of K_L events are also shown, overlayed with the distributions of K_S events divided by the fitted ratio. The two parameters of the fit are A (=P1 $\cdot 10^{-4}$) and D (=P2).

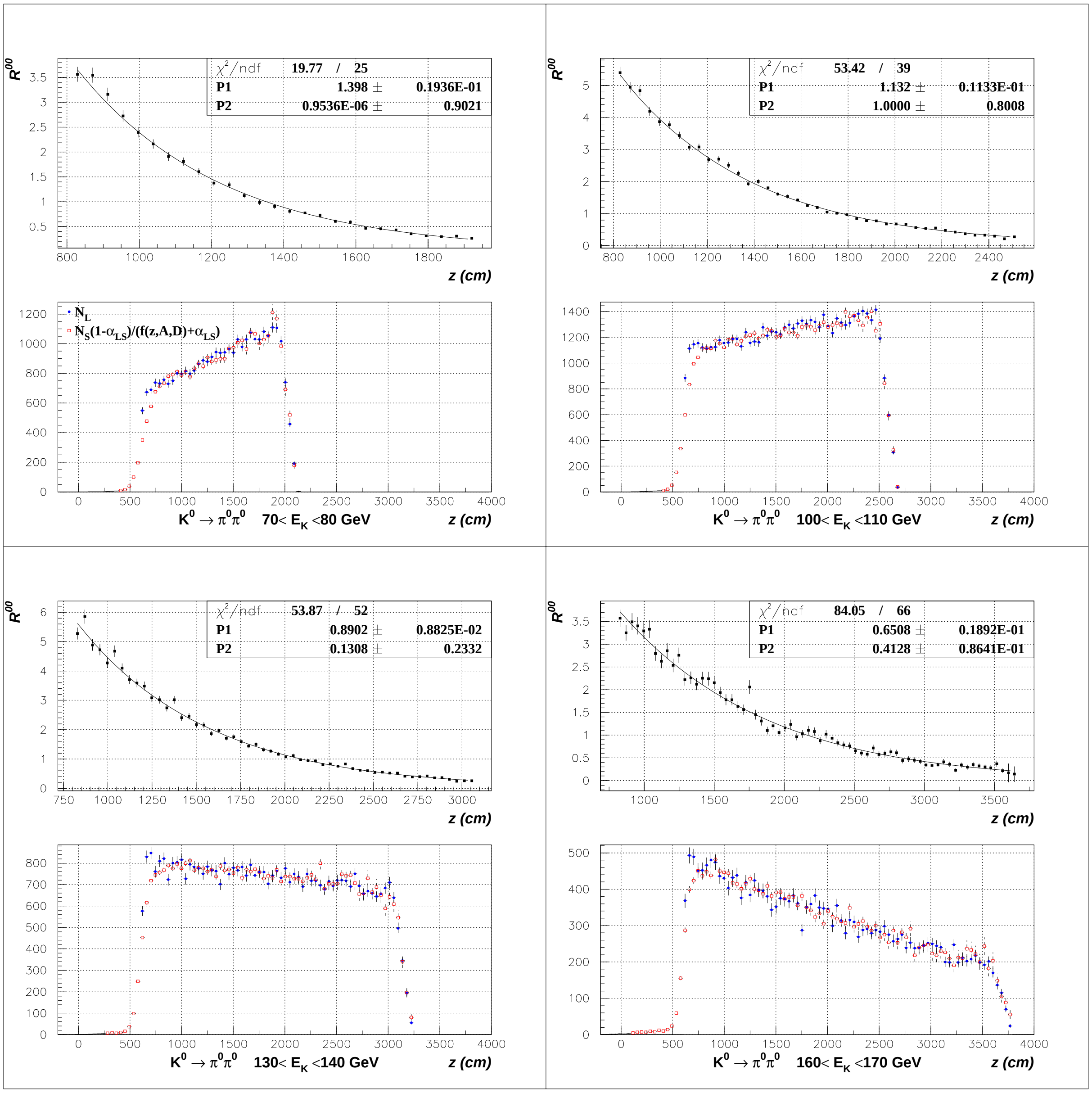

Figure 6.6: Results of the fit for neutral events. The two parameters of the fit are A (=P1 $\cdot 10^{-4}$) and D (=P2).

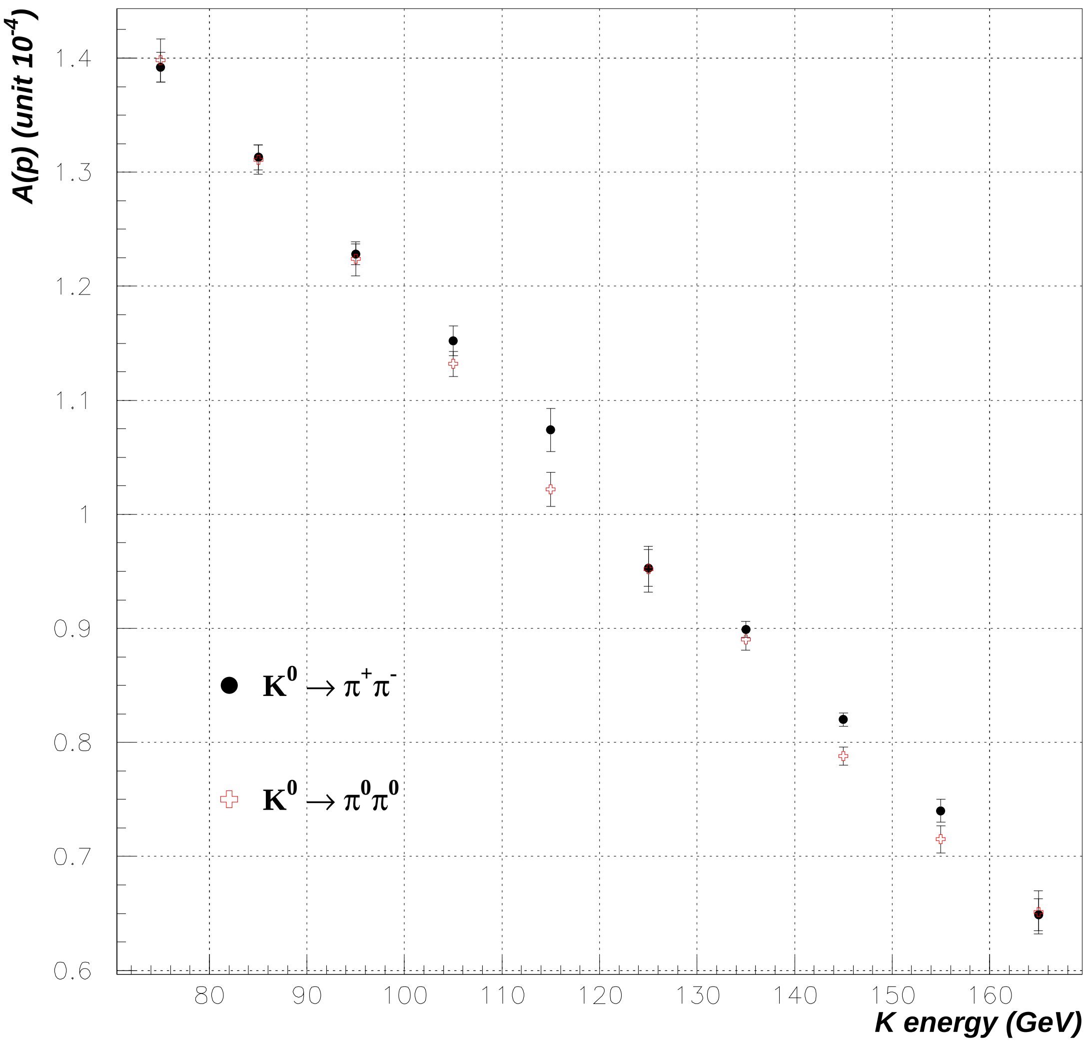

Figure 6.7: Comparison of normalization constants obtained from the fits of charged and neutral events.

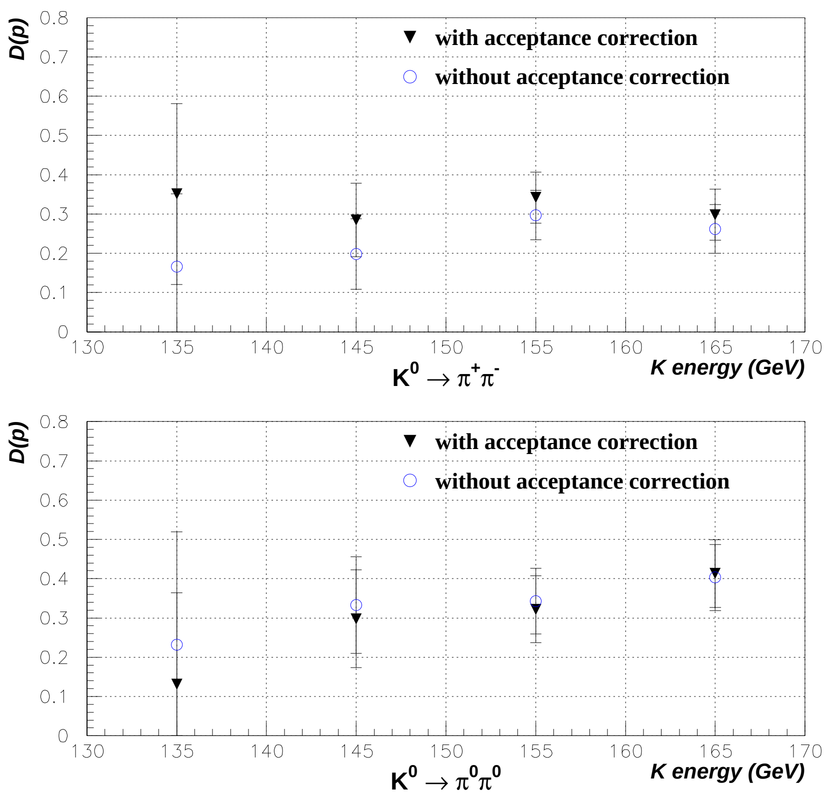

Figure 6.8: Values of D obtained with and without the acceptance correction

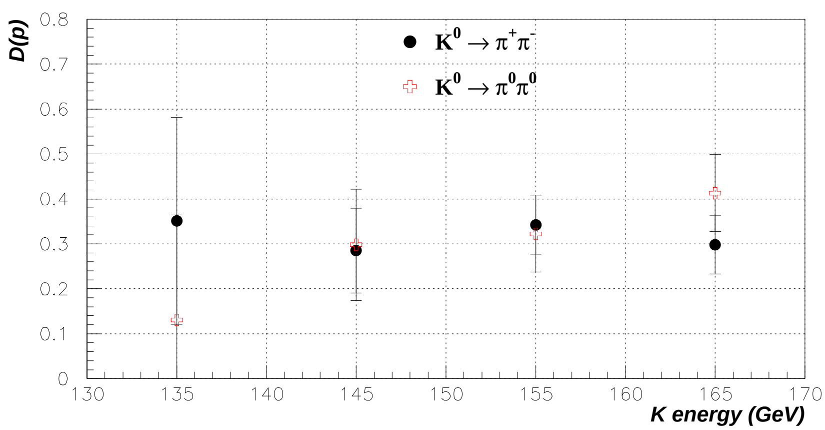

Figure 6.9: Final values of D obtained from charged and neutral events.

correction, that is 0.05.

The results are in good agreement with the expectations from the NA31 measurements [13, 41], as shown in fig. 6.10.

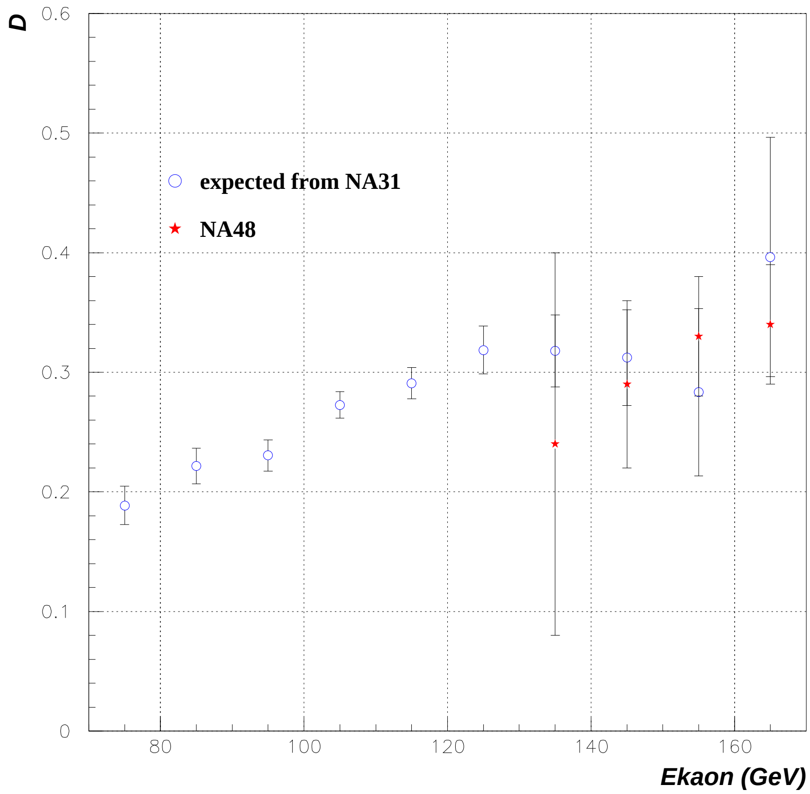

Figure 6.10: Comparison of measured D values with expectations from NA31 measurements.

6.3 Effect on ϵ'/ϵ

If we explicit the ϵ'/ϵ parameter in equation (6.6) using

$$\eta^{+-} \simeq \left(1 + \frac{\epsilon'}{\epsilon}\right) \qquad \eta^{00} \simeq \left(1 - 2\frac{\epsilon'}{\epsilon}\right)$$

and we neglect $Im(\epsilon'/\epsilon\ )$ $(\phi^{+-} = \phi^{00} = \phi)$, we can write the measured double ratio for a given bin as

$$R \simeq \frac{\int_{Z_i^{00}}^{Z_f^{00}} a^{00}(Z)w(Z)\left[\left(1-4Re\left(\frac{\epsilon'}{\epsilon}\right)\right)\mathcal{F}_L(\Delta Z_L)+\left(1-2Re\left(\frac{\epsilon'}{\epsilon}\right)\right)\mathcal{F}_I(\Delta Z_L)+\mathcal{F}_S(\Delta Z_L)\right]dZ}{\int_{Z_i^{+-}}^{Z_f^{+-}} a^{+-}(Z)w(Z)\left[\left(1+2Re\left(\frac{\epsilon'}{\epsilon}\right)\right)\mathcal{F}_L(\Delta Z_L)+\left(1+Re\left(\frac{\epsilon'}{\epsilon}\right)\right)\mathcal{F}_I(\Delta Z_L)+\mathcal{F}_S(\Delta Z_L)\right]dZ} \cdot \frac{\int_{Z_i^{+-}}^{Z_f^{+-}} a^{+-}(Z)\mathcal{F}_S(\Delta Z_S)dZ}{\int_{Z_i^{00}}^{Z_f^{00}} a^{00}(Z)\mathcal{F}_S(\Delta Z_S)dZ} \tag{6.9}$$

where

- Z_i and Z_f define the fiducial decay region;
- $\Delta Z_L = Z - Z_{KLT}$ and $\Delta Z_S = Z - Z_{KST}$ are the distances from the beam targets;
- a^{00} and a^{+-} are the acceptances for neutral and charged events, assumed to be equal for K_S and K_L;
- $$w(Z) = \frac{r_{\pi\pi}(Z - Z_{KST})}{r_{\pi\pi}(Z_{AKS} - Z_{KST})} \cdot \frac{r_{\pi\pi}(Z_{AKS} - Z_{KLT})}{r_{\pi\pi}(Z - Z_{KLT})}$$
  is the weighting function that contains the best estimate for D and is (arbitrarily) normalized to 1 at the AKS position;
- $$\mathcal{F}_L(Z) = |\epsilon|^2 e^{-\frac{ZM_K}{\tau_L P_K}} \tag{6.10}$$
  $$\mathcal{F}_S(Z) = e^{-\frac{ZM_K}{\tau_S P_K}} \tag{6.11}$$
  $$\mathcal{F}_I(Z) = D(P_K)|\epsilon|e^{-\frac{ZM_K}{2P_K}\left(\frac{1}{\tau_S}+\frac{1}{\tau_L}\right)}cos\left(\frac{c^2\Delta M}{\hbar}\frac{ZM_K}{P_K} - \phi\right) \tag{6.12}$$

After defining the integrals of the different contributions

$$\mathcal{L}_X = \int_{Z_i}^{Z_f} a(Z)w(Z)\mathcal{F}_X(\Delta Z_L)dZ \qquad \mathcal{S}_X = \int_{Z_i}^{Z_f} a(Z)\mathcal{F}_X(\Delta Z_S)dZ \qquad (X = L, I, S)$$

we get, to the first order in ϵ'/ϵ ,

$$
\begin{aligned}
R &= \frac{\mathcal{L}_L^{00}+\mathcal{L}_I^{00}+\mathcal{L}_S^{00}}{\mathcal{L}_L^{+-}+\mathcal{L}_I^{+-}+\mathcal{L}_S^{+-}} \cdot \frac{\mathcal{S}_S^{+-}}{\mathcal{S}_S^{00}} \cdot \\
&\left[1 - 6Re\left(\frac{\epsilon'}{\epsilon}\right)\left(\frac{2}{3}\frac{\mathcal{L}_L^{00}+\mathcal{L}_I^{00}/2}{\mathcal{L}_L^{00}+\mathcal{L}_I^{00}+\mathcal{L}_S^{00}} + \frac{1}{3}\frac{\mathcal{L}_L^{+-}+\mathcal{L}_I^{+-}/2}{\mathcal{L}_L^{+-}+\mathcal{L}_I^{+-}+\mathcal{L}_S^{+-}}\right)\right] = \\
&= \mathcal{A}\cdot\left[1-6Re\left(\frac{\epsilon'}{\epsilon}\right)\cdot(1-\delta)\right]
\end{aligned}
\qquad (6.13)
$$

Thus, two effects can be disentangled:

a) a systematic effect on R if the weighting function, due to the uncertainty on D, doesn't take into account the interference term correctly, producing $\mathcal{A} \neq 1$;

b) a dilution of ϵ'/ϵ by the factor $(1-\delta)$.

6.3.1 Systematic on R

The ratio $\mathcal{A}$ has been computed in 10 energy bins between 70 and 170 GeV. A difference between the true D and the values used in the weighting function has been simulated:

$$\Delta D = (D)_{true} - (D)_{estimated}$$

where for $(D)_{estimated}$ we use the values of NA48 '97 obtained in section 6.2 for $E_K > 130$ GeV, and those inferred from NA31 for lower energy.
The acceptance functions have been computed using version 28 of the NASIM generator.

The result is shown in figures 6.11 and 6.12. Being the effect dominated by the last three energy bins, we can use an uncertainty[3] $\pm$ 0.07 for D, resulting in an error of $\pm\ 1 \cdot 10^{-4}$ for the average double ratio.

The smallness of the effect is due to the similar behavior with Z of the acceptances for charged and neutral events (fig. 6.14) in the highest energy bins. The computation of $\mathcal{A}$ has been repeated after applying a distortion function

$$\phi(Z) = 1 + \delta a \left(2\frac{Z - Z_{min}}{Z_{max} - Z_{min}} - 1\right) \qquad (6.14)$$

[3]We add in quadrature the statistical error obtained from the fit and the estimated systematic (0.05).

independently to a^{00} and a^{+-}, varying δa between $\pm$ 2 % (this uncertainty has been estimated from data/MC comparison of z vertex distributions for K_S events). The resulting changes of $\mathcal{A}$ are contained within a few 10^{-5}, so that the size of the systematic on R is not essentially changed.

In fig. 6.13 the exercise has been repeated without taking into account the interference and K_S terms in the weighting function:

$$w(Z) = e^{-\frac{(Z-Z_{AKS})M_K}{P_K}\left(\frac{1}{\tau_S}-\frac{1}{\tau_L}\right)} \tag{6.15}$$

In this case a correction to the measured R value should be applied, amounting to $(-68 \pm 7)\ 10^{-4}$ for the last bin and $(-6.5 \pm 1.0)\ 10^{-4}$ on average.

6.3.2 Dilution of ϵ'/ϵ

The dilution factor $(1-\delta)$ has been obtained, varying the true D value as before (see fig. 6.15 and 6.16). This term depends very weakly on the acceptance functions. The effect reaches 12 % in the last bin but on the average is

$$\delta = 1.15 \pm 0.10\ \%$$

that is negligible for NA48.

6.4 Conclusions

The presence of K_S/K_L interference and pure K_S decays in the K_L beam must be considered in the ϵ'/ϵ analysis by including it into the K_L weighting function (or, less naturally, by applying an energy–dependent correction to the measured double ratio).

The production asymmetry parameter D can be directly measured from the NA48 data with the same level of accuracy of the values inferred from the NA31 measurements. We get a confirmation of the expectations that make us more confident about the values to be used in the analysis.

The systematic effect on the double ratio from the uncertainty on D turns out to be limited to $1 \cdot 10^{-4}$.

The dilution of ϵ'/ϵ due to the interference and K_S terms, integrated between 70 and 170 GeV, is also negligible, being 1.15 ± 0.10 %.

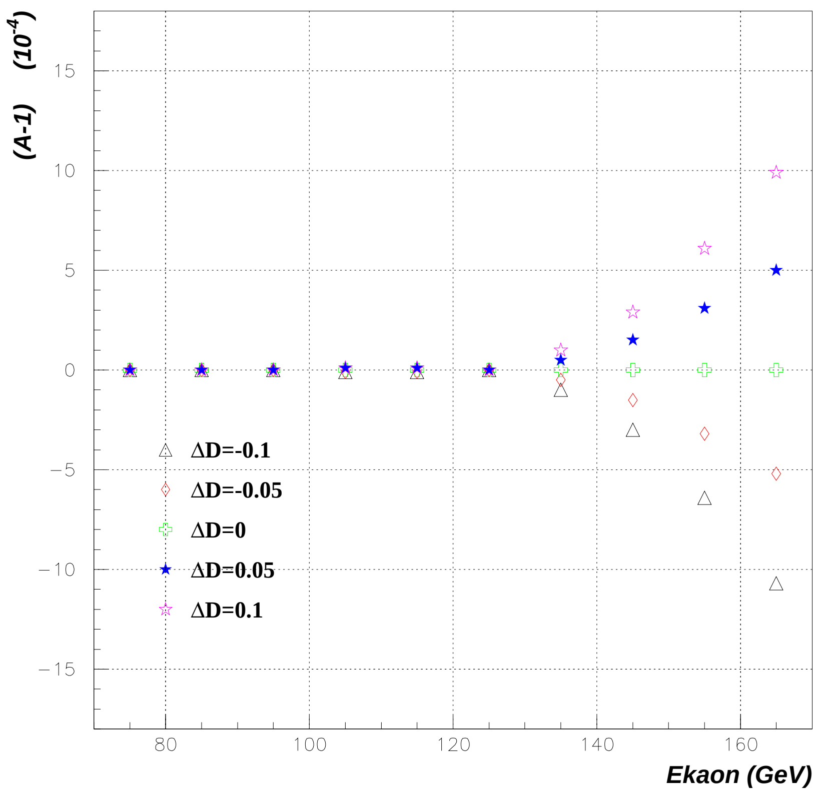

Figure 6.11: Systematic effect on the double ratio induced by an error ΔD on the production asymmetry parameter used in the weighting function.

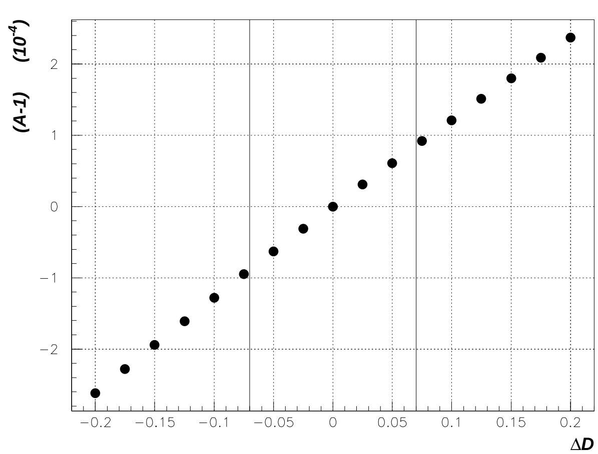

Figure 6.12: Systematic effect on the average double ratio. The lines mark our choice of $\pm$ 0.07 for the uncertainty on D.

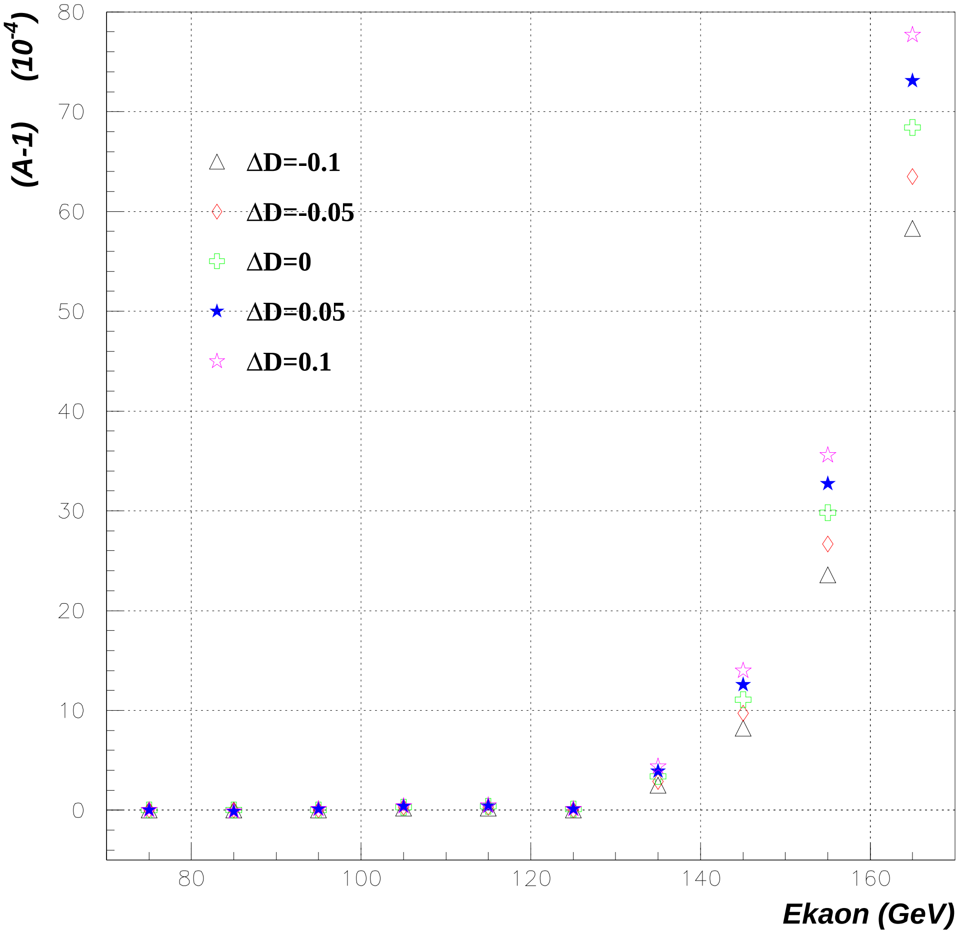

Figure 6.13: The same as fig. 6.11, but without taking into account the interference and K_S terms in the K_L weighting function.

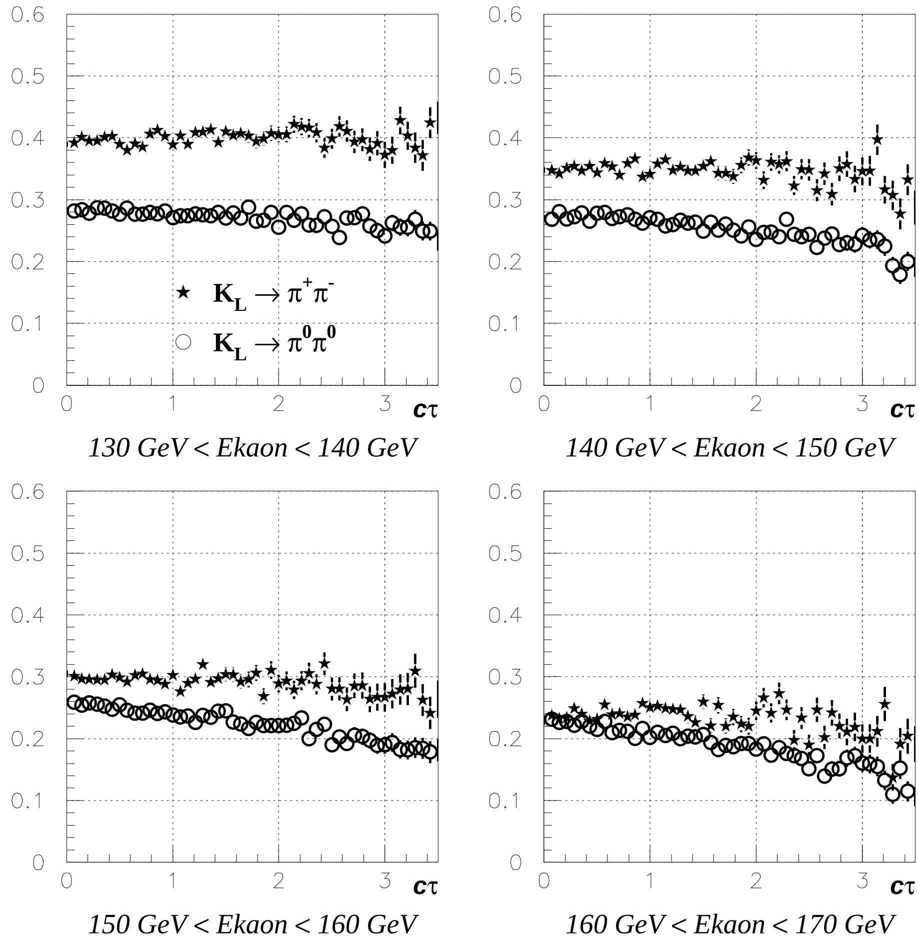

Figure 6.14: Efficiencies as a function of $c\tau$ for charged and neutral events

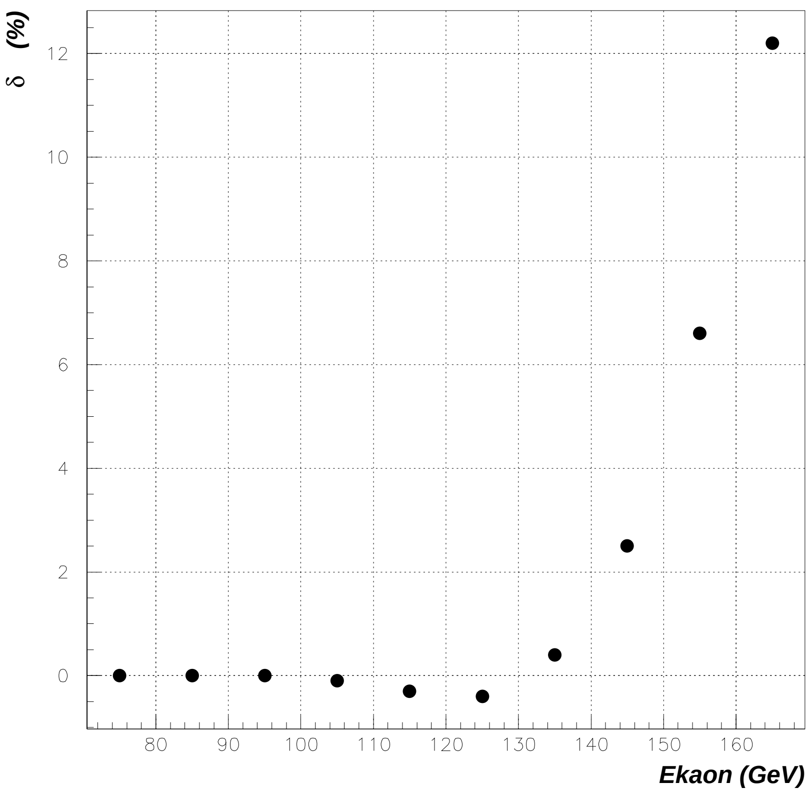

Figure 6.15: Dilution of ϵ'/ϵ due to the interference and K_S terms, as a function of energy.

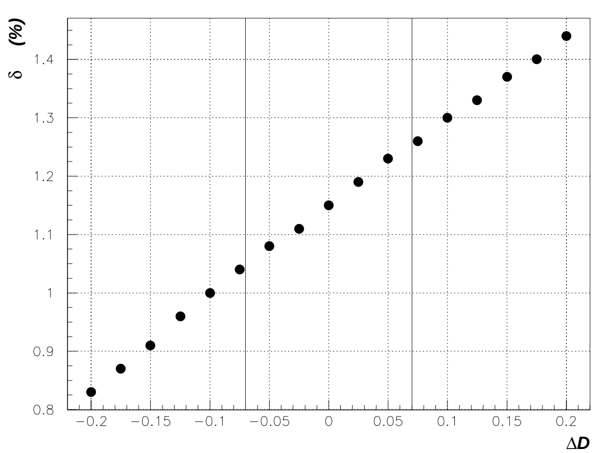

Figure 6.16: Dilution of ϵ'/ϵ for different values of D.

Chapter 7

The measured value of ϵ'/ϵ from 1997 data

During a 42 days run in September / October 1997, NA48 took the first data with all its detector components successfully installed. We have derived the double ratio from these data, by computing all the needed corrections, introduced in chapter 4, according to the procedures developed inside the collaboration. The obtained result for $Re(\epsilon'/\epsilon)$ is given.

7.1 Summary of cuts

The data are first selected by rejecting all the runs and single bursts where some pathological behavior in one or more detector was identified.

We summarize in the following all the cuts that were applied at event level. Most of them have been already described and justified in the previous chapters.

COMMON CUTS:

the event time is given by the charged hodoscope for charged events and by the LKr for neutral ones.

- no DCH overflows in the range $\pm$ 312.5 ns around the event time;
- no MBX deadtime bit at event time;
- K_S events are identified by the presence of a proton in the tagger within $\pm$ 2 ns around the event time;
- no hits in the AKS within $\pm$ 3 ns around the event time for identified K_S events.

CUTS FOR CHARGED EVENTS:

cuts are applied for each identified vertex in the event. If more than one vertex passes the cuts, the event is counted only once.

- event acquired by MBX trigger;
- kaon energy obtained from angle (equation 4.38) between 70 and 170 GeV;
- the reconstructed charges of the two tracks must have opposite sign;
- track momentum > 10 GeV/c, χ^2 of track fit must be good;
- closest distance of approach < 3 cm ;
- $$ASP \text{ (momentum asymmetry) } < MIN(0.62, 1.08 - .0052 * E_{kaon})$$
- position of tracks at DCH 1,2,4 must be at least 12 cm away from the center of chamber;

- $|M_{\pi^+\pi^-} - M_{K^0}|/c^2 < 3 * (1.755\ \mathrm{MeV} + E_{kaon} * 0.007372)$;

- $(p'_T)^2 < 0.0002\ (\mathrm{GeV/c})^2$ with the production target chosen according to vertex identification;

- center of gravity at LKr (see eq. 4.16) < 10 cm ;

- track extrapolations within LKr acceptance, including an inner radial cut at 15 cm, and a minimum distance of 2 cm from the dead column and the other dead cells;

- E (in GeV from LKr) / P (in GeV/c from DCH) < 0.8 (clusters are matched with tracks with a cut of 10 cm on the distance between the cluster center of gravity and the extrapolated track position);

- track extrapolations within MUV acceptance (outside a square of side 25 cm and inside a square with side of 260 cm, both centered on the K_L beam axis);

- track extrapolations must not match MUV hits, both in space and time (within $\pm$ 4 ns);

- $c\tau < 3.5$ (using energy from angle);

- hodoscope time must have been reconstructed[1];

- difference of track times within $\pm$ 6 ns ;

- vertex time within $\pm$ 20 ns from the center of the trigger timeslice.

CUTS FOR NEUTRAL EVENTS:

- event acquired by NUT $\pi^0\pi^0$ trigger;

the following cuts apply to single clusters (the cluster center of gravity is used to define the position):

- photon energy between 3 and 100 GeV ;

[1]the inefficiency of hodoscope time reconstruction is around 0.2 % and has been checked to be the same for K_S and K_L with negligible error

- cluster inside LKr fiducial volume, at least 2 cm away from the dead column and the dead cells;

for events having at least four photon candidates, the following cuts are applied to all the possible 4–cluster combinations:

- distance between any two photon candidates > 10 cm ;
- time difference between each cluster and the average of the four < 5 ns ;
- total energy between 70 and 170 GeV ;
- center of gravity (see eq. 4.19) < 10 cm ;
- $c\tau < 3.5$;
- no extra clusters with energy > 1.5 GeV within $\pm$ 3 ns the average time;
- $\chi^2_{2\pi^0} < 13.5$

If more than one combination pass all cuts, the one with lower $\chi^2_{2\pi^0}$ is used.

Selected events for the four decay modes are counted in **20 energy bins**. The K_L events are weighted with the function in (6.5).

7.2 Mistagging

Since the events are identified by mean of the tagger, the K_S events N_S and the weighted K_L events N_{Lw} must be corrected for the mistagging. To this extent, we also count the "mistagged" events N_{Sm} and N_{Lm}, namely the events which are tagger–identified as K_L (K_S) but are treated as K_S (K_L) for what concerns the weight and the $Z > 0$ cut. Following the notations of section 4.7, we denote with n the corresponding true quantities and with α_{LS} and α_{SL} the mistagging probabilities:

$$\begin{cases} N_{Lw} = n_{Lw}(1-\alpha_{LS}) + \alpha_{SL} n_{Sm} \\ N_S = n_S(1-\alpha_{SL}) + \alpha_{LS} n_{Lm} \\ N_{Lm} = n_{Lm}(1-\alpha_{LS}) + \alpha_{SL} n_S \\ N_{Sm} = n_{Sm}(1-\alpha_{SL}) + \alpha_{LS} n_L \end{cases} \tag{7.1}$$

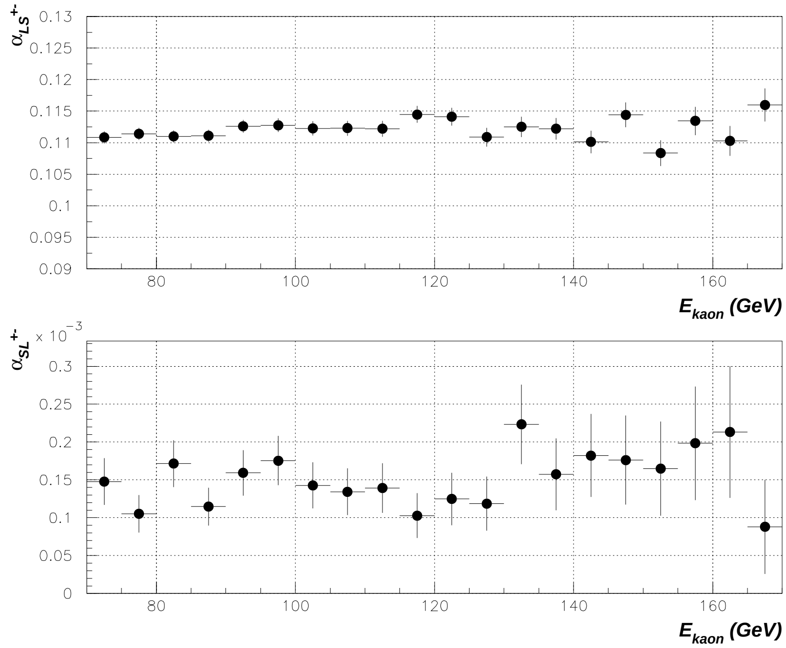

Figure 7.1: Mistagging probabilities for charged events, measured as a function of energy.

These relationships can be inverted to get the correction formulae

$$\boxed{\begin{aligned} n_{Lw} &= \frac{(1-\alpha_{SL})N_{Lw} \ - \ \alpha_{SL} n_{Sm}}{1-\alpha_{SL}-\alpha_{LS}} \\ n_S &= \frac{(1-\alpha_{LS})N_S \ - \ \alpha_{LS} n_{Lm}}{1-\alpha_{SL}-\alpha_{LS}} \end{aligned}} \tag{7.2}$$

The α_{LS} and α_{SL} parameters are measured for the charged mode by identifying the events with the vertex and by looking at the tagger response. We find

$$\alpha_{LS}^{+-} = 0.1120 \pm 0.0003 \ \%$$
$$\alpha_{SL}^{+-} = (1.5 \pm 0.01) \cdot 10^{-4}$$

They are found to be independent from energy, as expected (fig. 7.1).

These values are used to correct the event counts in each energy bin for both charged and neutral modes, while we treat the differences $\Delta\alpha_{LS}$ and $\Delta\alpha_{LS}$ (see 4.56 and 4.57) as systematic corrections. Their effect on the double ratio is estimated by changing α_{LS}^{00} and α_{SL}^{00} within the estimated range and looking at the resulting variations of R. We obtain:

$$\Delta\alpha_{LS} = (10 \ \pm \ 5) \cdot 10^{-4} \quad \Longrightarrow \quad \Delta R = (18 \ \pm \ 9) \cdot 10^{-4}$$

$$\Delta\alpha_{SL} \;=\; \pm\, 1 \cdot 10^{-4} \quad\Longrightarrow\quad \Delta R \;=\; \pm\; 5 \cdot 10^{-4}$$

in good agreement with the expected effect (eq. 4.55). The statistical errors on α_{LS}^{+-}, α_{SL}^{+-}, n_{Lm}, n_{Sm} lead to an uncertainty of $3 \cdot 10^{-4}$ on R.

7.3 Charged Background

In order to estimate the background contamination of the $K_L \to \pi^+\pi^-$ sample, that is expected to come only from K_{e3} and $K_{\mu 3}$ decays, two samples of K_L events with a well identified electrons or muons are selected. The K_{e3} sample is obtained by applying all cuts of the charged selection but the invariant mass, p_T', and E/P cuts, and requiring instead a well identified electron using $E/P > 0.9$. The same is done for the $K_{\mu 3}$ sample, where the anti-μ cut is released instead of E/P,and the muon is identified asking for a time coincidence of $\pm$ 2 ns between event and MUV hit times. The events in this sample are weighted as the K_L ones.

The different shape of the (M_{+-},${p_T'}^2$) distributions for the 4 samples (K_S , K_L , K_{e3} , $K_{\mu 3}$) can be used to derive the background levels by fitting the K_L distribution as the sum of the other 3 distributions with free coefficients, in some control region where the shapes are very different. The distributions are shown in figure 7.2. Events in all four samples are vertex–identified.

In the present analysis we use a simpler and robust method, consisting in integrating the distributions in the signal region, and in the two control regions shown in fig. 7.2. These are chosen in order to have a small contribution from signal (obtained from the K_S) and different ratios of $K_{\mu 3}$ to K_{e3} contributions. They have to be out of the kaon mass region in order to avoid the effect of high–p_T events from the collimators of the K_L beam line (discussed in section 7.8). The K_L events in the control regions will be the sum of three contributions:

$$\begin{cases} N_{L1} \;=\; \phi_\mu N_{\mu 1} + \phi_e N_{e1} + \phi_s N_{S1} & \text{(CR1)} \\ N_{L2} \;=\; \phi_\mu N_{\mu 2} + \phi_e N_{e2} + \phi_s N_{S2} & \text{(CR2)} \end{cases} \tag{7.3}$$

The contribution of signal (ϕ_s parameter) can be obtained by normalizing the K_S and K_L distributions at the peak (${p_T'}^2 < 5 \cdot 10^{-5}$ (GeV/c)^2, $|M_{+-} - M_K| < 2.5$ MeV/c^2) and is found to be relatively small ($\lesssim 10\%$), so that the uncertainty in the

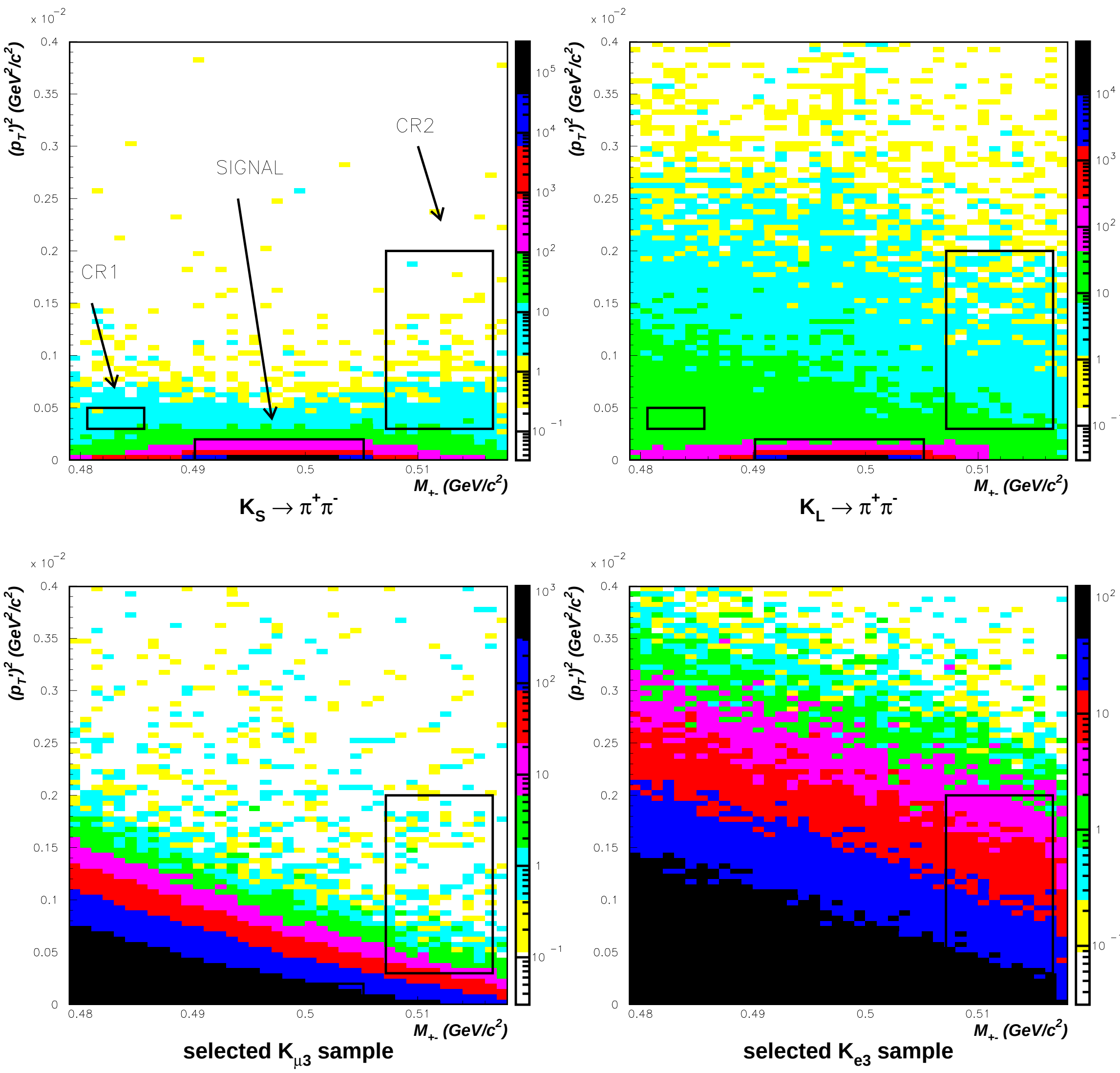

Figure 7.2: Distributions of $p_T'^2$ versus M_{+-} for the four event samples used in charged background analysis. The signal and control regions are also shown.

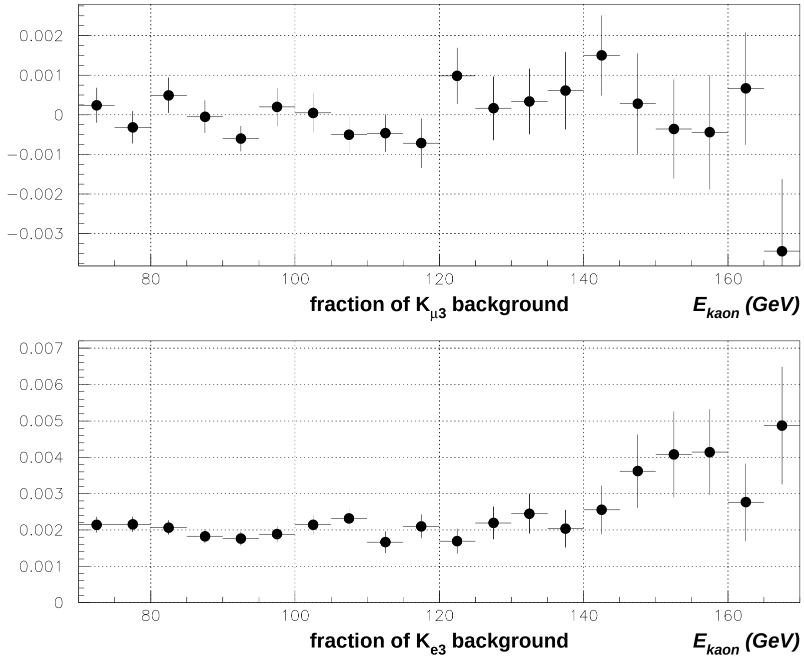

Figure 7.3: Computed fractions of $K_{\mu 3}$ and K_{e3} events to be subtracted from K_L charged events.

normalization does not introduce a significant error. The other two parameters are obtained by inverting equations (7.3):

$$\begin{cases} \phi_\mu &= \frac{(N_{L1}-\phi_s N_{S1})N_{e2}-N_{e1}(N_{L2}-\phi_s N_{S2})}{D} \\ \phi_e &= \frac{N_{\mu 1}(N_{L2}-\phi_s N_{S2})-(N_{L1}-\phi_s N_{S1})N_{\mu 2}}{D} \end{cases} \tag{7.4}$$

where

$$D = N_{\mu 1} N_{e2} - N_{e1} N_{\mu 2}$$

is the determinant of the equation system, that is inversely proportional to the errors on ϕ_μ and ϕ_e. This is why the control regions have been chosen in order to have a very different ratio of the K_{e3} to $K_{\mu 3}$ events ($N_{\mu 1}/N_{e1} \cdot N_{\mu 2}/N_{e2} \sim 100$). The resulting values of ϕ_e and ϕ_μ allow to compute the number of $K_{\mu 3}$ and K_{e3} events in the signal region. The result is shown in fig. 7.3, as a function of energy. The background turns out to be dominated by K_{e3} events and amounts, on the full energy spectrum, to 0.22 ± 0.02 %, where the error is the statistical one. The systematic error is estimated to be $\pm\ 4 \cdot 10^{-4}$ by repeating the computation with different control regions and looking at the corresponding change of the result. The computed fraction of background events is subtracted from the K_L charged sample for each energy bin.

7.4 Neutral Background

As anticipated in section 4.3.2, the contamination of $K_L \to 3\pi^0$ events in the neutral sample can be directly measured on the data themselves by looking at the tails of the $\chi^2_{2\pi^0}$ variable using the following procedure:

- a control region (CR) is chosen in the $\chi^2_{2\pi^0}$ distribution, well outside the signal region $\chi^2_{2\pi^0} < 13.5$. We will use $36 < \chi^2_{2\pi^0} < 135$;

- the amount of signal in the control region, due to misreconstruction, is estimated from the selected $K_S \to 2\pi^0$ events, after having subtracted the contribution of mistagged K_L . The K_S and K_L distributions are normalized in each energy bin using the events having $\chi^2_{2\pi^0} < 2.7$, that have negligible contamination;

- the difference between the K_L and K_S events in the CR results, as expected from MC simulations, in a nearly flat distribution that is linearly extrapolated backward to get the background level under the signal region. An extrapolation factor of 1.2 ± 0.2, obtained from Montecarlo to account for uncertainty in the shape of the background $\chi^2_{2\pi^0}$ distribution, is applied.

Fig. 7.4 shows the K_L and normalized K_S distributions for two different bins and for the full energy range (the K_S one is obtained as a sum of all the distributions normalized in each bin).

The use of the K_S events as an estimator for the signal requires some considerations. Bad χ^2 for good $2\pi^0$ events are produced by the tails of the energy reconstruction, that are not symmetric, being the main source the already cited energy underestimation due to hadron photoproduction. This means that signal events in the CR are shifted on average towards the calorimeter by the reconstruction, distorting the decay z distribution. For the K_L case, being the original decay distribution nearly flat, the events that, though generated at $z < 0$, enter the fiducial region, are compensated by those leaving the fiducial region at the opposite bound-

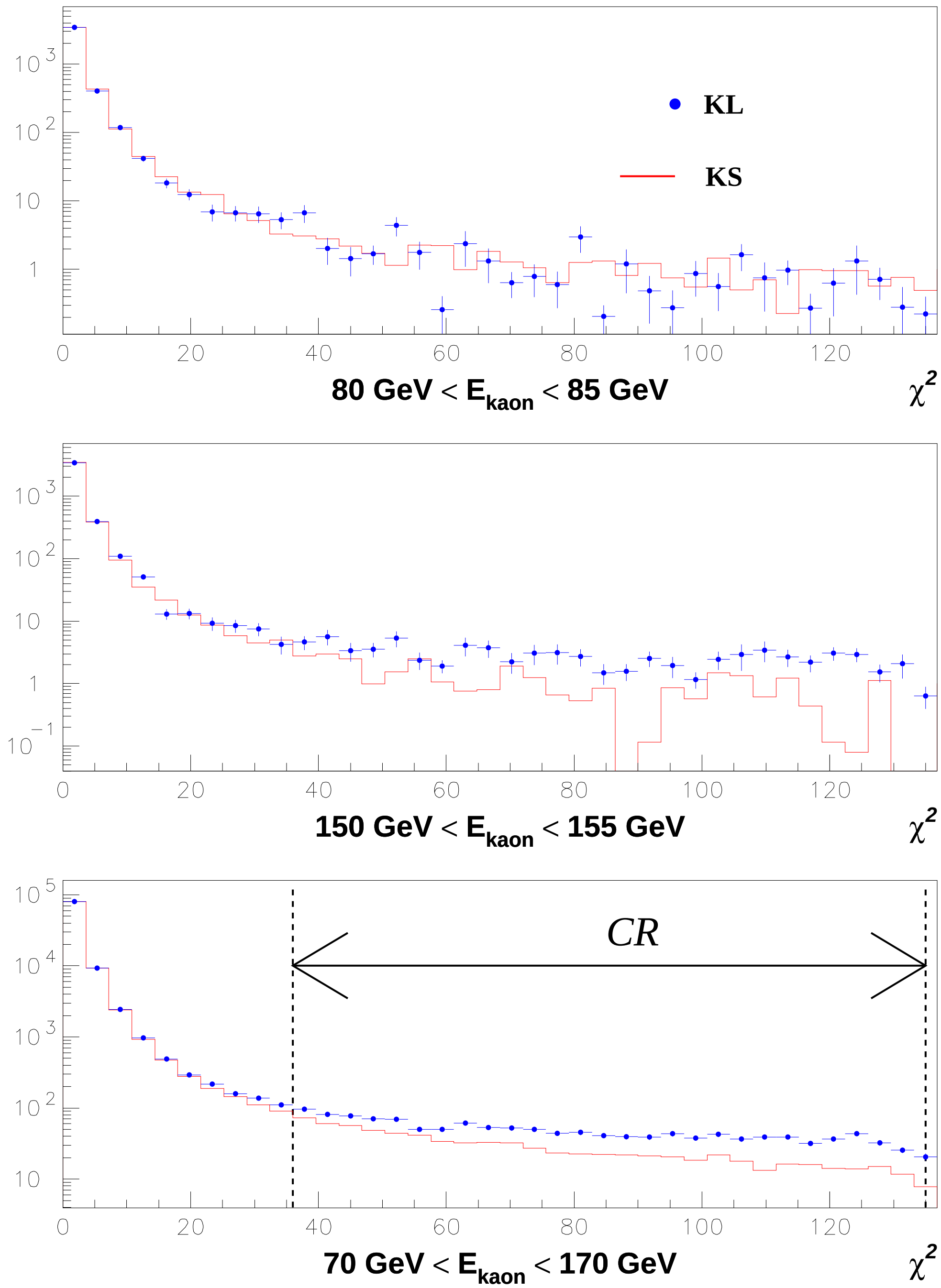

Figure 7.4: Distributions of $\chi^2_{2\pi^0}$ for K_L events, compared with the same distribution for K_S events, normalized to K_L in the very first bins. The difference of the two gives the level of background in the K_L sample.

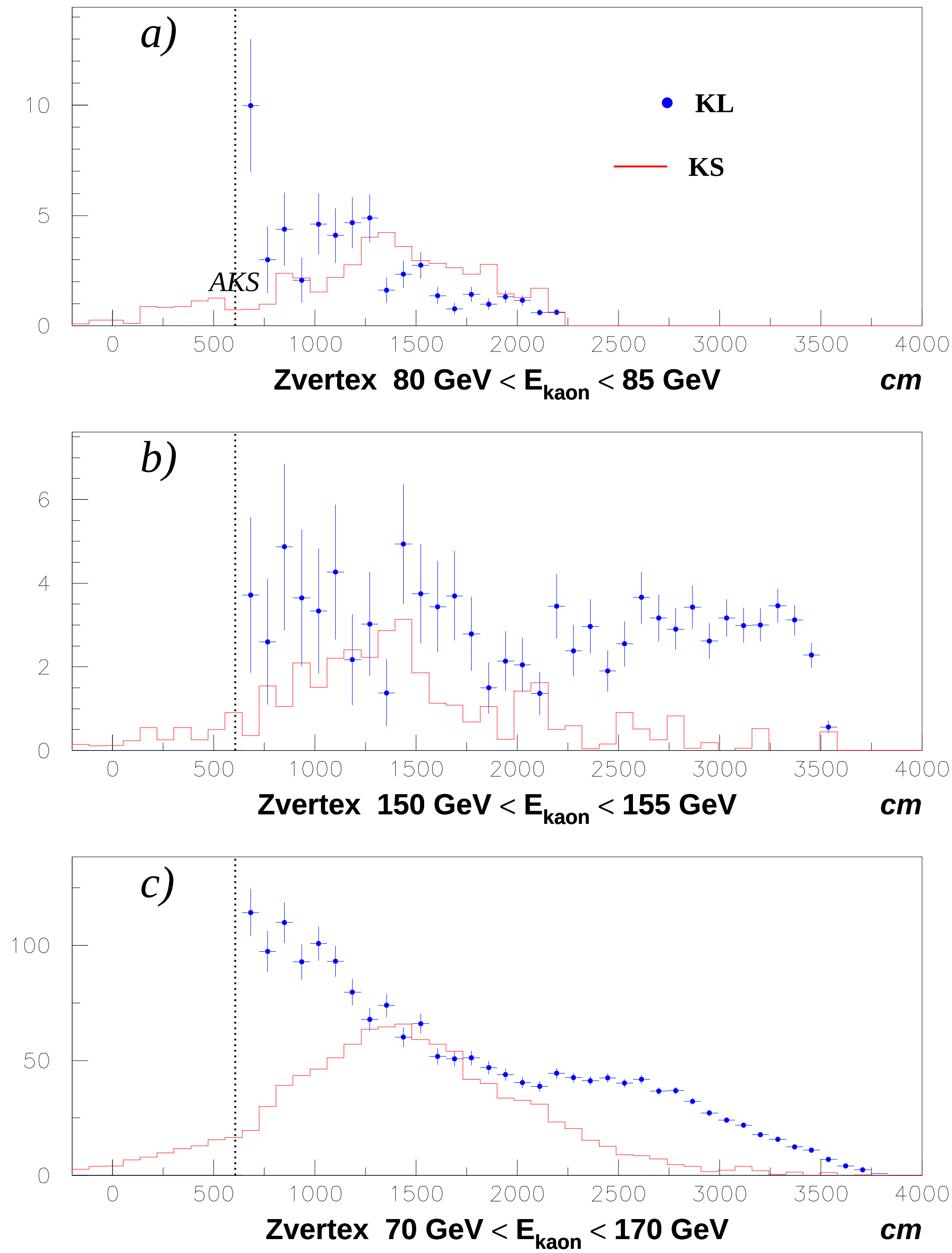

Figure 7.5: Reconstructed Z vertex distributions (in cm from K_S target) for the K_S and K_L events in the control region $36 < \chi^2_{2\pi^0} < 135$.

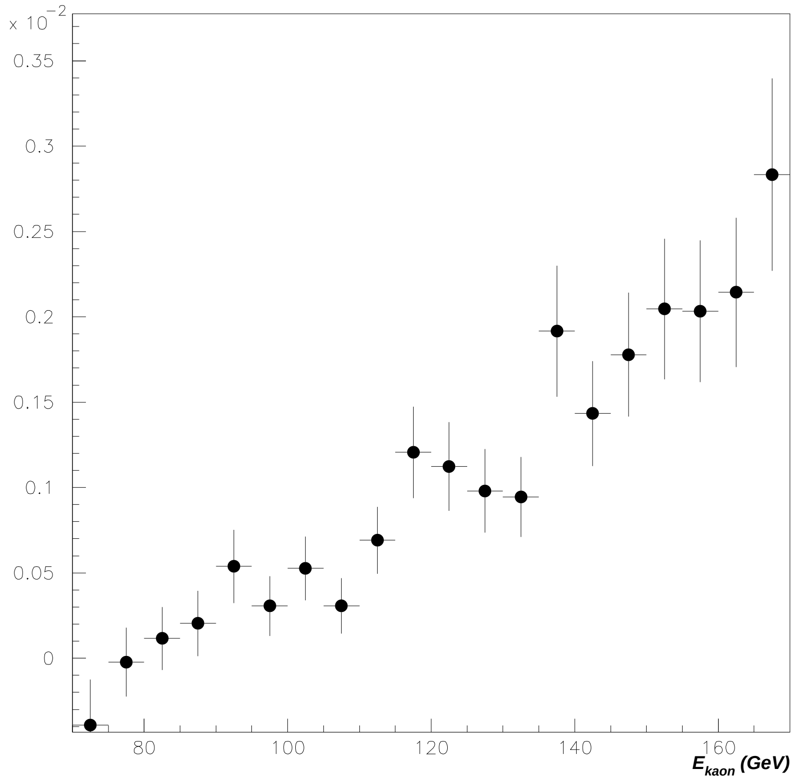

Fraction of neutral background in weighted KL

Figure 7.6: Computed level of $3\pi^0$ background in the final K_L sample, as a function of kaon energy.

ary ($c\tau < 3.5$) though generated inside[2]. For the K_S beam, the AKS veto avoids to have gains and losses around $z = 0$ and the only effect is the average event loss from $c\tau < 3.5$, statistically negligible because of the K_S lifetime. In fact, if we compare the Z decay distributions for K_S and K_L in the CR, we see that the distributions are quite different, but for the low–energy bins for which no relevant background is expected from Montecarlo, the integrals are indeed compatible within errors (see fig. 7.5a). For higher energies, the background appears at large values of Z (fig. 7.5b). Thus, it is strongly suppressed by the K_L weighting.

The fraction of background events as a function of energy is showed in fig. 7.6. It is subtracted in each energy bin from the $K_L \to \pi^0\pi^0$ sample. The average on the whole energy spectrum is $(10 \pm 2) \cdot 10^{-4}$, where the error is dominated by the

[2]This is strictly true only if we neglect the acceptance variation with Z. Since a 10 % accuracy on the background estimation is sufficient, the approximation is fully justified.

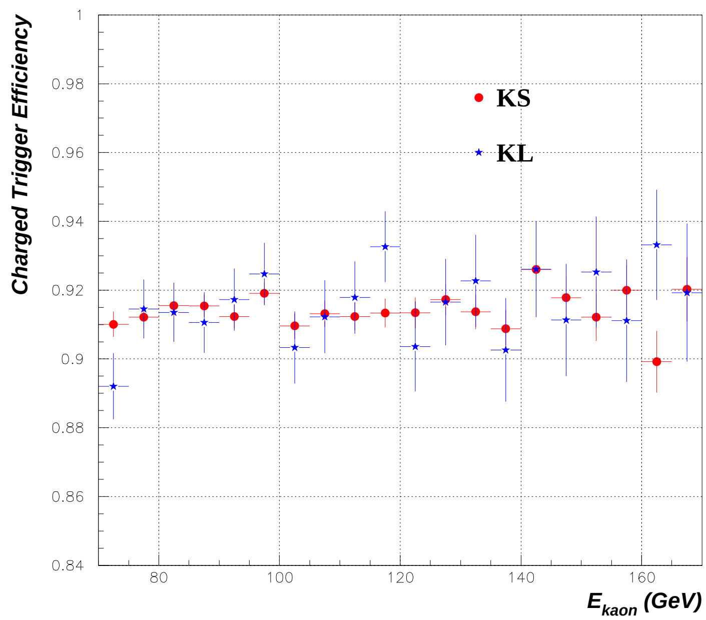

Figure 7.7: Measured charged trigger efficiency for K_S and weighted K_L events (identified by mean of the vertex).

uncertainty on the extrapolation factor.

7.5 Charged Trigger Efficiency

The efficiency of the trigger chain can be measured separately for K_S and weighted K_L events (vertex–identified) using the control triggers, as discussed in section 4.8.1. We get

$$K_S: \quad 0.9138 \pm 0.0010 \qquad \text{weighted } K_L: \quad 0.9143 \pm 0.0018$$

The correction coming from the measured difference is applied for each energy bin (see fig. 7.7), and the effect on the average R is

$$(\Delta R)_{charged\ trigger} = (6 \pm 23) \cdot 10^{-4}$$

7.6 Neutral Trigger Efficiency

The efficiency for K_S and weighted K_L , measured by mean of the $NHOD$ triggers, are

$$K_S: \quad 0.9986 \pm 0.0004 \qquad \text{weighted } K_L: \quad 0.9987 \pm 0.0010$$

Though the comparison is limited by the statistical accuracy of the control samples, the smallness of the inefficiency makes the possible effect on the double ratio negligible, since rate effects are not expected to generate a difference of inefficiency larger than 10 %.

7.7 Accidental activity

The events overlayed with random events (described in section 4.9) are used to account for a potentially different accidental activity affecting K_S and K_L events.

We use all the overlayed events, independently from the random type, rejecting only random events containing a dead time condition (overflow or MBX dead time bit). Events are identified with the tagger for both decay modes, and then corrected for mistagging.

The selections of events before and after the overlay are compared, and the following quantities are computed for each decay mode:

the number of *lost* events N_l, i.e. the events accepted before the overlay and rejected afterwards;

the number of *gained* events N_g, i.e. the events rejected before the overlay and accepted afterwards;

the difference of the weights for events accepted both before and after the overlay:

$$\Delta W = \sum w(Z') - \sum w(Z)$$

The resulting values, normalized to the events before the overlay ($\sum w(Z) + N_l$), are shown in figures 7.8 and 7.9.

The total variation (gains+ΔW−losses) is about -2 % for charged events, dominated by the DCH overflows that arise after the overlay, and -2.3 % for neutrals, dominated by the $\chi^2_{2\pi^0}$ cut.

In the neutral case there are more losses and gains for K_L than for K_S . This is due to the average increase of energy in LKr after the overlay, that moves backward the reconstructed vertex, causing event losses at the beginning of the fiducial region, and gains at its end. Neglecting the acceptance variation with Z, the losses are

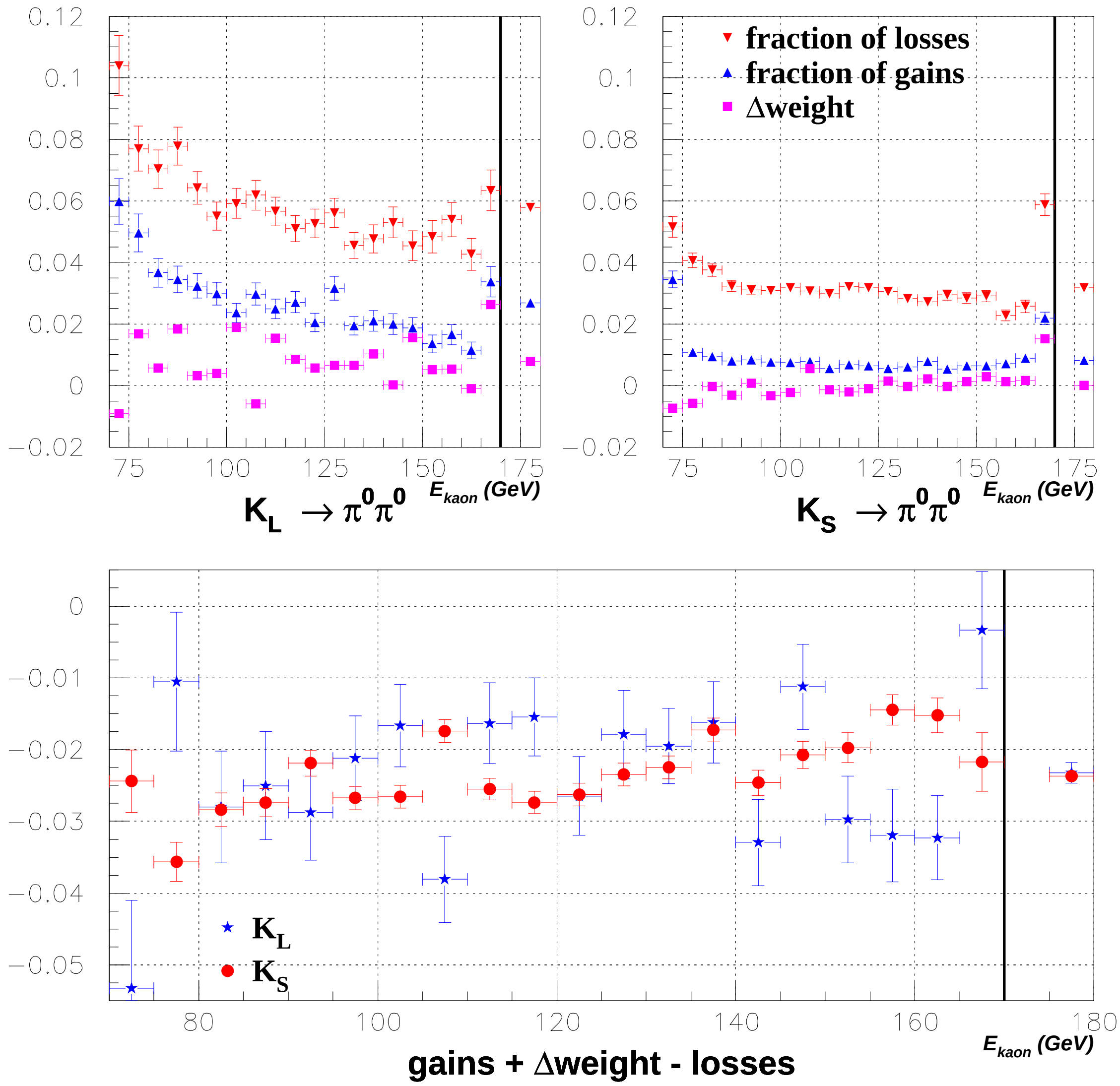

Figure 7.8: Effect of overlays for neutral events. The total losses, gains and change of weight are normalized to the number of events before the overlay. The last bin (after the vertical line) refers to the full energy spectrum

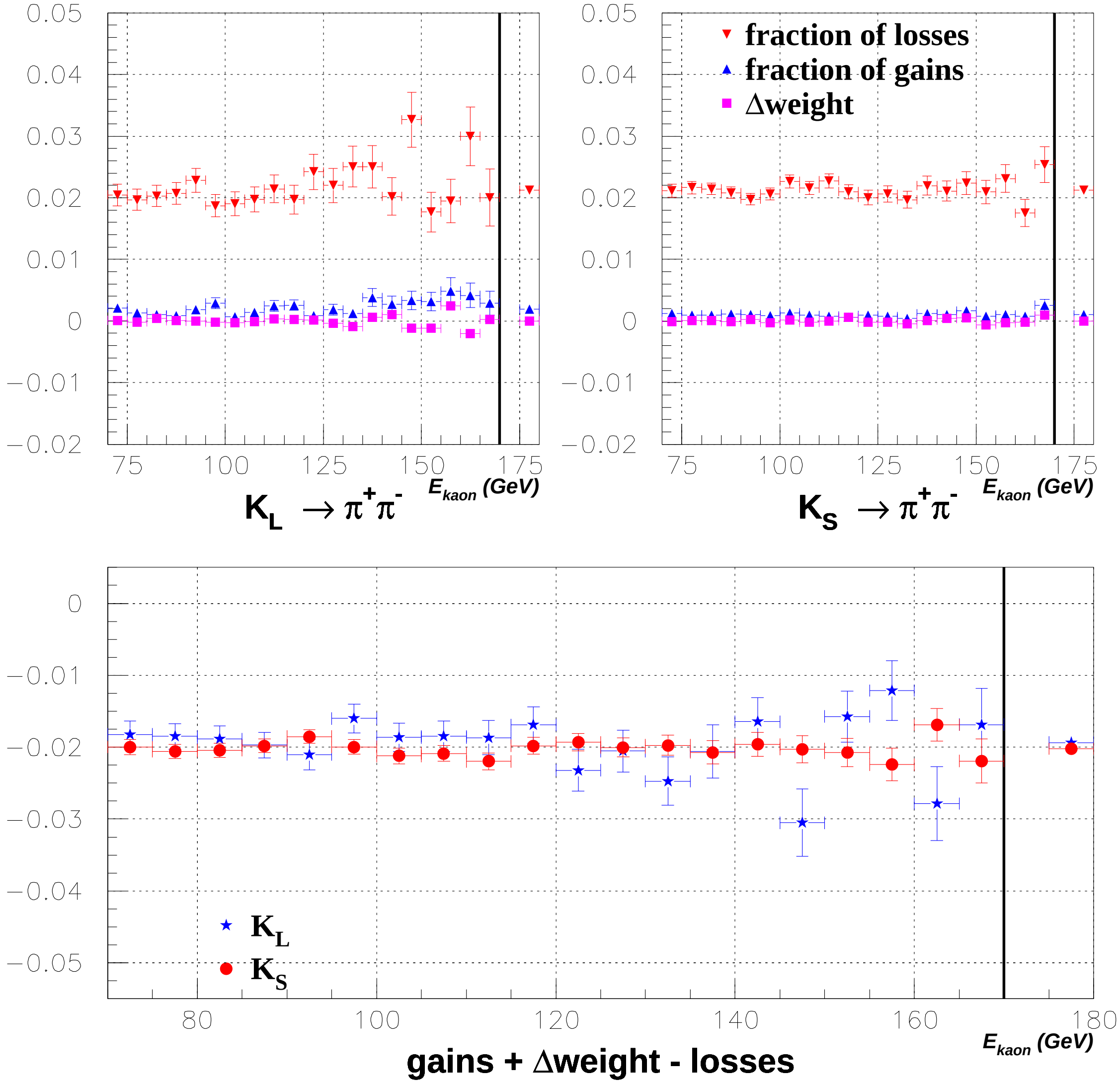

Figure 7.9: Effect of overlays for charged events.

exactly balanced by the gains and the average increase of the event weight (the effect is analogous to the one discussed in the neutral background section). In fact, the total event variation (gains+$\Delta W-$losses) is found to be the same for K_S and K_L .

The total energy variation after the overlay causes, especially in the neutral case, event migration from one bin to another. This is taken into account in ΔW when doing the analysis in energy bins (indeed, its value can be non null also for K_S events). We can also notice the increase of losses and gains in the first and last bins, due to migration across the energy range boundaries. However, the average shift of the energy spectrum is limited to a few 10 MeV, so that no significant slope is generated.

The correction for each decay mode is

$$\frac{N_{true}}{N_{measured}} = \frac{\sum w(Z) + N_l}{\sum w(Z') + N_g}$$

The correction on the double ratio results to be compatible with zero and no trend with energy is observed. Thus, we apply a global correction to R, computed to be

$$(\Delta R)_{accidentals} = (4 \pm 16) \cdot 10^{-4}$$

7.8 Regenerated K_S in the K_L beam

The charged events that are rejected by the p_T' cut were expected to be background or badly reconstructed signal events. The invariant mass distributions for such events shows instead a clear signal peak (fig. 7.10), only in the K_L case. The number of events under the peak is obtained by fitting the mass distribution with a gaussian plus a linear function. The result is that the signal events are 9.5 $\pm$ 2 % of the high–p_T events (${p_T'}^2 > 0.0002$ GeV^2/c^2) that pass the invariant mass cut (*in–mass* events).

The origin of these events has been identified [17] by extrapolating the reconstructed kaon direction back to the position of final collimator. After subtracting the contribution of background, obtained from the properly normalized distribution for high–p_T *out–of–mass* events, a peak corresponding to the position of the collimator border is observed (see fig. 7.11) . The decay distribution can be obtained in the

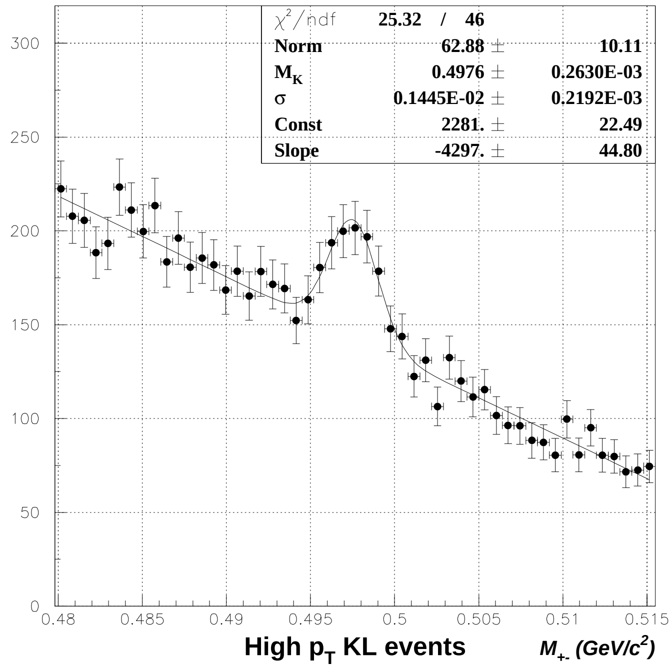

Figure 7.10: Mass distribution for high p_T K_L events.

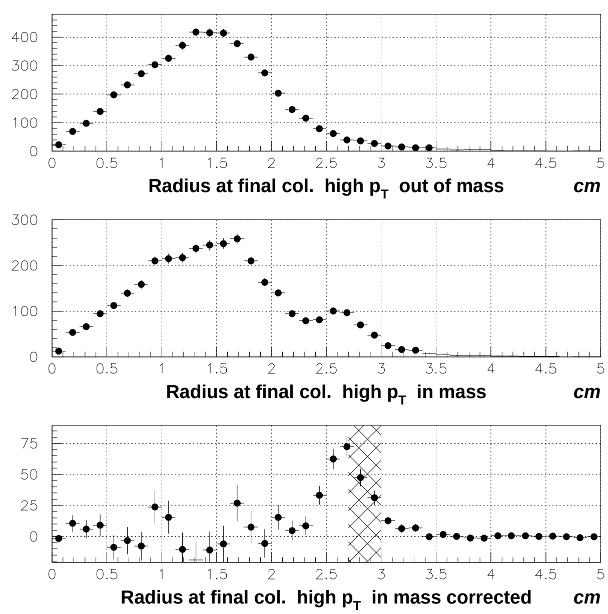

Figure 7.11: Distributions of radial kaon position, extrapolated backward at the position of the final collimator. The first two plots are for the high p_T out–of–mass and in–mass samples. The third one is obtained by subtracting the out–of–mass distribution, normalized to the 90.5 % of the in–mass events, from the second plot. The hatched region corresponds to the lips of the collimator.

same way and is compatible with the K_S lifetime (fig. 7.12a). Thus, the effect is presumably due to K_S regeneration in the lips of the final collimator. It is worth to stress that, due to the geometry of the K_L collimators, the regenerated kaons must have been scattered by both the defining and cleaning collimators.

The number of events of these kind that are accepted (having ${p'_T}^2$ <0.0002 GeV^2/c^2) is estimated by extrapolating backward the number of events as a function of ${p'_T}^2$ (fig. 7.13). The error is estimated by comparing the results obtained with different fit functions (exponential or polynomial functions). We find that the total number of high$-p_T$ event is a fraction

$$f^{+-}_{regen} = (11 \pm 2) \cdot 10^{-4}$$

of the charged K_L sample, and the accepted events are a fraction

$$f^{+-}_{regen\ low\ p_T} = (1.1 \pm 0.3) \cdot 10^{-4}$$

Since the same events are expected to contaminate the neutral sample, where they cannot be identified, we need to apply a correction to R amounting to

$$(\Delta R)_{regen} = \frac{1 + f^{+-}_{regen\ low\ p_T}}{1 + A\ f^{+-}_{regen}}$$

where the factor A accounts for the acceptance effect. In fact, since the K_S regenerated events have in principle a different energy spectrum (fig. 7.12b) and a different decay distribution than the K_L ones, their neutral and charged acceptances are not in the same ratio than for the K_L sample:

$$A \simeq \frac{\int_{E_{min}}^{E_{max}} dE \int_0^{3.5\lambda_S} dZ\ a^{00}(Z,E) e^{-2Z/\lambda_S(E)}\ (dN/dE)_{regen}}{\int_{E_{min}}^{E_{max}} dE \int_0^{3.5\lambda_S} dZ\ a^{+-}(Z,E) e^{-2Z/\lambda_S(E)}\ (dN/dE)_{regen}} \cdot \frac{N_L^{+-}}{N_L^{00}}$$

where $a(Z,E)$ are the acceptance functions, $(dN/dE)_{regen}$ the energy decay spectrum of regenerated events, and the factor $e^{-2Z/\lambda_S(E)}$ comes from the product of the natural decay distribution and the weighting function. The spectrum can be extracted from the energy distribution of the charged events, that has been parametrized (hatched curve of figure 7.12b).

Using the acceptances derived from our Montecarlo sample, we have computed $A = 0.9 \pm 0.1$, where the error is dominated by the uncertainty on the spectrum (we have applied an extra slope of ± 50 %/100 GeV).

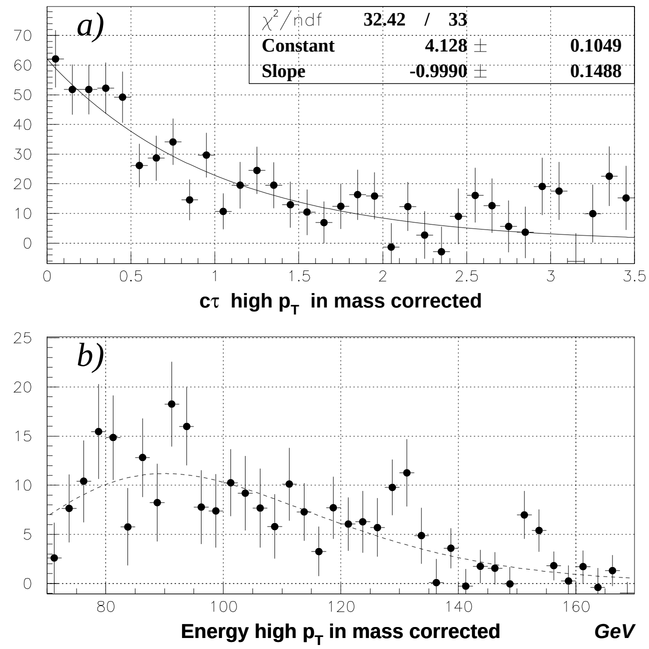

Figure 7.12: Longitudinal decay vertex (in K_S lifetimes) and energy distributions for the high–p_T events after background subtraction. A cut on the radial position at final collimator between 2.2 and 3.2 cm is also applied.

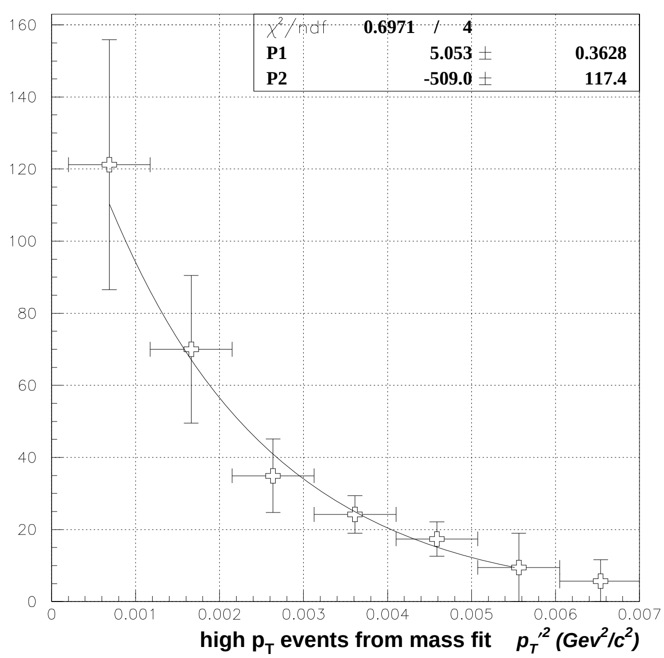

Figure 7.13: Number of fitted high–p_T events in bins of ${p'_T}^2$.

We conclude that the correction is

$$(\Delta R)_{regen} \;=\; (-10 \pm 3) \cdot 10^{-4}$$

7.9 Energy scale

The effect of the uncertainty on the neutral energy scale $\Delta\alpha = \pm 5 \cdot 10^{-4}$ given in section 4.5.1 has been measured by repeating the analysis after applying a scale factor $1 \pm 5 \cdot 10^{-4}$ to the measured cluster energies, and looking at the corresponding changes of R. As expected from expression 4.31, we get

$$(\Delta R)_{neutral\ energy\ scale} \;=\; \pm\, 5 \cdot 10^{-4}$$

If we combine in quadrature this error with the uncertainties on transverse scale, linearity, uniformity, photon energy and position corrections, (quoted in section 4.6), we get to a total systematic error from neutral reconstruction

$$(\Delta R)_{neutral\ reconstruction} \;=\; \pm\, 12 \cdot 10^{-4}$$

7.10 The result

The statistics of the selected events from the 1997 run is shown in table 7.1 before any correction, leading to a double ratio, averaged over the energy bins, of 0.9775 $\pm$ 0.0028 .

mode	$K_L \to \pi^0\pi^0$	$K_L \to \pi^+\pi^-$	$K_S \to \pi^0\pi^0$	$K_S \to \pi^+\pi^-$
unweighted	435.1	954.0	1039.9	2220.9
weighted	122.79	268.56		

Table 7.1: 1997 event statistics in thousand of events.

The set of corrections that have to be applied, described throughout this thesis, are listed in table 7.2.

We define the "systematic" error on R as the uncertainties on these corrections, even if most of them are of statistical nature, since the accuracy of the corrections is often limited by the statistics of the control samples (it is the case for the effects of charged trigger and accidentals, that are the largest sources of uncertainty).

The double ratio is plotted as a function of energy in fig. 7.14, after all the corrections that have been obtained in energy bins. The χ^2 for the hypothesis of a value independent on energy is 27.5 with 19 degrees of freedom. A suspected energy dependence of the result has been ruled out after extensive checks on all the sources of systematic error. Furthermore, this apparent trend with energy is strongly disfavored by the three additional data points outside the nominal energy range that are shown as well in fig. 7.14 but have not been used in the analysis.

Effect	per bin	Correction $\times 10^4$		
mistagging using $\alpha_{LS}^{+-}, \alpha_{SL}^{+-}$	yes	+ 61	$\pm$	3
mistagging $\Delta\alpha_{LS}$	no	+ 18	$\pm$	8
mistagging $\Delta\alpha_{SL}$	no		$\pm$	5
$\pi^+\pi^-$ background	yes	+ 23	$\pm$	4
$\pi^0\pi^0$ background	yes	− 8	$\pm$	2
charged trigger efficiency	yes	+ 6	$\pm$	23
acceptance	yes	+ 18	$\pm$	8
accidental activity	no	+ 4	$\pm$	16
K_S regeneration	no	−10	$\pm$	3
Neutral reconstruction	no		$\pm$	12
Charged reconstruction	no		$\pm$	5
Total		+112	$\pm$	34

Table 7.2: Systematic corrections applied to the double ratio. In the "per bin" column we have specified which correction are applied in energy bins. In this case the correction to R is obtained from the differences of the averaged values before and after the correction.

The corrected double ratio is $R = 0.9887 \pm 0.0028 \pm 0.0034$, leading to[3]

$$Re\left(\frac{\epsilon'}{\epsilon}\right) = (18.8 \pm 4.7 \pm 5.7) \cdot 10^{-4}$$

By adding the statistical and "systematic" errors in quadrature, we get the final result

$$\boxed{\mathbf{Re}\left(\frac{\epsilon'}{\epsilon}\right) = (\mathbf{18.8} \pm \mathbf{7.4}) \cdot \mathbf{10^{-4}}}$$

[3]the small difference between the result of the present analysis and the published one [26], that is well within the systematic uncertainties, is due to small differences in the methods used to compute the corrections and to the different Montecarlo sample we have used (only the uncorrelated MC was used in the official analysis).

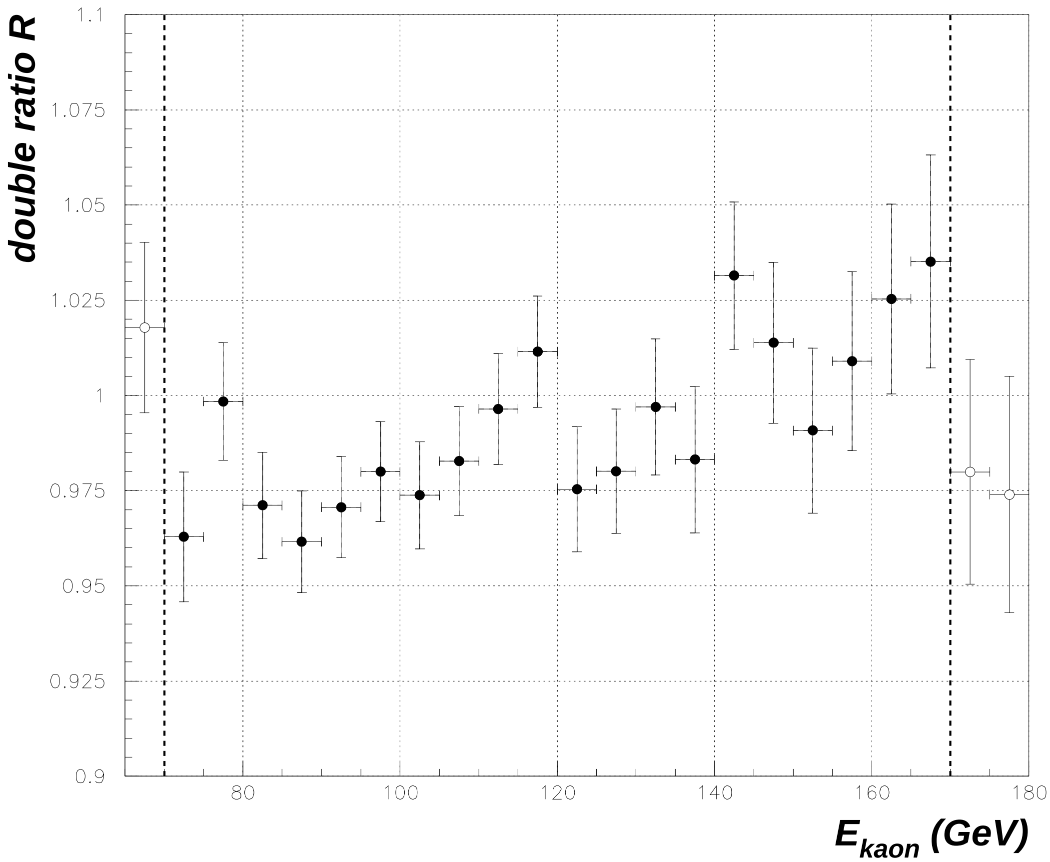

Figure 7.14: Result for the double ratio in energy bins. The corrections and uncertainties that have been applied for the full energy spectrum, and not on a bin by bin basis, are not included. Three energy bins outside the nominal energy range of the analysis (70 to 170 GeV) have been added as a check against a possible energy dependence of the result.

Conclusions

This thesis was devoted to the first result of the NA48 experiment on direct CP violation in kaon decays. It is the first outcome of a large experimental project, started in 1990, involving 16 institutions[4].

We have entered the collaboration in 1997, when the detector was completed and the data used in this analysis were being acquired. Thus, though we have participated to the data–taking during 1998 and 1999, our work in the experiment was mainly devoted to offline data analysis.

The determination of the value of $Re(\epsilon'/\epsilon)$ from the 1997 data sample involved the long and accurate work of many people. In this thesis we have introduced the analysis by summarizing our understanding of the strategy adopted in the collaboration to deal with the various effects that affect the measurement.

We have then discussed in detail our personal studies through which we have contributed to the final result. The differences in acceptance for the K_S and K_L beams have been investigated using a correlated Montecarlo technique that helped us in disentangle the various effects and allowed to obtain the required statistical accuracy with a relatively small sample. We have shown that the systematic uncertainty on this correction is limited to less than $1 \cdot 10^{-4}$ on ϵ'/ϵ . Furthermore, it is dominated by the discontinuity in the active calorimeter volume due to a column not connected to HV during the 1997 data–taking, so that the error will be smaller for the analysis of the data acquired afterwards.

We have also investigated the effect on the analysis of the "impurities" in the K_L beam, namely the contribution to $\pi\pi$ decays from pure K_S and K_S /K_L interference.

[4]The NA48 collaboration is: Cagliari, Cambridge, CERN, Dubna, Edinburgh, Ferrara, Florence, Mainz, Orsay, Perugia, Pisa, Saclay, Siegen, Torino, Vienna, Warsaw.

We have directly measured the amplitude of the interference term that is found to be consistent with the expected mixture of K^0 and $\bar{K}^0$ in the K_L beam line. We have also shown that, if the impurities are properly taken into account in the K_L weighting function, the effect on ϵ'/ϵ , averaged over the nominal energy range, is limited to a few 10^{-5}.

Finally, we have developed a computer program to compute the double ratio and all the main corrections that have to be taken into account, following the procedures developed inside the collaboration. The result is

$$Re\left(\frac{\epsilon'}{\epsilon}\right) \;=\; (18.8\;\pm\;7.4)\;\times 10^{-4}$$

that reproduces the official result recently published by the collaboration [26].

Though the accuracy of the measurement is still poor with respect to the potentiality of the experiment, this result by itself strongly points to a non–zero value of ϵ', confirming the result of the foregoing experiment NA31 $Re\left(\frac{\epsilon'}{\epsilon}\right) = (23.0 \pm 6.5) \cdot 10^{-4}$ and the recent result from KTEV $Re\left(\frac{\epsilon'}{\epsilon}\right) = (28.0 \pm 4.1) \cdot 10^{-4}$ [1].

The analysis of the 1997 data sample demonstrated the effectiveness of the technique used in NA48. In fact, the accuracy of the result was limited by the statistics of the main sample and of the control samples used to evaluate the effect of the trigger efficiency and of the accidental activity. Prospects for the on–going analysis of the data acquired during the 1998 and 1999 runs, corresponding to a statistics about seven times larger than the 1997 one, are thus very good. Another year of data–taking is foreseen to complete the ϵ' program, in order to reach the aimed accuracy of $2 \cdot 10^{-4}$ on $Re(\epsilon'/\epsilon)$.

Bibliography

[1] ALAVI-HARATI, A., ET AL. Observation of Direct CP Violation in $K_{S,L} \rightarrow \pi\pi$ Decays. *Phys. Rev. Lett. 83* (1999), 22.

[2] ARCIDIACONO, R. *Systematic effects on ϵ'/ϵ in the NA48 experiment at CERN: trigger efficiencies and correction due to accidentals.* PhD thesis, Università di Torino, 1999.

[3] BARR, G. D., ET AL. Proposal for a precision measurement of ϵ'/ϵ in CP violating $K^0 \rightarrow 2\pi$ decays. CERN-SPSC/90-22, July 1990.

[4] BARR, G. D., ET AL. A new measurement of direct CP violation in the neutral kaon system. *Phys. Lett. B317* (1993), 233–242.

[5] BELUSEVIC, R. Neutral kaons. KEK–PREPRINT–97–264.

[6] BERGAUER, H., ET AL. The Tagging Detector of the CP-violation Experiment NA48 at CERN. *Nucl. Instrum. Meth. A419* (1998), 623.

[7] BIINO, C. presentation at NA48 meeting, February 1999.

[8] BIINO, C., ET AL. The simultaneous long and short lived neutral kaon beams for experiment NA48. CERN–SL–98–033, 1998.

[9] BIZZETI, A., ET AL. The NA48 K_S monitor. NA48 note 97–29, 1997.

[10] BURAS, A. J. CP Violation and Rare Decays of K and B Mesons. hep–ph/9905437.

[11] BURAS, A. J. Theoretical Status of ϵ'/ϵ. hep–ph/9908395.

[12] CABIBBO, N. Unitary Symmetry and Leptonic Decays. *Phys. Rev. Lett. 10* (1963), 531.

[13] CAROSI, R., ET AL. A measurement of the phases of the CP–violating amplitudes in $K^0 \to 2\pi$ decays and a test of CPT invariance. *Phys. Lett. B237* (1990), 303.

[14] CASO, C., ET AL. Review of Particle Physics. Particle Data Group. *Eur. Phys. J. C3* (1998), 1–794.

[15] CECCUCCI, A. presentation at NA48 meeting, January 1999.

[16] CERN PROGRAM LIBRARY W5013. *GEANT, Detector Description and Simulation Tool*, October 1994.

[17] CHOLLET, C. presentation at NA48 meeting, March 1999.

[18] CHRISTENSON, J. H., CRONIN, J. W., FITCH, V. L., AND TURLAY, R. Evidence for the 2 π Decay of the K(2)0 Meson. *Phys. Rev. Lett. 13* (1964), 138.

[19] CIUCHINI, M., FRANCO, E., GIUSTI, L., LUBICZ, V., AND MARTINELLI, G. Combined analysis of the unitarity triangle and CP violation in the Standard Model. hep–ph/9910236.

[20] CIUCHINI, M., FRANCO, E., GIUSTI, L., LUBICZ, V., AND MARTINELLI, G. ϵ'/ϵ from lattice QCD. hep–ph/9910237.

[21] COHEN, A. G., RUJULA, A. D., AND GLASHOW, S. L. A Matter - Antimatter Universe? *Astrophys. J. 495* (1998), 539.

[22] DEBU, P., AND GRANIER, R. 1997 Charged Trigger Efficiency. NA48 note 98-8, 1998.

[23] DOBLE, N., GATIGNON, L., AND GRAFSTROM, P. A Novel application of bent crystal channeling to the production of simultaneous particle beams. *Nucl. Instrum. Meth. B119* (1996), 181.

[24] DORFAN, D. E., ET AL. Charge Asymmetry in the Muonic Decay of the K0(2). *Phys. Rev. Lett. 19* (1967), 987–993.

[25] Ellis, J., Gaillard, M. K., Nanopoulos, D. V., and Rudaz, S. The Phenomenology of the Next Lefthanded Quarks. *Nucl. Phys. B131* (1977), 285.

[26] Fanti, V., et al. A new measurement of direct CP violation in two pion decays of the neutral kaon. *Phys. Lett. B465* (1999), 335.

[27] Fischer, G., et al. A 40–MHz–pipelined trigger for K0 $\rightarrow 2\pi^0$ decays for the CERN NA48 experiment. *Nucl. Instrum. Meth. A419* (1998), 695.

[28] G. Lüders. *Kgl. Danske Videnskab Selskab, Mat.fys. Medd. 28*, 5 (1954).

[29] Gibbons, L. K., et al. Measurement of the CP violation parameter $Re(\epsilon'/\epsilon)$. *Phys. Rev. Lett. 70* (1993), 1203–1206.

[30] Giudici, S. LKr Energy Scale 1997. NA48 note 99-16, 1999.

[31] Glashow, S. L., Iliopoulos, J., and Maiani, L. Weak Interactions with Lepton – Hadron Symmetry. *Phys. Rev. D2* (1970), 1285.

[32] Goldhaber, M., Grodzins, L., and Sunyar, A. W. Helicity of Neutrinos. *Phys. Rev. 109* (1958), 1015.

[33] Grafstrom, P., et al. A Proton Tagging Detector for the NA48 Experiment. *Nucl. Instrum. Meth. A344* (1994), 487–491.

[34] Griesmayer, E., et al. Comparison of field calculations and measurements of a spectrometer magnet. *Nucl. Instrum. Meth. A361* (1995), 466.

[35] Iconomidou Fayard, L. presentation at NA48 meeting, June 1999.

[36] Kobayashi, M., and Maskawa, T. CP Violation in the Renormalizable Theory of Weak Interaction. *Prog. Theor. Phys. 49* (1973), 652.

[37] Landau, L. On the Conservation Laws for Weak Interactions. *Nucl. Phys. 3* (1957), 127.

[38] Lee, T. D., and Yang, C. N. Question of Parity Conservation in Weak Interactions. *Phys. Rev. 104* (1956), 254.

[39] LENTI, M. Neutral Tagging Dilution in 97 data using $K_L \rightarrow 3\pi^0$. NA48 note 99-16, 1999.

[40] LENTI, M. Neutral Tagging Inefficiency in 97 data: an alternative way. NA48 note 99-03, 1999.

[41] MANNELLI, I. Dilution. NA48 note 98–21, 1998.

[42] MASIERO, A. CP Violation for Pedestrians. CERN yellow book 94-04, 1994. Lectures given at the 1993 European School of High-Energy Physics.

[43] MELE, S. Indirect Measurement of the Vertex and Angles of the Unitarity Triangle. *Phys. Rev. D59* (1999), 113011.

[44] NIR, Y. CP Violation In and Beyond the Standard Model, July 1999. Lectures given at the 1999 SLAC Summer Institute.

[45] PALESTINI, S. The liquid krypton calorimeter for experiment CERN-NA48. *Nucl. Instrum. Meth. A367* (1995), 263.

[46] PARODI, F., ROUDEAU, P., AND STOCCHI, A. Constraints on the parameters of the V(CKM) matrix by End 1998. hep-ex/9903063.

[47] PECCEI, R. D., AND QUINN, H. R. CP Conservation in the Presence of Pseudoparticles. *Phys. Rev. Lett. 38* (1977), 1440–1443.

[48] SAKHAROV, A. D. Violation of CP Invariance, C Asymmetry, and Baryon Asymmetry of the Universe. *Pisma Zh. Eksp. Teor. Fiz. 5* (1967), 32–35.

[49] SCHWINGER, J. The Theory of Quantized Fields. 1. *Phys. Rev. 82* (1951), 914–927.

[50] UNAL, G. presentation at NA48 meeting, May 1999.

[51] V. SCHÖNHARTING. The NMC User's Guide. NA48 note 96-17, 1996.

[52] VAINSHTEIN, A. How penguins started to fly. The 1999 Sakurai Prize lecture, hep-ph/9906263.

[53] Vallage, B., et al. The charged trigger system of NA48 at CERN. *Nucl. Instrum. Meth. A419* (1998), 686.

[54] Vattolo, D. Neutral Tagging Efficiency with 1997 data. NA48 note 98-7, 1998.

[55] Watson, K. M. The Effect of final state Interactions on Reaction Cross–Sections. *Phys. Rev. 88* (1952), 1163–1171.

[56] Weinberg, S. A New Light Boson? *Phys. Rev. Lett. 40* (1978), 223–226.

[57] Wolfenstein, L. Violation of CP Invariance and the Possibility of Very Weak Interactions. *Phys. Rev. Lett. 13* (1964), 562–564.

[58] Wolfenstein, L. Parametrization of the Kobayashi–Maskawa Matrix. *Phys. Rev. Lett. 51* (1983), 1945.

[59] Wu, C. S., Ambler, E., Hayward, R. W., Hoppes, D. D., and Hudson, R. P. Experimental test of parity conservation in beta decay. *Phys. Rev. 105* (1957), 1413.

Acknowledgments

I would first like to express my gratitude to all the members of the NA48 collaboration who helped me to approach the experiment with their explanations, suggestions, encouragement and friendship.

I am particularly indebted with Jean Duclos, who introduced me to the correlated Montecarlo, with Sandro Palestini who helped me in the analysis about interference, with Louis Fayard, Augusto Ceccucci, and all my colleagues of the Florence group, and particularly Massimo Lenti and Gianmaria Collazuol, for discussions and suggestions.

I wish to thank professors Enrico Iacopini and Mario Calvetti for having always demonstrated me their confidence despite my poor communicability.

The nice time spent together in Geneva and elsewhere was an important part of my NA48 experience, and I want to thank for this, among many others, Gianmaria, Marco, Michela, Roberta (thank you also for the figures!), Giacomo and Sergio.

The last but maybe most important thought is for my family and all my friends for their patience and understanding.